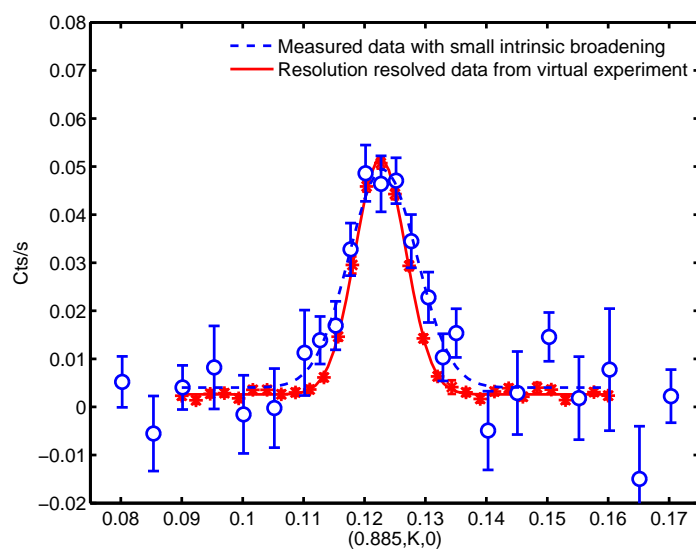


# Superoxygenated $\text{La}_{2-x}\text{Sr}_x\text{CuO}_{4+y}$ - virtual and physical experiments

PhD Thesis in Physics by

Linda Udby



Materials Research Division, Risø-DTU

&

Nanoscience Center, Niels Bohr Institute, University of Copenhagen

2009



# Contents

<b>1</b>	<b>Introduction</b>	<b>1</b>
1.1	Superconductivity . . . . .	1
1.2	High- $T_c$ superconductivity . . . . .	3
1.3	Experimental techniques . . . . .	5
1.4	Simulated neutron scattering . . . . .	5
1.5	Supplementary information to this thesis . . . . .	6
<b>2</b>	<b>Properties of LSCO</b>	<b>7</b>
2.1	$T$ - $x$ phase diagram . . . . .	8
2.2	$H$ - $r$ phase diagram . . . . .	9
2.3	Crystal structure . . . . .	11
2.4	Microscopic picture . . . . .	13
2.5	Static magnetism in LSCO . . . . .	15
2.6	Magnetic excitations in LSCO . . . . .	16
2.7	Length scales and morphology . . . . .	20
<b>3</b>	<b>Scattering methods</b>	<b>23</b>
3.1	Experimental neutron scattering . . . . .	23
3.1.1	The scattering process . . . . .	24
3.1.2	Triple axis spectrometer . . . . .	25
3.1.3	Ideal and imperfect crystals . . . . .	26
3.1.4	Resolution . . . . .	27
3.2	Hard x-ray diffraction . . . . .	29
3.3	Peak shapes and widths . . . . .	31
3.3.1	Gaussian line shape . . . . .	31
3.3.2	Lorentzian line shape . . . . .	32
3.3.3	Voigt line shape . . . . .	32
3.4	Domain size distributions . . . . .	33
3.5	Simulated neutron scattering . . . . .	36
3.5.1	Introduction to Mcstas . . . . .	36
3.5.2	Building an instrument in McStas . . . . .	37
3.5.3	Running McStas . . . . .	39
<b>4</b>	<b>Properties of LSCO+O</b>	<b>41</b>
4.1	Lightly hole-doped samples . . . . .	41
4.2	Highly hole-doped samples . . . . .	42
4.3	Sr/O co-doped single-crystals . . . . .	44
4.4	Phase diagram . . . . .	44

4.5	Crystal structure . . . . .	48
4.5.1	The Bmab phase and staging superstructure . . . . .	48
4.5.2	Twinning . . . . .	50
4.6	Structural Diffraction data . . . . .	52
4.6.1	LSCO+O $x=0$ . . . . .	52
4.6.2	LSCO+O $x = 0.04$ . . . . .	55
4.6.3	LSCO+O $x=0.065$ . . . . .	58
4.6.4	LSCO+O $x=0.09$ . . . . .	60
4.6.5	Summary and discussion of the structural diffraction data	61
4.7	The stripe model of LNSCO/LBCO . . . . .	66
4.8	Magnetic structure . . . . .	67
4.8.1	LSCO+O $x=0$ . . . . .	71
4.8.2	LSCO+O $x=0.04$ . . . . .	74
4.8.3	LSCO+O $x=0.065$ . . . . .	77
4.8.4	LSCO+O $x=0.09$ . . . . .	80
4.8.5	Summary and discussion of the magnetic diffraction data	83
<b>5</b>	<b>Virtual experiments on RITA-II</b>	<b>89</b>
5.1	RITA-II line width dependency . . . . .	89
5.2	Adding background to the simulated data . . . . .	90
5.3	Overview of the V-RITA-II instrument . . . . .	91
5.4	Source . . . . .	92
5.5	Guide-section . . . . .	93
5.6	Monochromator . . . . .	94
5.7	Collimators . . . . .	96
5.8	Samples . . . . .	98
5.8.1	Incoherent scatterer . . . . .	98
5.8.2	Powder . . . . .	99
5.8.3	Single crystal . . . . .	100
5.9	Filter . . . . .	100
5.10	Analyser . . . . .	102
5.10.1	Analyser angle . . . . .	102
5.10.2	Analyser mosaicity . . . . .	103
5.11	Detector . . . . .	107
5.12	Controlling the virtual experiment . . . . .	107
5.13	Setting up the imaging mode . . . . .	108
5.13.1	Finding analyser optimal position . . . . .	109
5.13.2	Setting electronic windows . . . . .	111
5.14	Testing the collimators . . . . .	114
5.15	Q-resolution in 2-axis mode . . . . .	117
5.15.1	Finding zero-point of $a_4$ and the absolute energy . . . . .	117
5.15.2	Comparing scans of several PowderN reflections to $Al_2O_3$	119
5.16	Q-resolution in 3-axis mode . . . . .	122
5.16.1	Ge single crystal . . . . .	122
5.16.2	Ge wafer . . . . .	122
5.17	Elastic energy resolution . . . . .	125
5.18	Summary and discussion of the virtual testing experiments . . .	127
5.18.1	Line width . . . . .	127

5.18.2 Intensity . . . . .	128
<b>6 Analysis of LSCO+O diffraction data by virtual experiments</b>	<b>131</b>
6.1 LSCO+O $x=0$ . . . . .	132
6.2 LSCO+O $x=0.04$ . . . . .	135
6.3 LSCO+O $x=0.065$ . . . . .	138
6.4 LSCO+O $x=0.09$ . . . . .	141
6.5 Summary and discussion of the virtual data analysis experiments	147
6.5.1 Line width . . . . .	147
6.5.2 Intensity . . . . .	147
<b>7 Conclusion</b>	<b>149</b>
7.1 Virtual test experiments . . . . .	149
7.2 Resolution line width by virtual experiments . . . . .	149
7.3 Intrinsic line width and transition temperatures . . . . .	150
7.4 Structure . . . . .	151
7.5 Phase separation . . . . .	152
7.6 Outlook . . . . .	152
<b>A BW5 hard x-ray experiments on <math>\text{La}_{2-x}\text{Sr}_x\text{CuO}_{4+\delta}</math> <math>x=0,0.04,0.09</math></b>	<b>i</b>
<b>B TriCS experiments on a large <math>\text{La}_2\text{CuO}_{4+\delta}</math> crystal</b>	<b>xxi</b>
<b>C V-RITA-II McStas code</b>	<b>xxxii</b>
<b>D Recent publications by L. Udby</b>	<b>li</b>

## List of Abbreviations

Abbreviation	Explanation
AFM	Antiferromagnet(ic) or antiferromagnetism
IC	Incommensurate
SC	Superconductor
LDoS	Local Density of States
HTSC	High- $T_c$ superconductor/superconductivity
BSCCO	$\text{Bi}_2\text{Sr}_2\text{CaCu}_2\text{O}_{8+x}$ or $\text{Bi}_2\text{Sr}_2\text{Ca}_2\text{Cu}_3\text{O}_{10+x}$
LSCO	$\text{La}_{2-x}\text{Sr}_x\text{CuO}_4$
LSCO+O	$\text{La}_{2-x}\text{Sr}_x\text{CuO}_{4+y}$ , also denoted by LSCO+O
LCO+O	$\text{La}_2\text{CuO}_{4+y}$ , also denoted by LSCO+O $x=0$
LNSCO	$\text{La}_{1.48}\text{Nd}_{0.4}\text{Sr}_{0.12}\text{CuO}_4$
LBCO	$\text{La}_{1.875}\text{Ba}_{0.125}\text{CuO}_4$
YBCO	$\text{YBa}_2\text{Cu}_3\text{O}_{6+x}$
PSI	Paul Scherrer Institute, CH-5232 Villigen PSI, Switzerland
ILL	Institut Laue-Langevin, F-38000 Grenoble, France
UConn	University of Connecticut, Storrs, 06269-3046 Connecticut, USA
VE	Virtual experiment
TAS	Triple Axis Spectrometer
RITA-II	A cold neutron TAS at PSI featuring a special seven blade analyser
V-RITA-II	The McStas virtual replica of the RITA-II instrument
IN14	A cold neutron TAS at ILL with high flux
PANDA	A cold spin-polarised neutron TAS at the FRM-II reactor D-85747 Garching, Germany
PG	Pyrolytic Graphite
TGA	Thermo Gravimetric Analysis
PSD	Position sensitive detector
$\mu\text{SR}$	The experimental technique of muon spin rotation

# List of Tables

2.1	Some of the allowed reflections in the La-214 series . . . . .	13
4.1	The samples investigated by diffraction in this thesis . . . . .	44
4.2	The diffraction experiments and their samples . . . . .	45
4.3	Fitting parameters of the staging peaks . . . . .	63
4.4	Comparison of (014)+staging intensity for different $x$ . . . . .	64
4.5	Fitting parameters of the (014) peak . . . . .	65
4.6	ZF intensity of IC AFM peaks for different doping $x$ . . . . .	84
4.7	Comparison of ZF IC AFM intensity for $x=0$ and $x=0.09$ . . . . .	85
4.8	The incommensurability as function of $x$ for LSCO+O . . . . .	86
5.1	Intensity for various limits of the source wavelength . . . . .	95
5.2	Simulated flux at sample position . . . . .	99
5.3	Mosaicitities of analyser blades by direct beam measurement . . . . .	103
5.4	Analyser angles as scanned, their set-point values and McStas position. . . . .	109
5.5	Collimator parameters, measured and simulated . . . . .	114
5.6	Measured A4 zero-point and absolute energy . . . . .	118
5.7	Simulated A4 zero-point and absolute energy . . . . .	119
5.8	Measured and simulated values of the energy resolution . . . . .	127
5.9	Precision of the performed virtual test experiments . . . . .	129
6.1	Precision of the performed virtual experiments on fundamental reflections of LSCO+O . . . . .	148



# List of Figures

1.1	Schematic drawing of the Meissner effect . . . . .	2
1.2	The crystal structure of $\text{La}_2\text{CuO}_4$ . . . . .	4
2.1	Generic $T$ - $x$ phase diagram of HTSC cuprates . . . . .	7
2.2	The DSZ phase diagram . . . . .	10
2.3	Structural phase diagram of LSCO and LBCO . . . . .	12
2.4	The magnetic structure of undoped $\text{La}_2\text{CuO}_4$ . . . . .	14
2.5	Magnetic phase diagram of LSCO . . . . .	16
2.6	The incommensurability $\delta$ as a function of onset of $T_c$ . . . . .	17
2.7	The spin fluctuation dispersion as a function of incommensurability $\delta$ . . . . .	18
2.8	The spin-gap and in-gap states in LSCO . . . . .	19
2.9	Evolution of the 'swiss cheese' model with Zn doping . . . . .	22
3.1	Schematic drawing of a neutron TAS . . . . .	26
3.2	Schematic drawing of a resolution ellipsoid . . . . .	29
3.3	A graphical representation of the scattering from a finite size system . . . . .	34
3.4	Lognormal domain size distribution and peak width . . . . .	35
4.1	The miscibility gap for low oxygenation . . . . .	42
4.2	A schematic 3D phase diagram for LSCO+O . . . . .	43
4.3	Field cooled d.c. magnetisation before and after oxidation of LSCO . . . . .	46
4.4	ZF $\mu\text{SR}$ measurements of LSCO+O . . . . .	46
4.5	Relationship between magnetic and SC volume fraction . . . . .	47
4.6	$Bmab$ and staging structure . . . . .	48
4.7	Staging peaks around $Bmab$ reflections . . . . .	50
4.8	Schematic drawing of twinning positions . . . . .	51
4.9	Longitudinal splitting of (020) due to twinning . . . . .	51
4.10	Scans along $L$ through (014) in LSCO+O $x=0$ . Voigt fits. . . . .	53
4.11	Scans along $L$ through (014) in LSCO+O $x=0$ . Gaussian fits. . . . .	54
4.12	Scans along $L$ through (014) in LSCO+O $x=0.04$ . Voigt fits. . . . .	56
4.13	Scans along $L$ through (014) in LSCO+O $x=0.04$ . Gaussian fits. . . . .	57
4.14	Scans along $L$ through (014) in LSCO+O $x=0.065$ . Voigt fits. . . . .	58
4.15	Scans along $L$ through (014) in LSCO+O $x=0.065$ . Gaussian fits. . . . .	59
4.16	Scans along $L$ through (014) in LSCO+O $x=0.09$ . Gaussian fits. . . . .	60
4.17	Comparing neutron and hard x-ray $L$ -scans through (014) for different $x$ . . . . .	61

4.18	Staging number and relative shift from $Bmab$ position . . . . .	62
4.19	Reciprocal space scan points of the 7 analyser blades of RITA-II . . . . .	65
4.20	The stripe model . . . . .	66
4.21	Intensity of scattering from spins diagonal to the Cu-O bonds . . . . .	68
4.22	Models for the magnetic order in La-based cuprates at $x=1/8$ doping . . . . .	69
4.23	Intensity of scattering from spins along Cu-O bonds . . . . .	70
4.24	The enumeration of the IC AFM peaks . . . . .	70
4.25	Transversal scans through (020) and (200) positions for LSCO+O $x=0$ . . . . .	71
4.26	The IC AFM peaks for LSCO+O $x=0$ . . . . .	72
4.27	Temperature dependence of an IC AFM peak for LSCO+O $x=0$ . . . . .	73
4.28	Scans through (010) and (100) for LSCO+O $x=0.04$ . . . . .	74
4.29	The IC AFM peaks for LSCO+O $x=0.04$ . . . . .	75
4.30	Temperature dependence of an IC AFM peak for LSCO+O $x=0.04$ . . . . .	76
4.31	Scans of (010) and (100) of LSCO+O $x=0.065$ . . . . .	77
4.32	Scans through the IC AFM points of LSCO+O $x=0.065$ . . . . .	78
4.33	Temperature dependence of an IC AFM peak for LSCO+O $x=0.065$ . . . . .	79
4.34	Scan through (-100) in LSCO+O $x=0.09$ . . . . .	81
4.35	IC AFM peak of LSCO+O $x=0.09$ . . . . .	81
4.36	Temperature dependence of an IC AFM peak of LSCO+O $x=0.09$ . . . . .	82
4.37	The relative measured peak intensities of the IC AFM peaks . . . . .	84
4.38	Model and calculated relative intensity of IC AFM peaks from spin stripes in 2 layers . . . . .	85
5.1	The V-RITA-II instrument . . . . .	92
5.2	Schematic drawing of the SINQ spallation target at PSI . . . . .	94
5.3	Beam characterisation just before the monochromator . . . . .	95
5.4	Focusing geometry of the monochromator in McStas coordinates . . . . .	97
5.5	Beam characteristics just after the monochromator . . . . .	97
5.6	Beam intensity at the sample position . . . . .	99
5.7	Peak width as function of mosaicity . . . . .	101
5.8	The simulated effect of a Be filter . . . . .	101
5.9	Values of $\Omega_A$ . . . . .	102
5.10	Rocking curves of analyser blades by direct beam measurement . . . . .	104
5.11	Rocking curves of analyser blades by beam from Ge wafer . . . . .	106
5.12	Simulated and measured scans of the blade angles for $\Omega_A = -57.58110$ . . . . .	106
5.13	Simulated and measured scans of the blade angles for $\Omega_A = -55.64111$ . . . . .	106
5.14	PSD image at the detector in monochromatic imaging mode using Vanadium as a sample . . . . .	112
5.15	The vertically summed PSD image . . . . .	113
5.16	Test of collimators . . . . .	115
5.17	PSD images using the three collimators as samples . . . . .	116
5.18	A4 positions of the (10-2) $\text{Al}_2\text{O}_3$ powder peak using different collimators . . . . .	118
5.19	A4 scan of $\text{Al}_2\text{O}_3$ (10-2) powder peak in different windows . . . . .	120
5.20	A4 positions of the $\text{Al}_2\text{O}_3$ powder peaks, measured and simulated . . . . .	121
5.21	Scans through the (111) Bragg reflection of a Ge single crystal . . . . .	123

5.22	Scans through the (111) Bragg reflection of Ge wafer . . . . .	124
5.23	Simulated and measured a4 scan through (111) of Germanium wafer . . . . .	125
5.24	The elastic energy resolution in each electronic window . . . . .	126
6.1	Measured and simulated scans through basic reflections of LCO+O $x=0$ . . . . .	133
6.2	Measured and simulated scans showing staging of LSCO+O $x=0$	134
6.3	Measured and simulated scans through basic reflections of LSCO+O $x=0.04$ . . . . .	136
6.4	Measured and simulated scans showing staging of LSCO+O $x=0.04$	137
6.5	Measured and simulated scans through basic reflections of LSCO+O $x=0.065$ . . . . .	139
6.6	Measured and simulated scans through (014) of LSCO+O $x=0.065$	140
6.7	Measured and simulated scans through basic reflections of LSCO+O $x=0.09$ . . . . .	143
6.8	Measured and simulated scan through the (-100) position of LSCO+O $x=0.09$ . . . . .	144
6.9	Measured and simulated IC AFM peak of LSCO+O $x=0.09$ . . .	144
6.10	Measured and simulated scans through basic reflections of LSCO+O $x=0.09$ . . . . .	145
6.11	Measured and simulated scan through the (014) position of LSCO+O $x=0.09$ . . . . .	146
7.1	Transition temperature in LSCO+O . . . . .	151
7.2	The intensity at the monitor position of RITA-II as function of energy . . . . .	154
A.1	Bragg peak of LSCO+O $x=0$ . . . . .	iii
A.2	Looking for LTT peaks of LSCO+O $x=0$ . . . . .	iv
A.3	Staging peaks of LSCO+O $x=0$ . . . . .	v
A.4	Gridscan of (014) and staging in LSCO+O $x=0$ . . . . .	vi
A.5	Temperature dependence of staging and (014) peaks for LSCO+O $x=0$ . . . . .	vii
A.6	X-ray scan positions looking for charge order . . . . .	viii
A.7	X-ray scans looking for charge order . . . . .	ix
A.8	'Charge order' peaks as function of temperature . . . . .	x
A.9	Bragg peaks of LSCO+O $x=0.04$ . . . . .	xii
A.10	Staging and (014) peaks for LSCO+O $x=0.04$ . . . . .	xiii
A.11	$H, K$ and $L$ -scans through staging and Bragg peaks of LSCO+O $x=0.04$ . . . . .	xiv
A.12	Looking for charge order in LSCO+O $x=0.04$ . . . . .	xv
A.13	Bragg peaks of LSCO+O $x=0.09$ . . . . .	xvii
A.14	Various peaks of LSCO+O $x=0.09$ . . . . .	xviii
A.15	Looking for charge order in LSCO+O $x=0.09$ . . . . .	xix
B.1	$L$ -scans through (0 -3 $L$ ) and (0 -1 $L$ ) for LCO+O $x=0$ . . . . .	xxv
B.2	Staging $T$ -dep and $H$ -scans of LCO+O $x=0$ . . . . .	xxvi
B.3	Peaks at the acclaimed direct oxygen positions . . . . .	xxvii

---

B.4	$L$ -dependence of $B_{mab}$ and direct oxygen peaks . . . . .	xxviii
B.5	Forbidden peaks at $(0\ 0\ L)$ for $L$ odd . . . . .	xxix

## Publications by Linda Udby

Z. Chang, Z. Li, L. Udby et. al, *SRPES studies of NO<sub>2</sub> reaction with vanadium oxide thin films on TiO<sub>2</sub>(110)-1×1*, Surface Science 505 (2002), pp. 71-80

L. Udby, B.M. Andersen and P. Hedegård, *Recursion method for the quasiparticle structure of a single vortex with induced magnetic order*, PRB 73 (2006), pp. 224510.

This publication is also included in Appendix D of this thesis.

C.R.H. Bahl, K. Lefmann, A.B. Abrahamsen, H.M. Rønnow, F. Saxild, T.B.S. Jensen, L.Udby, N.H.Andersen, N.B. Christensen, H.S. Jakobsen, T.Larsen, P.S. Häfliger, S. Streule and Ch. Niedermayer, *Inelastic neutron scattering experiments with the monochromatic imaging mode of the RITA-II spectrometer*, Nucl. Instr. Meth. B 246 (2006) pp 452-462

H.E. Mohottala, B.O. Wells, J.I. Budnick, W.A. Hines, Ch. Niedermayer, L. Udby, C. Bernhard, A.H. Moodenbaugh and F.-C. Chou *Phase separation in super-oxygenated La<sub>2-x</sub>Sr<sub>x</sub>CuO<sub>4+y</sub>*, Nature Materials 5 (2006) pp 377-382.

This publication is also included in Appendix D of this thesis.

K. Lefmann, P.K. Willendrup, L.Udby, B. Lebech, K. Mortensen, J.O. Birk, K. Klenø, P. Christiansen, J. Saroun, J. Kulda, U. Filges, M. Koennecke, P. Tregenna-Pigot, J. Peters, K. Leutenant, G. Zsigmond, P. Bentley and E. Farhi, *Virtual experiments: The ultimate aim of neutron ray-tracing simulations*, accepted for printing Jour. Neutr. Res. (2009)

L. Udby, N. H. Andersen, F. C. Chou, N. B. Christensen, S. B. Emery, K. Lefmann, J. W. Lynn, H. E. Mohottala, Ch. Niedermayer and B. O. Wells, *Magnetic ordering in electronically phase separated Sr/O co-doped La<sub>2-x</sub>Sr<sub>x</sub>CuO<sub>4+y</sub>*, <http://arxiv.org/abs/0904.0095>, accepted for printing in PRB (2009).

This publication is also included in Appendix D of the present thesis.

## Acknowledgements

I would like to thank my supervisors Niels Hessel Andersen and Kim Lefmann for educating support and fruitful discussions. Barrett O. Wells for lending me the samples and good discussions. Peter Willendrup and Erik Knudsen for support on McStas and other computer related issues, Uwe Filges for help with the McStas neutron source and gold foil measurements. Thomas Bagger Stibius Jensen for help during scattering experiments and Matlab code. Jonas Okkels Birk for providing information about the guide system to RITA-II and Matlab code. Hashini E. Mohottala and Samuel B. Emery for superoxygenation of the samples and providing supplementary data. Christof Niedermayer, Asger Bech Abrahamsen, Niels Bech Christensen, Jari í Hjöllum, Rasmus Toft-Pedersen, Jeff Lynn and Johan Chang for help during experiments and good discussions. Brian Møller Andersen and Per Hedegård for collaboration on the theoretical work. Jean-Claude Grivel for teaching me how to produce high- $T_c$  superconductors on my own, and Bente Lebech for teaching me classic virtues of neutron scattering. Ask Bojesen for LaTeX and personal support.

# Chapter 1

## Introduction

One of the major challenges of the industrialised world is the production and distribution of environmentally friendly energy. Even if huge parks of wind-mills at sea are realised the produced electricity still needs to be transported over hundreds of kilometres to the densely populated areas where it is needed. Superconducting cables could be used to transport the current with little or no loss if the current techniques of production of the cables are developed and superconductors with better characteristics are engineered.

In Section 1.1 the phenomenology of superconductivity is introduced, and a special class of superconductors known as high- $T_c$  superconductors (to which class the system studied in this thesis belongs) are introduced in Section 1.2. Some experimental techniques to study these materials are touched upon in Section 1.3. Among the widely used experimental techniques is neutron scattering which can also be quite accurately simulated by virtual experiments introduced in Section 1.4. Some of the supplementary information which is useful for this thesis has been included in the appendices which are introduced in Section 1.5.

### 1.1 Superconductivity

Superconductivity is a quantum mechanical phenomenon occurring in certain materials at temperatures below  $T_c$  and it is characterised by zero dc resistivity. Another property is the exclusion of magnetic flux so that the superconductor acts as a perfect diamagnet below  $H_{c1}$ , a phenomenon known as the (complete) Meissner effect [1]. When the magnetic field exceeds  $H_{c1}$ , superconductivity breaks down in type-I superconductors. Type-II superconductors do not expell the magnetic field completely from the volume of the sample, but allow fluxlines to penetrate in areas where superconductivity is suppressed, see Figure 1.1. In clean type-II superconductors, to which category the high- $T_c$  superconductors belong, the suppression of superconductivity in the so-called mixed state is modelled by vortices. The fluxlines within the superconductor in the mixed state form lattices which can be studied by e.g. small angle neutron scattering [2, 3]. Each vortex contains one flux quantum and as the field is increased the vortices pack more densely until at  $H_{c2}$  where the mixed state (vortex state) of type-II superconductors breaks down, and superconductivity is lost. A vortex can be trapped in an (immobile) region of suppressed superconductivity due to

e.g. crystal defects or impurities thereby 'pinning' the magnetic flux.

Superconducting cables might be part of the solution to the problem of generating and utilising current from the windmill parks at sea. Both in terms of the possibility to provide lighter generators for the huge windmills, since they would eliminate the use of heavy iron cores, and in terms of the ability to transport the produced current without loss even at low voltages[4]. The critical current which a superconducting cable can carry depends on the anisotropy of the superconductor which is affected by the alignment of the individual grains [5] and the chemical composition of the grain boundaries. In general, the critical current within each grain also scales with the amount of pinning of magnetic flux [4] which is generally large in the high- $T_c$  superconductors compared to the traditional elemental superconductors. The downside of superconducting cables is the need to cool them below  $T_c$  since they are just poor conductors in above this temperature.

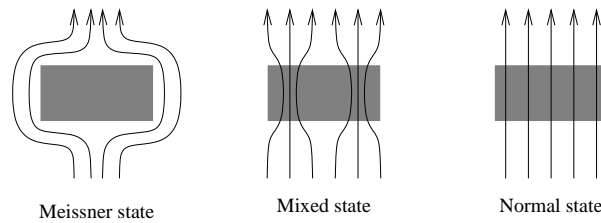


Figure 1.1: Schematic drawing of the Meissner effect. The left picture shows the complete expelling of the magnetic fluxlines from the SC below  $H_{c1}$ , the center picture shows the mixed state between  $H_{c1}$  and  $H_{c2}$  of a type-II SC and the rightmost picture show the magnetic field penetration in the normal state above  $H_{c2}$ .

The phenomenological Ginzburg-Landau equations introduced already in 1950 describe the superconducting phase transition by a complex order parameter which is non-zero in the superconducting state [6]. It was later interpreted as the expectation value of a pseudowavefunction  $\Psi(\mathbf{r})$  for the superconducting electrons in the Bardeen-Cooper-Schrieffer (BCS) microscopic theory for superconductivity. The BCS theory which was published in 1957 [7] describes superconductivity as attractive interaction between electrons mediated by phonons. Two electrons with opposite spin and momentum team up in Cooper-pairs which are bosons. The bosons condense below  $T_c$  and exhibit the collective (phase-coherent) behaviour called superconductivity. Type-I superconductors where the superconducting gap  $\Delta$  is constant in space are described well by this theory <sup>1</sup>, whereas it does not account for local variations of the gap which are important in type-II superconductors as described above.

<sup>1</sup>Detailed calculations of the different types of gaps and their quasiparticle energy are shown in [8]

## 1.2 High- $T_c$ superconductivity

A class of type-II superconductors known as high- $T_c$  superconductors (HTSC) were discovered in 1986 Johannes Georg Bednorz and Karl Alex Müller[9] and the term has since been used almost synonymously with the term high- $T_c$  cuprates referring to a class of perovskites which all contain one or more layers of  $\text{CuO}_2$ . After the discovery of HTSC Fe-based pnictides in 2008 [10], precision is however needed when referring specifically to high- $T_c$  cuprates. The cuprates are famous HTSCs because they were the first to exceed the  $\sim 30$  K limit predicted by the BCS theory hence calling for a new mechanism to be responsible for their superconductivity[11]. One major difference from conventional BCS superconductors where the Cooper-pairs form without any internal angular momentum (so-called s-wave superconductivity) is that the Cooper-pairs in the high- $T_c$  cuprates have an angular momentum (so-called d-wave superconductivity). The term 'high'- $T_c$  is sometimes confusing to the general public since the first HTSCs to be discovered ( $\text{La}_{2-x}\text{BaCuO}_4$  and  $\text{La}_{2-x}\text{SrCuO}_4$ ) still had  $T_c < 40$  K which is not very 'high' compared to e.g. room temperature. The crystal structure of  $\text{La}_{2-x}\text{SrCuO}_4$  (LSCO) is shown in Figure 1.2 and a substantial amount of the pioneering work by neutron scattering on this system has been performed at, or by people connected to, Risø National Laboratory<sup>2</sup> [12]. Since the first discovery of high- $T_c$  superconductivity in the limit of  $T_c$  has pushed upwards and the important discovery of  $\text{YBa}_2\text{Cu}_3\text{O}_{6+x}$  (YBCO)[13] and  $\text{Bi}_2\text{Sr}_2\text{Ca}_x\text{Cu}_{x+1}\text{O}_{8x+6-d}$  (BSCCO)[14] for which the  $T_c$  exceeded the temperature of liquid nitrogen (77 K). The current record holder is  $\text{HgBa}_2\text{Ca}_2\text{Cu}_3\text{O}_{8+\delta}$  with  $T_c = 164$  K under 31 GPa pressure [15]. The record is at present 15 years old and the main reason for the lack of improvement is that the mechanism behind high- $T_c$  superconductivity is still not fully understood at the present date 23 years and about 100,000 scientific papers after its discovery. The lack of a complete and general picture prevents the development of new materials with even higher  $T_c$ 's. The promised land of the research in HTSC is development of a room-temperature superconductor which would eliminate the need for cooling of e.g. superconducting cables.

Although the high- $T_c$  cuprate LSCO is not a primary candidate for cables it is important to study this structurally relatively simple system in order to understand the exotic and interesting phase diagram which has common features for all high- $T_c$  cuprates. The purpose of studying the exotic phases is the hope of eventually finding a quantum mechanical mechanism behind HTSC in general. An introduction to LSCO is made in Chapter 2. Of particular interest to this thesis is the underdoped region of the phase diagram of LSCO in which spin-density modulated order seems to compete with superconductivity.

In relation to investigating the mechanism of HTSC, superoxygenated  $\text{La}_{2-x}\text{Sr}_x\text{CuO}_{4+y}$  (LSCO+O) is particularly interesting since it is a 'clean' system in the respect that it consists of just two phases with different hole-content: One phase is a magnetically ordered phase and the other is a superconductor with  $T_c$  slightly above the value of optimally doped LSCO. Interestingly, these phases seem to

<sup>2</sup>which recently has become part of the Technical University of Denmark and is now called Risø-DTU

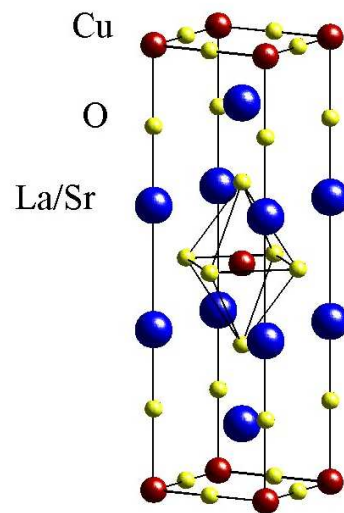


Figure 1.2: The high temperature tetragonal crystal structure of undoped  $\text{La}_2\text{CuO}_4$  (LCO). From [12].

coexist rather than compete as they do in LSCO. An introduction to LSCO+O is made in Chapter 4. Very recent work has shown that LSCO+O is a poor flux trapper compared to LSCO [16]. Previous studies on BSCCO have shown that the size of various defects has a strong influence on the flux trapping abilities of the cuprate: When they are small they are efficient pinning centres, but when they are much larger than the superconducting coherence length  $\xi_{\text{SC}}$ , they lose the ability to trap flux within the superconducting material ( see e.g. [17, 18, 19]). There are therefore several reasons to study the morphology of cuprate samples, in particular in the relatively simple LSCO+O system.

### 1.3 Experimental techniques

Various probes can be used to study the morphology of HTSC single crystals. A direct local probe on the atomic level is scanning tunnelling microscopy which has been used to measure checkerboard like LDoS patterns on BSCCO[20]. The pattern having modulations four Cu-atom sites wide are believed to reflect charge density modulation known as stripes. Stripes have also been observed in some of the other cuprates [21, 22] and which support spin density modulation with double periodicity. The spin density modulation in turn has been studied by direct microscopic modelling [8, 23]. The advantage of the direct modelling is that it is possible to study the effect on the LDoS of e.g. circulating super-current within a single vortex[24].

Global probes such as neutron- and hard x-ray scattering are very useful for investigating the structure of a sample. Specifically neutron scattering is an important tool for studying the magnetic structure. A short introduction to these techniques is made in Chapter 3. In Chapter 4 scattering data from LSCO+O are presented. The combined scattering from large real space regions is recorded in reciprocal space and as such only an average of the crystal structure can be deduced, not considering local variations. However careful data analysis in combination with virtual experiments can shed light on the size of the scattering regions.

### 1.4 Simulated neutron scattering

Virtual neutron experiments are characterised by simulating the absolute intensity from source to detector, producing data which can be analysed in a similar way as data from physical experiments. Preferably the neutron instrument as well as the sample is described in detail making the virtual experiment as realistic as possible[25]. This technique has been used in designing and/or optimising instruments but could in the future be widely used for planning physical experiments and for data analysis after the experiment has been performed.

It has been a major goal of this thesis to develop a method to perform detailed virtual neutron scattering experiments and compare these with physical measurements as a means of data analysis. This is done by building a virtual replica of the RITA-II triple axis spectrometer within the Monte Carlo neutron ray-tracing package called McStas. In the virtual experiments the same scans in the same setup as the physical experiments are performed. The physical neutron scattering experiments were carried out at RITA-II PSI, and the results are presented in Chapter 4. The corresponding virtual instrument V-RITA-II is described and tested in Chapter 5.

In Chapter 6 the virtual experiment technique is used to identify finite size broadening of diffraction peaks in LSCO+O. Instrumentally resolved peaks from non-oxygenated and homogenous but otherwise similar virtual crystals are simulated, thus producing the instrumentally resolved peak. The simulated peak width is then used to de-convolute intrinsic line width and thereby the finite-size broadening of the physically measured diffraction peaks.

---

A summary of the conclusions drawn from the scattering experiments, both the virtual and physical, is made in Chapter 7.

## 1.5 Supplementary information to this thesis

Not all the experimental data which I have obtained is included in the thesis, however reports from all the experiments exist and will be presented on demand. Two of the reports with particularly important supplementary data and which are representative of the experimental work which has been performed are included in unedited form in appendix A (hard x-ray diffraction) and B (neutron scattering).

For convenience of the reader, some of the publications related to this thesis are included in appendix D. For the particularly interested reader, the McStas code for the virtual instrument V-RITA-II is provided in appendix C.

## Chapter 2

# Properties of LSCO

This Chapter is devoted to a summary of the existing knowledge of LSCO with particular focus on the static magnetism in underdoped LSCO. More than one version of the temperature versus doping ( $T$ - $x$ ) phase diagram of HTSC cuprates exist but I will limit myself to a brief overview of one generic phase diagram which is schematically shown in Figure 2.1 and widely agreed upon. In Section 2.2 I will also briefly discuss the field dependent  $H$ - $r$  phase diagram of the Demler-Sachdev-Zhang (DSZ) model where  $r$  is a tuning parameter with relation to  $x$ . The different structural phases of La-based cuprates are discussed in Section 2.3 and a microscopic picture of what happens as holes are doped into the LCO mother-compound is presented in Section 2.4. In Sections 2.5 and 2.6, I will zoom in and place specific focus on the magnetic phase diagram of underdoped LSCO. Some length scales important to the discussion of HTSCs are summarised in Section 2.7.

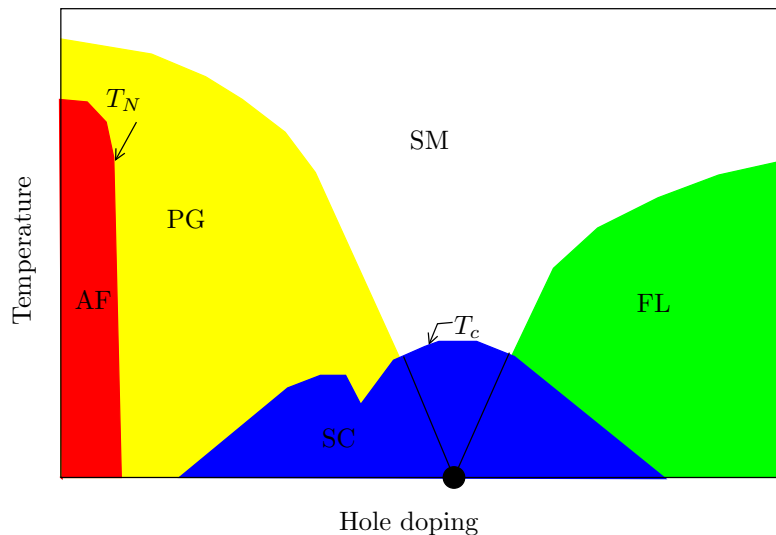


Figure 2.1: Generic  $T$ - $x$  phase diagram of the HTSC cuprates showing some of the general features as function of hole doping. The various labels are explained in the text.

## 2.1 $T$ - $x$ phase diagram

A temperature versus hole-doping phase diagram generic to the HTSCs is shown in 2.1 where the blue colour marks the superconducting region. The undoped cuprates are antiferromagnetic (AFM) insulators well explained by the Hubbard model which is described in Section 2.4. Superconductivity appears in LSCO for  $x = 0.055$ [26], and reaches a maximum of  $T_c \sim 38$  K for  $x \sim 0.16$  which is therefore called optimal doping. It disappears completely at  $x = 0.30$  and beyond this doping-level LSCO is well described by standard Fermi-liquid theory. The dip in the superconducting temperature is an anomaly occurring in some La-based cuprates close to  $1/8$  hole-doping which is of particular interest to this thesis and therefore a recurring topic.

Besides the antiferromagnetic insulating phase denoted by AF, the superconducting phase denoted by SC and the Fermi-liquid phase denoted by FL in Figure 2.1, the LSCO phase diagram contains two exotic phases: The pseudo-gap phase (PG) and the strange metal phase (SM). The term 'strange metal' stems from the in-plane resistivity scaling linearly with the temperature  $T$  below the Debye temperature  $\Theta_D$  in this regime - not with higher orders of  $T$  like in Fermi-liquids. In the heavily over-doped and non-superconducting region of the phase diagram the in-plane resistivity has been observed to scale with  $T^2$  for  $T < 50\text{K} \ll \Theta_D$  which was attributed to the electron-electron interaction of a Fermi-liquid[27].

The pseudo-gap phase and the evolution of it as a function of doping, temperature and applied magnetic field is still a subject of considerable debate[11]. The term 'pseudo-gap' refers both to existence of a gap in the static spin susceptibility in e.g. magnetisation measurements, but also gap in the electronic density of states. A gap in the density of states is expected below  $T_c$  in any superconductor. In the HTSC cuprates the internal angular momentum of the Cooper-pairs is reflected in the size of the gap depending on the direction in the crystal. The gap symmetry resembles that of an atomic  $d_{x^2-y^2}$  orbital[8], hence the term 'd-wave superconductivity'. It can be mapped by angle-resolved photo-emission spectroscopy which shows that the gap vanishes at  $k_x = k_y$  and is largest close to  $(k_x, k_y) = (\pi, 0)$ [28] which is seen by a strong suppression of the low-energy density of states at this point. This suppression persists even above  $T_c$  but the sharp peaks just above the V-shaped gap in the density of states, which are characteristic of the excitation of quasi-particles, are not present above  $T_c$ . Hence the gap is called a pseudo-gap.

In one school of interpretations, the quasi-particles are formed in the cuprates well above  $T_c$  but they only act as a coherent, superconducting condensate below  $T_c$ [29]. This theory is supported experimentally by the detection of vortex motion through a temperature gradient in HTSC samples[30, 31, 32, 33]. The vortices are regions with suppressed superconductivity and their number was found to increase with increasing temperature in the sample, eventually taking over and destroying superconductivity completely.

In another school of interpretations, the pseudo-gap phase is believed to relate to hidden order which vanishes within the superconducting dome at a quantum critical point (QCP) marked by the large black dot in Figure 2.1. The

presented version of the cuprate phase diagram is encouraged by the similarity to the one of certain heavy fermion compounds where a superconducting dome appears around an antiferromagnetic quantum critical point [34]. The existence and exact doping at which the QCP occurs at zero temperature and zero applied field is very difficult to identify due to the presence of superconductivity itself. The effects of a QCP can however be observed by critical spin fluctuations at temperatures of a few Kelvin in samples with dopings close to the critical doping. Such spin fluctuations have been observed in LSCO [35, 36].

At low temperatures (frozen) magnetic moments modulated in an incommensurate antiferromagnetic (IC AFM) way have been observed in the pseudogap phase. Even at the dopings where superconductivity sets in the IC AFM persists and seems to somehow co-exist with superconductivity. The transition temperature of the IC AFM is steeply peaked around  $x \sim 1/8$  and a dip in the  $T_c$  is observed at the same dopings as shown in Figure 2.1, a phenomenon known as the 1/8 anomaly. In materials such as  $\text{La}_{1.875}\text{Ba}_{0.125}\text{CuO}_4$  (LBCO) and  $(\text{La,Nd})_{1.875}\text{Sr}_{0.125}\text{CuO}_4$  (LNSCO) where the spin-density modulation is correlated to charge density waves (CDW) in a model known as 'stripes' (see Section 4.7) the suppression of the superconducting  $T_c$  around the hole doping  $x \sim 1/8$  is considerable. Thus SC and IC AFM seem to compete in this region of the phase diagram. Another feature of the 1/8 anomaly has been that the correlation length of the IC AFM islands seems to decrease steeply as doping departs from  $x = 1/8$ . The 1/8 anomaly has attracted particular attention recently [37, 38] and the static long-range IC AFM order of the so-called '1/8 state' will be a major topic in this thesis. The magnetism and magnetic excitations of LSCO are further explained in Sections 2.4 -2.6.

## 2.2 $H$ - $r$ phase diagram

The theoretical Demler-Sachdev-Zhang (DSZ) model [39] describes the competition of superconductivity and magnetism in the co-existence phase. In short it is a Ginzburg-Landau type model with repulsive coupling between the superconducting (SC) and spin-density wave (SDW)<sup>1</sup> order parameter near the magnetic phase transition. The predicted phase diagram as a function of the coupling constant  $r$  of the SDW order parameter and of the applied field  $\mu_0 H$  is shown in Figure 2.2. The  $r$  parameter is traditionally assumed to increase monotonically with doping ( $x$ ) but this interpretation has to be made with caution. A line of quantum critical points from A to M separates superconducting states with and without SDW order. The critical coupling parameter  $r_c$  presumably corresponds to a doping between  $x = 0.12$  and  $x = 0.144$  [40] considering the experiments on the left side [41, 37], and right side [42, 43, 37, 36] of the quantum critical line.

Specifically it is possible to go from the purely SC state to the coexistence (SC+SDW) phase by application of an external magnetic field as indicated by the arrow in the figure. Within the SDW+SC phase, the DSZ theory states that

<sup>1</sup>SDW and IC AFM order is used synonymously in this thesis for any (quasi-)static magnetic order having dominant Fourier components at the incommensurate scattering vector  $\mathbf{Q}_{\text{IC}}$

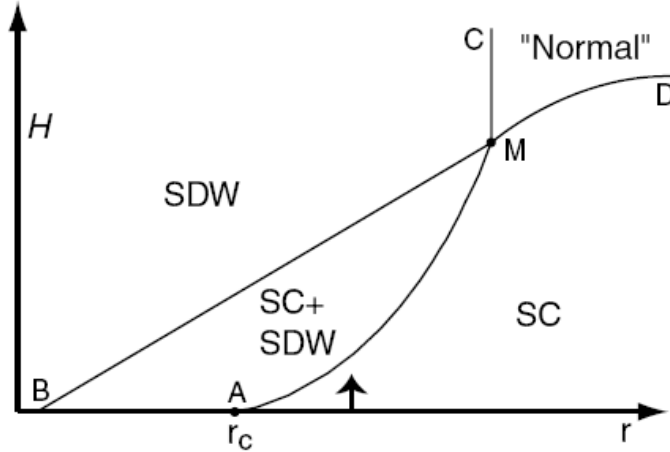


Figure 2.2: The DSZ phase diagram valid for slightly underdoped LSCO close to where SC and SDW coexist. The arrow on the diagram shows how a sample which initially has no SDW phase can be driven to the coexistence phase (SC+SDW) by application of an external magnetic field. At the point  $M$ ,  $\frac{H}{H_{c2}} = 1$ . From [39].

the elastic neutron scattering intensity of the SDW at the IC position should increase as function of applied field ( $\mu_0 H$ ) by

$$\Delta I \propto \frac{H}{H_{c2}} \ln \frac{H_{c2}}{H} \quad (2.1)$$

where  $H_{c2}$  is the upper critical field. This initially linear dependence on the applied field is different than the expected quadratic dependence if the magnetic moment was simply saturating by the applied field. The DSZ functional form of the intensity appears to match the experimental data well [37, 41] also in the prediction that beyond  $r_c$  the system can be pushed from the SC into the SC+SDW phase by application of a field [43, 37]. The critical field at which this transition to long range SDW order in the superconducting phase happens seems to depend steeply on the doping above the critical value. For example the critical field was reported to be 3 T for  $x = 0.144$ [43] but 7 T for  $x = 0.145$ [37].

An interesting and very recent investigation by inelastic neutron scattering has found a field-induced soft-mode driven quantum phase transition of LSCO with  $x = 0.145$ [36]. At zero applied field a spin gap of roughly 4 meV is present but at 7 T applied field this gap has collapsed completely and long-range (quasi-)elastic SDW order appears. Field induced low energy states in the spin gap have also been observed for LSCO with  $x = 0.163$ [42] and in LSCO doped by non-magnetic Zn impurities[44, 45, 46]. The low energy states be further elaborated on in Sections 2.5 and 2.6.

Although the DSZ model describes the functional form of the field effect of the LSCO compounds where it is observed, it does not predict the doping dependence of the strength of the field effect. Specifically the current model does not include the 1/8 anomaly, especially in the 'true 1/8' compounds which

apart from a  $\mu$ SR Bessel-like relaxation with  $\nu = 3.5$  MHz are characterised by incommensurate SDW order with  $\delta = 1/8$  and no field effect as observed by elastic neutron scattering[47, 3]. Examples of such compounds are LNSCO and LBCO, but also the Sr/O co-doped LSCO+O with  $x > 0$  as will be shown in this thesis. The SDW order of the 'true 1/8' compounds is IC AFM with incommensurability  $\delta \sim 1/8$  and long correlation length, and it is usually explained by the stripe picture [48] which will be further discussed in Section 4.7.

## 2.3 Crystal structure

The crystal structure of LSCO at high temperatures was shown in Figure 1.2. In this thesis work the axes within the  $\text{CuO}_2$  planes will always be denoted by  $a$  and  $b$  respectively, and the long axis by  $c$ . The notation refers to the orthorhombic lattice vectors ( $a \sim 5.3\text{\AA}$ ,  $a \sim 5.4\text{\AA}$ ,  $a \sim 13.2\text{\AA}$ ) unless explicitly stated otherwise (such as  $a_T \sim 3.8\text{\AA}$ ). The angles between the lattice vectors are  $90^\circ$  both in the tetragonal and orthorhombic notation. In the structural phase diagram of LSCO, which is shown in the left part of Figure 2.3, there is a transition from tetragonal to orthorhombic structure for  $x < 0.2$ , but there is a total of five types of structural phases known in the La-214 series[49]:

- The tetragonal phase at high temperatures (the HTT phase with space group  $I4/mmm$  for which the tetragonal lattice parameters  $a_T = b_T < c$ ).
- The orthorhombic phase with undetermined tilts ( $Fmmm$  with  $a < b < c$ ). The notation of this phase is sometimes also used for the HTT phase and then  $a = b < c$ .
- The orthorhombic phase at mid-temperatures  $\text{LTO}_1$  ( $Bmab$  with  $a < b < c$  also known simply as LTO).
- The orthorhombic phase at low temperatures  $\text{LTO}_2$  ( $Pccn$  with  $a < b < c$  also known as LTLO).
- The tetragonal phase at low temperatures (the LTT phase ( $PA_2/nm$ )  $a = b < c$ ).

Four of the phases can be classified with the order parameters ( $O_1, O_2$ ) which represent the tilting of the  $\text{CuO}_6$  octahedra around the  $[110]$  and  $[\bar{1}\bar{1}0]$  axis of the HTT structure (in tetragonal notation)[51]. For HTT  $O_1 = O_2 = 0$ , for  $\text{LTO}_1$   $O_1 \neq 0$  and  $O_2 = 0$ , for  $\text{LTO}_2$   $O_1 \neq O_2 \neq 0$  and for LTT  $O_1 = O_2 \neq 0$ .

The phases can be distinguished by their diffraction pattern, i.e. which scattering vectors  $\mathbf{Q} = (H, K, L)$  are 'allowed'. A comprehensive list of some of the reflections is provided in Table 2.1. The fundamental HTT reflections are allowed when  $H, K, L$  are all even or odd referring to the orthorhombic notation  $Fmmm$ . The  $Bmab$  phase in addition has allowed reflections for  $H, L$  even and  $K$  odd or  $H, L$  odd and  $K$  even[52]. However, if the crystals are twinned in the  $Bmab$  phase (see Section 4.5.2) one must note that  $(H0L)$  from one twin and  $(0KL)$  from another twin are in the scattering plane simultaneously[53]. Twinning is further explained in Section 4.5.2.

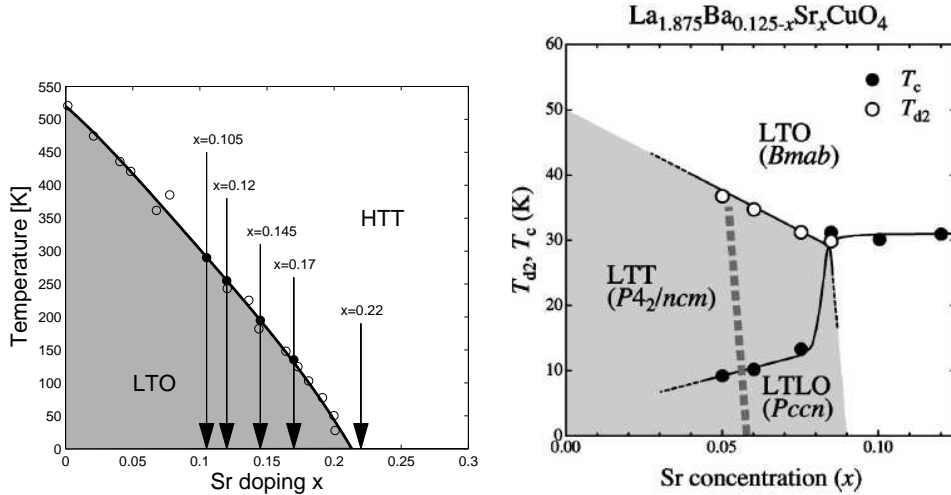


Figure 2.3: Left: LSCO phase diagram showing the transition between the tetragonal (HTT) and orthorhombic (LTO) phase. From [3]. Right:  $\text{La}_{7/8}\text{Ba}_{1/8-x}\text{Sr}_x\text{CuO}_4$  low temperature phase diagram showing the two orthorhombic phases (LTO and LTLO) and the low temperature tetragonal phase (LTT). From [50].

The orthorhombic phase with 'undetermined tilts' has the signature of missing peaks at the orthorhombic positions which should be there if the tilts were the same throughout the sample. In case the sample has intercalated oxygen it might contain a tilting superstructure known as staging which could be placed in the  $Fmmm$  category. Staging will be further discussed in Section 4.5.1.

$Pccn$  can be distinguished from  $Bmab$  since reflections with  $H, K$  odd and  $L$  even are allowed in  $Pccn$  (and LTT) but not in  $Bmab$ [50]. Whether the low-temperature phase is  $\text{LTO}_2$  or LTT can be determined by scans through the fundamental reflections in the  $(a, b)$  plane since the twinning will show as peaks with double features<sup>2</sup> if the  $a$  and  $b$ -axis have different lengths corresponding to  $O_1 \neq O_2 \neq 0$ .

If the twinning is too small to be resolved, the LTT phase can still be detected by a peaks at  $H$  odd and  $K, L$  even which are not allowed in any of the other phases. If a peak is found at e.g. (100) there is however a possibility that is is due to second order scattering from (200) which is observed at (100). In this case a filter can be inserted to select only first order scattering. If weak or diffuse scattering is observed in e.g. an allowed LTT position it should be followed as function of temperature. If no phase transition occurs within an appropriate temperature range it is reasonable to conclude that the scattering is not a signature of a particular structural phase.

Some doped lanthanum-cuprate compounds have low temperature transitions to one or more of these structures, for example LNSCO and LBCO are known to have a LTT phase, whereas LSCO has none. The structural phase

<sup>2</sup>depending on the position of the peak scattering from a twinned crystal produces up to four peaks with a tiny separation. Not all the peaks are always observed since they might not all be resolved by the instrumental set-up.

diagram of Sr/Ba co-doped  $\text{La}_{7/8}\text{Ba}_{1/8-x}\text{Sr}_x\text{CuO}_4$  is shown in the right part of Figure 2.3.

	HTT	$Fmmm$	LTO	LTLO	LTT
(111)	+	+	+	+	+
(200)	+	+	+	+	+
(020)	+	+	+	+	+
(002)	+	+	+	+	+
(014)			+	+	+
(104)				+	+
(110)				+	+
(100)					+
(010)					

Table 2.1: A table of some of the reflections in the La-214 series. All Miller indices are in orthorhombic setting (  $(\frac{2\pi}{a} \frac{2\pi}{b} \frac{2\pi}{c})$  with  $a \sim 5.3\text{\AA}$ ,  $b \sim 5.3\text{\AA}$  and  $c \sim 13.2\text{\AA}$  ). The reflections marked by '+' are allowed.

## 2.4 Microscopic picture

The essential mechanism responsible for the occurrence of high- $T_c$  superconductivity in the cuprates is generally believed to be contained within the  $\text{CuO}_2$  planes, a feature which is supported by the observation that the  $T_c$  increases with the number of  $\text{CuO}_2$  planes per unit cell [54].

In the un-doped mother compound  $\text{La}_2\text{CuO}_4$  (LCO) the Cu atoms form strongly hybridised bonds with oxygen thereby approximately being described by the atomic term  $[\text{Ar}]d^9$ , i.e. there is approximately one hole in the d-band per Cu atom. From this one would expect LCO to be metallic but as it turns out, it is in fact an antiferromagnetic (AFM) insulator, also known as a Mott insulator. This is because the holes on the Cu-sites can interact via the oxygen atoms through the super-exchange mechanism. A Mott insulator can be described by the Hubbard model for localised holes which contains delocalising kinetic energy terms to (next-)nearest neighbours ( $t, t'$ ) and a localising term  $U$  describing the on-site repulsion[8]

$$H_{Mott} = -\mu \sum_{i\sigma} c_{i\sigma}^\dagger c_{i\sigma} - t \sum_{\langle ij \rangle \sigma} c_{i\sigma}^\dagger c_{j\sigma} + t' \sum_{[ij] \sigma} c_{i\sigma}^\dagger c_{j\sigma} + U \sum_i n_{i\downarrow} n_{i\uparrow} \quad (2.2)$$

where  $\langle ij \rangle$  ( $[ij]$ ) denotes the sum of nearest (next-nearest) neighbours  $j$  of the Cu atom at site  $i$ ,  $\mu$  is the chemical potential,  $c_{i\sigma}^\dagger$  is the electronic creation operator at site  $i$  with spin  $\sigma$  and  $n_{i\sigma} = c_{i\sigma}^\dagger c_{i\sigma}$  is the occupation number operator.

If the repulsion is strong ( $t \ll U$  limit) the holes will be distributed one on each Cu site with alternating spins, i.e. a 3D antiferromagnet. In the case of LCO the antiferromagnetic transition temperature is quite high,  $T_N = 300$  K. The characteristic energy for the antiferromagnetic exchange interaction is

$J = \frac{4t^2}{U}$  and the model hence known as the  $t-J$  model. The magnetic structure of the un-doped parent compound LCO is shown in figure 2.4.

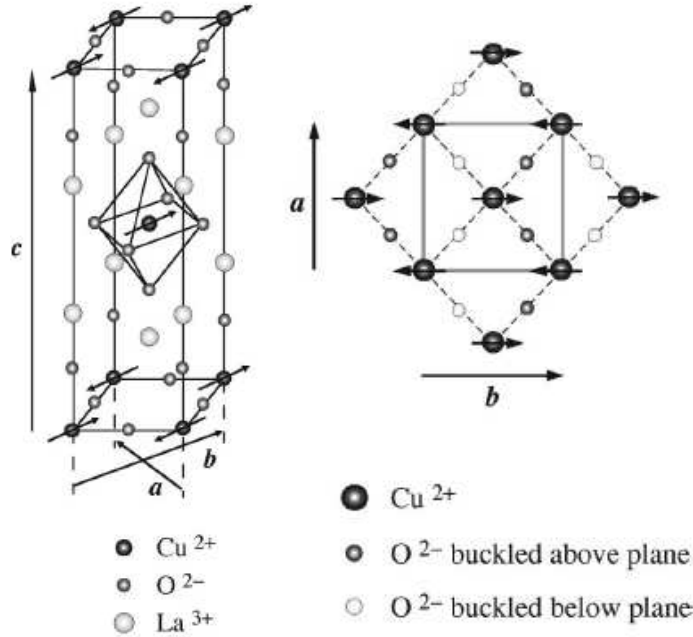


Figure 2.4: The magnetic structure of undoped  $\text{La}_2\text{CuO}_4$ . The orthorhombic structure for  $T < 550\text{K}$  is shown.

Exchanging some of the  $\text{La}^{3+}$  ions with  $\text{Sr}^{2+}$  (doping) to get  $\text{La}_{2-x}\text{Sr}_x\text{CuO}_4$  (LSCO) introduces fewer electrons in the perovskite structure and thus holes in the oxygen orbitals. A hole on a Cu site has been shown to hybridise strongly with a hole from a linear combination of orbitals on the 4 surrounding oxygens forming a Zhang-Rice singlet state (total spin=0)[40]. Thus some of the Cu atoms will go from charge +2 to +3. In the simple picture they will on average have atomic configuration  $[\text{Ar}]9^{9-x}$ , i.e.  $1+x$  holes in the d-band. It turns out that the localised hole state with the lowest energy is  $3d_{x^2-y^2}$  which then contains the doped hole. Doping gradually destroys the super-exchange and long-range antiferromagnetic order, and at a critical doping a superconducting ground state is favoured. For very large hole dopings superconductivity is suppressed in favour of a metallic ground state well described by Fermi-Liquid theory. This is the other extreme of the Hubbard model ( $t \gg U$  limit) in which the electrons prefer to delocalise.

Instead of exchanging  $\text{La}^{3+}$  with  $\text{Sr}^{2+}$  the parent LCO compound can be hole-doped by intercalating excess oxygen in the perovskite structure thus forming  $\text{La}_2\text{CuO}_{4+y}$  (LCO+O). The excess oxygen doping is generally believed to have a similar effect on the Cu ions as Sr doping. This is further treated in Chapter 4.

## 2.5 Static magnetism in LSCO

The magnetic properties throughout the phase diagram have proven to be immensely complex and sensitive to effects of disorder. However a couple of nice and fairly recent reviews by Julien [55] and Birgeneau et al. [56] give good overview of the vast amounts of studies. A common feature of the cuprates is that by doping the commensurate AFM develops into incommensurate (IC) AFM, which is seen in neutron scattering by peaks displaced  $\delta$  away from the AFM point. In LSCO this spin density modulation development happens gradually. The spins in undoped LCO point along the orthorhombic  $b$  axis and by slight doping ( $x < 0.02$ ) small regions with spin density modulation along  $b$  (i.e.  $\delta$  along  $K$ ) precipitates from the commensurate 3D AFM [57]. These are called diagonal spin density modulations (D-SDM) since they are modulated diagonally with respect to the Cu-O bonds. For dopings between 0.02 and 0.055 the commensurate AFM has vanished but the D-SDM remains. At the doping  $x = 0.055$  where superconductivity sets in, another interesting transition occurs where the spin modulation rotates to lie along the Cu-O bonds, the so-called parallel spin-density modulation (P-SDM). In LNSCO and LBCO the P-SDM is stabilised by the structural transition to LTT which is strongly coupled to charge ordering [58, 59] and the P-SDM is interpreted as spin stripes[60, 22]<sup>3</sup> with a periodicity of 8 (the so-called 1/8 state). But in LSCO and LSCO+O (as discussed in Chapter 4) no such structural transition is observed. And yet the P-SDM is observed in LSCO in zero applied field with increasing correlation length up to a doping of  $x = 1/8$  where the transition temperature is also sharply peaked (the so-called 1/8 anomaly). It is however still debated if the stripe picture is valid for LSCO since charge ordering corresponding to charge stripes has not yet been directly observed in this material. The incommensurability follows the hole-doping  $\delta = x$  in LSCO for  $0.03 < x < 1/8$  where  $\delta$  is defined in (pseudo-)tetragonal reciprocal lattice units [61, 62]. The magnetic phase diagram is shown in Figure 2.5.

For LSCO with  $x$  above  $\sim 0.13$ , P-SDM with  $\delta \sim 1/8$  can be observed at base temperature above a critical applied field which however increases rapidly with doping as discussed in Section 2.2.

SDW modulations have been observed in LSCO for  $0.02 \leq x < 0.14$ . Frozen moments have also been detected by  $\mu$ SR for  $0.02 \leq x \leq 0.12$  whereas for  $0.12 < x < 0.14$  static magnetic order has not been observed by muons, only by neutrons. This discrepancy could be explained if the magnetic order at these dopings is fluctuating on a timescale faster than  $10^{-6}$  s which is the interacting time for muons, but slower than  $10^{-10}$  s which is the interaction time for neutrons<sup>4</sup>. By neutron diffraction it has previously been observed that the correlation length of the IC AFM islands decreases abruptly when doping departs from  $x \sim 1/8$ [26, 63]. In this respect the weakly correlated small magnetic islands can be viewed as nanoparticles, an analogy which is further discussed in Section 2.6 below.

<sup>3</sup>The stripe model is further treated in Section 4.7

<sup>4</sup>A cold neutron triple-axis spectrometer typically has an energy resolution of  $\sim 0.2$  meV corresponding to 0.05 THz or  $2 \cdot 10^{-11}$  s

In LSCO+O, P-SDM with correlation length exceeding  $200 \text{ \AA}$  is observed at base temperature in ZF for all  $x$  as shown experimentally by our neutron diffraction data in Section 4.8. In LNSCO the spins have been proven to point along the stripes (along the Cu-O bond direction)[64] as shown in Section 4.7. I find that the relative intensity of our neutron diffraction data of LSCO+O in zero applied field can be explained with a similar spin arrangement as discussed in Section 4.8.5.

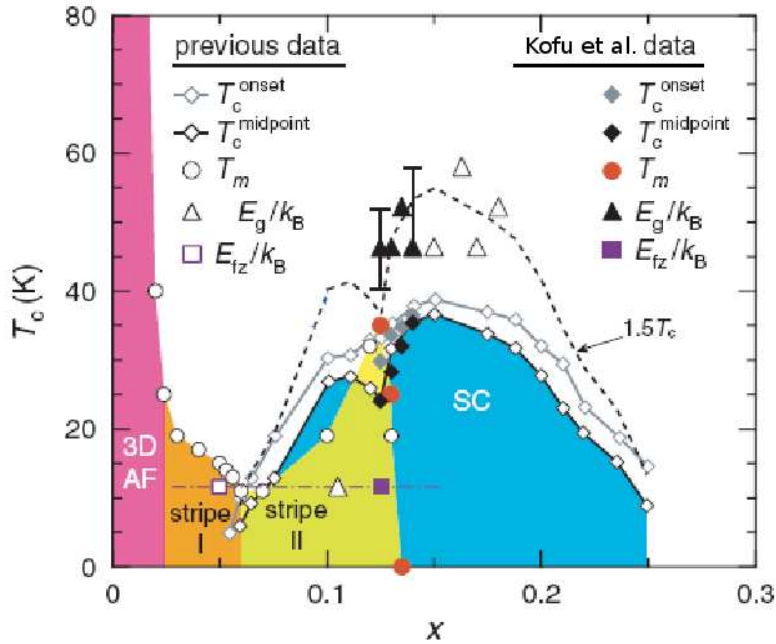


Figure 2.5: Magnetic phase diagram of LSCO. The figure is rather crowded but shows the thermal activation temperature ( $T = E/k_B$ ) both of the quasielastic IC AFM signal (squares) and of the magnetic fluctuations above the spin-gap (triangles) as a function of hole-doping  $x$ . The magnetic transition temperature  $T_m$  is measured by elastic neutron scattering. Stripe I is the D-SDM and stripe II the P-SDM phase mentioned in Section 2.5. The superconducting transition temperatures (diamonds) are obtained by bulk susceptibility measurements and the dashed curve is the  $T_c^{\text{midpoint}}$  curve multiplied by 1.5. It is seen that the thermal activation temperature of the spin gap is close to this curve. Modified from [38]

## 2.6 Magnetic excitations in LSCO

The magnetic excitations for energy transfers below  $\sim 20 \text{ meV}$  consist of nearly vertical rods extending from the incommensurate positions. For LSCO with  $0.07 \leq x \leq 0.12$  and LCO+O the wave vector of the low energy incommensurate scattering scales directly with  $T_c$  as shown in Figure 2.6. For  $0.12 < x < 0.2$  the incommensurability value remains  $\sim 1/8$  but the intensity of the low

energy incommensurate scattering is suppressed below  $T_c$ [65] which indicates the formation of a spin gap. These points suggest that the magnetic scattering is directly associated with high-temperature superconductivity [56]. Apart from the low energy part which is strongly doping-dependent the spin fluctuation dispersion of HTSC cuprates has a universal hour-glass like shape shown in Figure 2.7. The four incommensurate branches disperse inwards toward the AFM position (the 'waist'). The distribution of the spectral weight along the dispersion curve however varies strongly for the different HTSC cuprates. The compounds with  $T_c^{max} \sim 90$  K have strong intensity (the so-called resonance) at the 'waist' located at  $\hbar\omega \approx 40$  K [66] whereas the spectral weight in LSCO is more concentrated at lower energies (in the 'legs')[67].

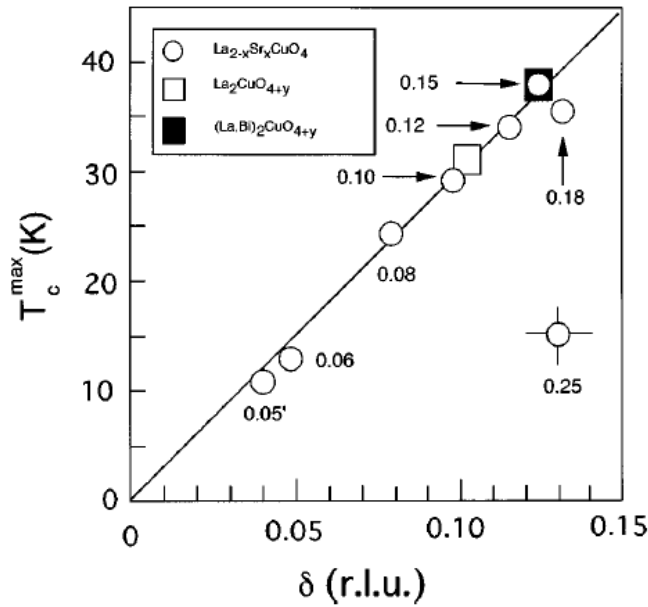


Figure 2.6: The incommensurability  $\delta$  for the low-energy incommensurate magnetic scattering as a function of onset of  $T_c$ . From [62].

Below  $T_c$  a spin-gap opens up for specific hole-dopings which is signalled by a redistribution of spectral weight at low energies. Close to optimal doping of LSCO ( $0.14 < x \leq 0.17$ ) the spin-gap is of the order 4-8 meV (in zero applied field) [69, 70, 71, 72, 2, 36]. For a long time no spin gap was observed near the special doping  $x \sim 1/8$ , but very recent results point to a hidden spin gap of 4 meV also for  $0.125 \leq x \leq 0.135$ [38]. The gap is hidden since the inelastic neutron signal is only partly suppressed, but a broad peak of spectral weight is observed at  $\hbar\omega \sim 1 - 1.5$  meV both for  $x = 0.125$  and  $x = 0.105$ [73]. This 'frozen moment' state has also been observed in the spin-glass phase of  $x = 0.05$ [74]. Somewhat puzzling the intensity decreases at zero energy transfer corresponding to the elastic IC AFM signal. The data for  $0.105 \leq x \leq 0.145$  are shown together in Figure 2.8.

As mentioned in Section 2.2 in-gap states can be induced by an applied field

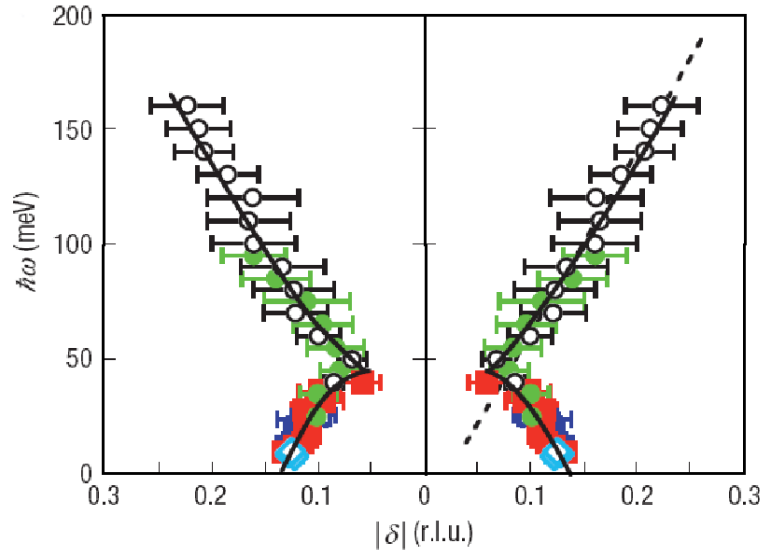


Figure 2.7: The spin fluctuation dispersion as a function of incommensurability  $\delta$ . The measurements are from LSCO with  $x = 0.16$  but the hourglass shape is generic for HTSC. From [68].

along the  $c$ -axis for the dopings that otherwise have a clean gap. An example is shown for  $x = 0.145$  in Figure 2.8(a) from [36] and similar states have been found previously for  $x = 0.163$  in [42] and  $x = 0.18$  in [75].

Another important and interesting observation in [38] is that the in-gap states are long-range correlated whereas the states above the gap have a substantially shorter correlation length. This suggests as a real space phase separation of two distinct magnetic phases: The superconducting phase with gapped spin fluctuations and non-superconducting regions with static IC AFM order which perhaps are explained by spin stripes[38]. Previously the correlation length of quasi-2D IC AFM islands  $\xi_{IC}$  as measured by elastic neutron scattering, was considered to decrease fast as doping departed from  $x \sim 1/8$ [63] and the relation to the correlation length of the in-gap states still needs to be made. It should however be mentioned that the correlation lengths in [38] are based on measurement with thermal neutrons and the energy resolution is rather poor  $\sim 1.2$  meV.

Since the coherence length of the IC AFM islands decreases abruptly when doping departs from  $x \sim 1/8$  they could be viewed as AFM nano-particles. In relation to this aspect a couple of analogies are worth mentioning. The magnetic anisotropy in AFM nano-particles introduces non-dispersive spin waves at specific precession frequencies depending on the distribution of domain sizes[77, 78] and the spectral weight of these states is distributed by thermal fluctuations (Bose factor). At temperatures higher than the anisotropy temperature only fluctuations exist and no (quasi-)elastic neutron scattering signal is observed. This is analogous to the situation of HTSC cuprates in the normal state. Furthermore the fluctuations slow down when the AFM nano-particles interact which has a particularly interesting analogy in underdoped LSCO in the SC

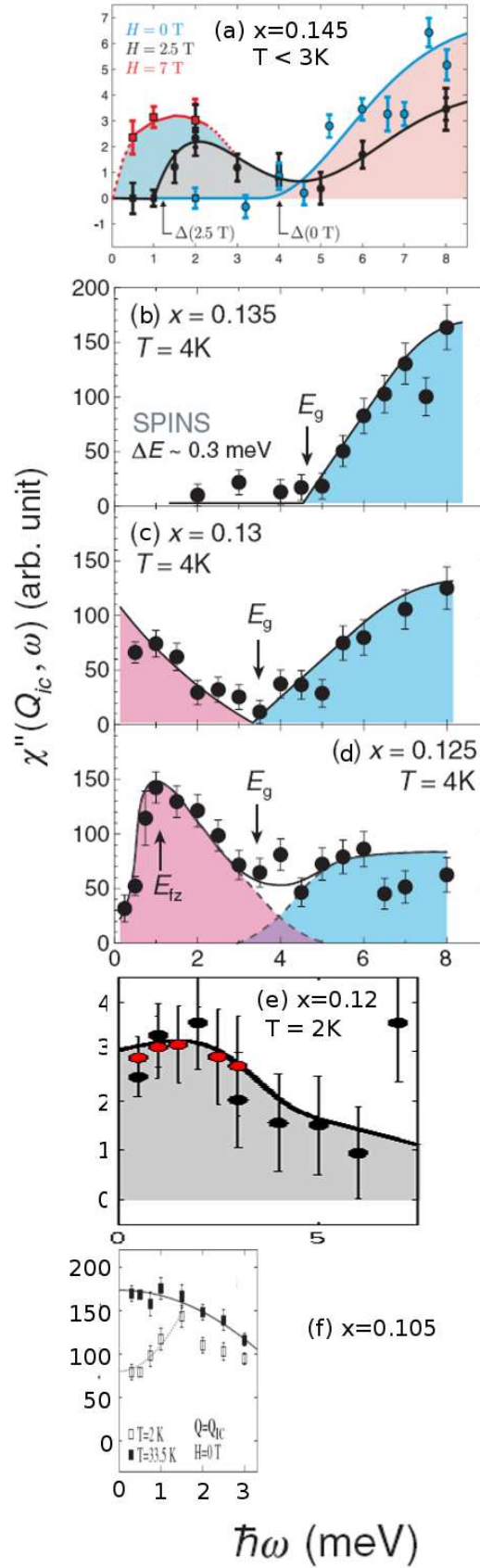


Figure 2.8: The spin-gap and in-gap states in LSCO. All figures have been put on the same energy scale for comparison. Data are shown for dopings between  $x = 0.145$  (figure (a) modified from [36]) and  $x = 0.105$  (figure (f) from [73]). Figures (b)-(d) are from [38] and (e) from [3]. In (f) the black data points are in ZF and the red data points are in 10 T applied field (to be published in [76]). The spin gap,  $E_g$  or  $\Delta$ , is  $\sim 4$  meV as shown for  $x > 0.12$  in zero applied field.

state where in-gap IC AFM states can be introduced by the interaction with an applied magnetic field as discussed in Section 2.2. In this picture the IC AFM islands in different  $\text{CuO}_2$  layers are aligned by application of a field along the  $c$ -axis through correlation of the vortices corresponding to interaction between particles.

## 2.7 Length scales and morphology

In the superconducting state, a fraction of the electrons form a superfluid Bose-Einstein condensate of Cooper-pairs, which is responsible for the screening of an external magnetic field. In conventional (s-wave) BCS superconductors where the superconducting gap  $\Delta_{\text{SC}}$  at  $T=0$  is constant in space, the superconducting (Pippard) coherence length can be calculated from the Fermi velocity  $v_F$  as [79]

$$\xi_{\text{SC}} = \frac{\hbar v_F}{\pi \Delta_{\text{SC}}} \quad (2.3)$$

which is popularly described as the 'size of a Cooper-pair'.  $\xi_{\text{SC}}$  is typically  $\mu\text{m}$  for conventional BCS superconductors and very short  $\sim 10\text{\AA}$  for HTSC[29]. The superfluid density (carrier density)  $n_s$  is orders of magnitude lower in HTSCs than in conventional BCS superconductors [29]. The penetration depth of an applied external field is related to the superfluid density (carrier density)  $n_s$  by

$$\lambda_{\text{SC}} \sim \sqrt{\frac{1}{n_s}} \quad (2.4)$$

which is based on the observation that  $\lambda_{\text{SC}}(\text{HTSC}) \ll \lambda_{\text{SC}}(\text{BCS})$ . For optimally doped LSCO,  $\lambda_{\text{SC}} \sim 2000 \text{\AA}$ [29]. A superconductor is classified by A. A. Abrikosov as the ratio of penetration depth and the superconducting coherence length  $\kappa = \frac{\lambda_{\text{SC}}}{\xi_{\text{sc}}}$  [6]. A type-I superconductor has  $\kappa < \frac{1}{\sqrt{2}}$  and a type-II superconductor has  $\kappa > \frac{1}{\sqrt{2}}$ , from which it is clear that HTSCs are extreme type-II superconductors.

Another important length scale in HTSC is the correlation length  $\xi_{\text{IC}}$  of the IC AFM, since a key to the complexity of the magnetism in the underdoped LSCO might lie in the morphology and fluctuations of the non-superconducting areas as mentioned in the previous section. Doping by non-magnetic Zn impurities at Cu sites has been used to study the nucleation of non-superconducting areas around the localised Zn impurities. The original  $\mu\text{SR}$  measurements of  $\text{La}_{2-x}\text{Sr}_x\text{Cu}_{1-y}\text{Zn}_y\text{O}_4$  with  $x = 0.15$  revealed two different signals from the same sample which were interpreted as coming from magnetic and non-magnetic regions, respectively[80]. The superconducting region was considered percolating, resembling swiss cheese where the holes would represent the non-superconducting regions surrounding the Zn impurities. A systematic study of underdoped LSCO with different degrees of Zn doping was carried out in [81] and the results for  $x = 0.13$  shown in Figure 2.9. As mentioned above, static magnetism has not been observed by  $\mu\text{SR}$  for  $0.12 < x < 0.14$  without Zn-doping probably because the spins fluctuate faster than a timescale of  $10^{-6}$

seconds which is illustrated in the first picture in Figure 2.9. As slight Zn doping is introduced the spins slow down in the vicinity of the impurity as shown in the next picture. Upon further Zn doping the spins freeze and coherent order is established as shown in the third picture and eventually the sample loses its superconducting ability as shown in the fourth picture. At even higher impurity dopings the spins start fluctuating fast again as shown in the last two pictures. For  $x \sim 0.12$  magnetic order is formed even without Zn doping in the major part of the sample but around 10% of the magnetic volume is nevertheless fluctuating fast. Since a small field-induced increase in the IC AFM intensity of a sample with  $x = 0.12$  is observed by elastic neutron scattering [37] it is tempting to interpret the applied field as having a similar effect as Zn-doping in slowing down and freezing the spins. Furthermore an IC AFM signal in the spin-gap of LSCO with  $x = 0.15$  in the superconducting phase, similar to the ones described in Section 2.2 for  $x = 0.145$  upon application of an external field, is observed by neutron scattering upon doping with Zn[44]. The analogy between Zn-substitution and application of an external field in slightly underdoped LSCO is therefore remarkable.

The phase separation in superconducting and magnetic regions in HTSCs is a hot topic since it may hold the key to the subtle balance of competing but coexisting superconducting and magnetic order parameters. In LCO+O with low hole-doping a phase separation occurs in AFM regions with  $y < 0.01$  and regions with  $y \geq 0.055$  having incommensurate low-energy spin fluctuations at the P-SDM positions and with incommensurability matching the  $T_c$ , see Figure 2.6. In Chapter 4 of this thesis, LSCO+O with high hole-doping is investigated and interestingly reveals another electronic phase separation into a phase similar to the 1/8 state described in section 2.5 and a phase with  $T_c$  just above the optimally doped LSCO. The size of the magnetic domains are investigated by careful de-convolution of the elastic magnetic neutron scattering peak by virtual experiments in Chapter 6.

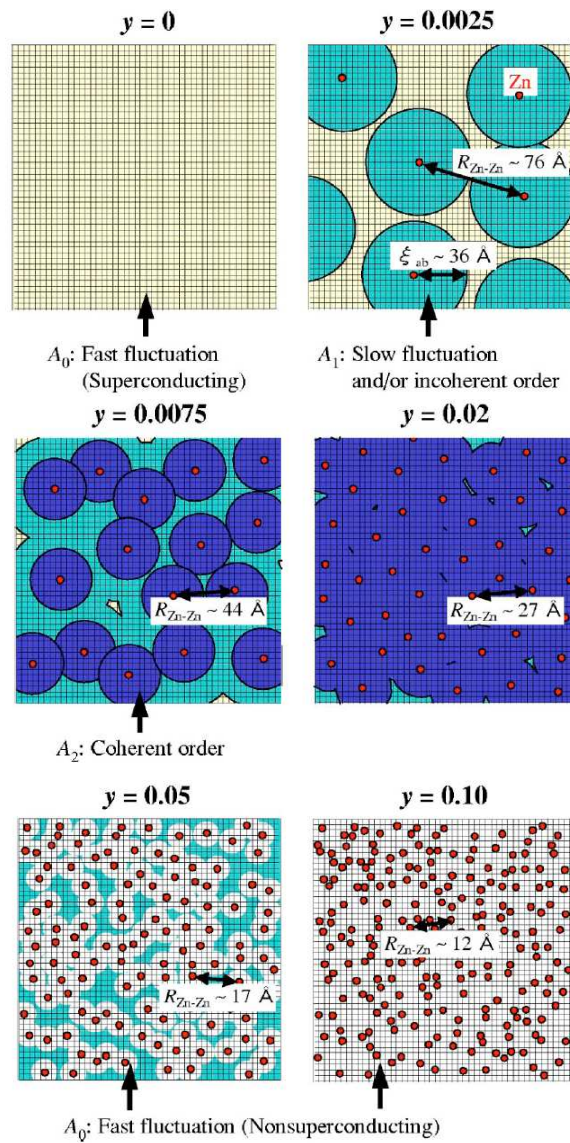


Figure 2.9: Evolution of the 'swiss cheese' model with Zn doping as seen by  $\mu$ SR. At low dopings the spins fluctuate faster than the muon interaction time. By slight Zn doping  $y = 0.0025$  the spins slow down and at  $y = 0.0075$  coherent order is established. Upon further doping the number of magnetically ordered domains grow and suppress superconductivity and finally the spins speed up again and fluctuate fast. From [81]

## Chapter 3

# Scattering methods

This chapter is devoted to a brief description of the two experimental methods of neutron scattering 3.1 and hard x-ray scattering 3.2. I describe some features generally applicable to the data analysis of both methods in 3.3 and 3.4. In the end of this chapter simulation by Monte Carlo neutron ray-tracing is described in section 3.5. The features of a neutron scattering from a triple-axis spectrometer (TAS) are brilliantly described by Shirane, Shapiro and Tranquada in [82] so Sections 3.1.1 - 3.1.4 follow along these lines.

### 3.1 Experimental neutron scattering

Neutrons are widely used to study the nuclear and magnetic structure and dynamical phenomena of condensed matter. An important instrument in neutrons scattering is the triple axis spectrometer (TAS) since it allows controlled measurement of the scattering function  $S(\mathbf{Q}, \omega)$  at a wide range of points in momentum ( $\hbar\mathbf{Q}$ ) and energy ( $\hbar\omega$ ) space. Since neutrons have zero net charge they interact very weakly with matter, enabling penetration through sample container (e.g. magnet or cryostat) used to control the environment and deep into the sample.

The neutrons used in scattering experiments are typically produced in a nuclear reactor by spontaneous fission of  $^{235}\text{U}$  or from a spallation source where neutrons are produced by bombarding a heavy metal target with high-energy protons. They are successively slowed down (moderated) by collisions with atoms of similar mass (hydrogen or deuterium) after which they are distributed with an average velocity corresponding to the temperature of the moderator. Hence the terms 'cold' or 'thermal' neutrons, referring to the typical energies of 0.1-10 meV or 5-100 meV respectively. A drawing of the spallation target SINQ at the Paul Scherrer Institute (PSI) in Switzerland is shown in Figure 5.2.

The scattering from a nucleus can be considered isotropic and characterised by the single scattering length  $b$  at the order of fm since the interaction between neutron and nucleus is very short-ranged compared to the neutron wave-length of thermal ( $0.9 \text{ \AA} < \lambda < 4 \text{ \AA}$ ) or cold ( $3 \text{ \AA} < \lambda < 8000 \text{ \AA}$ ) neutrons.

In structural neutron scattering the scattering amplitude from a sample is equal to the sum of the scattering from individual nuclei which greatly simplifies

the interpretation of the measurements, compared to e.g. x-rays which scatters from the electrons surrounding each atom.

The neutron has a magnetic moment which enables it to interact with unpaired electron spins in magnetic atoms with a strength comparable to that of nuclear interaction. It is therefore a powerful probe of the magnetic properties in solids.

### 3.1.1 The scattering process

The laws of momentum and energy conservation governing the scattering experiments are:

$$\mathbf{Q} = \mathbf{k}_i - \mathbf{k}_f \quad (3.1)$$

$$|\mathbf{Q}|^2 = k_i^2 + k_f^2 - 2k_i k_f \cos \theta \quad (3.2)$$

$$\hbar\omega = E_i - E_f \quad (3.3)$$

where the momentum transferred to the crystal is  $\hbar\mathbf{Q}$  and the angle between the incident and final beams is  $2\theta$  as shown in the inset of figure 3.1.

The goal of most neutron scattering experiments is to measure  $S(\mathbf{Q}, \omega)$  in order to determine the microscopic properties of the sample, such as nuclear or magnetic structure. This is possible since the (double differential) scattering cross-section is given by

$$\frac{d^2\sigma}{d\Omega_f dE_f} = N \frac{k_f}{k_i} b^2 S(\mathbf{Q}, \omega) \quad (3.4)$$

where  $S(\mathbf{Q}, \omega) = \frac{1}{2\pi\hbar N} \sum_{ll'} \int_{-\infty}^{\infty} dt \langle e^{-i\mathbf{Q}\cdot\mathbf{r}_{l'}(0)} e^{i\mathbf{Q}\cdot\mathbf{r}_l(t)} \rangle e^{-i\omega t}$  for nuclear scattering [83].  $N$  is the number of nuclei,  $\mathbf{r}_l$  is the coordinates of the scattering centres and  $\langle \rangle$  is the thermal average over initial states. It is seen that the scattering function only depends on the momentum and energy transferred from the neutron to the sample, not on the absolute values of  $\mathbf{k}_i$  or  $\mathbf{k}_f$ . The scattering can be conveniently divided into coherent and incoherent parts and several excellent books give details on the derivation of cross-sections for different scattering processes [84, 82]. The coherent scattering provides information about the cooperative effects among different atoms such as elastic Bragg scattering or inelastic scattering by phonons or magnons. Here I will only repeat the general formulas for the coherent cross-sections from [82] since this thesis will mainly deal with these. For coherent magnetic scattering the double differential cross-section is given by

$$\frac{d^2\sigma}{d\Omega_f dE_f} = N \frac{k_f}{k_i} p^2 e^{-2W} \sum_{\alpha, \beta} (\delta_{\alpha, \beta} - \hat{Q}_\alpha \hat{Q}_\beta) S^{\alpha\beta}(\mathbf{Q}, \omega) \quad (3.5)$$

where  $S(\mathbf{Q}, \omega) = \frac{1}{2\pi\hbar} \int_{-\infty}^{\infty} e^{-i\omega t} \sum_l e^{i\mathbf{Q}\cdot\mathbf{r}_l} \langle S_0^\alpha(0) S_l^\beta(t) \rangle$ . The  $p$  factor and the Debye-Waller factor  $e^{-2W}$  are explained below and  $\alpha$  and  $\beta$  can take the values  $x, y, z$  respectively. It is important to note that only the component of  $\mathbf{S}$  which is perpendicular to  $\mathbf{Q}$  contributes to the scattering amplitude as expressed by  $|\mathbf{S}_\perp|^2 = |\hat{\mathbf{Q}} \times (\mathbf{S} \times \hat{\mathbf{Q}})|^2 = |\mathbf{S} - \hat{\mathbf{Q}}(\hat{\mathbf{Q}} \cdot \mathbf{S})|^2 = \sum_{\alpha, \beta} (\delta_{\alpha\beta} - \hat{Q}_\alpha \hat{Q}_\beta) S_\alpha^* S_\beta$ . The  $p$

factor contains the magnetic formfactor of an atom ( $f(\mathbf{Q})$  which is the Fourier transform of the normalised unpaired spin density) since  $p = 0.2695 \cdot 10^{-12} \text{cm} \cdot g \cdot f(\mathbf{Q})$  where  $g$  is the Landé splitting factor. The temperature dependent Debye-Waller factor  $e^{-2W}$  has also been introduced here where for small instantaneous displacements of an atom from its equilibrium position  $\mathbf{u}$ ,  $W = \langle (\mathbf{Q} \cdot \mathbf{u})^2 \rangle$  in a crystal with orthorhombic axes.

For scattering from a crystal the coherent elastic differential cross-section is generally written as

$$\left. \frac{d\sigma}{d\Omega} \right|_{coh}^{el} = N \frac{(2\pi)^3}{V_0} \sum_{\mathbf{G}} \delta(\mathbf{Q} - \mathbf{G}) |F(\mathbf{G})|^2 \quad (3.6)$$

where  $F(\mathbf{G})$  is the static nuclear ( $F_N$ ) or magnetic ( $F_M$ ) structure factor and  $\mathbf{G}$  the corresponding nuclear ( $\mathbf{G}_N$ ) or magnetic ( $\mathbf{G}_M$ ) scattering vector. The static nuclear structure factor can be written

$$\mathbf{F}_N(\mathbf{G}_N) = \sum_j \bar{b}_j e^{i\mathbf{G}_N \cdot \mathbf{d}_j} e^{-W_j} \quad (3.7)$$

where  $\bar{b}$  is the average (or coherent) scattering length and the sum is over sites within the unit cell. It contains information of the atomic positions  $\mathbf{d}_j$  and the mean square displacements. The static magnetic structure factor

$$\mathbf{F}_M(\mathbf{G}_M) = \sum_j p_j \mathbf{S}_{\perp} e^{i\mathbf{G}_M \cdot \mathbf{d}_j} e^{-W_j} \quad (3.8)$$

where the sum is over sites within the magnetic unit cell. The scattering vector  $\mathbf{Q}$  will sometimes be denoted by the Miller indices ( $HKL$ ) referring to the reciprocal unit cell in this thesis.

### 3.1.2 Triple axis spectrometer

The advantage of a triple axis spectrometer (TAS) shown schematically in Figure 3.1, is that it allows to select  $E_i$ ,  $E_f$  and  $\mathbf{Q}$  freely and the resolution can be tuned to obtain sharper peaks and optimise the signal-to-noise ratio but often at the cost of intensity. The neutron beam coming from the moderator of the reactor or spallation source is 'white'. It typically has a 0.1-10 meV distribution for a cold neutron source (see Figure 5.3) and 5-200 meV for a thermal neutron source[82].

The selection of  $E_i = \frac{\hbar^2 k^2}{2m_n} = \frac{\hbar^2}{2m_n \lambda^2} = \frac{81.81 [\text{meV} \cdot \text{\AA}^2]}{\lambda_i^2 [\text{\AA}^2]}$  is done by Bragg scattering  $n\lambda_i = 2d \sin \theta_m$  at the monochromator. The monochromator is typically made of graphite, silicon or germanium with a relatively large mosaicity (around 20'-40') in order not to lose too much intensity. The beam after the monochromator is in general therefore only quasi-monochromatic with a (narrow) distribution of wavelengths around  $\lambda_i = \lambda$ ,  $\frac{1}{2}\lambda$ ,  $\frac{1}{3}\lambda$  etc. often rather divergent. The divergence can be made smaller by a collimator at the expense of a decrease in intensity which roughly scales with the collimation (depending on the wavelength spread). The higher order contamination of the beam can be removed by

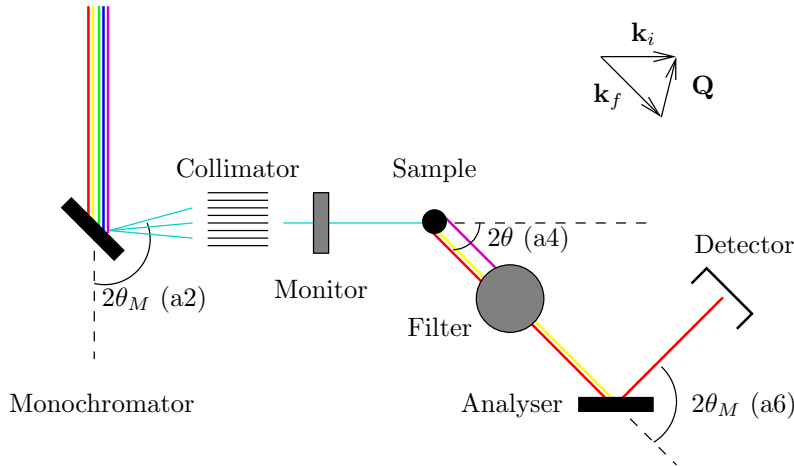


Figure 3.1: A schematic drawing of a neutron scattering triple axis spectrometer. The three axes are monochromator to sample, sample to analyser and analyser to detector, respectively. The inset shows the scattering triangle.

the use of a filter which scatters neutrons of energies above a threshold energy in all directions thereby removing them from the primary beam direction.

The scattering process at the sample can be elastic  $\hbar\omega = 0$  or inelastic  $\hbar\omega \neq 0$  and the scattering vector  $\mathbf{Q}$  is selected by rotating the second arm of the instrument by  $2\theta$ . In case of elastic Bragg scattering the scattering vector equals a reciprocal lattice vector in order to fulfil the Bragg condition and  $|\mathbf{Q}| = |\mathbf{G}| = 2|\mathbf{k}|\sin\theta$  where  $|\mathbf{k}_i| = |\mathbf{k}_f| = |\mathbf{k}|$ .

A TAS has four 'arms' controlled by rotation of the joints between them as shown in Figure 3.1. The scattering angle of the monochromator which is rotated by  $a1$  ( $\Omega_M$ ) is typically named  $a2$  ( $2\theta_M$ ), the sample is rotated by  $a3$  ( $\Omega$ ) with scattering angle  $a4$  ( $2\theta$ ) and the analyser is rotated by  $a5$  ( $\Omega_A$ ) with scattering angle  $a6$  ( $2\theta_A$ ). Some of these angles are denoted in Figure 3.1.

The count rate at the detector is usually normalised to the count rate at the monitor, as the flux coming from the neutron source can vary a lot in time. The monitor is usually positioned just before the sample and removes a small but constant fraction of the beam. More information about the specific components in a TAS is given in Chapter 5 where the cold neutron TAS called RITA-II which is situated at SINQ PSI in Villigen, Switzerland is described in detail. This particular spectrometer also features a seven blade analyser which can be used to simultaneously monitor different reciprocal space points at the same scattered energy - the so-called monochromatic imaging mode.

### 3.1.3 Ideal and imperfect crystals

The integrated intensity from a magnetic or nuclear reflection with structure factor  $F(HKL)$  can be calculated by

$$I = A \frac{\lambda^3 |F(HKL)|^2}{V_0^2 \sin 2\theta} \quad (3.9)$$

where  $A$  is a constant depending in the incident flux, the sample volume and the counting time,  $V_0$  is the unit cell volume and  $\frac{1}{\sin 2\theta}$  is called the Lorentz factor. This formula applies to a single perfect crystal, which is small enough for multiple scattering not to occur.

If multiple scattering from a single perfect crystal occurs the intensity in (3.9) is said to be reduced by primary extinction. Real crystals are often imperfect and can be thought of as composed by a mosaic of small blocks of perfectly aligned crystal planes. The orientation of these mosaic blocks is distributed around some average value, in which case (3.9) again applies to the intensity of the reflection if a rocking curve is performed. The distribution of the mosaics is often assumed to be Gaussian with standard deviation  $\eta$ , usually denoted as the 'mosaicity' or 'mosaic width' of the crystal.

If, however, enough of these small mosaic blocks are aligned down through the crystal, the top blocks will 'shadow' the lower lying blocks so the incident beam is weaker in the lower blocks since some of the beam has already been scattered from the top blocks. In this case the intensity from the mosaic crystal will again be less than predicted by (3.9), even if a rocking curve is performed, and secondary extinction is said to be significant. In case both primary and secondary extinction can be ignored the crystal is said to be ideally imperfect. Absorption effects have also not been taken into account in the intensity in (3.9) since we are only considering scattering.

Since neutrons interact only weakly with the crystal, most crystals with a finite mosaic spread can be considered ideally imperfect in neutron scattering experiments. By performing rocking scans (also called  $\omega$  scans or  $\Omega$  scans) at a constant  $2\theta$ , it is then possible to compare the structure factors of various magnetic and nuclear reflections[82].

### 3.1.4 Resolution

As described above because of the small scattering cross-section of neutrons and the limited neutron flux generally available one typically performs measurements with finite beam divergence and with monochromator and analyser crystals having large mosaic spreads. Therefore the energy and momentum transfers of the neutrons are distributed within a small region about the average values  $(\omega_0, \mathbf{Q}_0)$ . The measured signal at the detector is a convolution of the resolution of the spectrometer  $R(\omega - \omega_0, \mathbf{Q} - \mathbf{Q}_0)$  and the scattering function  $S(\mathbf{Q}, \omega)$ . The resolution of a TAS is brilliantly described in [82] and in this section I will simply sketch some of the important results from this book.

An effective collimation  $C_j$  limits the angular divergence of the beam for each of the four 'arms' of the TAS. The monochromator together with the collimations  $C_0$  before the monochromator and  $C_1$  just after the monochromator, selects a bundle of neutrons. This bundle of neutrons has wave vectors  $\mathbf{k}_i$  characterised by a distribution  $P_i(\mathbf{k}_i - \bar{\mathbf{k}}_i)$  where  $\bar{\mathbf{k}}_i$  is the average wave vector. Likewise the probability of a neutron with  $\mathbf{k}_f$  reaching the detector is described by the distribution  $P_f(\mathbf{k}_f - \bar{\mathbf{k}}_f)$  given by  $C_2$  and  $C_3$ .

The flux reaching the detector is

$$F_d(\bar{\mathbf{k}}_i, \bar{\mathbf{k}}_f) = \int d\mathbf{k}_i \int d\mathbf{k}_f F_i(k_i) P_i(\mathbf{k}_i - \bar{\mathbf{k}}_i) \frac{d^3\sigma}{dk_f^3} P_f(\mathbf{k}_f - \bar{\mathbf{k}}_f) \quad (3.10)$$

where  $\frac{d^3\sigma}{dk_f^3} = \frac{\hbar^2}{m_n k_f} \frac{d^2\sigma}{dE_f d\Omega_f} = \frac{\hbar^2}{m_n k_i} S(\mathbf{Q}, \omega)$  is the differential cross-section in Cartesian coordinates.  $F_i(k_i) = k_i \phi(k_i)$  is the neutron flux at the first collimator  $C_0$  where  $\phi(k) d\mathbf{k}$  is the number of neutrons at  $C_0$  with wave vectors in the range  $\mathbf{k}$  to  $\mathbf{k} + d\mathbf{k}$ .

If  $\phi(k_i)$  varies slowly compared to the distribution  $P_i(\mathbf{k}_i - \bar{\mathbf{k}}_i)$  it can be replaced by the average value

$$F_d(\omega_0, \mathbf{Q}_0) = \phi(\bar{k}_i) \int d\omega \int d\mathbf{Q} R(\omega - \omega_0, \mathbf{Q} - \mathbf{Q}_0) S(\mathbf{Q}, \omega) \quad (3.11)$$

which defines the resolution function

$$R(\omega, \mathbf{Q}) = \frac{\hbar^2}{m_n} \int d\mathbf{k}_i \int d\mathbf{k}_f P_i(\mathbf{k}_i) P_f(\mathbf{k}_f) \delta(\mathbf{Q} - \mathbf{k}_f + \mathbf{k}_i) \delta(\omega - \frac{\hbar}{2m_n} (k_i^2 - k_f^2)) \quad (3.12)$$

The resolution can be written in functional form in coordinates defined relative to  $\mathbf{Q}_0$  [85]

$$R(\omega - \omega_0, \mathbf{Q} - \mathbf{Q}_0) = R_0 e^{-\frac{1}{2} \Delta \mathbf{Q} \mathbf{M} \Delta \mathbf{Q}} \quad (3.13)$$

where  $\Delta \mathbf{Q} \approx (\frac{m_n}{\hbar Q_0} (\omega - \omega_0), Q_{\parallel} - Q_0, Q_{\perp}, Q_z)$  and  $\mathbf{M}$  is a  $4 \times 4$  matrix. Setting the argument of the exponential equal to a constant defines a 4-dimensional ellipsoid, and for a given spectrometer configuration the volume, shape and orientation of this ellipsoid depends only on  $(\omega_0, \mathbf{Q}_0)$ . However, the resolution matrix  $\mathbf{M}$  is not diagonal in general and the principal axes of the resolution ellipsoid do not coincide with the ones determined by  $\omega_0$  and  $\mathbf{Q}_0$ . If however, the beam divergence is small the resolution in the vertical direction  $\Delta \mathbf{Q}_z$  can be assumed uncoupled from the other three coordinates if the beam divergence is small [82].

The TAS in Figure 3.1 is shown in the so-called 'W' configuration which gives the best  $\mathbf{Q}$ -resolution. An example of the difference in line width of going from negative scattering angles (as in the 'W' configuration) to positive scattering angles is shown in Figure 5.18 where the figures in the left(right) column show line-scans through the powder cone on the negative(positive) scattering side. The spectrometer was in 2-axis mode, meaning that the last two arms of the TAS act as one straight arm, not using the analyser.

In symmetric conditions further simplifications can be made. Let us consider elastic scattering on a symmetric spectrometer in the 'W' configuration. Under these conditions both  $\Delta \hat{\mathbf{Q}}_{\parallel}$  and  $\Delta \hat{\mathbf{Q}}_z$  are principal axes of the resolution matrix. The longest principal axis is orthogonal to  $\mathbf{Q}_0$  and lying in the  $\Delta \mathbf{Q} \perp, \Delta \omega$  plane with a negative slope given by

$$\frac{\hbar\Delta\omega}{\Delta Q_{\perp}} = \frac{\hbar^2 k}{m_n} \cos\theta (1 + \tan\theta \tan(\theta - \theta_M)) \quad (3.14)$$

where  $\hbar\Delta\omega = \Delta E$ . If furthermore all collimations and mosaic widths have the same value  $\alpha$  and the scattering angles are moderate then  $\frac{\Delta E}{E} \sim \frac{2\alpha}{\tan\theta_m}$  and  $\frac{\Delta Q}{k} \sim \alpha$ . For  $\alpha = 40'$  this gives  $\Delta Q = 0.018\text{\AA}^{-1}$  and  $\Delta E = 0.16\text{ meV}$  for  $E = 5.0\text{ meV}$ .

Due to the elongated, canted nature of the resolution ellipsoid (see figure 3.2) the peak width depends on the way the resolution function is scanned through the structure defined by the scattering function  $S(\mathbf{Q}, \omega)$ . Because of this, and due to often asymmetric conditions of the spectrometer, virtual experiments where the resolution is taken into account by ray-tracing the neutrons through the various components of the spectrometer are very useful. A large portion of this thesis (Chapter 5) is dedicated to the task of building a specific spectrometer in great detail within a Monte-Carlo ray tracing setting in order to predict the effects of the spectrometer resolution of a particular line scan.

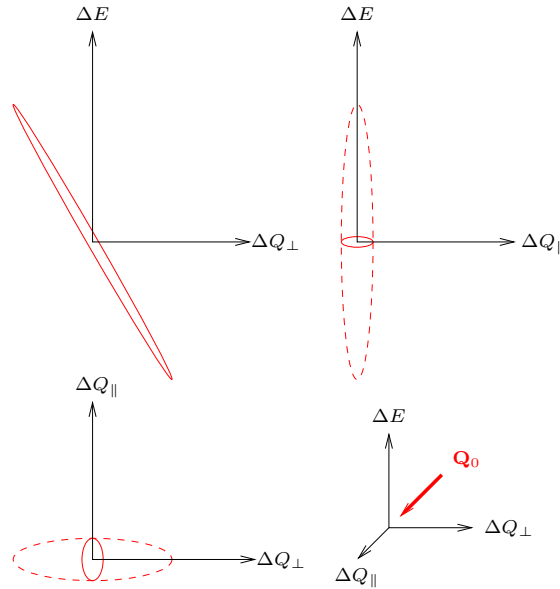


Figure 3.2: Schematic drawing of a resolution ellipsoid. The coordinate system in the lower right corner defines the coordinate system with respect to the average scattering vector  $\mathbf{Q}_0$  and the solid lines in each figure represent the cross-section of the resolution ellipsoid with the given plane. The dashed line show the projection of the ellipsoid unto the plane. Adapted from [82].

### 3.2 Hard x-ray diffraction

A complementary technique used to determine the structure of condensed matter systems is x-ray diffraction. The reader is referred to a recent and good textbook for thorough introduction [86]. X-rays are produced by acceleration of charged particles, usually electrons or positrons. X-rays interact with the

electrons in the sample wherefore the penetration depth is also limited. The absorption cross-section however decreases by the energy of the photons cubed and hard x-rays with  $E=100$  keV can penetrate several millimetres and thus probe the bulk properties of a sample. Since the x-rays interact with the electrons of the atoms in the material the interaction can not be considered point-like with respect to the wavelength  $\lambda[\text{\AA}] = \frac{12.398}{E[\text{keV}]}$  of the x-rays. The atomic form factor  $f(\mathbf{G})$  therefore enters the structure factor of the unit cell

$$F(\mathbf{G}) = \sum_j f_j(\mathbf{G}) e^{i\mathbf{G} \cdot \mathbf{d}_j} e^{-W_j} \quad (3.15)$$

where  $\mathbf{d}_j$  is the atomic positions,  $\mathbf{G}$  is a reciprocal lattice vector and  $W_j$  is the Debye-Waller factor described in Section 3.1.1. The differential cross-section is given by

$$\frac{d\sigma}{d\Omega} = r_0^2 N \frac{(2\pi)^3}{V_0} P |F(\mathbf{Q})|^2 \delta(\mathbf{Q} - \mathbf{G}) \quad (3.16)$$

where  $r_0$  is the Thomson scattering length and  $P$  is the polarisation factor which for some typical experiments is

$$P = \begin{cases} 1 & \text{synchrotron vertical scattering plane} \\ \cos^2 2\theta & \text{synchrotron horizontal scattering plane} \\ \frac{1}{2}(1 + \cos^2 2\theta) & \text{unpolarised source} \end{cases} \quad (3.17)$$

where  $2\theta$  is the scattering angle. The hard x-ray experiments in this thesis are performed in the synchrotron horizontal plane. Assuming all of the sample is illuminated, the number of X-ray photons scattered per second into a detector which covers the solid angle  $\Delta\Omega$  is

$$I = I_0 N \Delta\Omega \frac{d\sigma}{d\Omega} \quad (3.18)$$

where  $N$  is the number of unit cells in the sample and  $I_0$  is the incident intensity of photons. This result applies to a perfectly monochromatic and collimated incident beam on an infinite crystal. In real experiments however, the finite size of the crystal, or the scattering structure makes it possible to detect intensity at scattering angles which do not entirely fulfil the Bragg condition. Therefore the crystal has to be rotated a little (rocked) to collect the integrated intensity. Since the scattered beam is not perfectly collimated one also has to integrate over the direction of the final wave-vector and the resulting intensity per second is similar to the result for neutrons (3.9)

$$I = \Phi_0 r_0^2 P |F(\mathbf{Q})|^2 N \frac{\lambda^3}{V_0} \frac{1}{\sin 2\theta} \quad (3.19)$$

where  $\frac{1}{\sin 2\theta}$  is called the Lorentz factor and  $\Phi_0 \left[ \frac{\text{photons}}{\text{unit area} \times \text{sec}} \right]$  is the incident flux. This formula applies to an ideally imperfect single crystal (see section 3.1.3) in which no multiple scattering occurs. Since we were only considering scattering, absorption effects have also not been taken into account in (3.19).

### 3.3 Peak shapes and widths

The line shape of a diffraction peak is partially due to the instrumental resolution and partially due to the sample (broadening). For simplicity I will restrict the following calculations to a 1D reciprocal space.

#### 3.3.1 Gaussian line shape

In a neutron TAS the instrumental resolution line shape is close to a Gaussian

$$R(q) = a_1 e^{-\frac{(q-q_0)^2}{2\sigma_1^2}} \quad (3.20)$$

where the width  $\sigma_1$  depends on the scan direction. The additional line shape from the sample depends on the nature of the scattering i.e. the size and distribution function of the Bragg scattering domains or the nature of the correlation function for e.g. magnetic scattering. The resulting line shape  $P(q)$  is the convolution of the resolution function of the instrument  $R(q)$  with the sample line shape  $S(q)$

$$P(q) = (R * S)(q) = \int_{-\infty}^{\infty} R(q' - q)S(q') \quad (3.21)$$

If the scattering comes from a perfect crystal  $S(q)$  is the delta-function shaped structure factor. If the scattering comes from a distribution of finite domain size of crystallites, finite correlation lengths etc. the integrated scattering will result in broadened peaks with particular line shapes appearing in  $S(q)$ . The convolution of a Gaussian resolution (3.20) and a Gaussian sample broadening

$S(q) = a_2 e^{-\frac{(q-q_0)^2}{2\sigma_2^2}}$  is

$$(R^G * S^G)(q) = a_1 a_2 \int_{-\infty}^{\infty} e^{-\frac{(q'-q)^2}{2\sigma_1^2}} e^{-\frac{q'^2}{2\sigma_2^2}} dq' \quad (3.22)$$

$$= a_1 a_2 \int_{-\infty}^{\infty} e^{-\frac{(k-q/2)^2}{2\sigma_1^2}} e^{-\frac{(k+q/2)^2}{2\sigma_2^2}} dk \quad (3.23)$$

$$= a_1 a_2 \sqrt{\frac{2\pi\sigma_1^2\sigma_2^2}{\sigma_1^2+\sigma_2^2}} e^{-\frac{q^2}{2(\sigma_1^2+\sigma_2^2)}} \quad (3.24)$$

where  $q' = k + \frac{q}{2}$  has been introduced and the last step follows from  $\frac{(k-q/2)^2}{2\sigma_1^2} +$

$$\frac{(k+q/2)^2}{2\sigma_2^2} = \frac{\sigma_2^2+\sigma_1^2}{2\sigma_2^2\sigma_1^2} \left( k + \frac{\sigma_1^2-\sigma_2^2}{2\sigma_2^2\sigma_1^2} q \right)^2 + \frac{1}{2(\sigma_2^2+\sigma_1^2)} q^2.$$

Hence in case both the instrumental resolution and the scattering distribution are Gaussians one will measure a Gaussian line shape with FWHM

$$(w_m^G)^2 = \left( \sqrt{8 \ln 2} \sigma_1 \right)^2 + \left( \sqrt{8 \ln 2} \sigma_2 \right)^2 = (w_r^G)^2 + (w_b^G)^2 \quad (3.25)$$

where the subscript  $m$  is for measured,  $r$  is for resolution and  $b$  for broadening. From this relation  $w_b^G$  can be found if  $w_r^G$  is known. A Gaussian broadening of the scattering peak may result from a narrow distribution of domain sizes as I will discuss further in Section 3.4.

### 3.3.2 Lorentzian line shape

A Lorentzian broadening may result from an exponentially decaying function in real space. The simplest model for the correlation function in real space is exponentially decreasing[87]

$$\langle S_0^\alpha S_l^\alpha \rangle \propto e^{-\frac{w^L}{2} r_{0l}} \quad (3.26)$$

where  $\alpha$  can be either of  $x, y$  or  $z$  and the distance between spins at site 0 and  $l$  is  $r_{0l}$ . The decay parameter transfers to the HWHM of a Lorentzian function in reciprocal space when the exponentially decreasing function is Fourier transformed:

$$S^L(q) = \frac{w^L}{2\pi} \frac{1}{(q - q_0)^2 + (\frac{w^L}{2})^2} \quad (3.27)$$

with  $\text{FWHM} = w^L$  when Fourier transformed. Certain distributions of domain-sizes may also yield intrinsic Lorentzian broadening. Some examples are mentioned in Section 3.4.

The convolution of a Lorentzian instrumental resolution and a Lorentzian broadening will result in Lorentzian line shape with measured FWHM of

$$w_m^L = w_r^L + w_b^L \quad (3.28)$$

This can be seen using  $a = \frac{w_r^L}{2}$  and  $b = \frac{w_b^L}{2}$  and calculating

$$(R^L * S^L)(q) = \frac{ab}{(2\pi)^2} \int_{-\infty}^{\infty} dq' \frac{1}{(q' - q)^2 + a^2} \frac{1}{(q')^2 + b^2} \quad (3.29)$$

$$= \left[ \frac{a^2 b \tan^{-1}(\frac{q-q'}{a}) + a(a^2 - b^2 + q^2) \tan^{-1}(\frac{q'}{b})}{2\pi (a^4 - 2a^2(b^2 - q^2) + (b^2 + q^2))} \right] \quad (3.30)$$

$$+ \left. \frac{b \left\{ (b^2 + q^2) \tan^{-1}(\frac{-q+q'}{a}) + aq \ln \left( \frac{(q')^2 + b^2}{(q')^2 - 2qq' + a^2} \right) \right\}}{2\pi (a^4 - 2a^2(b^2 - q^2) + (b^2 + q^2))} \right]_{q'=-\infty}^{q'=\infty} \quad (3.31)$$

$$= \frac{a + b}{2((a + b)^2 + q^2)} \quad (3.32)$$

which is a Lorentzian with FWHM  $w_m^L = 2(a + b) = w_r^L + w_b^L$ . The resolution is typically Lorentzian in triple-axis (three crystal) x-ray diffraction experiments[88].

### 3.3.3 Voigt line shape

The measured line shape of a peak with a Lorentzian intrinsic broadening and Gaussian instrumental resolution will be a Voigt

$$V(u, s) = (R^G * S^L)(q) = \frac{\sigma_2}{2\pi} \int_{-\infty}^{\infty} dq' \frac{e^{-\frac{(q'-q)}{2\sigma_1^2}}}{\left(\frac{\sigma_2}{2}\right)^2 + q'^2} = \frac{s}{2\pi} \int_{-\infty}^{\infty} dt \frac{e^{-t^2}}{s^2 + (u-t)^2} \quad (3.33)$$

in one dimension with dimensionless variables  $t = \frac{q'-q}{\sqrt{2}\sigma_1}$ ,  $u = \frac{q}{\sqrt{2}\sigma_1}$  and  $s = \frac{\sigma_2}{\sqrt{2}\sigma_1}$ . The Gaussian FWHM is  $w_r^G = \sqrt{8 \ln 2} \sigma_1$  and the intrinsic Lorentzian FWHM  $w_b^L = \sigma_2$ . The measured width can be approximated by a parabolic expansion [89]

$$(w_m^V)^2 = w_b^L w_m^V + (w_r^G)^2 \quad (3.34)$$

It can however also be found from fitting the measured data to a Voigt and extracting the Lorentzian broadening  $w_b^L$ . From this the correlation length is found as  $2/w_b^L$ . Likewise an exponential distribution of domain sizes with average size  $2/w_b^L$  will result in Lorentzian broadening with FWHM  $=w_b^L$ , which will be further discussed in Section 3.4. If in this case the resolution is Gaussian the measured line shape can be fitted to a Voigt like described above.

### 3.4 Domain size distributions

Even after it has been determined that a peak is broadened due to a finite size domain effect and even if it can be determined from the  $\chi^2$  of fits to various functions which is the most appropriate, there might still be many ways of interpreting how the domains giving rise to this effect are distributed. Both the shape of each domain and the distribution of sizes have an effect on the shape of the peak.

Let us first consider the scattering intensity from a single domain. In the simple case of a one-dimensional system of  $N$  atoms in a chain with distance  $|\mathbf{a}|$  between them, the scattering intensity at a specific point in reciprocal space as observed at the detector is proportional to the function [86]

$$I_N(\mathbf{Q}) \propto \left| \frac{\sin(\frac{N}{2} \mathbf{a} \cdot \mathbf{Q})}{\sin(\frac{1}{2} \mathbf{a} \cdot \mathbf{Q})} e^{i \frac{N-1}{2} \mathbf{a} \cdot \mathbf{Q}} \right|^2 = \frac{\sin^2(\frac{N}{2} \mathbf{a} \cdot \mathbf{Q})}{\sin^2(\frac{1}{2} \mathbf{a} \cdot \mathbf{Q})} \quad (3.35)$$

for a particular number  $N$  of atoms in the domain. The function has global maximum with value  $N^2$  when  $\mathbf{a} \cdot \mathbf{Q} = 2\pi n$  with  $n$  an integer. So if  $\mathbf{a}$  is a lattice vector the global maximum occurs whenever  $\mathbf{Q}$  is a reciprocal lattice vector. The first zero occurs at  $\mathbf{a} \cdot \mathbf{Q} = a(2n+1)\pi$  where  $w = \frac{2\pi}{Na}$  is then the width in reciprocal space of the first peak. The intensity of the peaks for higher  $n$  is quickly suppressed as  $N$  increases and the primary peak can be approximated by a Gaussian of FWHM  $=w^G = 0.88w \sim w$ . The integrated area of the peak is proportional to the number of atoms  $N$ , regardless of whether the domain is 1D, 2D or 3D. The above discussion also applies if  $N$  is the number of unit cells instead of simple atoms. Eq. 3.35 is graphically represented in Figure 3.3. One

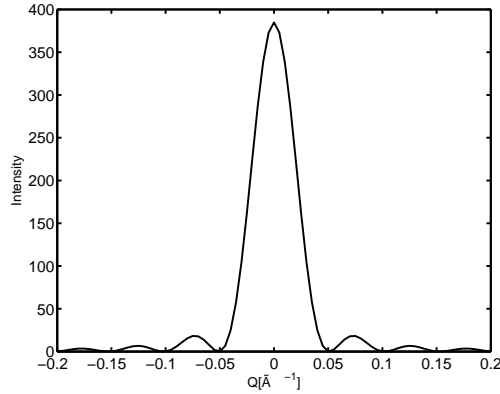


Figure 3.3: A graphical representation of Eq. 3.35. The area under the central peak of the curve is proportional to  $N$  since it is given by the amplitude ( $\propto N^2$ ) times the width ( $\propto \frac{1}{N}$ ).  $a = 2\pi$  and  $N = 19.6$  in this plot, referring to the weighted average of the domain size distribution in Figure 3.4.

extreme situation is therefore if all domains are of equal size  $D = Na$  which would result in a Gaussian peak shape with FWHM  $w^G = \frac{2\pi}{D^G}$  [90]. Another extreme situation in the one-dimensional case is if the domain size distribution is described by an exponentially decaying function with mean size particle size  $D^L = 2/w^L$ . In this case the peak shape is Lorentzian with FWHM= $w^L$ [90]. In general as the relative amount of domains of small size grows, the inclination of the diffraction peak to have Lorentzian like tails grows as well. In the following I will use  $D^G$  and  $D^L$  as 'apparent domain size' in each case.

In the more general scenario, for each domain consisting of  $N$  atoms the scattering can be approximated by a Gaussian and weighted according to a domain size distribution function. The integrated scattering from the crystal at a particular scattering vector is calculated from the sum of the scattering contributions from all domains. A peak of scattering intensity as function of scattering vector can be simulated this way. Numerical simulations have shown that the peak shape in the general case depends completely on the details of the domain size distribution [91]. In case of a Gaussian domain size distribution with mean size  $D$  between 50 and 200 Å and a FWHM of the distribution of the same size as  $D$  the resulting peak shape was Lorentzian like with FWHM= $w^L \rightarrow \pi/D$ . A Lorentzian shape of the diffraction peak can also be produced if the domain sizes are distributed by the so-called log-normal distribution

$$f(x, \mu, \sigma) = \frac{1}{x\sigma\sqrt{(2\pi)}} e^{-\frac{(\ln|x|-\mu)^2}{2\sigma^2}} \quad (3.36)$$

where  $x$  is the domain size and the distribution width and shape depends on the  $\sigma$  and  $\mu$  parameters. An example is shown in Figure 3.4 which gives a Lorentzian peak shape of the 'simulated' diffraction data in the right part of the figure. The average domain size is given by  $D = 0.88 \frac{2\pi}{w^L}$  for lognormal distributions with similar shape. The domains are assumed to be cubic. The estimate of the

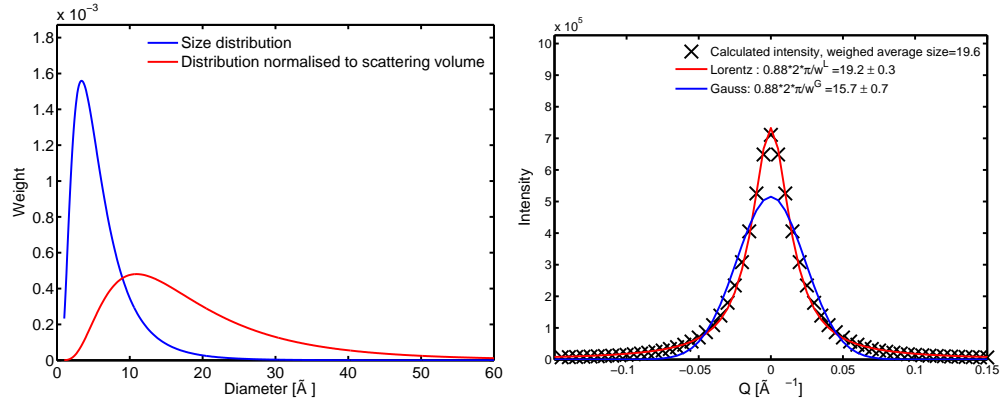


Figure 3.4: Left: Lognormal domain distribution for  $\mu = 0$  and  $\sigma = 0.625$ . The blue curve shows the domain size distribution, the red curve has adjusted scattering weight to particle size. Each domain of a particular size  $N$  contributes to the diffraction by Eq. (3.35). Right: The 'data points' in the main figure is the calculated intensity at the particular reciprocal lattice vector from the domain size distribution on the left. It is seen that this particular distribution gives a Lorentzian peak shape with  $w^L \sim 0.9 \cdot \frac{2\pi}{D} \text{Å}^{-1}$  where  $D = 19.6 \text{Å}$  is the weighted average domain size of the distribution shown by the red curve in the left figure. The Matlab code to produce this figure was kindly provided by Jonas O. Birk [92].

average domain size from the Lorentzian width  $w^L$  of a diffraction peak is in the lognormal distributed case  $0.88\pi = 2.8$  times larger than the estimate from an exponential distribution.

If the nature of the broadening cannot be decided from the line shape I will use a rule of thumb that the average domain size is somewhere between the apparent domain size of the Gaussian and Lorentzian extreme line shape.

Ideally one would be able to find the correct shape of a diffraction peak from fits. But even if it is possible to distinguish the shape there are still numerous interpretations of the domain distributions which it might reflect. Therefore the main effort in this thesis has been on identifying and de-convoluting the broadening width and not on the interpretation in terms of domain distributions. A simple finite size measure of apparent domain size is taken as  $D^G = 2\pi/w_b^G$  in case the broadening  $w_b^G$  of the diffraction peak is of Gaussian nature. In case the broadening is of Lorentzian nature the apparent domain size or correlation length is found by  $D^L = 2/w_b^L$ .

## 3.5 Simulated neutron scattering

A neutron scattering instrument consists of a series of optical components each of which modifies the beam in terms of e.g. divergence and wavelength spread. Some simple components might be modelled by the acceptance diagram method [93] where the neutron beam distribution is described by a constant or a simple function such as a Gaussian. In a real instrument there might however be strong correlations between the parameters of the neutron beam such as divergence and position and the analytical methods reach their limit of validity. Instead Monte Carlo methods[94] can be applied where integration over the microscopic event of each component is performed by random but uniform sampling of the neutron trajectories.

McStas is the leading Monte Carlo neutron ray-tracing simulation package and can be downloaded freely including a complete manual at [www.mcstas.org](http://www.mcstas.org).

### 3.5.1 Introduction to Mcstas

A good and detailed description of the Monte Carlo ray tracing method for simulating neutron instruments is given in the McStas manual[95] and I will simply outline some of the features in this section.

Instead of keeping track of every specific neutron as either present or lost in each component, the microscopic processes which lie behind the alteration of the beam can be described by probabilities (e.g. of absorption or scattering). In this way all neutrons are passed through the component but scaled according to e.g. the reflectivity of the component. Instead of counting neutrons in the simulation we account for the neutron histories, or rays as they are called. Each neutron 'ray' will be weighted according to the parameters of each component of the instrument. For example the weight adjustment happens at transmission through filters and collimators, reflection from guide walls and monochromators and scattering from all types of samples. The resulting neutron weight after passage of the  $m$ th component is

$$p_m = p_0 \prod_{j=1}^n \rho_j \quad (3.37)$$

where  $\rho_j$  is the weight factor of the  $j$ th component and  $p_0$  is the initial neutron weight. The sum of the weights of the rays is an estimate of the mean number of neutrons hitting the detector (or monitor) per. second in the physical experiment.

$$I = \sum_i p_i = n\bar{p} \quad (3.38)$$

where the sum is over the neutron rays and  $\bar{p}$  is the average weight factor. The monitor components keep track of the number of rays  $n = \sum_i p_i^0 = \sum_i 1$ , the intensity  $I = \sum_i p_i$  and  $M_2 = \sum_i p_i^2$ . The latter is a good approximation of the statistical variance of the neutron weights. If the weights of the neutron rays hitting the detector are similar  $p_i \approx \bar{p}$ , the uncertainty on the intensity is

$$\sigma(I) = \sqrt{M_2} = \sqrt{n\bar{p}} = \frac{I}{\sqrt{n}} \quad (3.39)$$

just as in physical neutron experiments.

Besides the physical processes the weight factors reflect, the weight factors can also be adjusted in case one only want to look at scattering in a particular direction within a solid angle interval  $\Delta\Omega$ . This is known as importance sampling and used for example in the source components where the interesting neutrons are the ones passing into the guide even if the source emits in a sphere covering the whole  $4\pi$  solid angle. The probability of passing into the guide  $P$  of course still needs to be correct even if we don't simulate trajectories outside the focusing window. This is taken care of by

$$f_{MC}\rho_j = P \quad (3.40)$$

where  $f_{MC}$  is the Monte Carlo choice reflecting the probability of a particular simulation process, and  $\rho_j$  is the weight multiplier. In the example above we take  $f_{MC}$  and  $P = \frac{\Delta\Omega}{4\pi}$  giving  $\rho_j = \frac{|\Delta\Omega|}{4\pi}$ .

In order to improve the efficiency of the simulations, a collection of  $s$  neutron histories at a particular component in the instrument might be sampled repeatedly  $r$  times giving in total of  $n$  rays. This is done by the `SPLIT` keyword in the `TRACE` section (described in Section 3.5.2). The `SPLIT` feature is used in the virtual replica of the RITA-II instrument which Chapter 5 is devoted to. The parameter `REP` controls the number of repetitions  $r = n/s$  and it should not exceed the dimensionality  $d$  of the Monte Carlo integration space in order for the sampling to be representative of the complete distribution of neutron histories[95]. In McStas  $d = 10$  (3 coordinates for position + 3 for velocity + 3 for spin + 1 for time) and I have used `REP`≤8.

### 3.5.2 Building an instrument in McStas

A neutron instrument is built in the McStas meta-language which can be edited either in the built-in editor of the graphical user interface (GUI) or through another editor of your choice. By the `mcrun` command the instrument file is translated by the McStas compiler into C code which is then translated by a C compiler. The resulting data are then saved to ASCII output files from the monitor components which can be visualised through `mcplot` or further handled and analysed in programs such as Matlab.

The elements of a McStas instrument are marked by different keywords. Below I will list only the ones I have used in the virtual RITA-II (V-RITA-II) instrument, the reader is referred to the McStas manual for a complete list and more extensive description

- `DEFINE INSTRUMENT name(par=10, string s="inputstring")`  
The input parameters in the header are by default floating point numbers with precision `double` but can also be strings if denoted like the above

example, enabling input of data files. The default values are declared in the header with the *par=value* syntax. The parameters may be scanned when running the instrument with the `-N` flag.

- `DECLARE %{ C_code %}`  
Optional section with declarations of global C parameters
- `INITIALIZE %{ C_code %}`  
Optional section where instrument settings may be modified
- `TRACE components`  
This section contains the list of components in the neutron instrument
- `END`  
The end of the instrument must be marked by this keyword

The components are read in from the specified directories (see the McStas manual) have file extensions `*.comp` and the structure

```
COMPONENT name = component_name( par1= value1, par2 = value2)
AT (x,y,z) RELATIVE reference
ROTATED (alpha,beta,gamma) RELATIVE reference
```

The position of the component in McStas coordinates ( $\hat{z}$  is downstream,  $\hat{y}$  is vertical in the opposite direction of gravity and  $\hat{x}$  is defined by a right-hand coordinate system) is written after the `AT` keyword. `reference` is the unique name of another component which might also be replaced by the `PREVIOUS` keyword. A component may be placed `ABSOLUTE` instead of `RELATIVE reference`. The component may also be `ROTATED` with respect to the `reference` component by  $(\alpha, \beta, \gamma)$  where  $\alpha$  is rotation around  $\hat{x}$  in degrees etc. If a value of a parameter in a component is another parameter which is also declared in the header of the instrument (the `DEFINE INSTRUMENT` section) it can be scanned when running the instrument.

When making a TAS from scratch it is a good idea to use an Arm component for every rotating motor of the instrument. Find the components which are always at a fixed position and set the others at relative distances to these. A template TAS is available in the McStas package which includes some TAS-MAD code to calculate the positions of the angles a1-6 from Miller index input referring to a single-crystal defined by a lattice and scattering plane. This so-called *HKL*-calculator is further treated in Section 5.8.3.

When building a virtual replica of a real neutron instrument all the components of course need to have their parameters adjusted accordingly. If the parameters are changed or scanned during the experiment they need to be placed as variables in the header of the McStas instrument.

In the task of comparing virtual experiments to physical ones it would be ideal if the settings of a particular scan could simply be read in from the datafile of the physical experiment. This however demands that all parameters, including scan parameters, distances and other settings such as whether the filter, perspex attenuator etc. are in the beam and which collimators are used, are recorded in the datafile. This is rarely the case and much time has been spent

in this thesis in tracking down and making a puzzle of these settings from technical drawings and sometimes incomplete logbooks. A common standard of datafile from neutron instruments worldwide including all this information would greatly improve the efficiency and accuracy of virtual experiments in the future. The NeXus data format [96] is a promising candidate which is able to contain all the needed information.

### 3.5.3 Running McStas

McStas can be downloaded freely from the website [www.mcstas.org](http://www.mcstas.org). Depending on your operative system follow the instructions in the manual which can also be downloaded at the McStas homepage. McStas has a GUI (`mcgui`) which is good for new users but I prefer to run it from a terminal through shell scripts. A quick guide below gives the most important commands.

To simulate neutron rays in McStas type

```
> mcrun RITA.instr
```

A number of flags can be used in this call e.g.

```
--format = PGPLOT
--help
-n
-N
-d
```

The plotting format can be e.g. PGPLOT or MATLAB, `n` is the number of neutrons histories ('rays') to simulate, `N` is the number of scan points and `d` is the directory where to put the simulated patterns. An example is

```
> mcrun -d staging01 -N 21 -n \$1 RITA.instr A4=-72,-70 COLL_MS=40
```

where the parameters mentioned explicitly in the call overrules the values set in the instrument and the variables with `$` are prompted for. This call can be put in e.g. a shell script for easier access to recall.

To plot the simulated patterns in directory `[dir]` use

```
> mcplot [dir]
```

The intensities in the plots are the mean neutrons hitting the detector per second. It is also possible to visualise the instrument and neutron paths instead of recording simulated neutron patterns:

```
> mcdisplay RITA.instr A4=-71 COLL_MS=40
```

where only the format and help flag can be used.

Documentation on the specific components in the instrument-file can be viewed by

```
> mcdoc [component name]
```



## Chapter 4

# Properties of LSCO+O

As discussed in Chapter 2 it is possible to dope  $\text{La}_2\text{CuO}_4$  with holes by exchanging some of the La atoms by Sr. But another method of hole-doping exist named superoxygenation in which an excess non-stoichiometric amount of oxygen is intercalated in the  $\text{La}_2\text{CuO}_4$  structure. The processes in the samples depend on the level of hole doping and therefore samples with low doping are noted as  $\text{La}_2\text{CuO}_{4+\gamma}$  and  $\text{La}_{2-\zeta}\text{Sr}_\zeta\text{CuO}_4$  respectively, whereas samples with higher hole-doping  $n_h > 0.055$  are denoted by  $\text{La}_2\text{CuO}_{4+y}$ ,  $\text{La}_{2-x}\text{Sr}_x\text{CuO}_4$  and  $\text{La}_{2-x}\text{Sr}_x\text{CuO}_{4+y}$  respectively. Our superoxygenated samples are denoted by LSCO+O followed by the Sr doping level  $x$ . The structural phases refer to the notation in Section 2.3.

### 4.1 Lightly hole-doped samples

Early studies of super-oxygenated  $\text{La}_2\text{CuO}_{4+\gamma}$  have shown that in samples with  $0.01 < \gamma < 0.055$  an oxygen phase separation takes places into an oxygen-poor phase with  $\gamma \leq 0.01$  which is an AF insulator with  $T_N \approx 250\text{K}$ , and an oxygen-rich phase with  $\gamma \approx 0.055$  which is a superconductor with  $T_c \approx 32\text{K}$  [97, 98, 53, 99, 100]. The structural miscibility gap is shown in the left part of Figure 4.1. The formation of bulk superconductivity at such low oxygen hole-dopings compared to the superconducting onset of Sr doping ( $n_h = 0.055$ ) was explained by a difference in the mobility of doped holes in the two systems[101]. In  $\text{La}_2\text{CuO}_{4+\gamma}$  small spin-polarized clusters inside which the holes are highly mobile are by (slow) diffusion able to form a 3D percolative network which supports superconductivity even at very small dopings whereby superconductivity and commensurate AFM can co-exist in the same sample[102]. The onset for the diffusion process of the spin-polarized hole-clusters is  $T \approx 150\text{K}$ . In another theory of dilute holes in a Mott insulator the individual holes are considered highly mobile band-holes which at finite but very low concentration attract each other and electronic phase separation into hole-poor and hole-rich subphases occurs [103]. In both models however, the charge compensation ions restrict the degree of phase separation, as long as they are immobile. In  $\text{La}_2\text{CuO}_{4+\gamma}$  the excess oxygen ions are mobile above  $T \approx 240\text{K}$  while the Sr ions in  $\text{La}_{2-\zeta}\text{Sr}_\zeta\text{CuO}_4$  remain randomly distributed and immobile. In  $\text{La}_{2-\zeta}\text{Sr}_\zeta\text{CuO}_4$  the hole motion is mainly 2D due to the low mobility of the holes and therefore the percola-

tion is mainly 2D the threshold for bulk superconductivity occurs at a higher doping[104].

In  $\text{La}_2\text{CuO}_{4+\gamma}$  several factors influence the volume fraction of each phase. In particular the superconducting volume fraction strongly depends on the thermal treatment. Slow cooling from RT favours the SC regions[101]. Interestingly a strong magnetic field ( $\sim 3$  T) also favours SC in the dilute hole-doped  $\text{La}_2\text{CuO}_{4+\gamma}$ . The mechanism was explained by the increase of the diffusion constant of the spin-polarized hole clusters on application of a strong field[101].

When the temperature is raised above 240 K the excess oxygen becomes mobile and the percolative network is destroyed. In  $\text{La}_{2-\zeta}\text{Sr}_\zeta\text{CuO}_4$  the destruction of the conducting subsystem occurs at much higher temperatures  $T > 330$  K[102]. Both the AFM and the conducting (SC) phase have orthorhombic structure although in some samples the  $Bmab$  signature peaks were missing in the oxygen-rich phase wherefore it was denoted  $Fmmm$ [97].

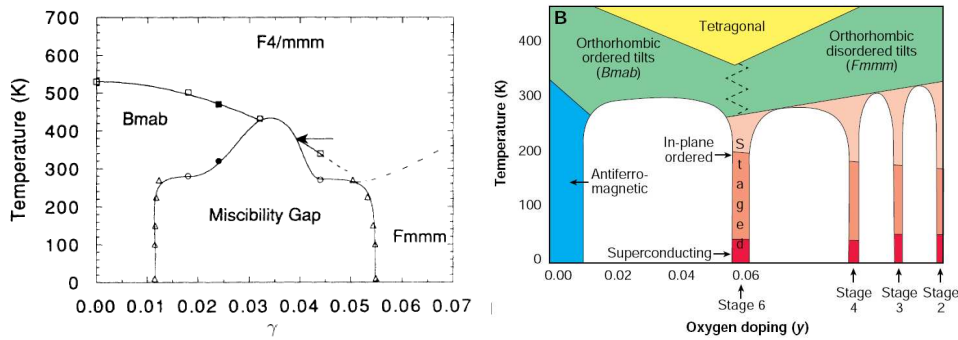


Figure 4.1: (Left) The miscibility gap for low oxygenation level  $\gamma$  as determined by neutron powder diffraction. The phase denoted by  $Fmmm$  Modified from [105].(Right) New miscibility gaps appear for higher oxygenation levels  $y$ . From [106].

## 4.2 Highly hole-doped samples

The oxygen-rich superconducting phase was originally denoted  $Fmmm$  because the orthorhombic ( $Bmab$ ) superstructure peaks were missing. This was later attributed to a superstructure called staging which is a modulation of the  $\text{CuO}_6$  octahedral tilts (presumably reflecting the intercalated oxygen) along  $c$ , see Section 4.6. The staging model was originally proposed for  $\text{Li}_2\text{NiO}_{4+y}$ [107] which is structurally similar to  $\text{La}_2\text{CuO}_{4+y}$ . For adequate hole-dopings (right part of Figure 4.1) this superstructure is seen consistently by diffraction as satellites in L-scans through fundamental  $Bmab$  reflections with position  $(H, K, L \pm \delta_L)$  where  $\delta_L = \frac{1}{n}$  and  $n$  is the staging number[53, 99, 108, 109, 110, 111].

More recent studies on highly oxygenated (superoxygenated)  $\text{La}_2\text{CuO}_{4+y}$  ( $y \geq 0.055$ ) have revealed another type of phase separation in this oxygen-rich region between i) an IC AFM phase with  $T_N \sim 40$  K and ii) a superconductor with  $T_c \geq 40$  K [99, 110]. The first miscibility gap (described in Section 4.1)

and the second miscibility gap ( between phases i) and ii) ) are both shown in the phase diagram in Figure 4.2. The magnetically ordered phase is closely related to the anomalous 1/8-hole-doped non-super-oxygenated LBCO or LNSCO. The superconducting phase has a high  $T_c$  and therefore is probably near optimal doping with  $n_h \approx 0.16$ . The latter phase will therefore be called hole-enriched from this point in order to separate it from the the term oxygen-rich (or hole-rich) to which both these phases belong.

Very recently we have observed two phases similar to i) and ii) in Sr/O co-doped  $\text{La}_{2-x}\text{Sr}_x\text{CuO}_{4+y}$  single-crystals as well, through means of bulk measurements and  $\mu\text{SR}$ [112]. The high  $T_c \approx 40\text{K}$  had previously been observed in superoxygenated powder samples[113] of  $\text{La}_{2-x}\text{Sr}_x\text{CuO}_{4+y}$ . The structure refinement of these powder samples with  $x = 0.05/y = 0.135(4)$  and  $x = 0.09/y = 0.109(5)$  both in the  $Bmab$  phase showed no sign of a phase-separation into oxygen-rich and oxygen-poor parts[113] and the interstitial oxygen was found to play an analogous rôle to Sr doping in increasing the hole concentration of the system.

The susceptibility and  $\mu\text{SR}$  measurements of our superoxygenated  $\text{La}_{2-x}\text{Sr}_x\text{CuO}_{4+y}$  single-crystals (LSCO+O) were a central part of the thesis work of H. E. Mohottala [114] but some of the figures are reproduced in Section 4.4 at convenience of the reader. The main topic of this chapter is to investigate the crystalline and magnetic structure of LSCO+O single crystals by neutron and hard x-ray diffraction. The samples of interest are five single crystals of LSCO+O with four different dopings  $x=0, 0.04, 0.065$  and  $0.09$  respectively.

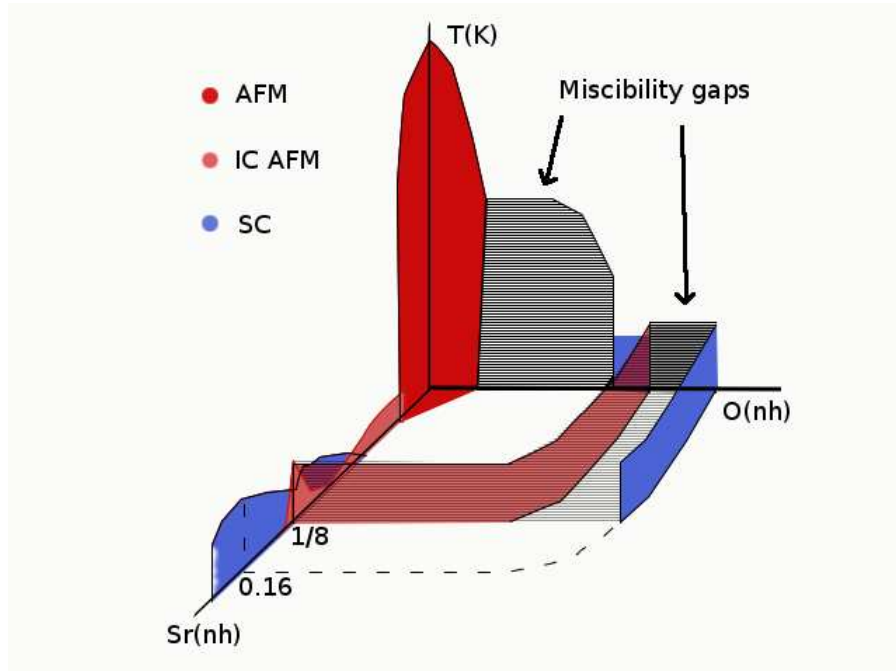


Figure 4.2: A schematic 3D phase diagram for LSCO+O. The miscibility gaps are explained in Sections 4.1 and 4.2. The arc phases of  $n_h \sim 0.125$  and  $n_h \sim 0.16$  are explained in Section 4.4. Modified from [112]

### 4.3 Sr/O co-doped single-crystals

Several powder and single crystal samples of LSCO+O were prepared by Hashini E. Mohottala at the University of Connecticut (UConn) by electrolysis in the years leading up to 2005. The superoxygenation process took place in a NaOH solution over a period of several months. Low electrolysis currents were used which restricted the voltage to a maximum limit of 0.6 V preventing electrolysis of water. The samples had Sr doping content of  $x=0$ , 0.04, 0.055, 0.065, 0.09, 0.115 and 0.14 and the results from bulk measurements and  $\mu$ SR are shown in Section 4.4.

I have studied four of these samples, which are single crystals, by diffraction in this thesis. Unfortunately the samples are very brittle and even though I handled them very carefully they often broke during shipment. Each piece of crystal is given a unique name in Table 4.1.

A fifth furnace-grown crystal hlc0.011c ( now labelled samples sLSCO\_0\_A and sLSCO\_0\_B) was superoxygenated by Samuel B. Emery at Uconn during 2007. It has  $x=0$  but it is much larger than sLSCOc\_0 even after it broke into two pieces. A comprehensive list of which samples were investigated during the various diffraction experiments is shown in Table 4.2.

All samples were maximally oxygenated and in the hole-rich part of the phase diagram beyond the first miscibility gap.

Ori. name / doping / prod. year	Name	m [g]
? / $x=0$ / 2005	sLSCOc_0	0.025
hlc0.011c / $x=0$ / 2007	sLSCO_0A	0.8
	sLSCO_0B	0.545
hlSCO.005c / $x=0.04$ / 2005	sLSCO_0.04A	0.034
	sLSCO_0.04B	0.018
	sLSCO_0.04C	0.016
	sLSCO_0.04D	0.02
hlSCO.006c / $x=0.065$ / 2005	sLSCO_0.065A	0.091
	sLSCO_0.065B	0.066
hlSCO.008c / $x=0.09$ / 2005	sLSCO_0.09	0.417

Table 4.1: The samples investigated by diffraction in this thesis. The table shows the various crystal pieces as per 26th November 2007. All pre-oxidised crystals were grown by the travelling zone method in an optical furnace except sLSCOc\_0 which was grown in a ceramic crucible. All samples have  $T_c^{onset} \sim 40$  K.

### 4.4 Phase diagram

As seen from the SQUID measurements in Figure 4.3 the onset of the superconducting transition occurs at  $T_c \sim 40$  K for all LSCO+O samples with  $x < 0.14$ <sup>1</sup>. This includes the samples with  $x=0$ , 0.04, 0.065 and 0.09 mentioned in Table

<sup>1</sup>though not all doping are reproduced in the figure

	x=0	x=0.04	x=0.065	x=0.09
RITA-II 2005_I	sLSCOc_0	sLSCO_0.04A-D		sLSCO_0.09
RITA-II 2005_II			sLSCO_0.065A-B	sLSCO_0.09
BW5 2006	sLSCOc_0	sLSCO_0.04A-C		sLSCO_0.09
RITA-II 2006		sLSCO_0.04A-C?		sLSCO_0.09
SPINS 2007				sLSCO_0.09
BW5 2007			sLSCO_0.065A?	sLSCO_0.09
BT7 2007	sLSCO_0_A			
RITA-II 2008		sLSCO_0.04B		sLSCO_0.09
TriCS 2008	sLSCO_0_B			
IN14 2008		sLSCO_0.04A	sLSCO_0.065A	
BW5 2008	sLSCOc_0	sLSCO_0.04B		sLSCO_0.09

Table 4.2: A list of the diffraction experiments performed in this thesis work, where they were performed and which sample they were performed on. Some of the original crystals have broken into smaller pieces over the years and this table proved an overview of the various pieces.

4.1 which this thesis will concentrate on. The transition curve of sLSCOc\_0 is not shown but it is similar to the one of sLSCO\_0\_A-B.

As seen from the  $\mu$ SR measurements in Figure 4.4 the magnetic transition temperature  $T_N = T_c \sim 40$  K i.e. the magnetic transition coincides with the superconducting transition for all samples<sup>2</sup>. The ZF  $\mu$ SR frequency is the same for all samples with  $x < 0.14$  as shown in the right part of Figure 4.4. It is a strong indication that, at least from a local point of view, the nature of the magnetic phase is the same irrespective of Sr content. The value of the ZF  $\mu$ SR frequency is  $\nu \sim 3.5$  MHz which is the same as for LBCO and LNSCO [37] and it is concluded that the local ordered moment in LSCO+O is very similar. However probes such as neutron diffraction are needed to determine the magnetic structure.

No sign of any other magnetic or superconducting phase was detected in the samples and it seems that the nature of the two phases in superoxygenated LSCO+O is generic. The sum of the phase volumes is constant, but the individual volume fractions of the two phases vary in a non-monotonic manner as function of Sr content as seen in Figure 4.5<sup>3</sup>. Presumably the volume fractions are determined by the total hole concentration rather than specific chemistry in the Sr/O co-doped crystals. We believe that the phase separation is driven by the interaction of the doped holes themselves[112]. i.e. is an electronic phase separation. This has lead us to propose the phase diagram in Figure 4.2. In this schematic phase diagram the IC AFM phase is marked by a single signature although it covers different periodicity and responses to an external magnetic field.

<sup>2</sup>The  $\mu$ SR response as function of temperature is not shown for x=0.065 but it also has  $T_N=40$  K

<sup>3</sup>The sum of the phase fractions is constant by  $\sim 60\%$  i.e. less than 100%, but the SC volume fraction is assumed to be underestimated by bulk measurements due to both trapped flux and flux penetration into small superconducting regions. See supplementary material of [112].

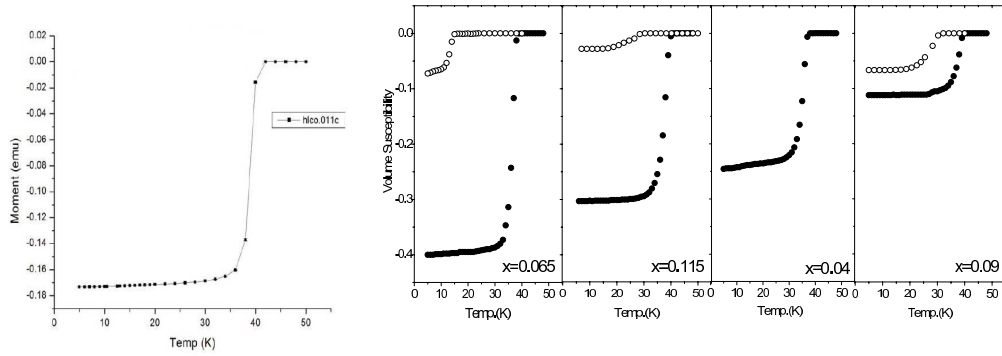


Figure 4.3: Field cooled d.c. magnetisation before (open ) and after (closed symbol) oxidation. It is seen that the onset  $T_c \sim 40\text{K}$  for all superoxygenated samples irrespective of Sr content. Left figure (for the sLSCO\_0 sample) kindly provided by Samuel Emery. Right figure from [112].

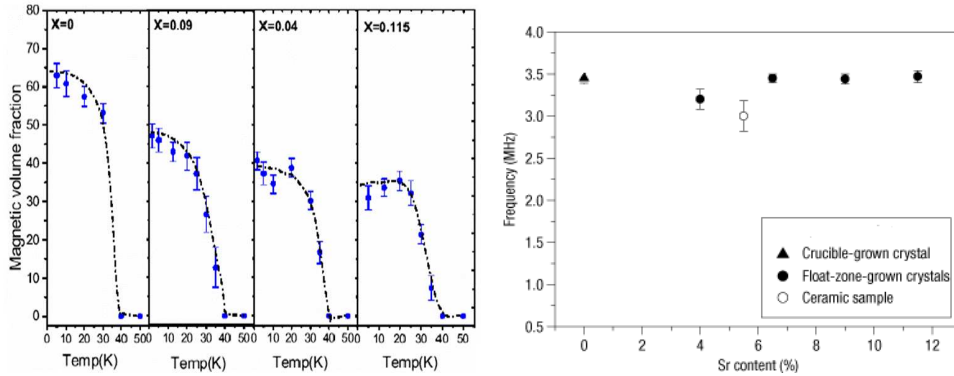


Figure 4.4: ZF  $\mu\text{SR}$  measurements. Left:  $T_M \sim 40\text{K}$  for all superoxygenated samples irrespective of Sr content. Right: All samples have same ZF frequency. In conclusion the magnetic phases are identical in all samples. From [112].

All the LSCO+O samples studied in this thesis have hole-dopings which place them in the (electronic) phase separation region between the red and blue arc of Figure 4.2. In the following I elucidate the nature of nanoscale morphology of this phase separation by neutron diffraction studies of single crystals of LSCO+O with Sr dopings of  $x=0$ , 0.04, 0.065 and 0.09 respectively. The staging order is presented in Section 4.6 and the static IC magnetic ordering in Section 4.8.

In Chapter 6 the resolution limited peak width of several of these experiments presented are found by means of virtual experiments. From these results, even a small broadening of the measured peaks due to finite size effects can be de-convoluted. From the broadening the coherence length of the SDW and the sizes of the staging domains can be inferred.

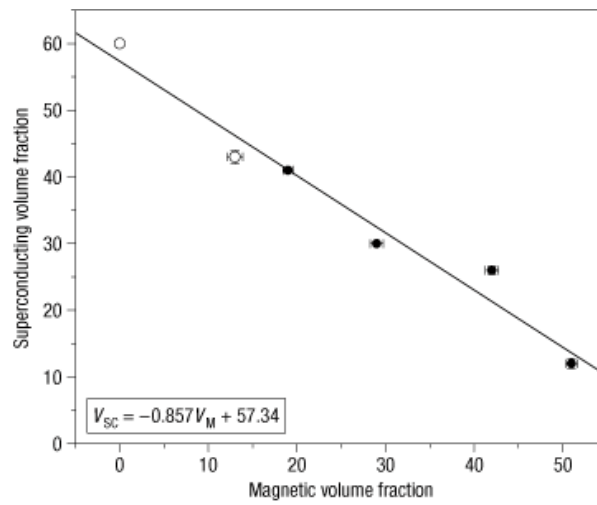


Figure 4.5: Negative linear relationship between magnetic volume fraction (from ZF- $\mu$ SR) and superconducting volume fraction (from SQUID). The sum of the volume-fractions is constant irrespective of Sr content. From [112].

## 4.5 Crystal structure

The notation in this section refers to the general one in Section 2.3. It is common practice in neutron diffraction of LSCO to consider the high temperature tetragonal (HTT) phase in the unconventional orthorhombic  $F4/mmm$  setting in which it has allowed reflections for  $H, K, L$  all even or odd. At the temperature  $T_o$ , which is dependent on the Sr content of the sample, there is a phase transition to the orthorhombic  $Bmab$  phase also known as the low temperature orthorhombic (LTO) phase. The advantage of using the  $F4/mmm$  setting above  $T_o$  is that the unit cell changes only slightly during the phase transition and that  $c$  is always the long axis. Furthermore the tetragonal to orthorhombic transition might not be to a conventional LTO phase but to an orthorhombic phase where the  $Bmab$  peaks are missing, usually denoted as the  $Fmmm$  phase. Throughout this thesis reference is made to the orthorhombic unit cells unless explicitly stated otherwise. In the orthorhombic phases the lattice parameters fulfil  $a < b < c$ .

All the LSCO+O crystals of this thesis work has peaks at the  $Bmab$  allowed positions (see Table 2.1) but some of the crystals also has superstructure (staging) peaks around the  $Bmab$  positions. There was no indication of a phase transition to a LTLO or LTT phase upon further cooling, at least for  $x=0, 0.04$  and  $0.09$  in which a temperature dependent peak at the (110) was searched for, but not found.

### 4.5.1 The $Bmab$ phase and staging superstructure

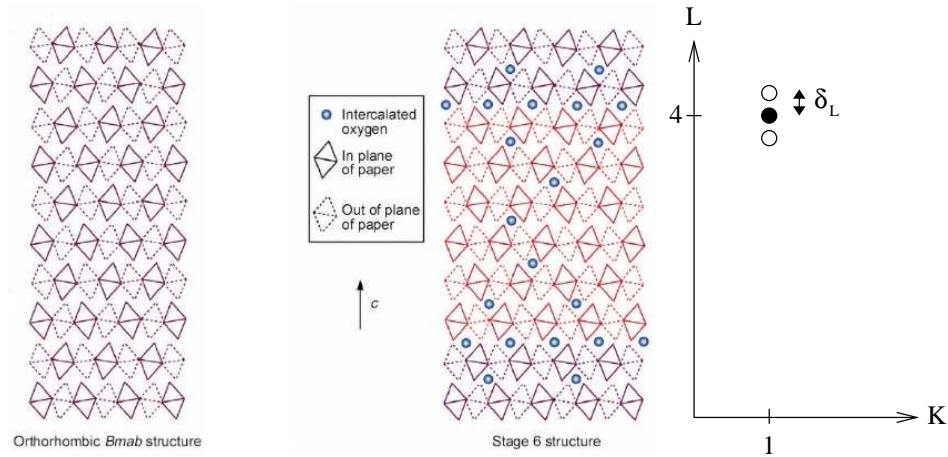


Figure 4.6: The leftmost panel shows the  $Bmab$  structure of LCO. The full-line octahedra are in the plane of the paper whereas the dotted ones are canted out of plane. The centre panel shows the intercalated oxygen giving the staging structure in LSCO+O. The tilts in one layer-domain are shown in red colour and the tilts in the other layer-domain shown in purple. In this example the unit cell length of the staging structure is  $6c$ , where  $c$  is the long axis of the  $Bmab$  unit cell. The position of one of the  $Bmab$  peaks (●) and the staging satellites (○) is shown in the rightmost panel.

The  $Bmab$  reflections which have  $H, L$  even and  $K$  odd or  $H, L$  odd and  $K$  even, result from the tilting of the  $\text{CuO}_6$  octahedra[53] as shown in Figure 4.6 and explained in Section 2.3. For LSCO+O at low Sr doping there are peaks at non-integer values of  $L$  i.e.  $(H, K, L \pm \delta_L)$  in the vicinity of the  $Bmab$  peaks indicating an additional periodicity along  $L$  which is larger than the orthorhombic unit cell. These peaks are observed around all  $Bmab$  allowed peak positions. Satellites around seven different  $Bmab$  positions are shown in Figure 4.7. It has previously been argued [53] that the periodicity stems from an ordering of the intercalated oxygen along the long-axis which makes a tilt reversal favourable at the planes with the largest density of excess oxygen. This periodicity called staging defined as  $n = \frac{1}{\delta_L}$  develops slowly by annealing at about RT in atmospheric pressure for low Sr contents, i.e. high super-oxygenation levels. The staging model was originally proposed by J. M. Tranquada for  $\text{La}_2\text{NiO}_{4+y}$ [107] in which the average position of the intercalated oxygen is similar. The measured value of  $\delta_L$  often corresponds to non-integer layer spacings ( $n$ ) which can be explained in terms of defects in the staging structure such that the structure contains a mixture of distinct layer spacings[49]. The staging in non-Sr-doped super-oxygenated  $\text{La}_2\text{CuO}_{4+y}$  crystals has been investigated before[99, 53], but in Sr-doped super-oxygenated single-crystals of  $\text{La}_{2-x}\text{Sr}_x\text{CuO}_{4+y}$  this investigation is the first to the best of my knowledge. Other structural properties of Sr/O co-doped powder have however been investigated previously [113, 115, 116].

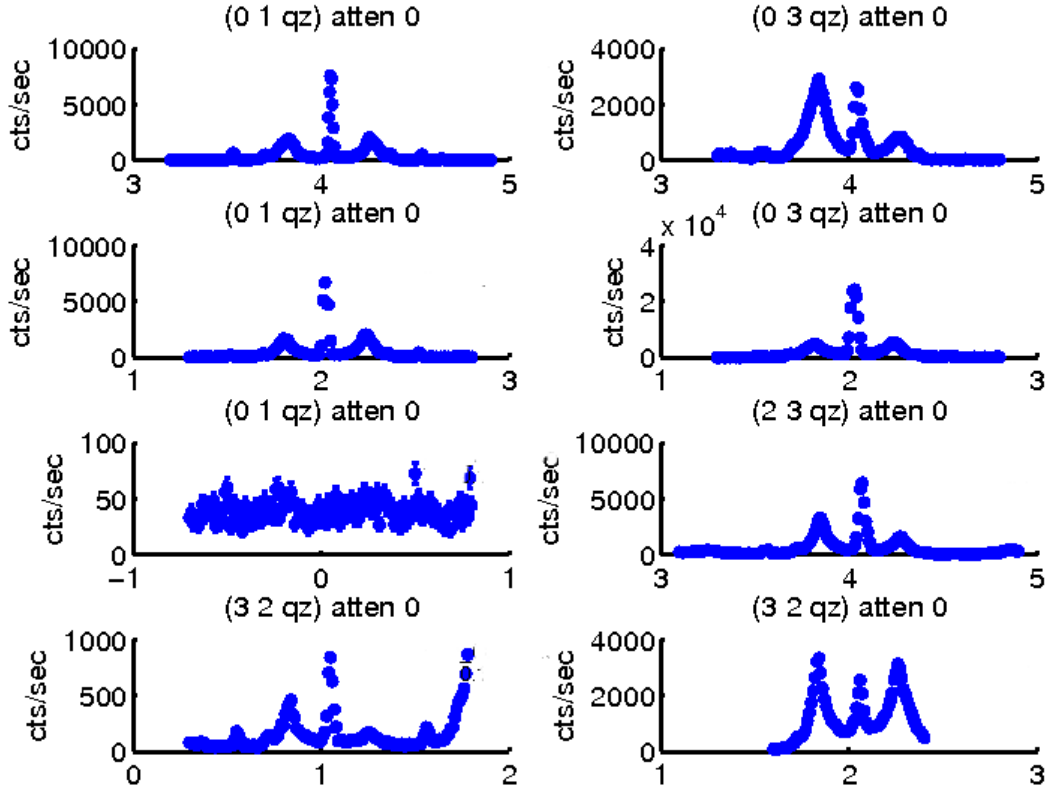


Figure 4.7: Hard x-ray diffraction  $L$ -scans ( $q_z$ -scans) of sLSCOc\_0 taken at BW5 with 100 keV photons at  $T \sim 10$  K. The (010) and (322) peaks are not allowed in the  $Bmab$  phase, hence there is no staging around (010). However there seems to be staging around (322) but the peak at this position might be the (232) of the twin domain which is indeed allowed in  $Bmab$ . All scans except (0 1 0) lined up on central peak.

#### 4.5.2 Twinning

Unfortunately it is difficult to perform a detailed structure analysis of LSCO+O crystals in the LTO phase due to twinning. The symmetry reduction at the phase transition leads to the occurrence of twin domains corresponding to the two different tilt axes (100) and (010) of the  $\text{CuO}_6$  octahedra[51]. The different tilt axes lead to domain walls along (110) and (1-10). In figure 4.8 it is shown how twinning around (110) and (1-10) each produces two domains respectively. I.e. in the general case up to four twin domains are produced and up to four peaks are seen in the  $Bmab$  phase centred around the positions of the allowed reflections. The angular splitting between the peaks on the reciprocal lattice axes for two different domains is given by

$$\Delta = 2\alpha = 90 - 2 \tan^{-1} \frac{b}{a} = 2 \tan^{-1} \frac{a-b}{a+b} \quad (4.1)$$

The lattice parameters depend on the Sr content both in LSCO and LSCO+O and the concomitant splitting due to twinning decreases with increasing  $x$  as

seen in Figure 4.9.

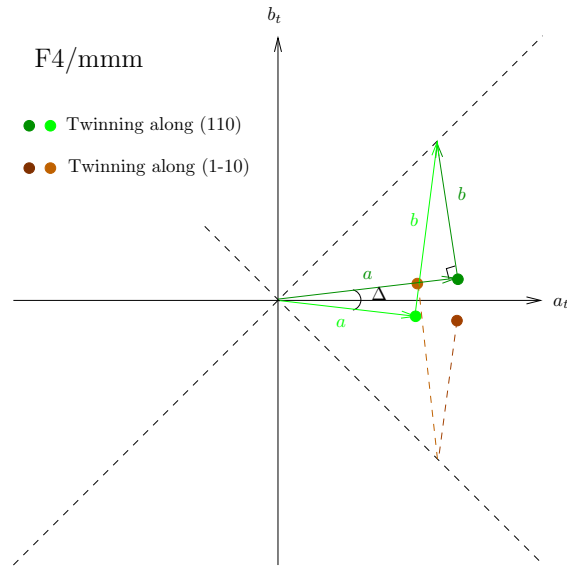


Figure 4.8: A schematic drawing of the four twinning peaks surrounding the position of the corresponding peak above  $T_o$

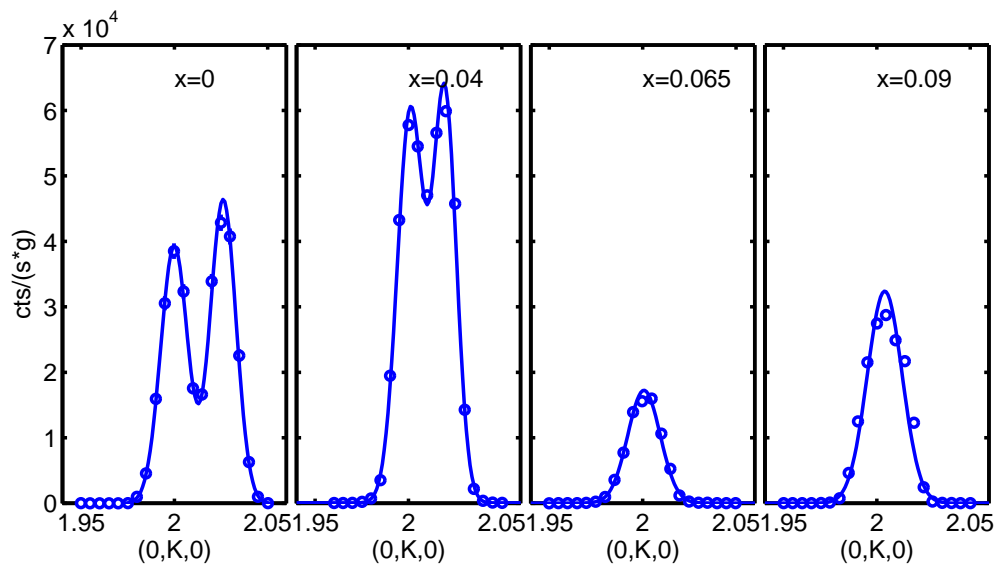


Figure 4.9: The longitudinal splitting of (020) due to twinning decreases with Sr content. All measurements were done on LSCO+O single crystals at RITA-II and used  $40^\circ$ -S- $40^\circ$  configuration. The small intensity of peaks of the  $x=0.065$  and  $x=0.09$  is probably due to extinction since the crystal weight and size increases with Sr content. The lines are fits to one or two Gaussians respectively.

## 4.6 Structural Diffraction data

All neutron scattering data in this section have been scaled by monitor count and then multiplied by the same constant factor (555) for average monitor counts per second. This number was appropriate for 5 meV neutrons and 40' collimation at RITA-II in 2005 but was used hereafter in order to compare data intensities even if the flux changed slightly from experiment to experiment. All neutron scattering data in this section were taken at RITA-II using a vertically focusing monochromator,  $E_f = E_i = 5$  meV, 40' collimation before the sample, a radial Be filter and the analyser in imaging mode giving a geometric collimation of 40' after the sample for each analyser blade. The monochromatic imaging mode (or simply 'imagemode' for short) simultaneously detects scattering from different reciprocal space points but at the same energy. More details of the monochromatic imaging mode are given in Section 5.13. The samples were placed in a cryogenic container and cooled down at a rate no faster than 2 K/min.

### 4.6.1 LSCO+O $x=0$

A small (50 cts/s) peak at (110) was observed by hard x-ray diffraction[117] in sLSCOc.0 but since it was not temperature dependent below 300 K it probably was not a signature of an LTO<sub>2</sub> or LTT phase. I conclude that the sample is in the LTO<sub>1</sub> (*Bmab*) phase for all the investigated temperatures below 320 K but with a staging superstructure which might originate from a separate *Fmmm* phase. The low temperature lattice parameters were found to be  $a = 5.30(3)\text{\AA}$ ,  $b = 5.37(3)\text{\AA}$  and  $c = 13.20(3)\text{\AA}$ .

The staging structure of the crucible grown sLSCOc.0 sample was studied both by neutron- and hard x-ray diffraction. The data are presented two times in separate figures 4.10 and 4.11 to allow for two different fitting methods which were equally good by comparison of  $\chi^2$ . The fitting methods are explained in the caption of the figures. As seen from the figures the central (014) peak is resolution limited whereas the staging peaks are finite size broadened by  $0.022\text{\AA}^{-1}$  or  $0.033\text{\AA}^{-1}$  at low temperatures depending on the fitting method (see also Table 4.3). The intrinsic broadening is proven by means of McStas virtual experiments which are further treated in Chapter 6.

The temperature dependence of the peaks are shown in the insets of figures 4.10 and 4.11. As the orthorhombic transition occurred for  $T_o > 320\text{K}$  we were not able to reach it with our cryogenic sample environment. The staging transition temperature is  $T_s=300(5)$  K as confirmed by hard x-ray diffraction, see Appendix A. This is the same transition temperature as reported earlier in LCO+O crystals with much lower oxygen content [106, 53]. The transition does however seem to occur in jumps probably originating from the staging being a mixture of unresolvable levels, so the lower staging levels also have a lower transition temperature. This is particularly visible in the hard x-ray data of Figure A.5 of A for  $n < 4$  for which the transition temperature is roughly 170 K, but the same tendency is seen in the neutron data in Figure 4.10. The average staging value at low base temperature measured by neutrons corresponds to  $n \sim 4$ . Small peaks at  $\delta_L=0.5$  are also observed (see Figure 4.7).

The float-zone grown sLSCO\_0\_B sample was investigated at TriCS (see appendix B) showing a stage 4 phase with transition temperature of  $T_s = 290(10)$  K similar to the sLSCOc\_0 sample. This shows that the oxygenation process creates reproducible staging numbers. There is however also a much larger fraction of the peak at  $\delta_L=0.5$  present in this crystal indicating a higher total level of oxygenation for the float-zone grown crystal than the crucible-grown. It has been debated whether the peaks at  $\delta_L=0.5$  represent a stage 2 structure or are a signature of the ordering of the oxygen which has half the period of the staging. Lee et al.[108] observed peaks acclaimed to originate directly from the ordering of oxygen. When the crystal was cooled fast and the supposed oxygen ordering destroyed, these peaks disappeared and the peaks with  $\delta_L=0.5$  were suppressed. I have observed peaks at the same positions both by hard x-ray and neutron scattering, see Figure B.3. The peaks also had similar temperature dependence and only partly recovered after a fast cool.

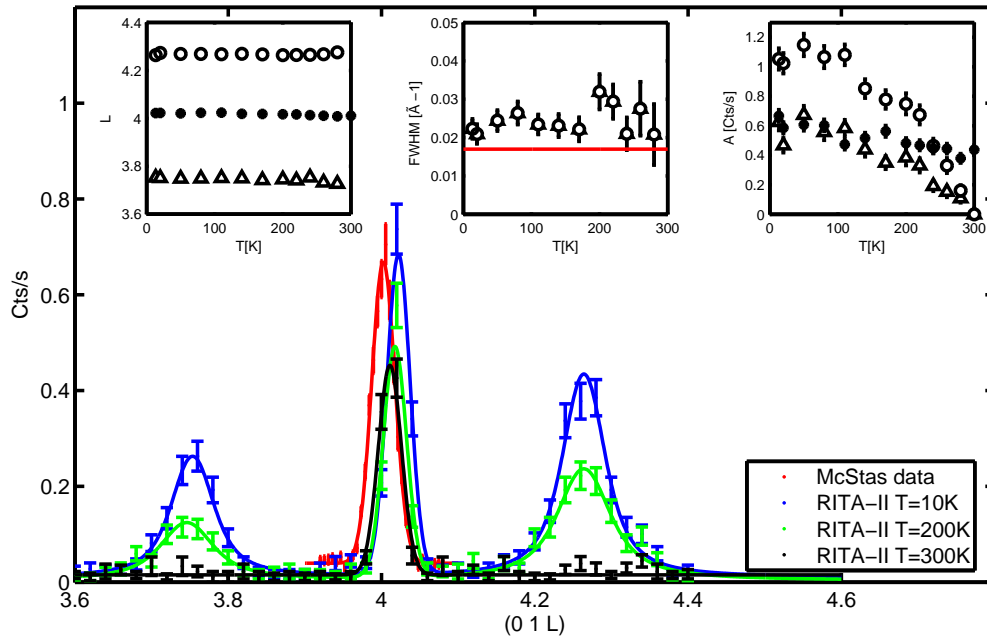


Figure 4.10: Main: Neutron diffraction scans along  $L$  through (014) in the non-Sr-doped crystal and the simulated resolution resolved (014) peak (McStas data). The lines are fits to a Gaussian + 2 Voigts. The insets show fitted data. The left, centre and right insets show the position, FWHM and area of the (014) peak ( $\bullet$ ) and the two staging peaks ( $\circ$ ) and ( $\triangle$ ), respectively. The red line shown in the centre inset is the Gaussian FWHM from virtual experiments of the (014) peak which is kept fixed as the Gaussian part in fitting the staging data to Voigts. It is the internal Lorentzian FWHM which is plotted as the ( $\circ$  and  $\triangle$ ) data points in the centre inset.

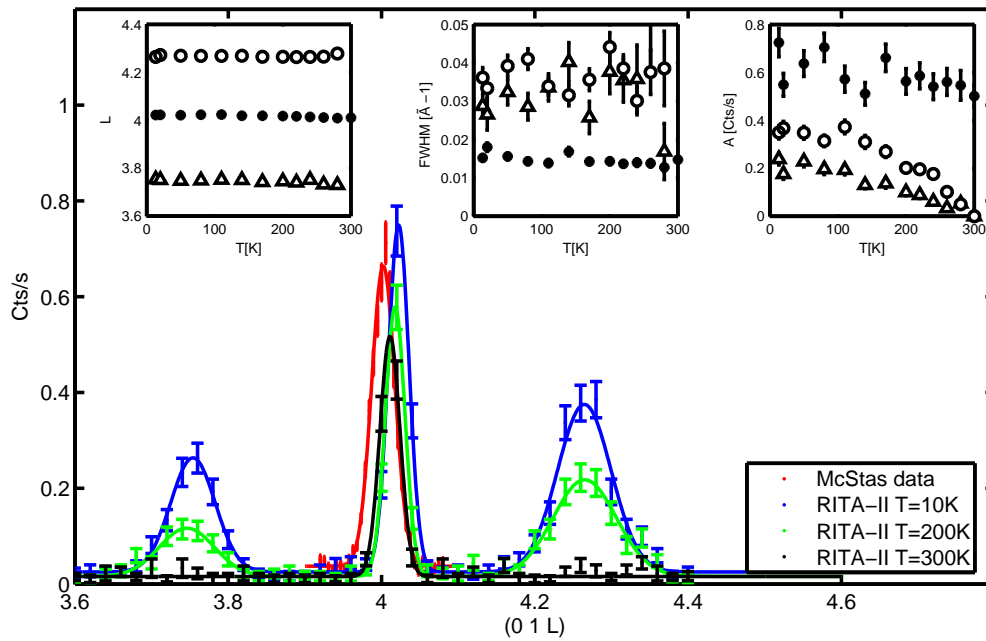


Figure 4.11: Main: Neutron diffraction scans along L through (014) in the non-Sr-doped crystal and the simulated resolution resolved (014) peak (McStas data). The raw data are the same as in Figure 4.10 but the lines are fits to 3 Gaussians. The insets show fitted data to 3 Gaussians. The left, centre and right insets show the position, FWHM and area of the B<sub>mab</sub> peak (●) and the two staging peaks (○) and (△), respectively. The data points shown in the centre inset is the fitted Gaussian FWHM of the resolution resolved (014) peak (●) and the internal Gaussian width of the staging peaks (○ and △).

### 4.6.2 LSCO+O $x = 0.04$

No peak at  $(110)$  was observed in LSCO+O with  $x=0.04$ [117] and I conclude that there is no low temperature transition to  $\text{LTO}_2$  or LTT. The sample probably has a  $\text{LTO}_1$  ( $Bmab$ ) structure at low temperatures but with a staging superstructure which might originate from a separate  $Fmmm$  phase. The low temperature lattice parameters were found to be  $a = 5.32(3)\text{\AA}$ ,  $b = 5.38(3)\text{\AA}$  and  $c = 13.19(1)\text{\AA}$ .

The staging structure has been studied both by neutron- and hard x-ray diffraction. Figure 4.12 shows the neutron diffraction data from the sample which later broke into pieces sLSCO\_0.04A-D. The data are presented two times in separate figures 4.12 and 4.13 to allow for two different fitting methods which were equally good by comparison of  $\chi^2$ . The fitting methods are explained in the caption of the figures. As seen in the figures both the central  $(014)$  peak and the staging peaks at  $\delta_L \sim 4.2$  corresponding  $n$  between 5 and 6 are finite size broadened. The intrinsic width is  $0.046\text{\AA}^{-1}$  or  $0.063\text{\AA}^{-1}$  for the staging peaks (see also Table 4.3) and  $0.023$  or  $0.039\text{\AA}^{-1}$  for the  $(014)$  peak at low temperatures (see also Table 4.5) depending on the fitting method. The intrinsic broadening is proven by means of McStas virtual experiments which is further treated in Chapter 6.

The insets of Figure 4.12 show the fitted parameters of the scans as function of temperature. The orthorhombic transition occurs at  $T_o=150(20)$  K (confirmed by hard x-rays) which curiously is lower than the staging transition temperature of  $T_s=245(15)$  K.

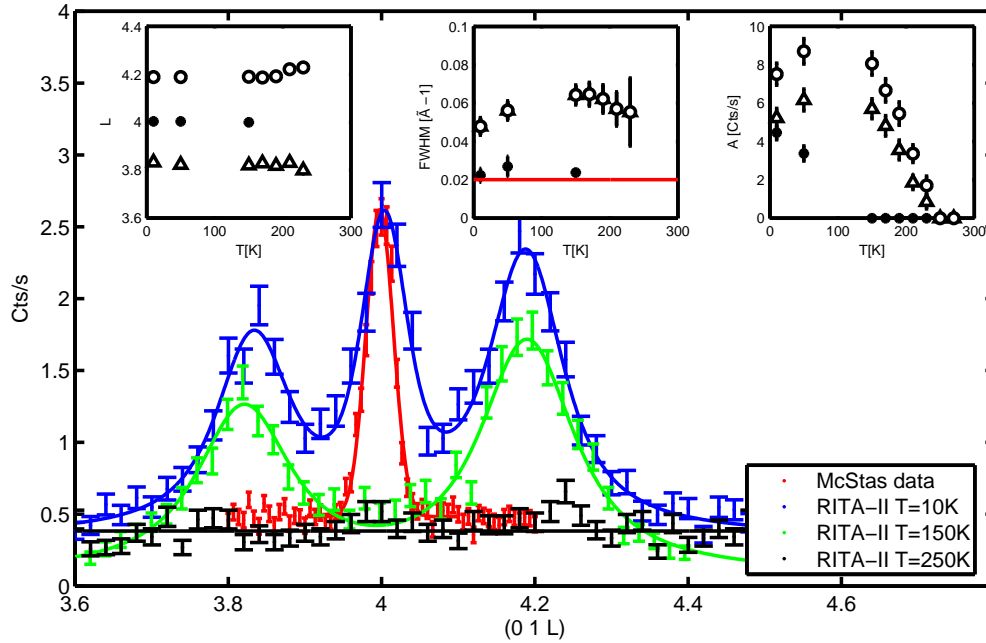


Figure 4.12: Main: Neutron diffraction scans along  $L$  through (014) in the LSCO+O  $x=0.04$  crystal and the simulated resolution resolved (014) peak (McStas data). The lines are fits to 3 Voigts. The insets show fitted data. The left, centre and right insets show the position, FWHM and area of the (014) peak ( $\bullet$ ) and the two staging peaks ( $\circ$ ) and ( $\triangle$ ), respectively. The red line shown in the centre inset is the Gaussian FWHM of the simulated resolution limited (014) peak, which is kept fixed as the Gaussian part in the fit to 3 Voigts. It is the intrinsic Lorentzian FWHMs which are plotted in the centre inset as the ( $\bullet$ ), ( $\circ$  and  $\triangle$ ) data points.

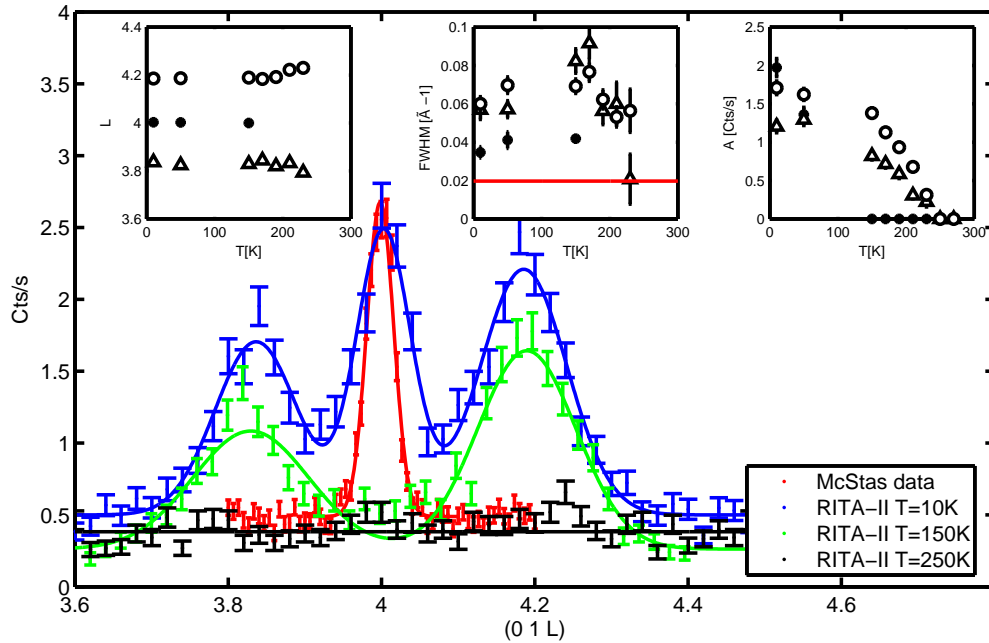


Figure 4.13: Main: Neutron diffraction scans along  $L$  through  $(0\ 1\ 4)$  in the  $x=0.04$  crystal and the simulated resolution resolved  $(014)$  peak. The raw data are the same as in Figure 4.12 but the lines are fits to 3 Gaussians. The insets show fitted data to 3 Gaussians. The left, centre and right insets show the position, FWHM and area of the  $(014)$  peak ( $\bullet$ ) and the two staging peaks ( $\circ$ ) and ( $\triangle$ ), respectively. The red line show in the centre inset is the Gaussian FWHM of the simulated resolution resolved  $(014)$  peak. The fitted data points shown in the centre inset is the intrinsic Gaussian FWHM of the  $(014)$  peak ( $\bullet$ ) and the the staging peaks ( $\circ$  and  $\triangle$ ), de-convoluted from the measured FWHM by use of the simulated resolution width.

### 4.6.3 LSCO+O $x=0.065$

The data in this section were taken on the sLSCO\_0.065 sample before it broke into the A and B parts. The low temperature lattice parameters were found to be  $a = 5.32(2)\text{\AA}$ ,  $b = 5.36(3)\text{\AA}$  and  $c = 13.15(3)\text{\AA}$ . The data are presented two times in separate figures 4.14 and 4.15 to allow for two different fitting methods which were equally good by comparison of  $\chi^2$ . In Figure 4.14 it is seen that the (014) peak is instrumentally resolved compared to the McStas virtual experiment which is treated in Chapter 6. No apparent staging peaks are observable. Underneath this peak there is however a broader feature which might originate from a disordered tilt pattern with no particular periodicity along L. The intrinsic width of this feature is  $33\text{\AA}^{-1}$  or  $65\text{\AA}^{-1}$  depending on the fitting method (see also Table 4.3).

The insets of Figure 4.14 show the fitted parameters of the scans as function of temperature. The orthorhombic transition occurs at  $T_o=240(5)$  K (confirmed by hard x-rays)[118] while the transition temperature of the disordered tilts occurs around  $T_s=200(10)$  K.

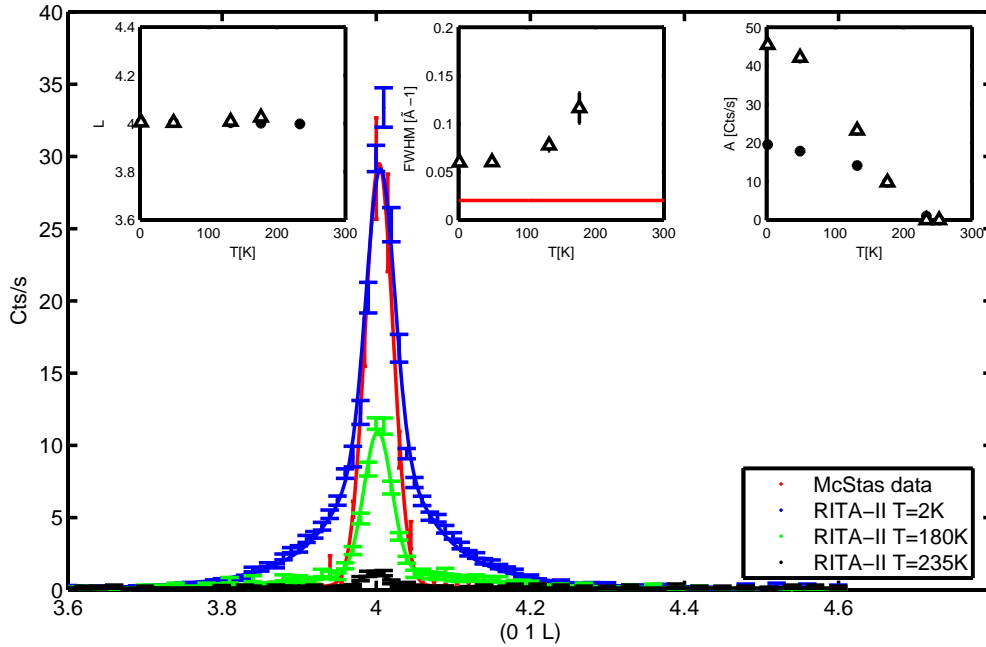


Figure 4.14: Main: Neutron diffraction scans along  $L$  through (0 1 4) in the LSCO+O  $x=0.065$  crystal and the simulated resolution resolved (014) peak, the lines are fits to a Gaussian and a Voigt. The insets show fitted data. The left, centre and right insets show the position, FWHM and area of the narrow (014) peak ( $\bullet$ ) and the disordered tilts peak ( $\triangle$ ) below it. The red line shown in the centre inset is the simulated Gaussian FWHM of the resolution limited (014) peak which is kept fixed as the Gaussian part in fitting the disordered tilts data to a Voigt. It is the intrinsic Lorentzian FWHM of the disordered tilts which is plotted as the ( $\triangle$ ) data points in the centre inset.

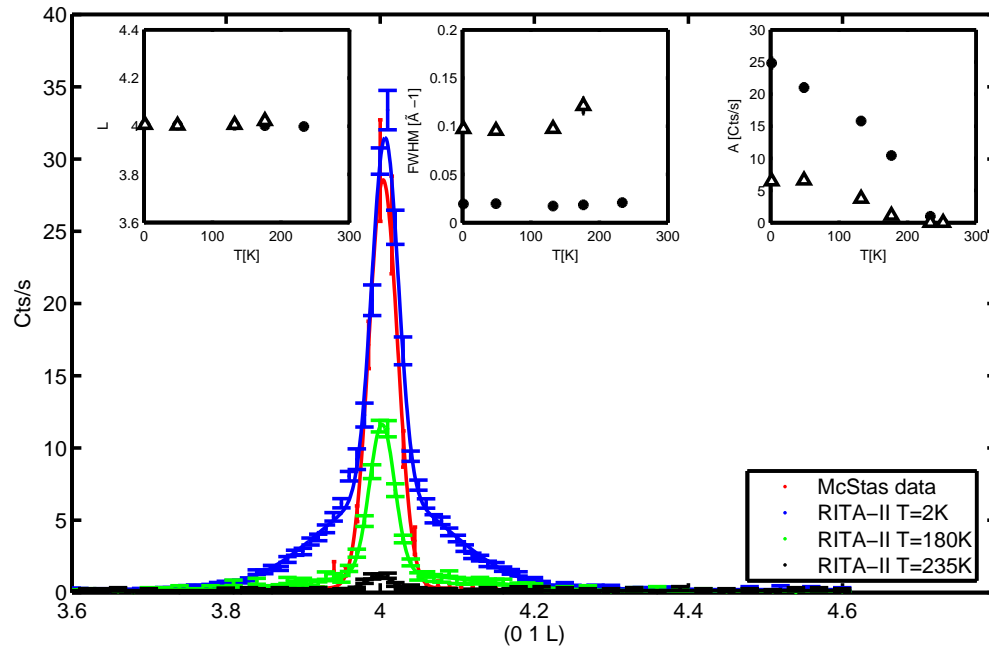


Figure 4.15: Main: Neutron diffraction scans along L through  $(0\ 1\ 4)$  in the LSCO+O  $x=0.065$  crystal and the simulated resolution resolved  $(014)$  peak. The raw data are the same as in Figure 4.14 but the lines are fits to 2 Gaussians. The insets show fitted data to 2 Gaussians. The left, centre and right insets show the position, FWHM and area of the narrow  $(014)$  peak ( $\bullet$ ) and the disordered tilts peak ( $\blacktriangle$ ) below it. The data points in the centre inset is the resolution limited Gaussian FWHM of the narrow  $(014)$  peak ( $\bullet$ ). This has been used to find the intrinsic width of the disordered tilts which is shown as the ( $\blacktriangle$ ) data points in the centre inset.

#### 4.6.4 LSCO+O $x=0.09$

By hard x-ray diffraction weak diffuse scattering was observed at (110) but no change in the intensity was seen below RT[118]. I conclude that there is no transition to LTO<sub>2</sub> or LTT below the LTO<sub>1</sub> (*Bmab*) phase. The low temperature lattice parameters were found to be  $a = 5.33(2)\text{\AA}$ ,  $b = 5.34(3)\text{\AA}$  and  $c = 13.14(2)\text{\AA}$ . An L-scan through the (014) peak was performed on the sLSCO\_0.09 sample in order to compare it to the staging structures of the superoxygenated crystals with lower Sr content. As seen from Figure 4.16, the (014) peak is resolution limited and actually significantly narrower than the McStas virtual experiment which is elaborated in Chapter 6. This is probably due to the anisotropic mosaicity of the sample which is not modelled in the virtual sample. The orthorhombic transition as measured by the (014) peak occurs at  $T_o=300(5)$  K (confirmed by hard x-rays)[118]. It is apparent from Figure 4.16 that no sign of a staging or disordered tilt structure is present in this sample. This is also supported by hard x-ray diffraction on the same sample [118].

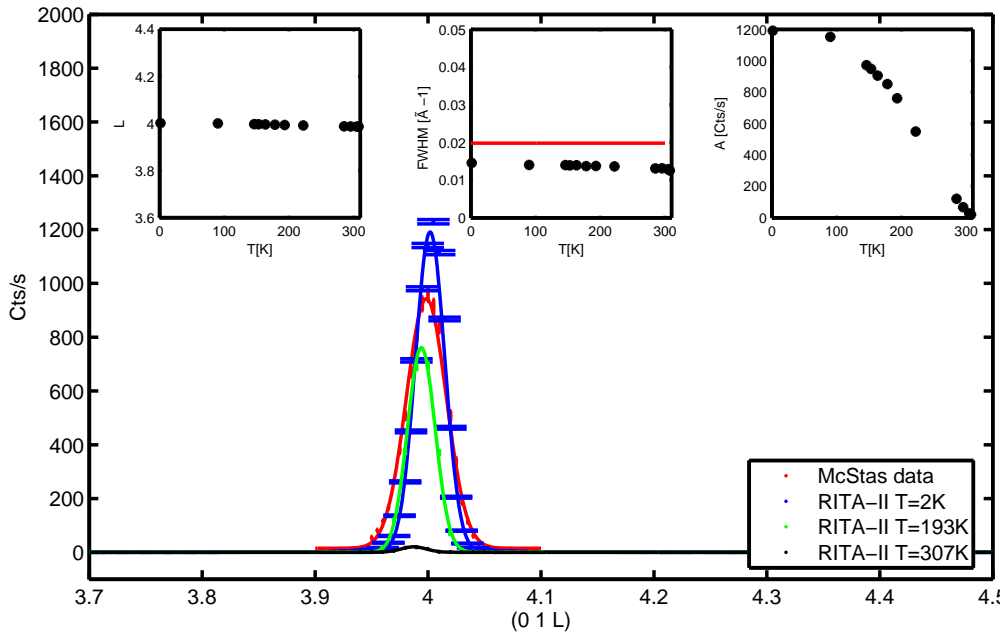


Figure 4.16: Main: Neutron diffraction scans along  $L$  through (014) in the LSCO+O  $x=0.065$  crystal and the simulated resolution resolved (014) peak, the lines are fits to a Gaussian. The insets show fitted data to 2 Gaussians. The left, centre and right insets show the position, FWHM and area of the (014) peak. The FWHM shown in the centre inset is the Gaussian FWHM of the (014) peak and the red line is the Gaussian FWHM of the simulated (014) peak.

#### 4.6.5 Summary and discussion of the structural diffraction data

As in non-superoxygenated LSCO, no transition to the LTLO or LTT phase was observed in any of the LSCO+O samples and it was concluded that the structure of the Sr/O co-doped LSCO+O samples in the superconducting phase is  $Bmab$ , albeit with some superstructure due to the intercalated oxygen for  $x < 0.09$ .

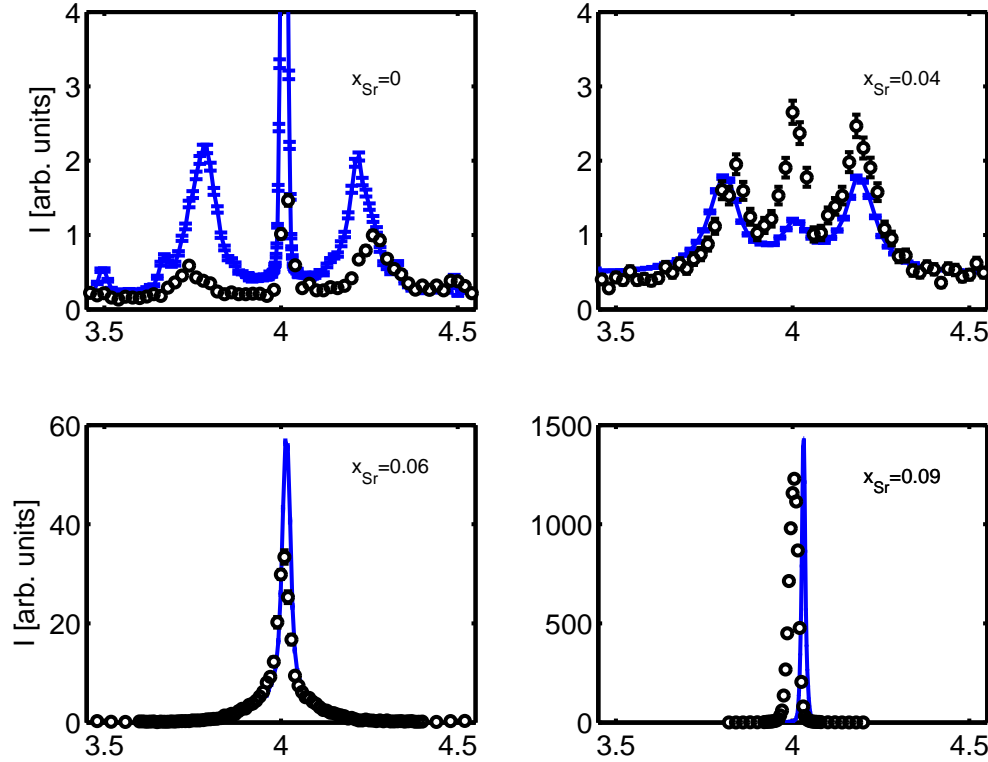


Figure 4.17: Comparing neutron (black) and hard x-ray (blue)  $L$ -scans through (014) for different values of  $x$ . The data have been arbitrarily scaled.

Figure 4.17 shows the low-temperature staging for different dopings as seen by both neutrons and hard x-rays. The lattice parameter was not adjusted at low temperature in the hard x-ray data of  $x=0.09$  and the peak position is therefore slightly off  $L = 4$ . The features of the scans with respect to existence, shape and position of the central and staging peaks are seen to be similar apart from the better resolution in the hard x-ray data. The position of the staging peaks are seen to be very similar for  $x=0.04$  but slightly different for  $x=0$  (see also Figure 4.18 left) in the two experiments. This might be explained by slightly different cooling conditions which influence the ordering of oxygen as elaborated below.

The staging value increases with Sr content which indicates a lower amount of intercalated oxygen. This is expected if there is an upper limit for the total Sr/O hole-doping as a result of the superoxygenation process, as the oxygen content would then be too low to form an ordered lattice for  $x > 0.04$ . There is however also the possibility that the excess oxygen anti-correlates with Sr and

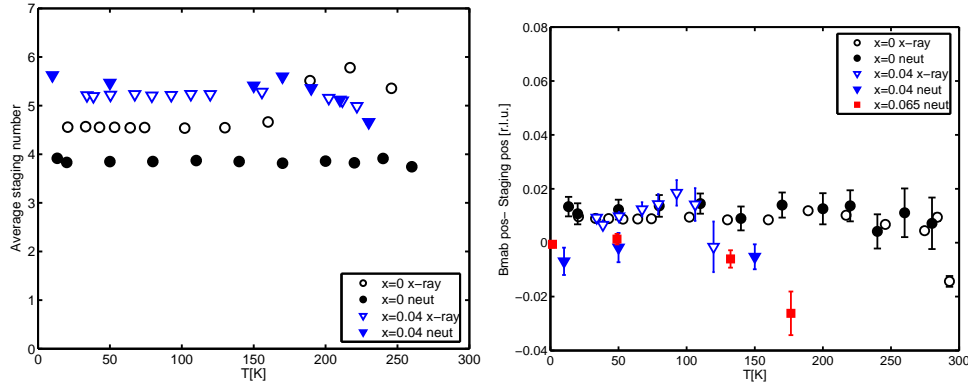


Figure 4.18: (Left) Staging number of superstructure peaks around (014). (Right) Shift of  $Bmab$  position with respect to centre of the staging peak position relative to the  $Bmab$  L position. (Both) Black symbols are for  $x=0$ , blue for  $x=0.04$  and red for  $x=0.065$ . Fits to Voigts of x-ray data marked by open symbols and neutron data by closed symbols .

the staging therefore increasingly disorders with increasing Sr content since Sr is expected to be homogeneously, but randomly distributed. Certainty of the oxygenation level could be obtained by thermogravimetric analysis (TGA) but since this is a destructive process it has not yet been carried out for all dopings. It has however been carried out on a  $m=0.056$  g piece broken off the  $x=0.065$  crystal. The result was  $y=0.032$ , i.e. lower than  $y \sim 0.1$  previously found in non-Sr doped LCO+O with similar  $T_c$ [109], supporting that the intercalated oxygen content decreases with Sr content. However, in order to compare with the rest of the samples presented in this thesis a systematic study needs to be carried out. Such a study would be very useful and not too destructive as all the samples have already broken into smaller pieces some of which could be used in the TGA process.

It has previously been proposed that the ordering of the intercalant oxygen in a lattice and the concomitant staging is directly responsible for the high  $T_c \sim 40$  K of LCO+O since quenching from above the proposed oxygen ordering of 330 K produces a considerably lower  $T_c \sim 33$  K[108]. Since we however observe  $T_c = 40$  K in all our LSCO+O samples irrespective if they are staged or not the mechanism producing the high  $T_c$  must be more complex. As in [108] we also observe that the staging structure depends strongly on the cooling conditions for  $x=0$ [119]. After a fast cool the transition temperature of the staging peaks on heating are unusually low, and after a consecutive slow cool, the staging was disordered. The staging structure of the  $x=0.04$  crystal was however not affected by the cooling rate. Nevertheless all staging data shown in this thesis are produced after an initial slow cooling from RT to base temperature by a rate less than 2 K/min unless explicitly stated otherwise. After an initial slow cool the staging value remains constant for each sample for the main part of the temperature range but decreases slightly close to the phase transition for  $x=0.04$  as seen in Figure 4.18 (left). This means that close to the phase transition the periodicity of the superstructure decreases. In the  $x=0$  crystal the situation is opposite but there is also a clear but instrumentally unresolved structure of contributions from both stage 3,4, and 6 as seen by hard x-rays in Figure A.5.

In this case the longest periodicity sustains at highest temperatures.

Small peaks at  $\delta_L = \pm 0.5$  are seen in the scattering data for  $x=0$ . It has previously been discussed whether these peaks are due to oxygen ordering or a separate stage 2 structure. The argument for oxygen ordering [108] is that the periodicity of the oxygen layers  $n \sim 2$  is half of the staging period  $n \sim 4$  which it would be for oxygen in the intercalated oxygen-layer model shown in Figure 4.6. Localised incommensurate in-plane peaks with the same periodicity along  $c$  are also observed at  $(\pm 0.04, \pm 0.27, \pm 0.5)$ , see appendix B. These peaks are however also observed by hard x-ray scattering [120] for which the oxygen scattering cross-section is negligible so the scattering would have to be from concomitant deformation of the position of the heavier atoms in the structure. The peaks sustain at 350 K which was the highest measured temperature due to the limitation of the cryostat. No peaks are however observed in  $x=0.04$  corresponding to half the staging period. The expected positions would be  $2\delta_L = 0.36$ , and no peaks are observed here although the position is in the tail of the main staging peak and a separate peak could be overlooked.

The width of the staging peaks at base temperature suggest the correlation length (domain size) along  $c$  decreases with increasing  $x$ , see Table 4.3. The apparent domain-size (which depends on the nature of the intrinsic line width) is between 90 and 190 Å for  $x=0$ , between 40 and 100 Å for  $x=0.04$  and between 33 and 65 Å for the disordered tilts in the  $x=0.065$  crystal. In the staged cases the correlation length only corresponds to roughly the repetition distance of the superstructure in the crystal, i.e. the staging structures do not form continuously throughout the crystal. The width of the staging peaks increase close to the phase transition in both cases implying that the staging domains loose correlation as they approach the phase transition.

	$x = 0$	$x = 0.04$	$x = 0.065$	$x = 0.09$
McStas gFWHM [ $\text{\AA}^{-1}$ ]	0.017(1)	0.020(1)	0.021(1)	0.015(1)
T[K]	300(5)	245(15)	200(10)	-
$w_{\text{mea}}^G$ [ $\text{\AA}^{-1}$ ]	0.036(3)	0.067(4)	0.098(2)	-
$w_b^G$ [ $\text{\AA}^{-1}$ ]	0.033(3)	0.063(4)	0.096(2)	-
$D^G = \frac{2\pi}{w_b^G}$ [ $\text{\AA}$ ]	190(17)	98(6)	65(1)	-
$w_b^L$ [ $\text{\AA}^{-1}$ ]	0.022(3)	0.046(3)	0.060(2)	-
$D^L = \frac{2}{w_b^L}$ [ $\text{\AA}$ ]	91(12)	43(3)	33(2)	-

Table 4.3: Fitting of the low-temperature neutron diffraction L-scans through (014) both using Gaussian free fit and Voigt fit with fixed Gaussian width giving Lorentzian width  $w_b^L$ . Data of the staging are peaks shown in the table.

The summed intensities of the (014)+staging structure at base temperature ( $T < 10$  K) are shown in Table 4.4. The intensity is summed for analyser blades 4-6 which covers  $K \in [-0.97, 1.03]$  (see Figure 4.19) and includes all of the broad staging peaks. Since the resolution is very relaxed in the vertical direction which is along  $H$  all intensity from these structures is assumed to be detected. It is seen that the intensity increases exponentially with increasing  $x$  even after scaling by the intensity of a Bragg peak in the respective sample or

after scaling by mass. This result is counter-intuitive since based on prediction by Crystallographica one would expect the structure factor (and therefore the intensity) to grow roughly by the tilt angle. This prediction is based on the refined structural model of LCO+O[98] and varying the  $y$  component of the apical oxygen O(2) between 0 and  $0.25b$  which is the main influence of the octahedra tilt. However as the doping increases, the tilt angle decreases in LSCO+O [113] and one would expect *decreasing* intensity with doping, not *increasing*. The mechanism therefore has to be more complicated and future crystallographic study with focus on modelling the staging structure might shed light on this interesting property.

$x$	$m$ [g]	$I_{(014)}$	$I_{tot}$	$\frac{I_{tot}}{m}$	$\frac{I_{tot}}{I_{002}}$
0	0.025	0.031(3)	0.093(3)	3.7(2)	$2 \cdot 10^{-4}$
0.04	0.091	0.31(2)	1.11(4)	12.2(4)	$7 \cdot 10^{-4}$
0.065	0.159	0.73(7)	3.28(7)	20.6(4)	-
0.09	0.429	40.3(1)	40.3(1)	93.9(2)	$2 \cdot 10^{-2}$

Table 4.4: Table of the data shown in Figure 4.19. The integrated intensity of the peak at (014) and the total integrated intensity of the (014) peak plus staging satellites. The areas have been found from fits to 1-3 Gaussians respectively. In the last column the intensities have been scaled by the sample weight

The peaks at (014), which most likely are a signature of the  $Bmab$  phase, are resolution limited in all samples except  $x=0.04$ , see Table 4.5. It has been suggested that the  $Bmab$  and staging peaks arise from separate phases, one being oxygen-poor and one being oxygen-rich[53]. The position of the average of the staging peaks of  $x=0$  and 0.04 is shifted by 0.01 rlu with respect to the position of the (014) peak as seen by hard x-ray data fits in figure 4.18(right)<sup>4</sup>. This would correspond to the lattice parameter of the  $Bmab$  structure being 0.2-0.3% shorter than the lattice parameter of the staging structure in both the  $x=0$  and 0.04 crystals. Since the (014) peak also disappears at *lower* temperatures than the staging peaks in  $x=0.04$  the (014) peak also cannot be the basis of a staging superstructure in the same domain at least in this crystal.

This opens the question as to whether the (014) might be a commensurate AFM peak and not a structural peak. However, since the transition temperature of the (014) peak is higher than 320 K for  $x=0$  and since  $T_N = 300$  K for the AFM phase of undoped LCO (as seen in Figure 2.3) magnetic scattering from an undoped part of the sample cannot be responsible for the scattering at (014). Furthermore no signs of the AFM phase have been observed in any of the samples by means of  $\mu$ SR. This would have been quite visible as a much higher frequency of the ZF  $\mu$ SR signal than the observed. Hence we conclude that there is no hole-poor (undoped or close to undoped) phase in any of the samples.

So even if part of the sample is not oxygen-enriched or is even oxygen-poor it is not hole-poor, supporting the conclusion that the phase separation in

<sup>4</sup>However the neutron data fits only support this conclusion for  $x=0$ .

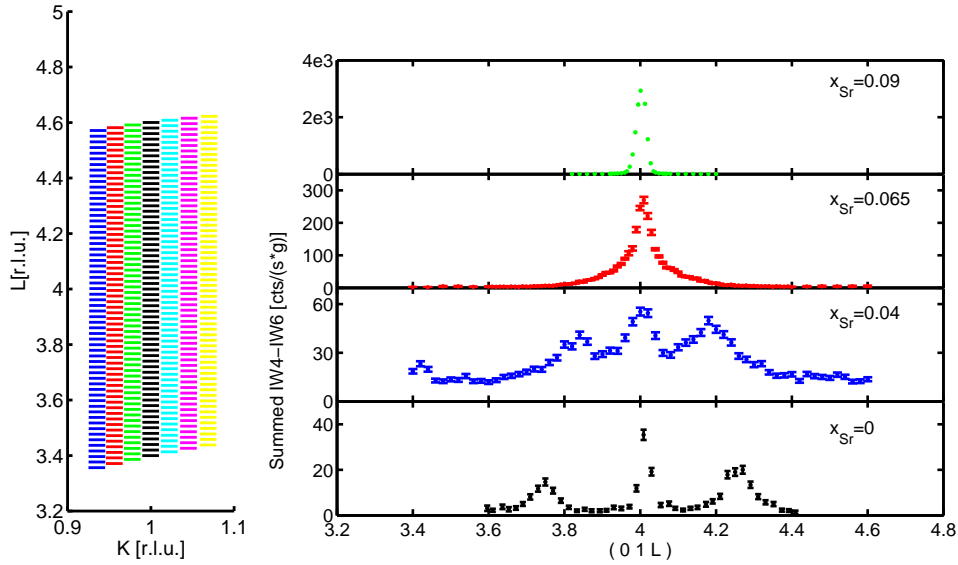


Figure 4.19: (Left) The part of the reciprocal space that the 7 analyser blades of RITA-II cover in the L-scan through (014). Window 4 is green, window 5 black and window 6 turquoise. (Right) Neutron diffraction L-scans through (014) for the 4 superoxygenated LSCO-crystals at base temperature ( $T \sim 10\text{K}$ ). The counts are summed from windows 4-6 thereby integrating over 0.06 rlu along K and including all of the broad staging peaks. Finally the counts have been normalised to sample weight.

the IC AFM/ SC phases of highly hole-doped LSCO+O is indeed electronic in nature and does not have to do with particular O/Sr chemistry. This is puzzling especially in the  $x=0$  case where the oxygen-poor  $Bmab$  phase is long-correlated out-of-plane, the peaks being resolution limited at least along the  $c$ -axis. The electronic phase separation must be a phenomenon mainly decided by in-plane correlations. This is further supported by the fact that the (014)  $Bmab$  peak is also resolution limited for  $x=0.065$  and  $0.09$ .

	$x = 0$	$x = 0.04$	$x = 0.065$	$x = 0.09$
McStas gFWHM [ $\text{\AA}^{-1}$ ]	0.017(1)	0.020(1)	0.021(1)	0.015(1)
T[K]	$\geq 320$	150(20)	240(5)	300(5)
$w_{\text{mea}}^{\text{G}}$ [ $\text{\AA}^{-1}$ ]	0.015(1)	0.039(2)	0.0194(5)	0.0145(1)
$w_{\text{b}}^{\text{G}}$ [ $\text{\AA}^{-1}$ ]	-	0.034(2)	-	-
$D^{\text{G}} = \frac{2\pi}{w_{\text{b}}^{\text{G}}}$ [ $\text{\AA}$ ]	res. lim	185(11)	res. lim	res. lim
$w_{\text{b}}^{\text{L}}$ [ $\text{\AA}^{-1}$ ]	-	0.023(3)	-	-
$D^{\text{L}} = \frac{2}{w_{\text{b}}^{\text{L}}}$ [ $\text{\AA}$ ]	res. lim	87(8)	res. lim	res. lim

Table 4.5: Fitting of the low temperature neutron diffraction L-scans through (014) both using Gaussian free fit and Voigt fit with fixed Gaussian width giving Lorentzian width  $w_{\text{b}}^{\text{L}}$ . Fitting parameters of the (014) peak are shown in the table.

## 4.7 The stripe model of LNSCO/LBCO

The magnetic structure of LCO which is the un-doped parent compound of the HTSC cuprates was shown in Figure 2.4. The spins are aligned along the  $b$ -axis and the AF modulation is along the  $a$ -axis[121]. By hole-doping, the antiferromagnetism gets modulated (incommensurate) as described in Section 2.4, so instead of having a repetition period of 2, the period increases to roughly 8. In crude terms that means the antiferromagnetic pattern is something like  $(\uparrow\uparrow\uparrow \cdot \downarrow\uparrow\downarrow \cdot)$  or  $(\uparrow\downarrow \cdot \downarrow\uparrow \cdot \cdot)$  below  $T_N$ . Besides the modulation the spins might rotate so they are no longer aligned with the  $b$ -axis (see Section 2.4). This is what is observed in LNSCO and LBCO. As we shall see in Section 4.8.5 this spin arrangement is also consistent with the neutron scattering measurement of LSCO+O in this thesis work which is presented in Sections 4.8.1-4.8.4

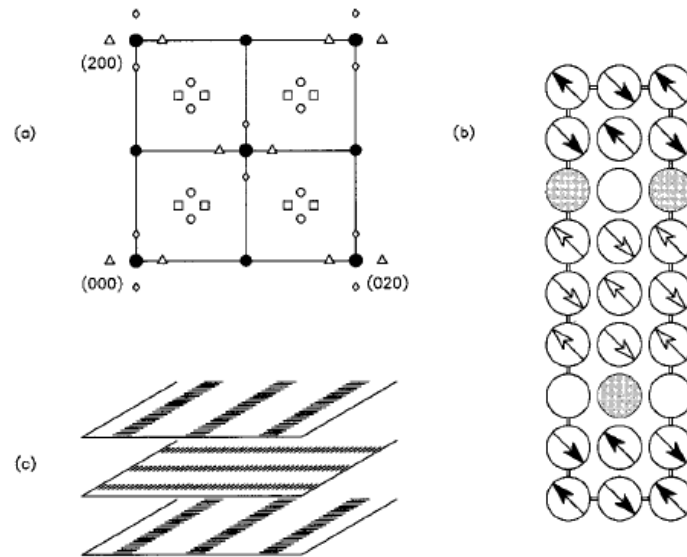


Figure 4.20: The stripe model. a) The positions of the SDW peaks are shown by  $\circ$  and  $\square$  symbols and the position of the CDW peaks by  $\triangle$  and  $\diamond$ . The different symbols of each structure refers to the scattering intensity coming from two different stripe domains. The coordinates refer to the  $I4/mmm$  tetragonal unit cell for which Bragg peaks are shown by  $\bullet$ . b) Model of the spin and charge arrangement for hole-doping  $n_h \sim 1/8$ . Arrows indicate the presence of magnetic moment and the shading of the arrowheads distinguish antiphase domains, but the direction of the arrow is not an indication of the spin direction. The filled circle denotes the presence of one dopant-induced hole centred on a Cu site. The charge order within the stripe has not been observed but serves as a reminder of the hole per Cu atom ratio is  $1/2$ . The Cu-O bonds are vertical and horizontal, respectively. c) A possible arrangement of the different stripe domains producing peaks at the positions indicated in a). The long axis ( $c$ ) is vertical. From [60].

The IC AFM in LBCO and LNSCO has been explained by the so-called

stripe model[48, 60, 122] shown in Figure 4.20 where spatial modulation of spins (IC AFM) and charge densities (CDW) account for the neutron diffraction observations. The stripe model was originally proposed for the nickelate  $\text{La}_2\text{NiO}_{4+y}$ [107] for which the interstitial oxygen atoms are refined to an average position similar to the one in LSCO+O[49]. The nickelate however remains insulating even at high hole dopings ( $y > 0.1$ )[123] for which the stripes appear[124]. An IC AFM phase which could be explained in the stripe picture is also found in LSCO+O as will be shown in the next sections.

In the stripe model of LNSCO and LBCO dynamic stripe correlations of spins and holes are stabilised and locked in by the transition to the LTT phase[125]. In LSCO+O, however, no phase transition to LTT was observed as concluded in Section 4.6.5, and the crystals remain in the LTO phase when they are superconducting.

## 4.8 Magnetic structure

In the magnetic structure of the undoped LCO compound peaks at  $(H0L)$  are allowed for  $H$  odd and  $L$  even and peaks at  $(0KL)$  are allowed for  $K$  odd and  $L$  odd[121].

The IC AFM peaks of the hole-doped La-based cuprates are seen experimentally by neutron scattering as (up to) a quartet of peaks around e.g. the  $(100)$  and  $(010)$  positions in orthorhombic notation.

In twinned LSCO crystals there has been discussion of whether the quartet of peaks around  $(100)$  and  $(010)$  arise from separate twin-domains (see Section 4.5.2) indicating that only peaks around  $(100)$  would be allowed for each single structural twin domain. However it has been shown for LCO+O that one single structural twin domain produces a quartet of peaks around both  $(H00)$  and  $(0K0)$  for  $H = K \sim 1$  [99]. The correlation along the  $c$  axis was proven to be very short ranged leaving the IC AFM modulations to lie in the  $(a, b)$  plane. In [99] the spin arrangement of LCO+O was considered similar to the one of undoped LCO (with spins roughly along the  $b$ -axis) albeit incommensurate, which however seems incompatible with their observation of IC AFM peaks of similar intensity around both  $(010)$  and  $(100)$  originating from the same single structural twin domain. The spin arrangement of [99] is shown schematically in Figure 4.21 for a single structural twin domain. Since only the spin projection perpendicular to the scattering direction contributes to the structure factor (see Equation (3.8)), the intensities around the  $(100)$  and  $(010)$  should be widely different as seen in Figure 4.21. This was however not observed in [99].

One quartet of peaks (from a single structural domain) can arise from different models of spin arrangements, see Figure 4.22. The model in Figure 4.22(a) produces only two peaks around the AFM point but in case the scattering is due to an incoherent superposition of two equally populated spin arrangements of this type but with orthogonal propagation vectors there will in total be a quartet of peaks around the AFM point. It was recently shown from analysis of the intensity of IC peaks around AFM points in different BZ that such a superposition is an appropriate model for LNSCO [64]. Neutrons scatter only on the part of the magnetic moment which is orthogonal to the scattering vector and if the spins are pointing along the  $b$ -axis ( $K$ -axis), the largest intensity of the IC

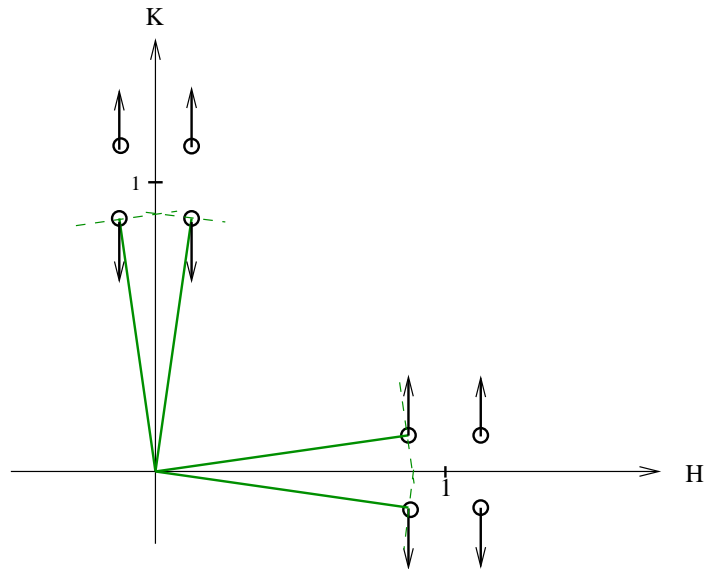


Figure 4.21: Intensity of scattering from spins diagonal to the Cu-O bonds, i.e. roughly along the orthorhombic  $b$  axis (along the  $K$  axis in reciprocal space). The spins are shown as black arrows. The direction of the arrow is not important, only that it is parallel to  $b$ . The green lines represent the direction of the scattering vector  $\mathbf{Q}$  and the orthogonal directions to the scattering vectors shown as green dashed lines. It is seen that the scattering intensity should be much smaller for the quartet around (010) than (100) since the projection of the spins onto the orthogonal of  $\mathbf{Q}$  (green dashed lines) is much smaller for spins around (010) than (100).

scattering should be seen for peaks close to the  $a$ -axis, i.e. the  $(1 \pm \delta_H, \pm \delta_K, 0)$  peaks. If the spins of each spin-domain point co-linearly along the Cu-O bonds as shown in Figure 4.23 the quartet of peaks around (010) in the 1. Brillouin zone (BZ) would have approximately equal intensity whereas the peaks originating from the 'blue' spin domain would have much larger intensity than the 'red' around (310) in the 2. BZ. This is indeed what is observed in LNSCO[64].

Since the magnetic signal in the LSCO+O crystals of this thesis is quite small (due to the small size of the crystals and only part of their volume being magnetic) and the signal is expected to decrease with the length of the scattering vector  $Q$ , I was limited to investigate magnetic peaks within the 1. BZ, the positions are shown in Figure 4.24. Our measurements nevertheless support the stripe model of LNSCO to be valid for LSCO+O also. The enumeration of the IC AFM peaks is introduced for convenience of the reader and referred to in the following sections. All the neutron scattering data in this section were normalised to the monitor count and multiplied by the average monitor count per second.

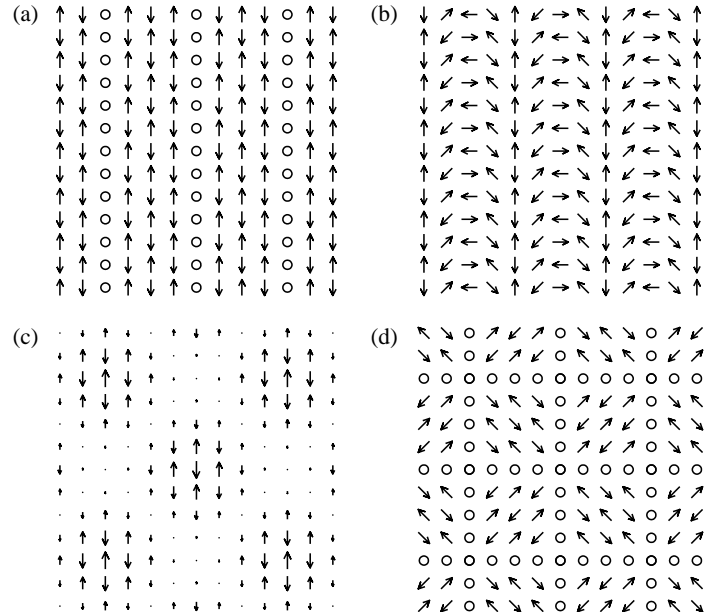


Figure 4.22: Models for the magnetic order in La-based cuprates at  $x=1/8$  doping. The Cu-O bond directions are vertical and horizontal as opposed to figures 4.21, 4.23 and 4.24 in this section. (a) One- $\mathbf{Q}$  domain with charge stripes (lines of open circles) and collinear spin order [2]. (b) One- $\mathbf{Q}$  domain with helical spin order. (c) Collinear two- $\mathbf{Q}$  structure of a diagonally modulated commensurate AFM [14]. (d) Two- $\mathbf{Q}$  order of charge and spins in a non-collinear structure. From [64]

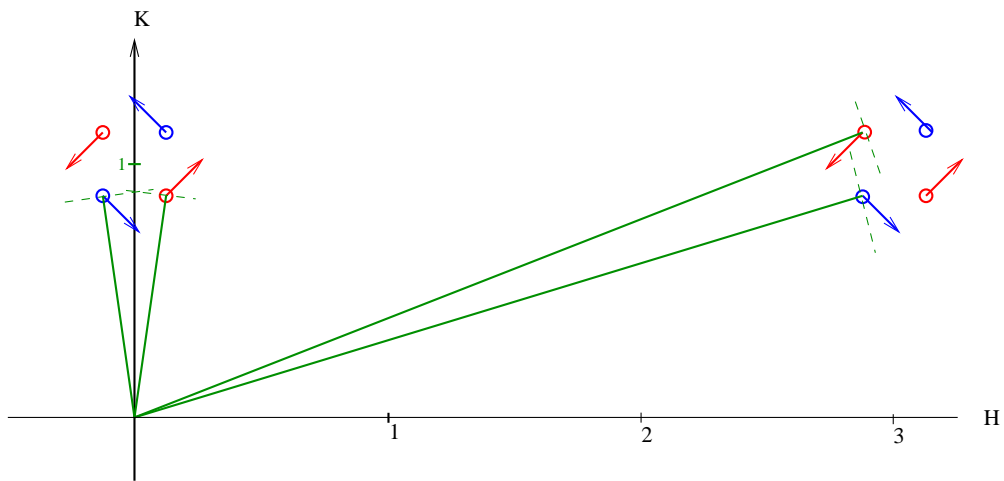


Figure 4.23: Intensity of scattering from spins along Cu-O bonds. The green lines represent the direction of the scattering vector  $\mathbf{Q}$ . It is seen that the projection on the orthogonal of  $\mathbf{Q}$  (dotted lines) is much smaller for the red arrows around (310) than for the blue. Adapted from [64]

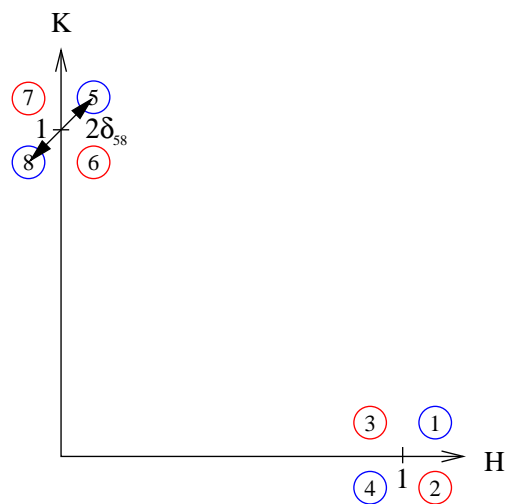


Figure 4.24: The enumeration of the IC AFM peaks which the matrix in the caption of Figures 4.26, 4.29 and 4.29 refers to. An example of the notation of the incommensurability values of Table 4.8 is also shown.

### 4.8.1 LSCO+O $x=0$

The neutron diffraction data of the sLSCO\_0A sample in this section were produced at the thermal TAS BT7 at NIST using  $E=14.7$  meV neutrons and 50' collimation before and after the sample. The data are part of the on-going thesis work of Samuel B. Emery (UConn).

The transversal scans through the (020) and (200) Bragg peaks are shown in Figure 4.25.

Figure 4.26 shows  $a_3$  scans of the IC AFM peaks and the corresponding widths of the Bragg peaks from Figure 4.25 are marked by a red line. It is seen that the IC AFM peaks are not broadened with respect to the Bragg peaks.

The temperature dependence of an IC AFM peak is shown in Figure 4.27 both with and without an applied field. The transition temperature is  $T_N = 41(1)$  K in both cases from linear linear fits close to the phase transition. It is seen that there is close to 100% field effect at base temperature by application of 6.9 T magnetic field.

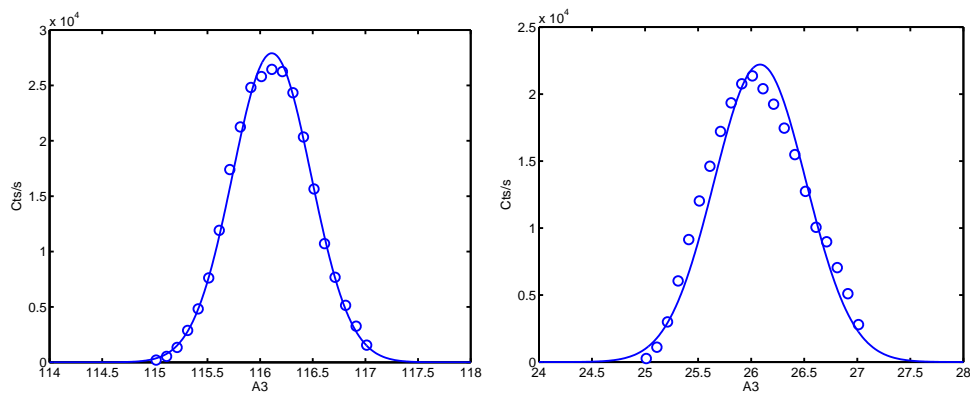


Figure 4.25: Transversal scans through (020) and (200) positions for LSCO+O  $x=0$ . The lines are Gaussian fits.

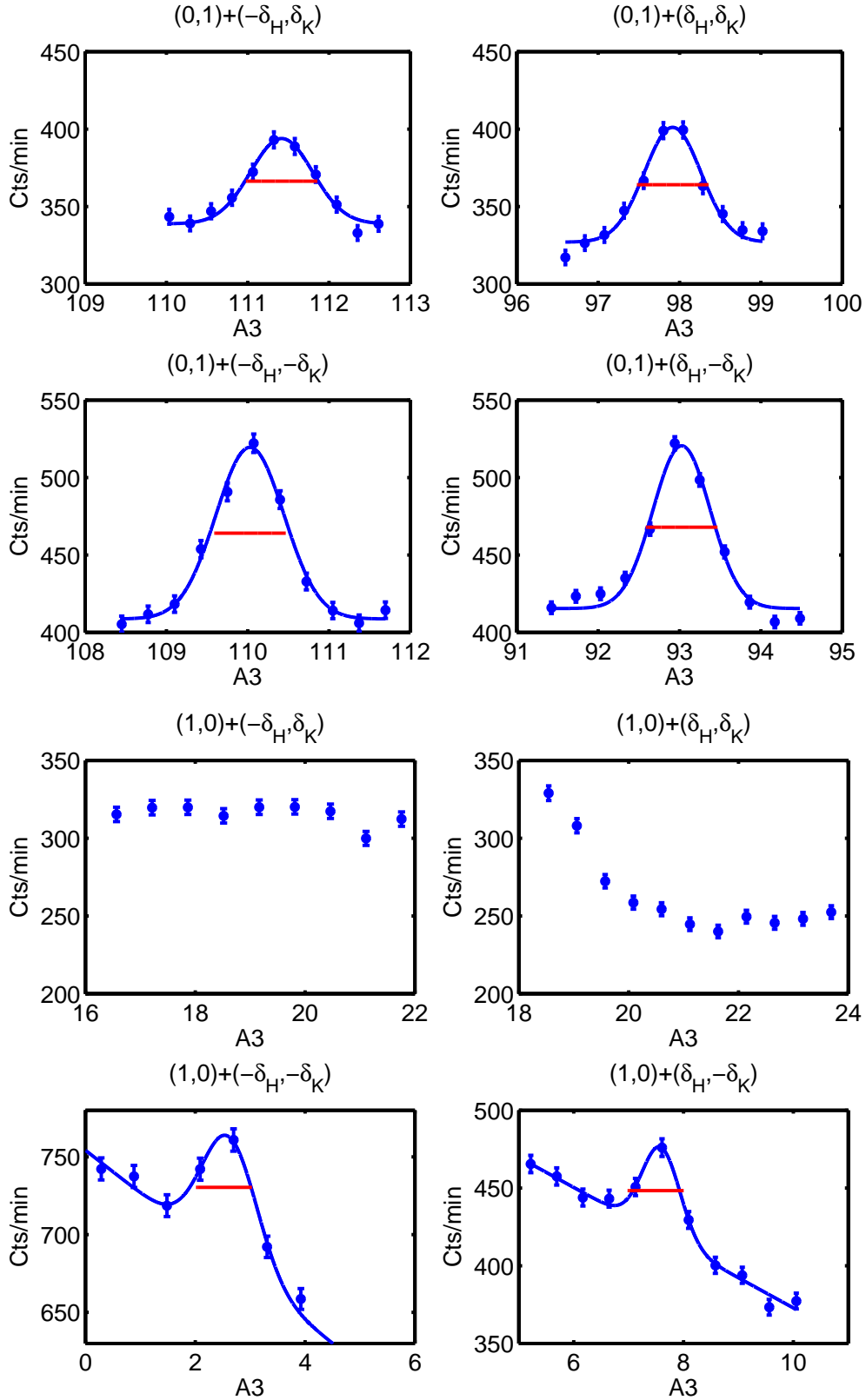


Figure 4.26: Scans through the IC AFM peak positions for LSCO+O  $x=0$  measured at BT7 with 14.7 meV. The eight scans in the figure are listed for the  $\begin{bmatrix} 7 & 5 \\ 8 & 6 \\ 3 & 1 \\ 4 & 2 \end{bmatrix}$  positions where the numbers refer to Figure 4.24. The red lines show the width of the transversal scans through (020) and (200) respectively as shown in Figure 4.25. Data from thesis work of Samuel B. Emery.

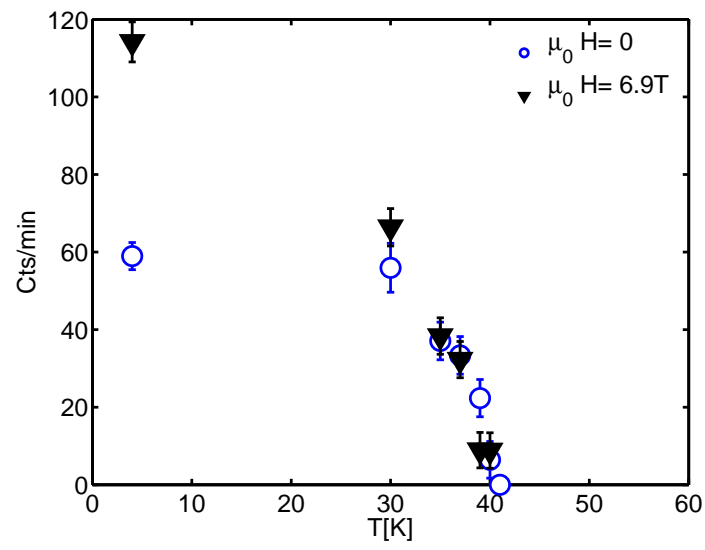


Figure 4.27: Temperature dependence of an IC AFM peak for LSCO+O  $x=0$  at  $(0.132, 0.89, 0)$  in ZF and 6.9 T. Data from thesis work of Samuel B. Emery.

### 4.8.2 LSCO+O $x=0.04$

The neutron diffraction data in this section were produced at the cold TAS IN14 at ILL using  $E=4.66$  meV neutrons and 40' collimation before and after the sample. It was necessary to use the high-flux IN14 instrument since the sample was too small for measurement of the magnetic signal at e.g. the RITA-II instrument.

Since the main focus was on the incommensurability value,  $a_3$  scans do not exist for all the IC peaks in this section. However, since the IC AFM peaks and the peaks measured at (100) and (010) have similar  $\mathbf{Q}$ , their widths in  $a_3$  are expected to be the same. The resolution is relatively relaxed compared with the mosaicity so the top point of the peak is considered to be contained fully within the resolution ellipsoid. Therefore comparison between peak amplitudes is possible, albeit with caution. From Figure 4.28 it is seen that the resolution is wider in the longitudinal than the transversal direction in the vicinity of the IC AFM peaks. I will however consider the resolution to be circular within 15% error with diameter of the average width of the longitudinal and transversal scans. The average width of (010) and (100) are marked by red lines in 4.29 of the IC AFM peaks. No finite size broadening of the IC AFM peaks with respect to the width of the Bragg peaks was observed.

The temperature dependence of an IC AFM peak is shown in Figure 4.30. The transition temperature is found to be  $T_N = 47(8)$  K but is probably overestimated due to the sparse number of data points available.

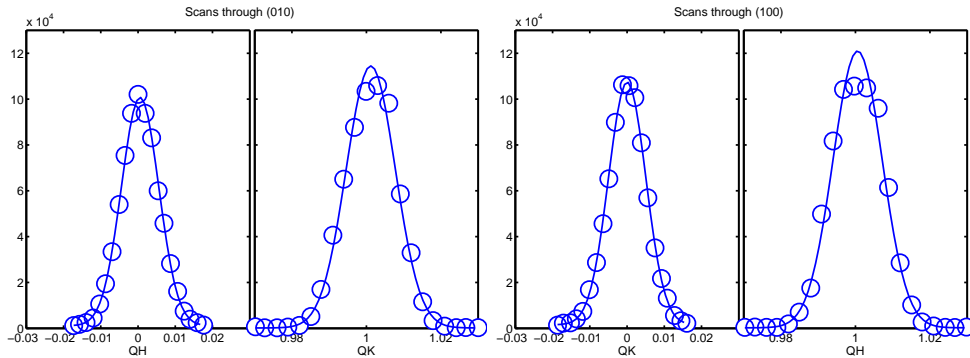


Figure 4.28: Longitudinal and transversal scans through (010) and (100) positions for LSCO+O  $x=0.04$ . Any splitting due to twinning is not resolved in this setting. The data are taken with the Be filter out and the intensity is due to second order scattering from (020) and (200) respectively.

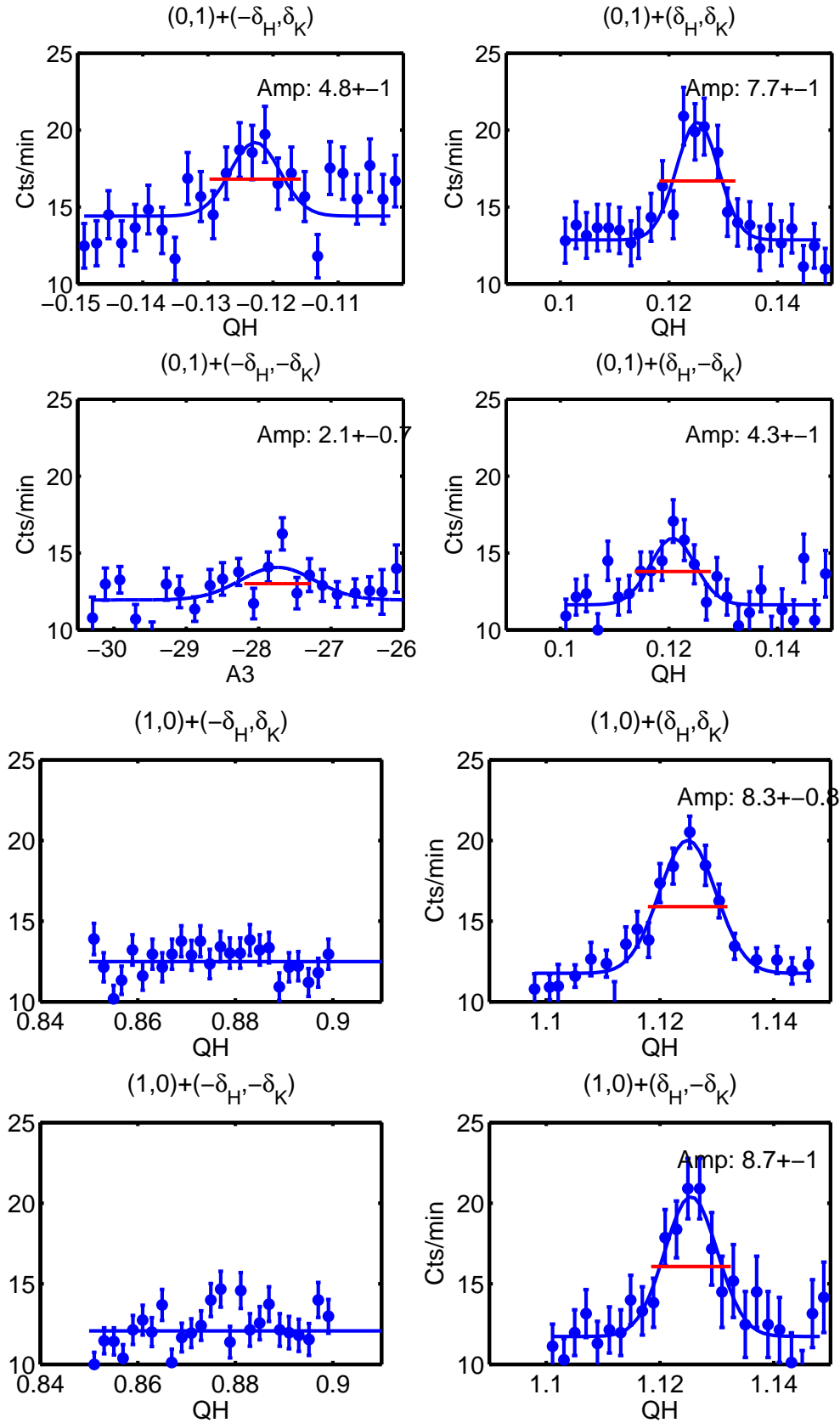


Figure 4.29: Diagonal scans through the IC AFM points in 1. BZ for LSCO+O  $x=0.04$ . The positions of the scans are listed for the  $\begin{bmatrix} 7 & 5 \\ 8 & 6 \\ 3 & 1 \\ 4 & 2 \end{bmatrix}$  positions referring to Figure 4.24. The red lines show the average of the transversal and longitudinal widths as shown in Figure 4.28 of the peaks at (010) and (100), respectively.

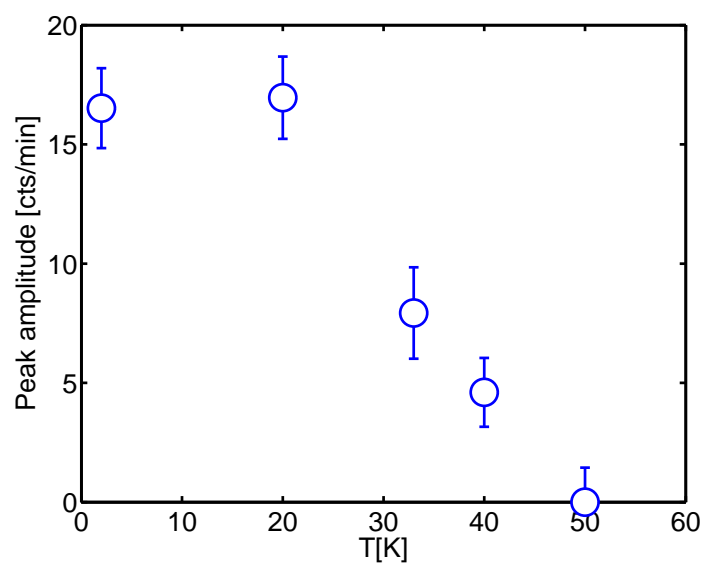


Figure 4.30: Temperature dependence of the amplitude of the peak at  $(1.125 \ 0.125 \ 0)$  for LSCO+O  $x=0.04$

### 4.8.3 LSCO+O $x=0.065$

The neutron diffraction data in this section were produced at the cold TAS IN14 at ILL using  $E=4.66$  meV neutrons and 40' collimation before and after the sample. It was necessary to use the high-flux IN14 instrument since the sample was too small for measurement of the magnetic signal at e.g. the RITA-II instrument.

Since the main focus was on the incommensurability value  $a_3$  scans do not exist of all the IC peaks in this section. However since the IC AFM peaks and the peaks measured at (100) and (010) have similar  $Q$  their widths in  $a_3$  are expected to be the same. As the major and minor axis of the resolution ellipsoid at (100) and (010) are the same within 15%, the resolution is close to circular in the scattering plane as shown in Figure 4.31. No finite size broadening with respect to the width of the Bragg peaks was observed as seen in Figure 4.32. The resolution is considered relaxed with respect to the mosaicity and comparison between the IC AFM peak amplitudes is possible even though the scans are in a diagonal direction. It is seen that the amplitude of the low- $Q$  peaks is 50% or less of the high- $Q$  peaks.

The temperature dependence of an IC AFM peak is shown in Figure 4.33. By a piecewise linear fit to the data point just above and below the transition (not shown) the transition temperature is found to be  $T_N = 40(3)$  K.

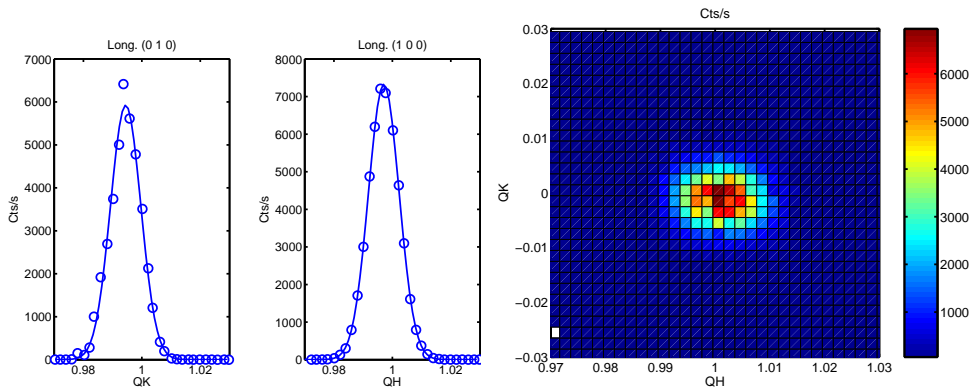


Figure 4.31: Left: Longitudinal scans of (010) and (100) of LSCO+O  $x=0.065$  without Be filter, showing no resolvable splitting due to twinning. Gaussian width 0.005 rlu. Right: Grid-scan of (100) showing almost circular resolution at this energy.

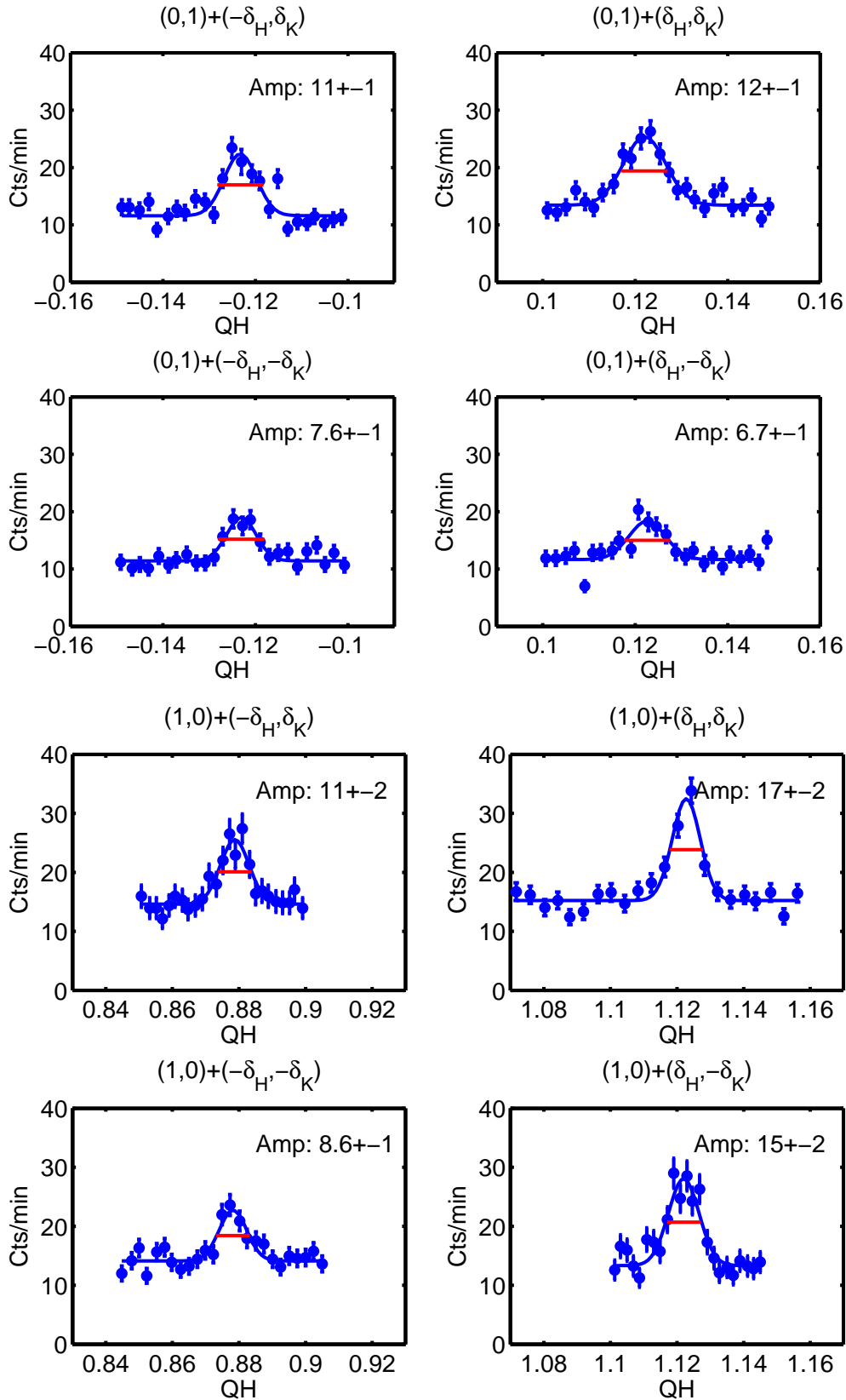


Figure 4.32: Diagonal scans through the IC AFM peaks around (010) and (100) of LSCO+O  $x=0.065$ . The positions of the peaks in the figure are listed for the  $\begin{bmatrix} 7 & 5 \\ 8 & 6 \\ 3 & 1 \\ 4 & 2 \end{bmatrix}$  positions referring to Figure 4.24. The red lines show the average of the transversal and longitudinal width through the (010) and (100) positions, respectively.

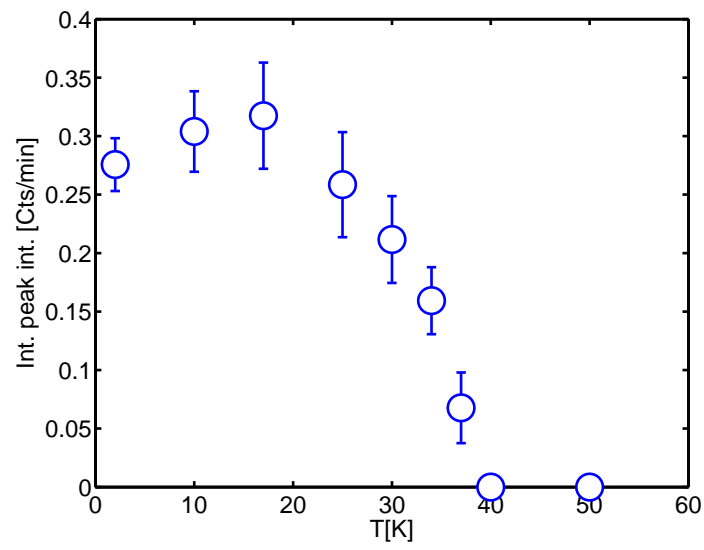


Figure 4.33: Temperature dependence of an IC AFM peak for LSCO+O  $x=0.065$ . Fitted areas of the peak at (QH 0.125 0) are plotted as function of temperature

#### 4.8.4 LSCO+O $x=0.09$

The neutron diffraction data in this section were measured at the cold TAS RITA-II using 5 meV neutrons and 40' collimation before the sample. A 'radial' Be-filter was used after the sample which allows the scattered beam to hit the seven blades of the analyser in imaging mode (see Section 5.13 for details about the special analyser of RITA-II). The geometrical collimation is  $\sim 40'$  from the sample to each analyser blade.

The scattering from the high- $Q$  IC AFM positions was unfortunately not visible due to the second order (20 meV) scattering from the Al cryostat which was at the same scattering angle. One of the low- $Q$  peaks are shown in Figure 4.35. The measured peak has FWHM  $w_m^G = 0.0130(14)$  r.l.u. as determined by a simple Gaussian fit on sloping background, which is slightly broader than the line width in the same scan direction at the  $(-100)$  position having  $w_r^G = 0.0101(1)$  r.l.u.<sup>5</sup> shown in Figure 4.34. For comparison the simulated value found in Section 6.4 of the line width at  $(-100)$  is  $w_r^G = 0.0111(2)$ .

If the IC AFM peak is fitted to a Gaussian the combined width is the sum of the internal width  $w_b^G$  and the resolution in quadrature (see Eq. 3.25) giving  $w_b^G = \frac{2\pi}{5.337\text{\AA}} \sqrt{0.0130^2 - 0.0101^2} = 0.010(1) \text{\AA}^{-1}$ . The estimated apparent correlation length is  $2\pi/w_b^G = 640 \pm 130\text{\AA}$ .

Since a simple model for the correlation function is exponentially decreasing in real space the line shape would be Lorentzian in reciprocal space. When convoluted with the Gaussian resolution the resulting line shape would be a Voigt. The data in Figure 4.35 are subtracted the background above  $T=40$  K and the Gaussian width is fixed at  $w_r^G$ . Then the Lorentzian FWHM of the Voigt fit is  $w_b^L = 0.005(2)$  rlu =  $0.006(2) \text{\AA}^{-1}$  giving apparent correlation length of  $2/w_b^L = 340 \pm 120 \text{\AA}^{-1}$ .

The temperature dependence of the IC AFM peak is shown in Figure 4.36, with and without applied field. By a linear fit (not shown) the transition temperature is found to be  $T_N = 40(4)$  K in both cases. Furthermore the peak position, width and intensity does not change within errors as seen in Figure 2 of [47] which is included in Appendix D. From Figure 3 of the same article it is seen that there is no enhancement of the IC AFM peak up to 13.5 T applied field.

---

<sup>5</sup>This was measured by 2. order scattering off the structural  $(-200)$  peak (without Be filter) but the resolution is similar in angular space

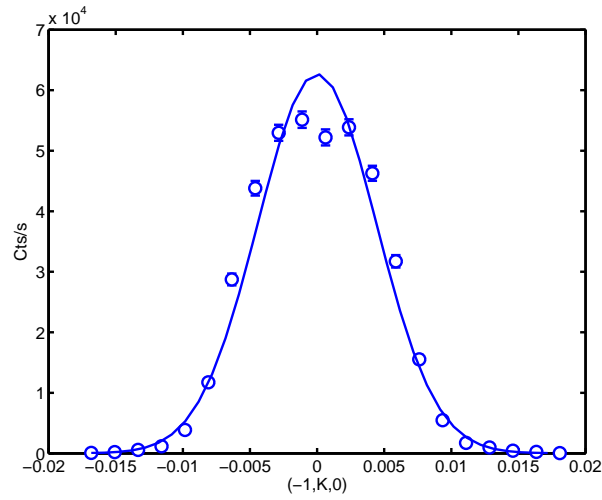


Figure 4.34: Scan through  $(-100)$  in LSCO+O  $x=0.09$ , showing the resolution at this position and in the  $K$  scan direction. The peak is actually second order scattering off  $(-200)$ .

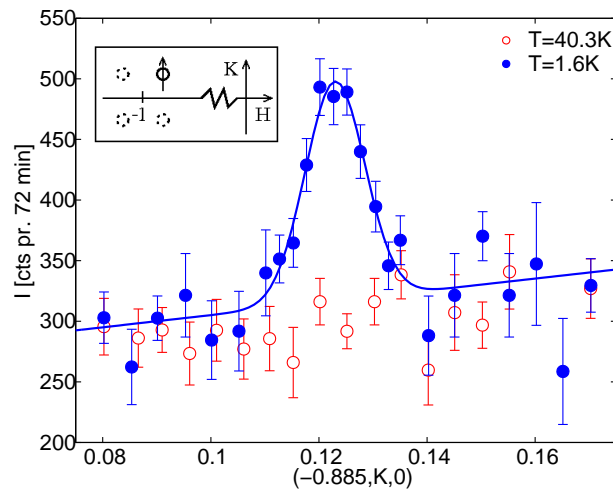


Figure 4.35: IC AFM peak of LSCO+O  $x=0.09$ . The scans performed through  $(-0.885,0.123,0)$  along the  $K$ -direction. The scans are taken above and below  $T_N$  in zero applied field, the solid line is a Gaussian fit. The inset shows the peak position and scan direction. From [47].

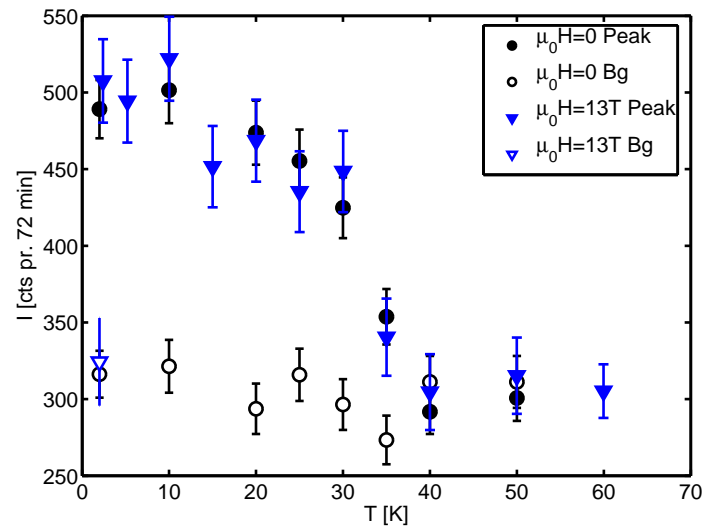


Figure 4.36: Temperature dependence of the LSCO+O  $x=0.09$  IC AFM peak intensity at  $\mu_0H = 0$  (in cryostat) and  $\mu_0H = 13.5$  T (in magnet, after field-cooling) respectively. The  $\mu_0H = 13.5$  T data are scaled (from the ratio of Bragg peak intensity in the cryostat and magnet respectively) and subtracted a constant background. From [47].

### 4.8.5 Summary and discussion of the magnetic diffraction data

Unfortunately the angular range at IN14 did not allow us to measure outside the first BZ at 5 meV so we were confined to measuring the IC peaks around (100) and (010). Likewise due to the relatively long counting times I was often confined to measure scans in only one direction.

If the spins are aligned collinearly along the Cu-O bond directions the intensity of peaks with equal length of  $\mathbf{Q}$  should also have comparable intensities when not taking extinction into account and considering scattering from just a single plane. I.e. finite intensity should be observed in both quartets around (100) and (010). This is qualitatively what we observe for all dopings and thus the in-plane spin arrangement is probably as in LNSCO [64].

Considering the spins within a single  $\text{CuO}_2$  plane where the spins are collinear along the Cu-O bonds we would only expect a small difference in the intensity of the peak of each quartet. This is because the  $2^\circ$  difference in direction of  $\mathbf{Q}$  gives rise to only a 5% higher intensity in the high- $Q$  peaks than the low- $Q$  peaks of the same quartet. However, for  $x = 0.065$  (and to some extent also  $x = 0.04$ ) we observe larger intensity at the high- $Q$  peaks (number 1, 2, 5 and 7) with respect to the low- $Q$  peaks (number 3, 4, 6 and 8) referring to the enumeration of Figure 4.24. The measured relative intensity of the peaks for each sample in this thesis work is summarised schematically in Figure 4.37. For  $x = 0.04$  and  $0.065$  it is seen that the low- $Q$  peaks do indeed have a lower intensity than the high- $Q$  ones, but the effect is more than 50% which cannot be explained by the length of projection of the magnetic moment along  $\mathbf{Q}$ .

Therefore a simple model of the stripe unit-cell has been used to calculate the relative intensities of the scattering peaks. The unit-cell of 128 Cu atom positions in 2 layers of stripes is shown in Figure 4.38(left). The coherent magnetic elastic cross-section is written as

$$\frac{d\sigma_M}{d\Omega}(\mathbf{Q}) = N \frac{(2\pi)^3}{V_0} \sum_{\tau} |pe^{-W}|^2 |\mathbf{S}_{\perp}(\mathbf{Q})|^2 \delta(\mathbf{Q} - \mathbf{G}) \quad (4.2)$$

$$\mathbf{S}_{\perp}(\mathbf{Q}) = \mathbf{Q} \times (\mathbf{S}(\mathbf{Q}) \times \mathbf{Q}) \quad (4.3)$$

$$\mathbf{S}(\mathbf{Q}) = \sum_j \mathbf{m}_j e^{i\mathbf{Q} \cdot \mathbf{d}_j} \quad (4.4)$$

from Equations 3.6 and 3.8.  $\mathbf{m}_j$  is the moment at site  $j$ . The value is either (1,1), (-1,-1), (1,-1), (-1,1) or (0,0) depending on the site. The magnetic moments are represented by differently coloured dots in Figure 4.38 and the coordinates refer to the  $F4/mmm$  setting. In this simple model we have used  $|pe^{-W}|^2 = 1$  although  $p$  contains the  $\text{Cu}^{2+}$  formfactor which is highly anisotropic[82, 126]. However for the quartet of peaks around e.g. (100) the scattering vector is almost the same and the calculated relative intensity distribution is qualitatively correct. It is seen from Figure 4.38(right) that within the 2 stripe layer model there should be roughly 50% lower intensity in the low- $Q$  peaks with respect to the high- $Q$  peaks which is qualitatively what is observed for  $x=0.04$  and  $x=0.065$ . Unfortunately similar data for the  $x = 0.09$  crystal have not been measured yet. As is seen in Figure 4.37 the situation seems to be the opposite for  $x = 0$  in an applied field of  $\sim 7$  T where the intensity is

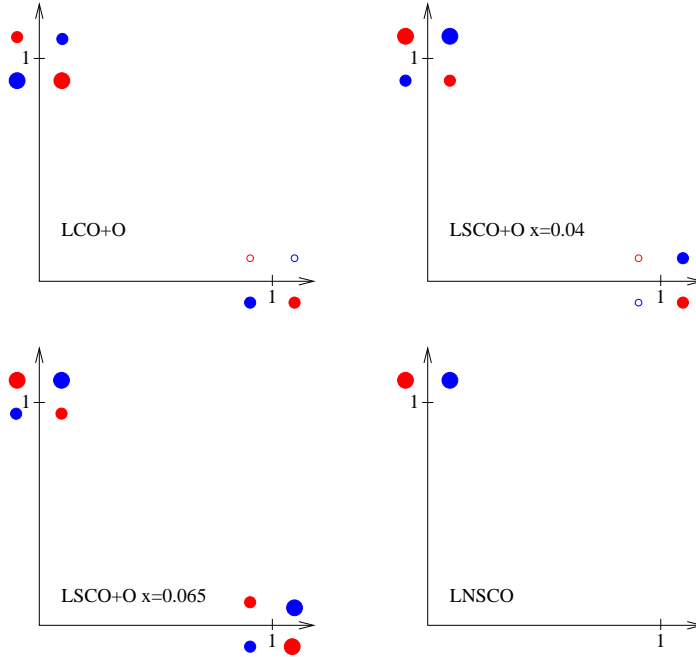


Figure 4.37: The relative measured peak intensities for each crystal in the first BZ schematically shown where the size of the circle represents the intensity of the peak. The figure representing LCO+O shows the relative peak intensities at 6.9T applied field, the other figures are at zero field.

higher for the low- $Q$  peaks. It would be interesting to measure all the LCO+O peaks again without applied field to see whether the distribution is similar to the other superoxygenated crystals and LNSCO. Inter-comparison of the intensities of IC AFM peaks with similar  $Q$ -length for different doping values  $x$  is shown in Tables 4.6 and 4.7. It is seen that within 35% the value is constant for all the crystals which is to be expected if the magnetic structure is similar. No higher precision was obtainable in the comparison since there is so much variation of the peak intensity even for the same  $Q$ -length in the same sample and it is difficult to compare measurements on different instruments.

Instr.	$x$	Mass[g]	Peak [rlu]	$I_{IC}[\frac{cts}{s}]$	$\tilde{I}_{IC}[\frac{cts}{(s \cdot g)}]$	$I_{100}[\frac{cts}{s}]$	$\frac{I_{IC}}{I_{100}}$	$V_M$	$\frac{I_{IC}}{I_{100} \cdot V_M}$
IN14	0.04	0.035	(0.125,0.875)	0.07	2.1	$2.0 \cdot 10^3$	$3.5 \cdot 10^{-5}$	0.42	$0.8 \cdot 10^{-4}$
IN14	0.065	0.091	(0.125,0.875)	0.14	1.6	$6.8 \cdot 10^3$	$2.0 \cdot 10^{-5}$	0.19	$1.1 \cdot 10^{-4}$
RITA	0.09	0.429	(0.885,0.123)	0.043	0.1	$1.0 \cdot 10^3$	$4.3 \cdot 10^{-5}$	0.51	$0.8 \cdot 10^{-4}$

Table 4.6: Comparative table of ZF intensity of IC AFM peaks for different doping  $x$  of LSCO+O at 5 meV scattering energy. All intensities are peak amplitudes. The (100) peak is actually 20 meV scattering off (200) but the numbers in the column still compares.  $V_M$  is the magnetic volume fraction as measured by ZF- $\mu$ SR.

In LSCO the incommensurability value follows the Sr doping for  $0.06 < x < 1/8$  as discussed in Chapter 2. Previous experiments on superoxygenated

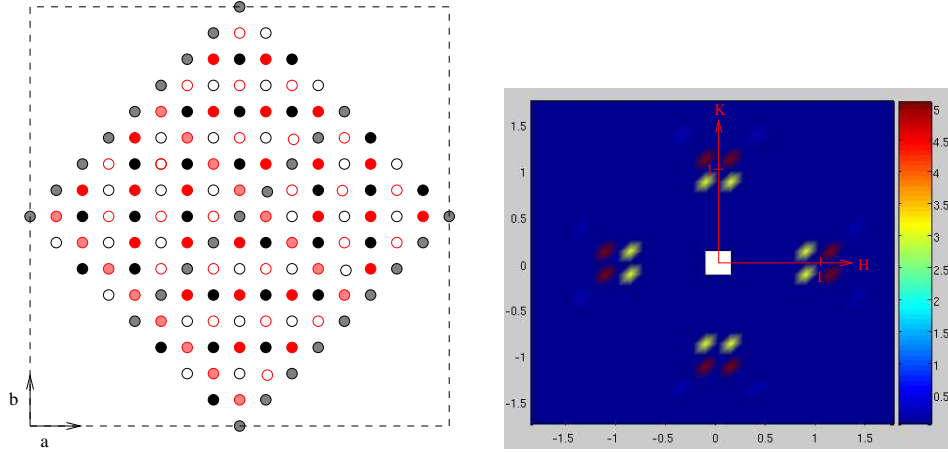


Figure 4.38: (Left) The 128 magnetic moment unit-cell of spin stripes in 2 layers are shown in the figure, the spin directions in the  $c = 0$  layer is collinear with the stripe direction ( $a+b$ ), the ones in the next layer ( $c = 1/2$ ) are collinear with the stripes in that layer ( $a-b$  direction). The  $c = 0$  layer is shown in black and white colours the  $c=1/2$  layer in red colours. Full colour dots represent spins in one direction and white dots represent spins in the opposite direction. Gray (pink) dots represent Cu atoms with no spin (0.5 holes on average). (Right) the magnetic cross-section in the  $(H, K)$  reciprocal lattice plane calculated from Equation 4.2 using the 128 atom unit-cell.

Instr.	$x$	Mass[g]	Peak [rlu]	$I_{IC}[\frac{cts}{s}]$	$\tilde{I}_{IC}[\frac{cts}{(s^*g)}]$	$I_{200}[\frac{cts}{s}]$	$\frac{I_{IC}}{I_{200}}$	$\frac{F_{IC}^2}{F_{200}^2}$
BT7	0	0.8	(0.132,0.89)	0.81	1.0	$2.9 \cdot 10^4$	$2.8 \cdot 10^{-5}$	$1.4 \cdot 10^{-5}$
RITA	0.09	0.429	(0.885,0.123)	0.038	0.09	$2.3 \cdot 10^3$	$1.7 \cdot 10^{-5}$	$1.1 \cdot 10^{-5}$

Table 4.7: Comparison of ZF IC AFM intensity for  $x=0$  and  $x=0.09$ . All intensities are the Gaussian fitted areas from scans resembling rocking curves. Data at BT7 taken at 14.7 meV, data at RITA taken at 5 meV.

LCO+O with similar doping degree to the samples used in this thesis work have all found an incommensurability value of  $\sim 1/8$ [99, 110]. In our LSCO+O crystals, the measured incommensurability value is quite similar to the one previously measured in LCO+O, irrespective of Sr content  $x$  as seen in Table 4.8. The incommensurability values are shown in two ways: As the distance between the IC AFM peaks in  $\text{\AA}^{-1}$  calculated by

$$2\delta [\text{\AA}^{-1}] = \sqrt{(\Delta Q_H \frac{2\pi}{a})^2 + (\Delta Q_K \frac{2\pi}{b})^2} \quad (4.5)$$

where  $a$  and  $b$  are orthorhombic lattice units in each experiment and  $(\Delta Q_H, \Delta Q_K) = \mathbf{Q}_{IC}^i - \mathbf{Q}_{IC}^j$  where  $\mathbf{Q}_{IC}^i$  and  $\mathbf{Q}_{IC}^j$  are the fitted reciprocal lattice positions of two separate IC AFM peaks. Since the incommensurability corresponds to a modulation which is close to being along the in-plane Cu-O bonds, it is also calculated in pseudo-tetragonal lattice units ( $a_T = \frac{a+b}{2\sqrt{2}}$ ) by

$$\delta^T \left[ \frac{2\pi}{a_T} \right] = \delta \cdot \frac{a_T}{2\pi} = \delta \cdot \frac{a+b}{4\pi\sqrt{2}} \quad (4.6)$$

Since not all the eight peaks had measurable intensity above the background level some of the incommensurabilities have been estimated from the position of a single peak. These are marked by  $\sim$  in Table 4.8.

The incommensurability value for all the samples in both stripe directions lie between 0.119 and 0.127 i.e. it is equal to 0.123 within two standard errors of 0.002. I conclude that the incommensurability is  $1/8$  within errors for all  $x$ , corresponding to an in-plane spin-modulation along the Cu-O bonds with periodicity 8.

	$x = 0$	$x = 0.04$	$x = 0.065$	$x = 0.09$
$2\delta_{14} [\text{\AA}^{-1}]$	$\sim 0.405$	$\sim 0.415$	0.414(6)	-
$\delta_{14}^T \left[ \frac{2\pi}{a_T} \right]$	$\sim 0.123$	$\sim 0.125$	0.125(2)	-
$2\delta_{32} [\text{\AA}^{-1}]$	$\sim 0.422$	$\sim 0.417$	0.405(6)	$\sim 0.397$
$\delta_{32}^T \left[ \frac{2\pi}{a_T} \right]$	$\sim 0.127$	$\sim 0.125$	0.122(2)	$\sim 0.119$
$2\delta_{58} [\text{\AA}^{-1}]$	0.411(6)	0.415(6)	0.408(6)	-
$\delta_{58}^T \left[ \frac{2\pi}{a_T} \right]$	0.125(2)	0.125(2)	0.123(2)	-
$2\delta_{76} [\text{\AA}^{-1}]$	0.415(6)	0.405(6)	0.410(6)	-
$\delta_{76}^T \left[ \frac{2\pi}{a_T} \right]$	0.125(2)	0.122(2)	0.123(2)	-

Table 4.8: The incommensurability as function of Sr doping  $x$  for superoxygenated crystals, the notation refers to Figure 4.24 and Equations 4.5 and 4.6. The standard deviation is calculated from the error on the fitted positions of the IC AFM peaks. In some cases the incommensurability value is based on one (instead of two) peaks and these are denoted by  $\sim$ .

The widths of the IC AFM peaks are comparable in all experiments. For  $x = 0, 0.04, 0.065$  where the experiments were performed at BT7 and IN14, this width is within the resolution limit as determined from first or second order scattering off (020) and (200). In the case of  $x = 0.09$  the experiments were performed at RITA-II with good  $Q$ -resolution and it turned out that the peak was in fact slightly broadened. The correlation length of the IC AFM regions however still exceeds  $340 \pm 120 \text{\AA}$ . Previous magnetisation measurements have shown that there is an order of magnitude less flux-pinning in LSCO+O than in LSCO with similar hole-doping [16]. Since regions where the superconductivity is suppressed have to be small to act as effective pinning centres, the small flux-pinning in LSCO+O supports that the regions where the superconductivity is suppressed, must be much larger than the in-plane superconducting coherence length of roughly  $10 \text{\AA}$  [16]. In the DSZ theory where superconductivity and magnetism compete, suppression of superconductivity in a region would allow for IC AFM to grow and hence the IC AFM regions in LSCO+O would be large, which is what we observe by neutron scattering.

There seems however to be a distinct difference in the IC AFM signal from the LSCO+O samples with respect to the under-doped [41] and close-to

1/8 hole-doped non-super-oxygenated LSCO results[127, 2] since the neutron diffraction studies presented in this thesis have shown no field-enhancement of the static IC magnetic signal up to 13.5 Tesla in super-oxygenated LSCO+O with  $x > 0$  (see Figure 4.36). In LSCO+O with  $x = 0$  a field effect was observed (Figure 4.27), but it has previously been suggested that the degree of magnetic order in superoxygenated LCO+O is related to the amount of oxygen disorder [108]. In the LCO+O crystal of [108] an enhancement of about 80% of the IC AFM peak intensity was observed either by application of a 7.5 T field or by fast cooling. In the same sample it was found that peaks at  $(\pm 0.09, \pm 0.024, 5 \pm 0.5)$ , which were attributed to direct oxygen ordering, were suppressed after the fast cooling[108]. However, since I have observed similar peaks in LCO+O both by neutron diffraction ( see appendix B) but also by hard x-rays[120], the 'direct oxygen' scattering must primarily be due to an in-plane incommensurable periodic arrangement of the heavier atoms between every other unit cell along  $c$ . Due to the observation in LCO+O[108] of a field enhancement when 'the direct oxygen' peaks are missing after fast cooling, it is natural to assume that a possible field effect is connected to oxygen ordering in LSCO+O samples.<sup>6</sup>

The mechanism behind might be similar to the one found in YBCO. In YBCO [129, 130] oxygen ordering facilitates itinerant doped holes thereby favouring SC, whereas oxygen disorder does not favour SC. In this scenario SC would be favoured in slowly cooled oxygen ordered LCO+O at least at zero applied field. Applying moderate fields hereafter allows IC AFM regions to grow to a plateau volume. In LCO+O oxygen disorder can be introduced by fast cooling. In LSCO+O, which can be viewed as doping LCO+O with Sr, the homogeneously distributed Sr anti-correlates to the excess oxygen, creating an increasingly disordered oxygen distribution with increasing Sr content [131]. Thus following this scenario, in LSCO+O with  $x$  above a certain level and fast-cooled LCO+O, SC regions are not particularly favoured over IC AFM regions even at zero applied field. This can explain why we see little or no enhancement of the magnetic signal by application of a field in the LSCO+O system for  $x = 0.09$ .

From Figure 4.27 it is seen that the field effect of the IC AFM in LCO+O is most pronounced at low temperatures. This is similar to the field effect of the inelastic scattering from the IC point in optimally doped LSCO  $x \sim 0.16$ [42].

If we turn to the slightly doped  $\text{La}_2\text{CuO}_{4+\gamma}$  and  $\text{La}_{2-\zeta}\text{Sr}_\zeta\text{CuO}_4$ , SC was thought to be contained within a percolating network of small spin-polarised clusters which were attracted to their counter-ions (Sr or intercalated O ions). Under special cooling conditions where the percolating network was not able to form, the AFM was favoured[101, 102, 104]. If the counter-ions are intercalated O ions it should in principle be possible to form a regular intercalated oxygen-lattice by application of a magnetic field via the attraction to the spin-polarised clusters. A study of the staging structure as a function of applied field in LSCO+O would therefore be highly interesting in the context of investigating the mechanism behind the electronic phase-separation in this material.

---

<sup>6</sup>In connection with this I have also searched for the 'direct oxygen' peaks in slowly cooled LSCO+O  $x = 0.09$  but not found any[128]. Since this sample was not staged, no 'direct oxygen' peaks were expected to be found in correspondence with my findings.



## Chapter 5

# Virtual experiments on RITA-II

The definition of a virtual experiment is a complete simulation of an experiment, from source over sample to detector [25]. Of course the description of the virtual instrument including the sample should be as close as possible to the physical instrument. The neutron rays must have absolute intensity units and preferably the virtual instrument should be controlled like the physical instrument. This chapter is devoted to describing, building, and testing a virtual replica of the RITA-II TAS at SINQ, PSI, Switzerland. The virtual RITA-II (V-RITA-II) is built with the neutron Monte Carlo ray-tracing package McStas and tested against physical experiments at RITA-II. Particular focus is placed on reproducing the line width of particular scans for various sample types, but the absolute intensity is also investigated.

### 5.1 RITA-II line width dependency

A series of neutron diffraction experiments were performed at the RITA-II TAS at PSI. The experiments presented in Section 5.4-5.15.1 had the purpose of testing and adjusting the various components of V-RITA-II. The resolution of the finely tuned virtual instrument is then investigated by comparing to the line width of physical experiments on different types of ideal samples in Sections 5.15.2- 5.16. Virtual and physical diffraction experiments are performed on LSCO+O in Chapter 6. The samples in the virtual experiments are homogeneous and by de-convoluting the effective resolution, I have deduced the broadening due to finite size effects in LSCO+O single crystal samples.

The effective resolution of the instrument and thereby the line width of a particular scan on RITA-II depends on

- Divergence of the beam before the monochromator: Size of source, geometry and m-values of guide elements
- Divergence of collimators
- Geometrical factors: Sizes of components and distances between them
- Mosaicity of the monochromator and analyser

- Absolute energy of the incoming and scattered beam
- Sample parameters:
  - Shape and size ( valid for all samples including incoherent scatterer, powder, single-crystal)
  - Particle size in sample (valid for powder)
  - Mosaicity and uncertainty in lattice parameters (valid for single-crystal)
- Point-spread function of the position sensitive detector (PSD)

In the following sections, each of these points will be accounted for..

## 5.2 Adding background to the simulated data

The analysis of the data from the virtual and physical experiments is carried out similarly. The background from e.g. sample environment is however not simulated at present. Instead a flat background with controlled spread is generated from the ratio of the peak amplitude  $I_p^m$  and background intensity  $I_{bg}^m$  of the physically measured data with errors  $e_p^m$  and  $e_{bg}^m$ , respectively. The superscript  $m$  denotes physically *measured* data. The dependence of the intensity on scattering vector is implicit by the subscript  $p$  for peak position and  $bg$  for background position outside the peak. The simulated background is calculated by the following procedure: The simulated (peak) intensity is  $\tilde{I}_p^s$  with error bar  $\tilde{e}_p^s$ , where the superscript denotes *simulated*. We are then to calculate the background level  $I_{bg}^s$  with error  $e_{bg}^s$ . The ratio of the error at the peak position and in the background must be the same for the simulated data as for the measured. Therefore the error of the background to be added to the simulated data is calculated as  $e_{bg}^s = \tilde{e}_p^s \frac{e_{bg}^m}{e_p^m}$ . Afterwards, the background intensity is calculated as

$$I_{bg}^s = \tilde{I}_p^s \frac{I_{bg}^m}{I_p^m} + \text{randn} \cdot e_{bg}^s \quad (5.1)$$

where randn is a random number function which picks a number distributed by a Gaussian around 0 with  $\sigma = 1$ . Finally the simulated intensity including background is

$$I^s = I_{bg}^s + \tilde{I}^s \quad (5.2)$$

with error

$$e^s = \sqrt{(e_{bg}^s)^2 + (\tilde{e}_p^s)^2} \quad (5.3)$$

### 5.3 Overview of the V-RITA-II instrument

The McStas code for the V-RITA-II instrument is included in appendix C. It is based on a simple model made by Stine N. Klausen and Kim Lefmann primarily used only up to the sample position. The present model includes heavy extensions and detailed changes in order to make the model comparable to physical experiments.

In general I have tried to separate the huge amount of parameters into two types: Ones which might be changed during an experiment e.g. during a scan and these are declared in the `DEFINE INSTRUMENT` header. And the other type that are generally describing physical properties and remain constant through the experiments which are declared in the `DECLARE` section. The values of some of the last type of parameters are calculated from the values of other parameters in the `INITIALIZE` section. Examples are the curvature angle of the monochromator and the position of the coarse collimator blades. Wherever possible I have used the same name of the variables as in the physical RITA-II.

The `TRACE` section contains the components of the instrument. The instrument is divided into a primary part which ends just before the monitor and a secondary part which covers the rest of the instrument. In the primary part, the neutron propagates from the source, down the guide section, reflects from the vertically focusing monochromator and passes through a collimator. There is an option to take out the neutron trajectories to be (re)used in a virtual source or by a `SPLIT` keyword just before the monitor.

In the secondary part the neutron propagates to the monitor, passes through a slit and scatters off a Plexiglass attenuator (if inserted) to hit the sample. The neutrons scattering from the sample pass through a slit to a radially collimating Be-filter (if inserted) and through a double slit that simulates the shielding of the detector bank. The neutrons that are reflected from either of the seven analyser blades pass through a coarse collimator which is designed to remove cross-talk from analyser blades and finally hits the PSD detector which is divided into seven electronic windows. In V-RITA-II the electronic windows are simulated by seven separate PSD-type monitors.

I have divided the components into parts described in the following sections of this chapter: Source, guide-section, monochromator, collimators, samples, filter, analyser and detector. The separate parts of V-RITA-II are tested in the following sections, and the setup described by the main optics the neutron passes on its way through the instrument. For example MF(5meV)-40min-mon-D-Ge-D-radBe-AI(5meV)-PSD means the **M**onochromator is in **F**ocusing mode with primary energy 5 meV. From the monochromator the beam passes a 40' collimator on the way to the monitor and then a **D**iaphragm slit before hitting the **G**e sample. The neutrons that scatter from the sample in the appropriate direction then pass through another **D**iaphragm slit and through the **r**adially collimated **B**e filter to hit the **A**nalysers which is in **I**maging mode and scatters 5 meV neutrons to the **P**SD. The diaphragm slits setting are denoted by MS (slit after monochromator) and SS (slit after sample) followed by L, R, T, B for left, right, top, bottom, respectively.

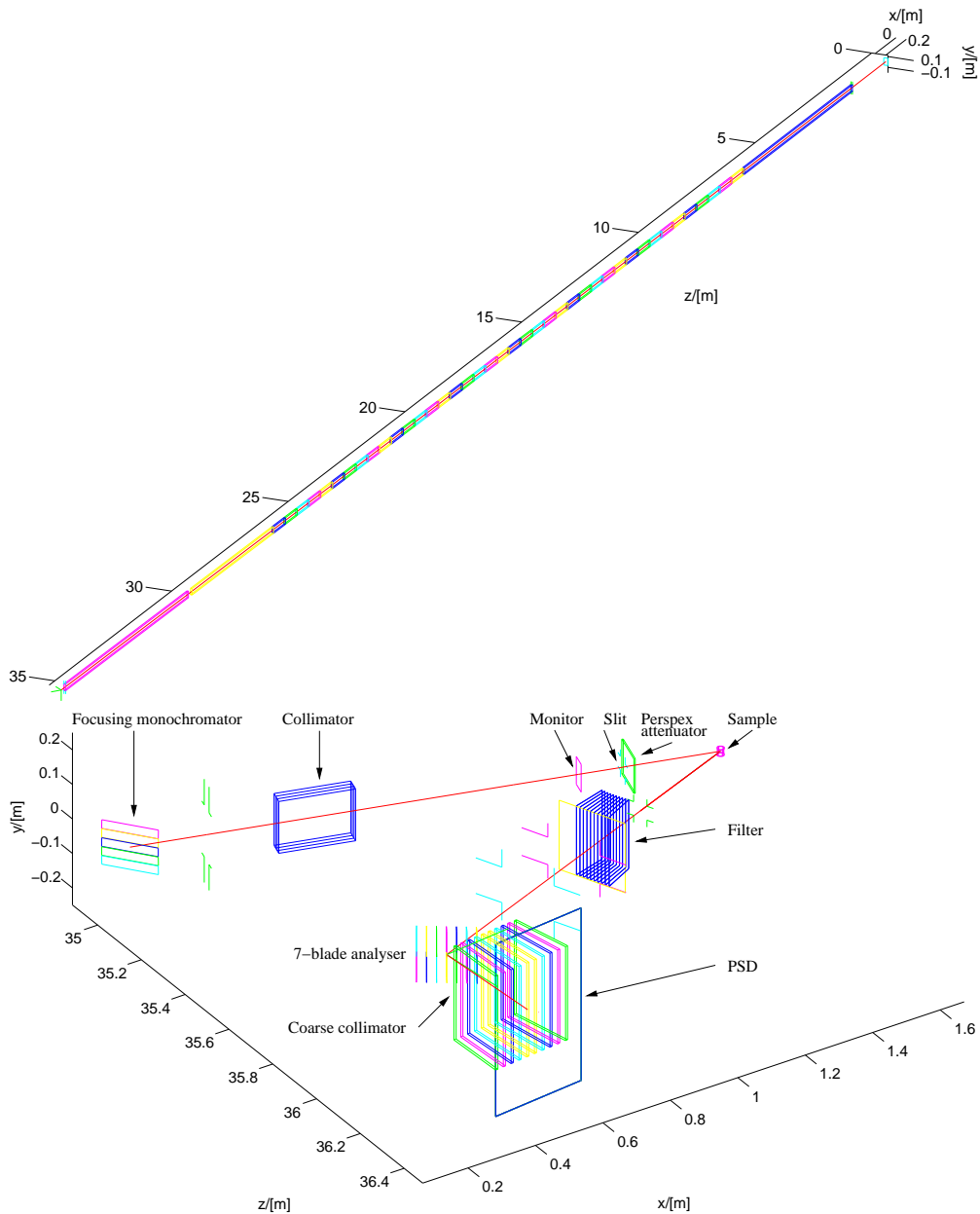


Figure 5.1: The V-RITA-II instrument. The guide system leading from the cold source to the neutron TAS is shown at the top. In the bottom part of the figure RITA-II is shown blown up at another angle for better overview.

## 5.4 Source

At the SINQ spallation source a continuous beam of neutrons are produced. Some of the neutrons are moderated by liquid deuterium to form the so-called cold neutron source which feeds the RITA-II instrument among others. A drawing of the target station is shown in Figure 5.2. The SINQ target was briefly updated to the MEGAPIE target (August-December 2006) but it has now re-

turned to the original target. The intensity of neutrons coming from the target has been improved over the years and therefore absolute intensities cannot be simulated very precisely. The same source with the same parameters will however be used for all the virtual experiments regardless of the date the physical experiments were performed. In the future Au-foil measurements before the monochromator will be made in order to compare absolute intensities. The best current description (for  $L_{\min}=0.1$   $L_{\max}=10$ ) of the cold source made by Uwe Filges is

```
/* 2007 spectrum at source window */
COMPONENT source = Source_gen4 (
  h = 0.135, w = 0.08, xw = 0.03, yh = 0.12,
  dist = 1.465, Lmin=lmin, Lmax=lmax,
  T1=301.287, I1=(1.27e13/4/PI),
  T2=105.655, I2=(3.818e12/4/PI),
  T3=25.379, I3=(2.331e12/4/PI),
  HETailA=8.306e11/4/PI, HETailL0=-0.398)
AT (0,0,0) RELATIVE armSource ROTATED (0,0,0) RELATIVE armSource
```

The source intensity is normalised to 1 mA proton current hitting the target. It is seen that a substantial part of the neutrons are thermal ( $T_1=301.287$ ,  $I_1=\frac{1.27 \cdot 10^{13}}{4\pi}$ ), but the guide transmits a higher fraction of the cold neutrons. In order to make the simulations more efficient the BPH and BPL parameters have been introduced which control the bandpass generated by the source. Only rays with wavelength  $\lambda$  between  $L_{\min}=BPL \cdot l_0/MONO\_N$  and  $L_{\max}=BPL \cdot l_0/MONO\_N$  are traced from the source, where  $MONO\_N$  is the order of the monochromating reflection and  $l_0$  is the primary wavelength chosen by the monochromator scattering angle. The primary wave length is always 4.045 Å corresponding to 5.00 meV in the remainder of this chapter and Chapter 6, unless explicitly stated otherwise.

## 5.5 Guide-section

The geometry of the guide system was recently thoroughly investigated by Jonas O. Birk and I have implemented the data in the V-RITA-II model. The guide system, the simulated as well as the physical, primarily consists of a 'curved guide' made from 40 straight Guide components of dimensions  $0.03\text{m} \times 0.12\text{m} \times 0.5\text{m}$  each of which is rotated slightly with respect to the previous. The main change to the RITA-II model of Stine Klausen [133] in this part of the instrument was an addition of two straight guide segments of 3.45 m and 5.2 m respectively with a 0.15 m gap between them after the 40 curved guide segments. There were also minor adjustments of the mirror parameters to  $R = 0.88$ ,  $R_0 = 0.995$ ,  $Qc = 0.0217$ ,  $W = 1/334$ ,  $M = 2.15$  giving  $\alpha = (R_0 - R)/(Qc * (M - 1)) = 4.61$ .

Gravity has not been implemented in the simulations since the effect is insignificant for these experiments as will be explained below. At the detector

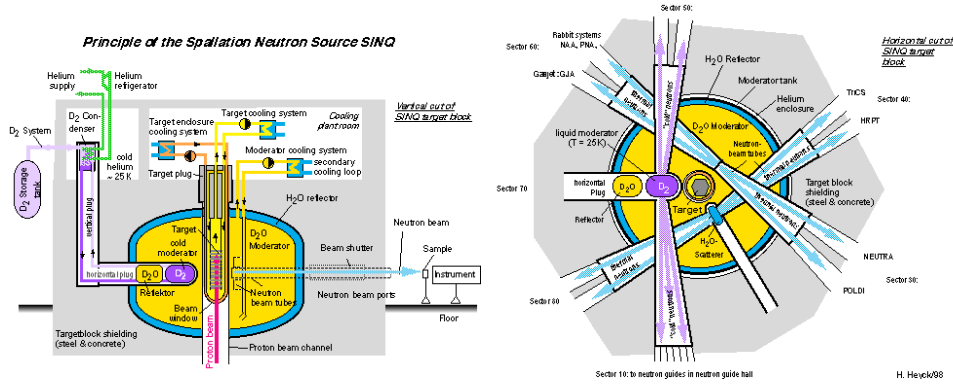


Figure 5.2: Schematic drawing of the SINQ spallation target at PSI. (Left) Side view of the target station. The protons are ejected vertically to hit the target. The guide system of RITA-II 'looks' at the cold moderator (purple). (Right) Top view of the target station. The guide to RITA-II is connected to the bottom purple cone. From [132].

all simulated neutrons have energies above 5 meV. During a free fall along the 35 m guide length 5 meV neutrons drop 6 mm, but will be reflected from the guide walls. The drop scales by  $v^{-2}$  where  $v$  is the velocity of the neutron, hence neutrons with higher energies drop even less. It is seen in Figure 5.3 (top) that the intensity distribution at the guide end without gravity is homogeneous without gravity. If gravity had been implemented those neutrons in the bottom part of the no-gravity-guide which have passed without reflection would simply be reflected before the gravity-guide end thus leaving a homogeneous beam at the end of the gravity-guide similar to the non-gravity-guide. After leaving the guide the neutron at most pass through the entire RITA-II instrument which is about 3 m from the monochromator. During this distance the neutrons drop 50  $\mu\text{m}$  due to gravity which is insignificant compared to the size of the beam, sample and components. Thus gravity has not been implemented in any of the simulation in this thesis work. The divergence distribution in Figure 5.3 is slightly shifted to the positive x due to the curvature of the guide to the left-hand side downstream. The wavelength and energy distribution of the white beam at the end of the guide is shown in the bottom part of Figure 5.3.

Using  $L_{\text{min}}=0.101\text{\AA}$  and  $L_{\text{max}}=101\text{\AA}$  corresponding to energies between  $8.0\mu\text{eV}$  and  $8.0\text{eV}$ , the simulated flux at the end of the guide system is  $\Phi = \frac{1.38 \cdot 10^{10} \text{ n/s}}{(3 \cdot 12) \text{ cm}^2 \cdot 2 \cdot \text{mA}} = 3.81 \cdot 10^8 \frac{\text{n}}{\text{s} \cdot \text{cm}^2 \cdot \text{mA}}$ . This value is within 2% of the simulated and measured flux in 2002 of  $3.74 \cdot 10^8 \frac{\text{n}}{\text{s} \cdot \text{cm}^2 \cdot \text{mA}}$  for the same source wavelength interval [133]. The intensities just before the monochromator are shown in Table 5.1 for various bandpass (BP) values of the source.

## 5.6 Monochromator

The monochromator can be translated inside the housing but we used it in untranslated setting and it is hence placed 35.08 m from the source, and 0.15

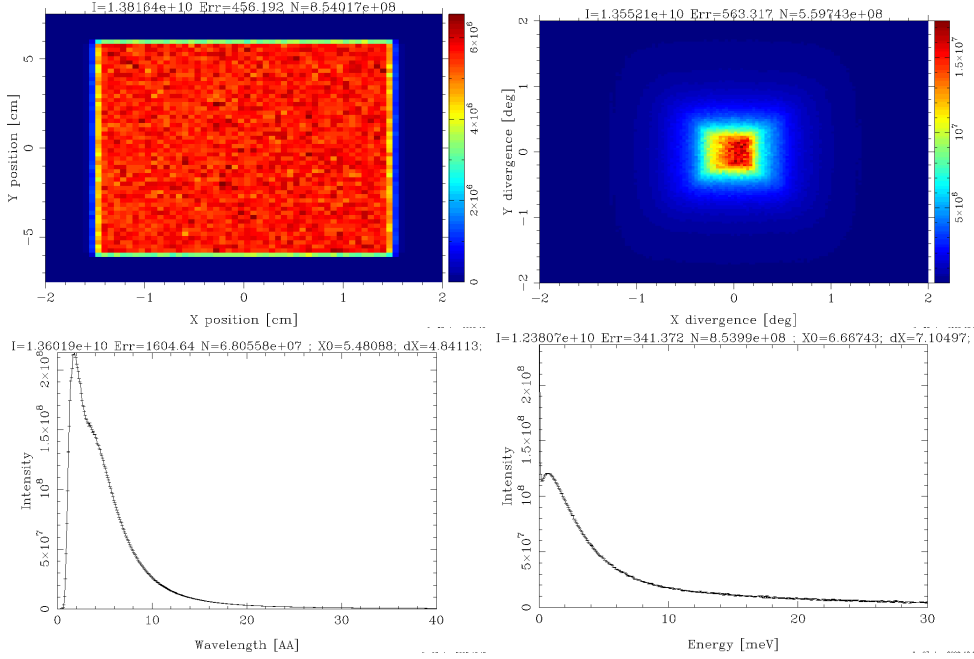


Figure 5.3: A simulated PSD image(top left), divergence monitor (top right) and wavelength monitor (bottom left) and energy monitor (bottom right) of the beam just before the monochromator using BP 0.01-10 ( $\lambda=0.405-40.5\text{\AA}$ ) for the source. Gravity not implemented.

BP	$\lambda[\text{\AA}]$	Energy [meV]	$I_{\text{psd\_guide\_end}}$ [cts/(s*cm <sup>2</sup> )]
0.95-1.05	3.84-4.25	4.53-5.55	$2.01 \cdot 10^7$
0.45-1.05	1.82-4.25	4.53-24.7	$1.41 \cdot 10^8$
0.1-1.05	0.405-4.25	4.53-500	$1.94 \cdot 10^8$
0.1-10	0.405-40.5	0.0500-500	$3.78 \cdot 10^8$
0.01-10	0.0405-40.5	0.00500-500	$3.78 \cdot 10^8$
0.025-25	0.101-101	0.008-8000	$3.81 \cdot 10^8$

Table 5.1: Table of the simulated intensity for various limits of the source wavelength

m after the end of the guide system. There is a small uncertainty of a couple of centimetres in this length since it was not possible to retrieve drawings of or measure the distance and it was estimated from photographs.

The monochromator is made from 5 slabs of PG, each modelled by the `monochromator_flat` component, in order to be able to monochromatise and vertically focus the beam from the guide onto the sample. The wavelength(s)  $\lambda_i = \frac{2\pi}{|\mathbf{k}_i|}$  of the beam after the monochromator is decided by the Bragg condition  $n\mathbf{Q} = 2\mathbf{k}_i \sin \theta_M$  where  $|\mathbf{q}|$  is the value of the Q parameter which is put to 1.87325 appropriate for the PG (002) reflection. A primary wavelength  $\lambda$  is selected by the value of  $\sin \theta_M$  but the beam also contains contributions from higher order scattering ( $n > 1$ ) so  $\lambda_i \in \left[\frac{\lambda}{n}\right] = \left[\lambda, \frac{\lambda}{2}, \frac{\lambda}{3} \dots\right]$  with the same setting of  $\sin \theta_M$ .

In the simulations assuming the neutron-rays coming from the guide are

parallel, the focusing angle  $u$  is found from

$$\sin u = \frac{\sin v}{2 \sin \theta_M} \quad (5.4)$$

where  $\tan v = h/L_1$  and  $h$  is the vertical distance between the centre and neighbouring focusing slab and  $L_1$  is the distance from the monochromator to the sample, see Figure 5.4.

The `Monochromator_flat` component assumes the PG crystal to be infinitely thin which means that multiple scattering effects are not simulated. It also means that the reflectivity  $r_0$  is used as a parameter for the scattered neutron weight rather than the atomic scattering cross section. This implies that the scattering efficiency does not vary with neutron wavelength or the order of the reflection which might not be a very good approximation in physical experiments on real monochromator crystals. For ideally imperfect crystals the integrated intensity for example is proportional to the wavelength cubed, see Equation (3.9).

A list of measured reflectivity for first order scattering from the (002) reflection of pyrolytic graphite as function of wave vector is available at the McStas website[134] (a similar curve is found in [135]) and in this list the reflectivity at 5 meV is 0.81 while it is 0.63 at 20 meV. A fixed value of  $r_0=0.8$  is implemented in my V-RITA-II model as most experiments are performed at this energy and the simple `monochromator_flat` component which is used for each slab of the monochromator does not take a reflection list as input.

The `Monochromator_flat` component assumes the variance of the lattice parameter to be zero, but it has input parameters for horizontal and vertical mosaicity, both of which are orthogonal to the scattering vector. The producer of the slabs lists the mosaicity as 37' in this plane and both mosaicity parameters (assumed to be similar to the intrinsic mosaicity) are put to this value. The simulated beam profile and energy spectrum just after the monochromator is shown in Figure 5.5.

## 5.7 Collimators

The RITA-II instrument has a choice of four linear collimators (10',20',40' or 80') to be placed immediately after the monochromator. They are simulated by the `Collimator_linear` component in V-RITA-II. The exact collimation parameter to be used in the McStas version of three of the collimators is found by VE in Section 5.14.

RITA-II has a special feature of seven analyser crystals and in order to remove the cross-talk between them a coarse collimator has been incorporated which is basically an adjustable radial collimator. The present coarse collimator is an improved version of the one investigated in [136]. It is attached in front of the PSD and made by 10 vertical neutron absorbing plates (B-Al) each of which is 7 mm thick. The eight central plates are used to define the beam from each of the seven analyser blades, and the outer two plates have been incorporated to allow for an expansion of the seven-blade analyser to a nine-blade analyser. The collimator is divided into a left and right part, each consisting of 5 plates.

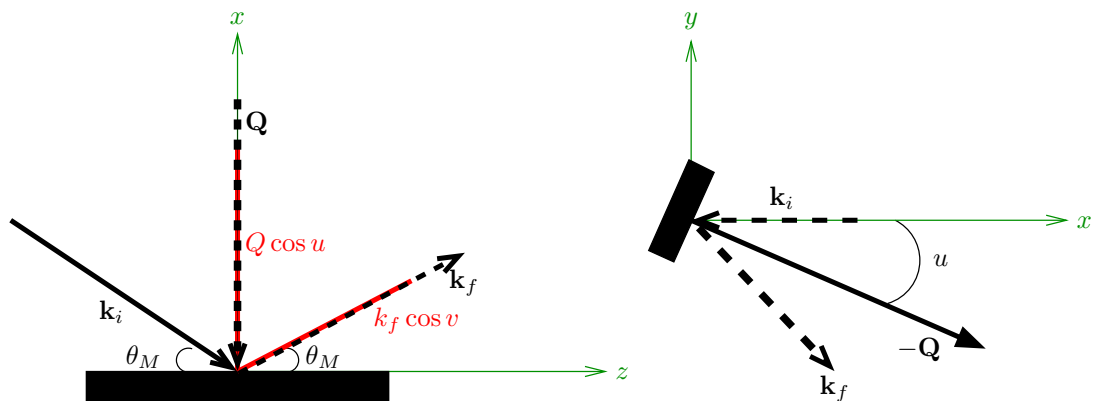


Figure 5.4: Focusing geometry of the monochromator in McStas coordinates. (Left) Top view, the incoming wave vector  $\mathbf{k}_i$  is assumed to be in the  $(z, x)$  plane and the scattered ray is into the paper. The red lines are the projections of the scattering vector  $\mathbf{Q}$  and outgoing wave-vector  $\mathbf{k}_f$  onto the  $(z, x)$  plane. The angle  $v$  described in the text (but not shown in the figure) is the angle between  $\mathbf{k}_f$  and the  $(z, x)$  plane. (Right) Side view, the scattering vector is in the  $(x, y)$  plane of the paper while the incoming and outgoing vectors marked by dashed arrows are out of the plane of the paper. The angle between the scattering vector  $\mathbf{Q}$  and the  $x$ -axis is  $u$ .

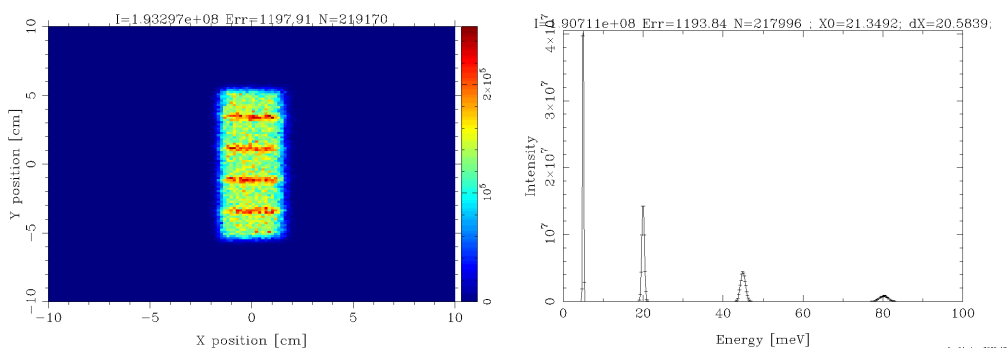


Figure 5.5: A simulated PSD image and energy monitor of the beam just after the monochromator using BP 0.01-10 for the source.

The end of the plates closest to the analyser can move at gearing 1:3:7:9 through the parameters LC (left collimator) and RC (right collimator) respectively. It is modelled in V-RITA-II by 10 Absorber slabs with same dimensions and gearing but the values of LC and RC cannot be directly transferred. In V-RITA-II they are simply the size of the angle between the outer plates and the plane which incorporates the centre of the middle analyser blade and the centre of the detector. The outer plate is then rotated by  $9 \cdot LC/9$  and the others moved accordingly by  $7 \cdot LC/9$ ,  $5 \cdot LC/9$ ,  $3 \cdot LC/9$  and  $LC/9$  respectively and similar for RC but with a negative sign. The optimal values of LC and RC are determined through an iterative procedure described in Section 5.13

## 5.8 Samples

At the sample position (1.54 m downstream from the monochromator in the normal setting and without collimator) the integrated beam intensity for 5 meV neutrons is reduced to  $3.62 \cdot 10^6 \frac{n}{s \cdot mA}$  in the central  $1 \text{ cm}^2$  part of the beam. This matches the measured and simulated values found in [133] within 3% which also referred only to the first order scattered neutrons from the monochromator. The beam is distributed over an area of  $\pi * 3.6^2 \text{ cm}^2$  as shown in Figure 5.6.

When looking at the semi-monochromatic beam which also includes higher order scattering the average flux through this area is  $3.1 \cdot 10^6 \frac{n}{s \cdot \text{cm}^2 \cdot mA}$ . Recent gold foil measurements by Uwe Filges on the un-filtered beam from the monochromator found  $3.27 \cdot 10^6 \frac{n}{s \cdot \text{cm}^2 \cdot mA}$  in the central 10 mm diameter part of the beam for focussed monochromator at 5meV setting. In comparison the simulated flux through a similar cross-section of the beam is  $1.11 \cdot 10^7 \frac{n}{s \cdot \text{cm}^2 \cdot mA}$  when allowing also for higher order scattering from the monochromator. As discussed in Section 5.6 the overestimated intensity by McStas is probably due to the `Monochromator_flat` component which is used in the description of the focusing monochromator. As discussed in Section 6.5 the reflectivity of PG(002) is  $\sim 0.8$  at 5 meV and  $\sim 0.6$  at 20 meV but this does not explain the factor of 3 higher simulated intensity at the sample position than measured when including higher order neutrons.

In most experiments higher order neutrons are however not passed to the detector so the simulated intensity should match the measured one in most virtual experiments.

The simulated flux at the sample position for various collimations between monochromator and sample are shown in Table 5.2.

The sample environment was not simulated and all samples were approximated by boxes or cylinders. In the next release of McStas (v2.0) a description file containing information of the surface geometry of the sample generated from the Geomview 3D visualisation programme can be read into any sample component to generate an exact replica of the sample geometry.

### 5.8.1 Incoherent scatterer

A standard incoherent scatterer such as vanadium or Plexiglas is used on RITA-II in order to set up the various modes of the analyser. In the virtual experiments they are both simulated by the isotropic elastic incoherent scat-

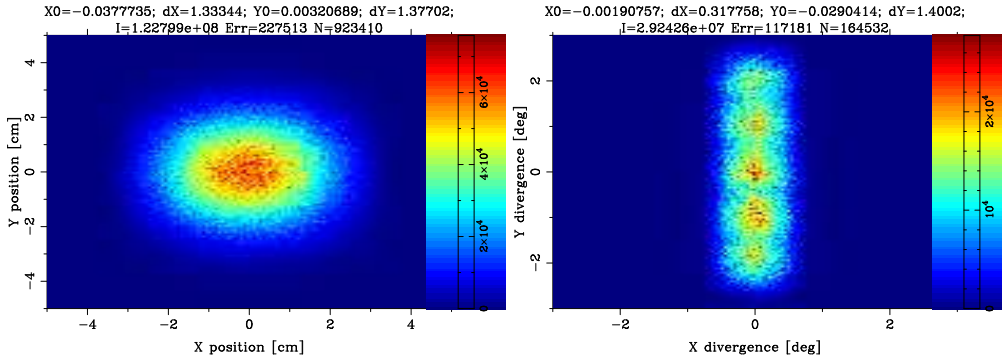


Figure 5.6: A simulated PSD image and divergence monitor of the beam at the sample position using BP 0.01-1.05 for the source and no collimation or filter before the sample position.

Collimation [min]	$I_{\text{psd\_sample\_pos}}$ [cts/(s*cm <sup>2</sup> )]
Open	$1.0 \cdot 10^7$
79.2	$8.2 \cdot 10^6$
39	$6.1 \cdot 10^6$
19.6	$3.6 \cdot 10^6$
9.7	$1.8 \cdot 10^6$

Table 5.2: Table of the simulated flux at the sample position through the  $2 \times 2\text{cm}^2$  central sample area for various collimations after the monochromator. All simulations used BP 0.01-1.05 ( $\lambda=(0.405-4.25\text{\AA})$ ). The beam has a radius of  $3.6\text{cm}^2$  which can be seen by logarithmic plotting if the intensity (not shown).

terer `V_sample` component with appropriate incoherent- and absorption cross-section. The default values of the incoherent and absorption cross-sections are valid for vanadium. I have calculated the appropriate values for Plexiglass ( $\text{C}_5\text{O}_2\text{H}_8$ )<sub>n</sub> from the density ( $1.19\text{g/cm}^3$ ) to be  $\sigma_{\text{inc}}=4.7\text{ barns/\AA}^3$  and  $\sigma_{\text{abs}} = 0.019$ . The coherent scattering ( $\sim 10\%$  for large scattering angles) is not simulated.

There is an option to focus the tracing from the `V_sample` to a selected area with radius `focus_r` in a specific direction downstream indicated by the index of a component (`target_index`) counting from the `V_sample`.

Besides use as a sample, sheets of Plexiglas are also used just before the sample to attenuate the beam in order not to saturate the detector with e.g. Bragg peak scattering from the sample.

## 5.8.2 Powder

A standard sapphire pressed powder sample is frequently used at RITA-II to find the zero-point of the scattering angle and calibrate the energy. In the virtual experiments it is simulated by the `PowderN` sample component which takes a reflection list as input. The list can be generated by e.g. `Crystallographica`, `Lazy` or `Fullprof` and should contain columns with  $h, k, l, j, d, F^2$  where  $j$  is the multiplicity,  $d$  is the d-spacing and  $F$  is the structure factor of the reflection  $(h, k, l)$ . The `PowderN` sample also takes the incoherent- and absorption

scattering cross-sections into account but does not model multiple scattering. Information about the lattice parameters and number of atoms in the unit cell also needs to be entered. Besides these a range of other parameters such as the Debye-Waller factor and relative line width ( $\Delta d/d$ ) can be entered or taken from the header of the reflection list file.

### 5.8.3 Single crystal

The main goal with building and testing the V-RITA-II is in order perform do virtual experiments on idealised single crystals (called virtual samples) and compare them with physical experiments on real crystals. The `Single_crystal` component models a thick, flat single crystal with elastic coherent scattering and multiple scattering. An elastic isotropic incoherent background and absorption in the crystal can also be simulated. To simulate the Bragg reflections `Single_crystal` takes in a crystal reflection list with  $F^2$  in barns ( $10^{-24}\text{cm}^2$ ) and this is corrected in the reflection list generated by Crystallographica which has the unit  $\text{fm}^2$ . Mosaicity is modelled by an isotropic Gaussian broadening perpendicular to the scattering direction (the `mosaicity` parameter). The mosaicity  $\eta$  is defined as the standard deviation  $\sigma$  of a Gaussian distribution of mosaic blocks. It is measured by an `a3` scan which is fitted to a Gaussian with  $\text{FWHM}=\sigma\sqrt{8\ln 2}$ . The effect of mosaicity on the peak width is shown in Figure 5.7. The uncertainty in lattice spacing is modelled by a Gaussian broadening along the scattering vector (the `deltad_d` parameter).

The sample environment such as a cryostat was not implemented in the simulations.

When using a single crystal sample the virtual experiment can be controlled by the value of the Miller indices ( $HKL$ ) of the sample as explained in Section 5.12.

## 5.9 Filter

In the experiments where it is desirable to filter out the higher order energies from the scattered beam a Bragg-scattering filter is often used. It consist of a powder which Bragg scatters most of the neutrons below a cutoff  $\lambda_{cut} = 2d_{max}$  where  $d_{max}$  is the largest d-spacing of the powder. Due to the powder the beam will for  $\lambda < \lambda_{cut}$  be scattered in a Debye-Scherrer cone away from the main beam direction. The filter is therefore transparent only to  $\lambda > \lambda_{cut}$  or analogously  $E < E_{cut}$  as seen in Figure 5.8. Two types of powder filters are generally available for cold neutrons, a Be filter with  $E_{cut} = 5.24\text{meV}$  and a BeO filter with  $E_{cut} = 3.74\text{meV}$ . A final energy is most often chosen close to (but below)  $E_{cut}$ . In V-RITA-II a radial Be filter is used in imaging-mode at  $E_f = 5.0\text{ meV}$ . This is simulated by two components: The `Filter_gen` component and the `Exact_radial_coll_fix` component<sup>1</sup>. It is worth to note that powder filters need to be cooled in order to transmit neutrons below  $E_{cut}$

<sup>1</sup>the `Exact_radial_coll` is a contributed component by Roland Schedler. I have fixed a minor bug in this component.

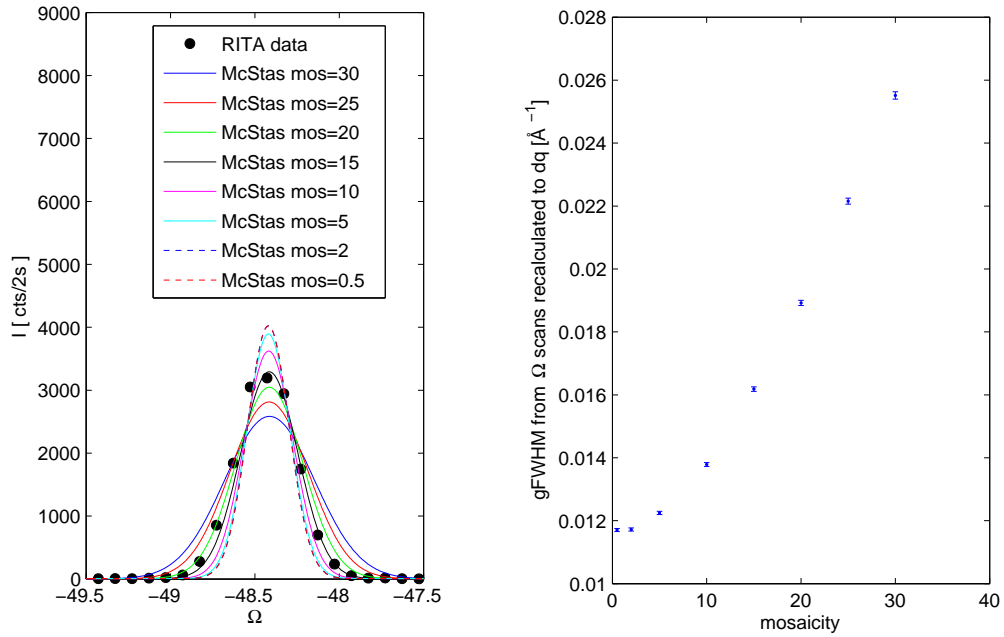


Figure 5.7: (Left) Measured rocking curve through a fundamental Bragg peak of a single crystal (black points) and simulated rocking curves using different mosaicity parameter. It is seen that `mosaicity=15` fits the data well. (Right) The fitted FWHM converted to reciprocal lattice units converges, as expected, by decreasing mosaicity

efficiently since cooling reduces the amount of inelastic scattering by phonons. The `Filter_gen` component reads in a transmission file recorded for this particular radial Be filter when cooled to  $\sim 80$  K.

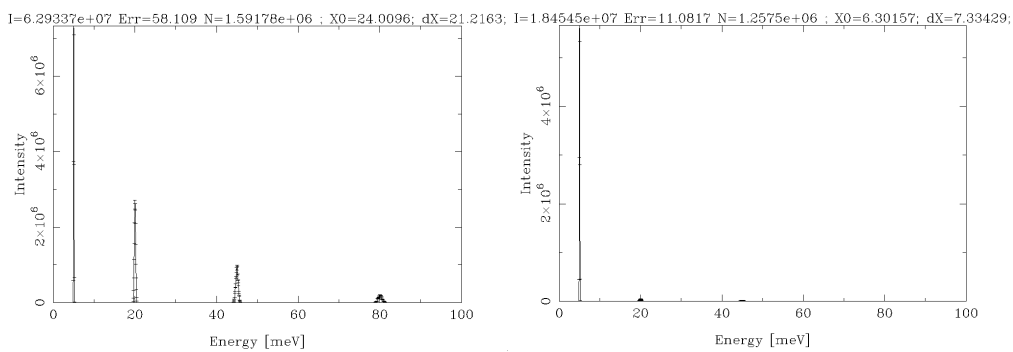


Figure 5.8: The simulated effect of a Be filter. To the left the energy distribution after the monochromator with  $2\theta_M = 74.15^\circ$  is shown without a filter, to the right the radial Be filter has been inserted. The position of the monitors is approximately 2 m downstream from the focusing monochromator.

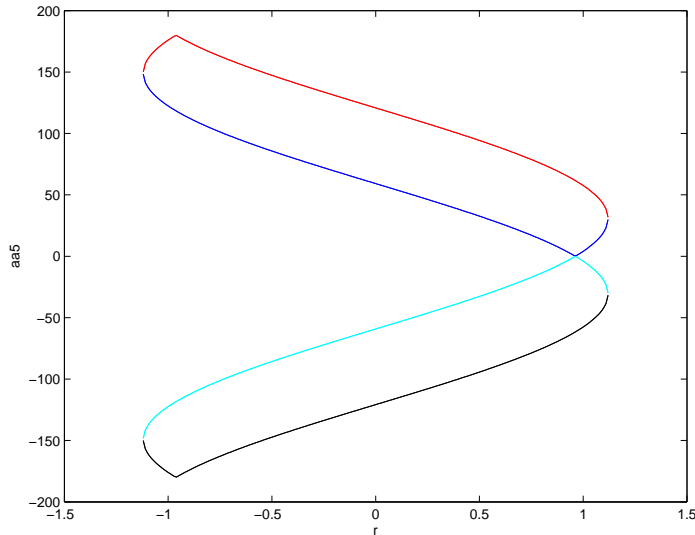


Figure 5.9: The solutions to Eq. 5.5 from which  $\Omega_A$  is calculated.

## 5.10 Analyser

The principle of the analyser is the same as the monochromator and in RITA-II it is also based on the PG(002) reflection, like the monochromator. The analyser is however made from 7 blades with individual rotation motors called ca2-ca8 which rotate around the vertical direction ( $y$  in McStas coordinates). Due to the name of their motors they are called blade 2-8 respectively. They are set in a rack which rotates by the motor aa5 which is also known as  $\Omega_A$ . Until 2006 each blade consisted of two PG slabs, top and bottom part respectively. After 2006 blades 4,5,7,8 has had alterations, the main alteration being replacing the two slabs on blade 5 by a large slab in the centre and two smaller slabs at the top and bottom edges.

### 5.10.1 Analyser angle

From [137] the optimal analyser rack angle is calculated by

$$\cos \Omega_A = \frac{r \sin 2\theta_A \pm (\cos 2\theta_A + R)\sqrt{1 - r^2 + R^2 + 2R \cos 2\theta_A}}{1 + R^2 + 2R \cos 2\theta_A} \quad (5.5)$$

Where  $R=(0.338+0.0215)/1.195$  is the ratio between the distance from analyser to detector<sup>2</sup> and analyser to sample and  $r$  is the ratio between the distance between the interception points at the detector and the distance between the analyser blades. The value  $r=1$  is chosen as the smallest reasonable value due to beam divergence, and the only meaningful solution to 5.5 at this value is  $aa5 = \Omega_A = -57.58$  as is seen in Figure 5.9<sup>3</sup>.

<sup>2</sup>the distance measured to the front of the detector is 0.338m, from drawings there is 0.0215m from the front to the first detection wire

<sup>3</sup>at RITA-II the angle of the analyser rack is called aa5 not a5 as in the single analyser setup described in Section 3.1.2

### 5.10.2 Analyser mosaicity

Two experiments with matching virtual experiments have been performed in order to estimate the mosaicities of the PG slabs of the 7 analyser blades. In one experiment from 2008 we used a Ge wafer as sample, and the other used the direct beam and was carried out by Ch. Niedermayer before 2006.

#### Direct beam measurement of analyser mosaicity

The direct beam was used to measure the mosaicities of the individual PG pieces of the analyser. Setup was MF(8meV)-20min-8.7mmplexi-mon-D-D-open-singleAna(8meV)-PSD. By moving a4 an appropriate amount for each blade on the analyser rack to be hit by the direct beam, rocking curves of each analyser blade were performed, covering the top/bottom part with neutron absorbing material in order to measure each part of the blade at a time. A similar setup has been used in a virtual experiment to assign the values of mosaicitities in the RITA instrument which give the closest resemblance to the physical instrument.

The experimental data actually reveals a small Lorentzian component with FWHM of several degrees but the integrated intensity never exceeds 10% of the Gaussian contribution. This contribution might originate in thermal diffuse scattering from the graphite or from a partially Lorentzian mosaic distribution. Since mosaicity in the `monochomator_flat` component in McStas is strictly Gaussian the mosaicity has been found by matching the FWHM of the Gaussian part of the experimental data to Gaussian FWHM of the McStas data. The fits are shown in Figure 5.10 and values of the corresponding McStas mosaicity input to the `Monochromator_flat` component are listed in Table 5.3.

The simulations used BP 0.95-1.05 i.e. only neutrons with energy close to 8 meV were simulated whereas in the physical experiment also higher order neutrons passed to the detector. Later it was checked that including higher order neutrons in the simulations only changes the simulated mosaicity up to 5% on each analyser blade.

The 8.7mm Plexiglas in the beam was also not simulated at this stage of building V-RITA-II, hence the simulation data in Figure 5.10 have been scaled by a factor 0.007. Later on it was however checked that when the 8.7mm Plexiglas was inserted the simulations needed only a scaling factor of 0.2. The widths of the rocking curves were the same with the Plexiglas inserted within 5%. The simulated intensity in blade 8 is smaller than the measured since the slit setting MSR=MSL=25 apparently cuts off a small part of the beam at analyser blade 8. In the physical experiment the real slit setting might have been slightly different, and the mosaicity found by the virtual experiment uncertain.

2l	2u	3l	3u	4l	4u	5l	5u	6l	6u	7l	7u	8l	8u
38.7	43.0	31.1	35.5	27.2	30.4	36.6	35.9	31.5	36.1	33.1	37.2	46.8	51.3

Table 5.3: Mosaicities of the analyser in arc minutes as found by matching the virtual experiment to the direct beam measurements. Each analyser blade is listed by the number of the ca-motor and 'u' for upper PG slab 'l' for lower

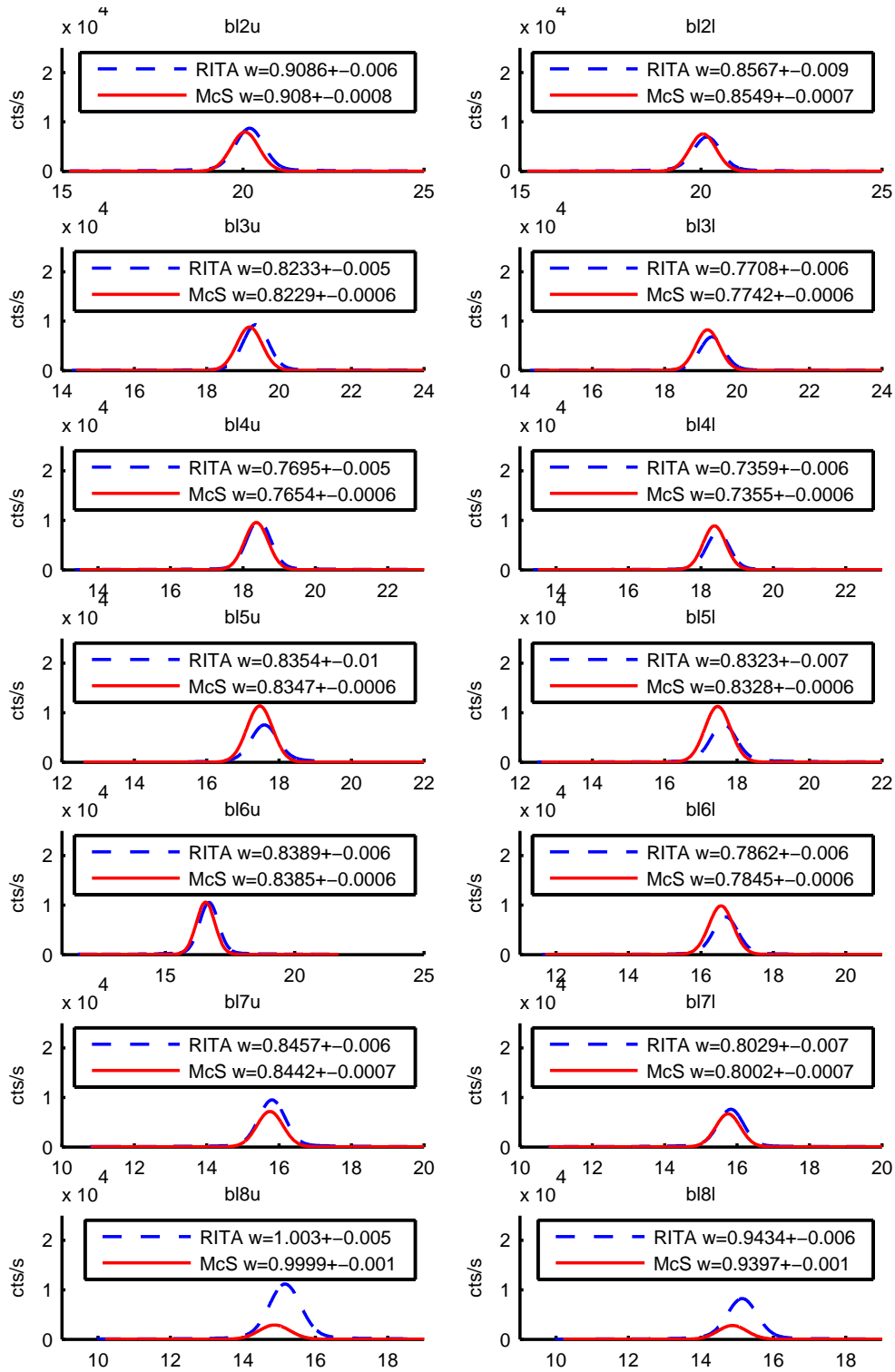


Figure 5.10: Simulations and rocking curves of the 7 blades in the direct beam setup, the upper and lower part is irradiated separately and shown on separate curves. Blue lines are fits to physical experimental data, red lines are fits to the virtual experiments.

### Ge-wafer measurement of analyser mosaicity

In the attempt to get another and newer measurement of the mosaicity of the analyser PG slabs, we used a Ge wafer as sample and the setup was MF(5meV)-40min-mon-D-Ge\_wafer-D-radBe-AI(5meV)-PSD. The diaphragm slits were set to MSL=15 MSR=15 MST=25 MSB=25 SSL=25 SSR=30 SST=40 SSB=40.

The scattered beam from the Ge (111) reflection was tilted by  $g_u=-1$  to hit only the upper part of the analyser blades and  $g_u=3$  to hit only the lower parts of the blades. The angle of each blade was scanned separately using the proper  $a_4$  value to hit that particular blade with the Ge (111) reflection.

The wafer has practically no mosaicity so the scattered beam is highly collimated and monochromatic. Hence the idea was that the width of the ca2-ca8 scans could be taken as the actual mosaicity of each analyser blade. The data are shown in Figure 5.11. However, Gaussian fits do not match the data very well since there is also a Lorentzian component judging from a much smaller  $\chi^2$  in fitting with a Lorentzian+Gaussian. The Lorentzian component is in many cases up to 50% as seen from the components of the fits in Figure 5.11. Lorentzian tails have previously been observed as mentioned in the previous subsection but with a much smaller amplitude. At present the large Lorentzian contribution in this experiment is not fully understood.

Since at present only Gaussian mosaicities are implemented in the McStas sample and monochromator components I have chosen to use the mosaicities found from the direct beam experiment instead. Most of the experiments on LSCO+O presented in this chapter are also made before 2006 where the results from the direct measurement of the analyser should be applicable.

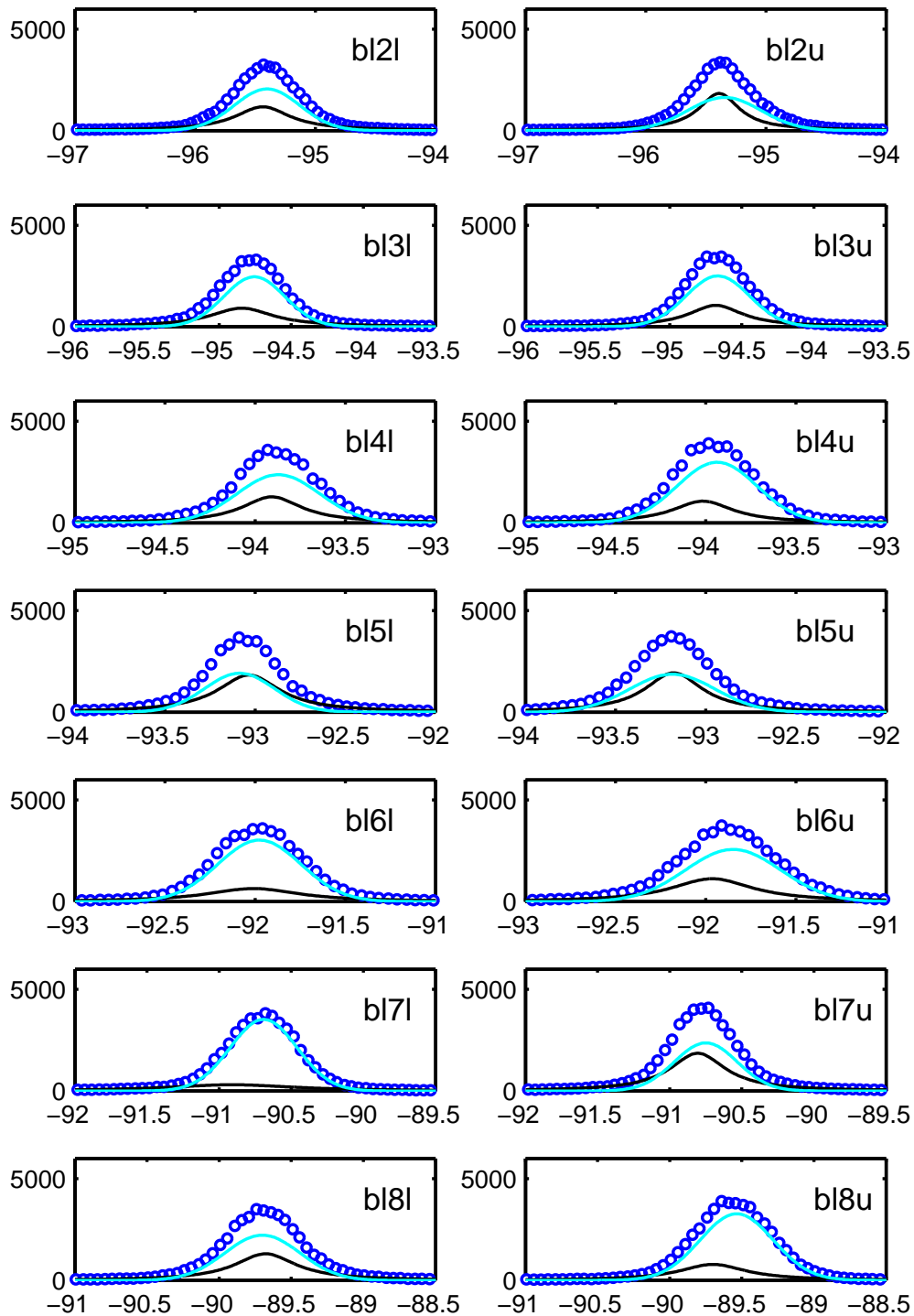
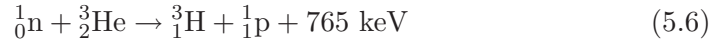


Figure 5.11: Rocking curves of the 7 blades in the Ge wafer setup, the upper and lower part of each blade is irradiated separately and shown on separate curves. Dark blue points are physically measured data, light blue curves are the Gaussian part and black curves the Lorentzian part of the combined best fits to the data.

## 5.11 Detector

The position sensitive detector is a box containing a mixture of  ${}^3\text{He}$  and Ar gas and a electrode wire-grid at high voltage ( $\sim 1.5$  kV). When a neutron enters the detector box, Tritium and a proton is produced by the following process



The process ionises the Ar and the free electron is accelerated by the high voltage towards the electrode wires thus creating a charge cloud in the stopping gas which is then detected by the electrode wires as an electrical pulse. The efficiency of a  ${}^3\text{He}$  gas detector is given by  $\eta \propto 1 - e^{-N\sigma_a d}$  where  $N$  is the number density of the  ${}^3\text{He}$  atoms (regulated by the gas pressure),  $d$  is the thickness of the detector and  $\sigma_a$  is the cross-section for  ${}^3\text{He}$  [138]. The cross-section is inversely proportional to the neutron velocity [139] hence the absorption cross-section of 5 meV neutrons is 2 times larger than for 20 meV. If the efficiency at 5 meV neutrons is 80% the efficiency at 20 meV would be 66%, i.e. a larger portion of the slow neutrons are detected. The PSD has  $128 \times 128$  pixels defined by the crossing of the detection wires which are placed in a grid of 3 layers where each layer have wires along either the x or y direction. The active area is 0.275 m wide (as shown in section 5.13.2) and assumed 0.5 m high making each pixel  $2.15 \times 3.9 \text{ mm}^2$ .

By direct line-of-sight (RITA-II in 2-axis mode the sample-detector distance is 1.555m) from a point source at the sample position the angle that spans the detector is  $10.1^\circ$  which matches a slit setting of  $\text{SSL}=\text{SSR}=30$ . The detector shielding has an opening of  $10.7^\circ$  with respect to the sample position which will cut off intensity from samples which have a larger radius than 1cm.

The detector is divided into areas of detection corresponding to scattering from each blade - the so-called electronic windows.

To simulate the uncertainty in the detected position the neutron hits the detector I have implemented a point spread function (PSF) in the `PSD_monitor_psf` component. After propagation to the surface of the detector a random number from a Gaussian distribution with `psf` as standard deviation is added to the (x,y) position of the neutron. By experiments using a Cd plate perforated by 1 mm diameter holes in front of the detector the FWHM of the PSF was found to be 7.4mm in [136], giving an appropriate value of 0.0031 m for the `psf` parameter.

## 5.12 Controlling the virtual experiment

The virtual experiment in terms of scans is controlled exactly as the real experiment. For some applications the experiment is simply scanning a motor, such as `a1`, and the corresponding motor-parameter (`A1`) is scanned in the virtual experiments. However, when using a single crystal as sample there is the option of controlling the physical RITA-II and V-RITA-II by HKL instead of motor positions. In the virtual experiment this is the so-called Qmode. The Qmode is invoked by assigning a value other than zero to any of the variables `QM`, `QH`, `QK` or `QL`, which correspond to  $|\mathbf{Q}|$  and the Miller-indices of the scattering vector,

respectively. As in the physical experiments, simulations in the Qmode requires the lengths of the lattice vectors (AS,BS,CS), a description of the unit-cell by three vectors (AAX,AAZ,AAZ),(BBX,BBY,BBZ) and (CCX,CCY,CCZ) and the angles between them called CC,AA and BB respectively. One also has to define the scattering plane by two vectors  $\mathbf{A}=(AH,AK,AL)$  and  $\mathbf{B}=(BH,BK,BL)$ . When defining the crystal lattice vectors there is an option to do so in either reciprocal or direct space. Whichever is chosen they should be defined as a right-hand coordinate system by their projections in the McStas local coordinate system. I.e. if the crystal system have orthogonal axes and the  $\mathbf{a}$  and  $\mathbf{b}$  are along the McStas x- and z-axes respectively, then (AAX,AAZ,AAZ)= $(-|\mathbf{a}|,0,0)$ , (BBX,BBY,BBZ)= $(0,|\mathbf{b}|,0)$  and (CCX,CCY,CCZ)= $(0,0,|\mathbf{c}|)$ . Of course one could also choose (AAX,AAZ,AAZ)= $(|\mathbf{a}|,0,0)$ , (BBX,BBY,BBZ)= $(0,|\mathbf{b}|,0)$  and (CCX,CCY,CCZ)= $(0,0,-|\mathbf{c}|)$ , the correct solution depends on which way the crystal was oriented in the physical experiment, i.e. which lattice vectors were defined as  $\mathbf{A}$  and  $\mathbf{B}$  scattering vectors respectively in TASCUM.

The orientation matrix is computed by the TASMAD code by which (AH,AK,AL) is parallel to the incoming neutron wave vector  $\mathbf{k}_i$ , and for an orthorhombic system (BH,BK,BL) is perpendicular to  $\mathbf{k}_i$ . However in TASCUM on RITA-II (AH,AK,AL) is defined to be perpendicular to  $\mathbf{k}_i$  (90 degrees clockwise), making (BH,BK,BL) parallel to  $\mathbf{k}_i$  in the orthorhombic case. This means that e.g. the (HK0) plane is used as scattering plane if  $\mathbf{B} = (1, 0, 0)$  and  $\mathbf{A} = (0, 1, 0)$ , and (H0L) used when  $\mathbf{B} = (1, 0, 0)$  and  $\mathbf{A} = (0, 0, 1)$ .

The incoming and scattered energy is controlled by the EI, EF and EN parameters regardless if the virtual instrument is in Qmode or not. Only two parameters should have a value assigned as the third will be calculated from  $EN = EI-EF$  etc.

If a value other than zero is specified by the user for any of the A2, A4 or A6 variables and the value is not equal to the value calculated by the virtual instrument from the setting of EI,EF and EN, the value of the particular parameter will be overwritten by the user input and the values of EI,EF and EN adjusted accordingly. The values of A1, A3 and A5<sup>4</sup> can however be freely specified by the user. If they are set other than zero they will however still override the values calculated by the virtual instrument from the Bragg conditions etc.

### 5.13 Setting up the imaging mode

The seven blade analyser has the possibility of a broad range of different modes (point-to-point focusing, energy dispersive modes etc.) [140]. One of the preferred modes is however the monochromatic imaging mode with which seven reciprocal space points are measured simultaneously and at the same energy. When the scattering rate from the sample is low the imaging mode can save a lot of time by e.g. measuring points in the peak and background simultaneously. Optimising for the imaging mode is an iterative procedure using an incoherent scatterer such as Vanadium both in the physical RITA-II and V-RITA-II. The procedure in RITA-II is described by a note [141] and command routine called

<sup>4</sup>the A5=  $\Omega_A$  parameter in V-RITA-II corresponds to the aa5 rotation of the analyser rack in physical RITA-II

`cascan_imag.tas` written by C. R. H. Bahl.

In the present simulations, first some default values of the 7 electronic windows W2-W8 are set, 10 pixels wide with 1 pixel in between<sup>5</sup>.

With the calculated value of the optimal rotation of the analyser-rack each analyser blade angle ca2-ca8 is scanned and each ca-motor set to the fitted ca-value of maximum intensity. The detector collimator (RC & LC) is scanned, the LC positions of maximum intensity in electronic window 2 is noted and the RC positions of maximum intensity in electronic window 8 is noted. The RC and LC values is used henceforth and the ca-motors, the RC and LC scanned again until convergence.

### 5.13.1 Finding analyser optimal position

The best fitted values of the mosaicities of the 14 different PG pieces of the 7-blade analyser were found and described in 5.10.2. These values were hard-coded in the instrument file.

RITA-II was used in 3-axis mode by writing 'tasub const kf' and the setup was MV(5meV)-40min-mon-D-Vanadium-D-radBe-AI(5meV)-PSD. The diaphragm slits were set to MSL=10 MSR=10 MST=25 MSB=25 SSL=10 SSR=10 SST=25 SSB=25. The monochromatic imaging mode was set up by scanning the ca-motor of each blade simultaneously and optimising their position. The fitted values and the set-point values of the blade angles are shown in Table 5.13.1. Each angle was driven to the optimal position and put to the set-point value. We removed the coarse collimator and scanned a6 finding an optimal value at 74.5, which was then changed to set-point value 74.16 (=a2).

The pre-set values used in the physical measurements for sample to analyser

Motor	Fitted position	Set-point	Diff	McS pos 1	McS pos 2
ca2	-95.80	-95.43	0.37	-95.85	-97.86
ca3	-94.91	-94.69	0.22	-94.79	-96.80
ca4	-93.92	-93.83	0.09	-93.79	-95.77
ca5	-92.93	-93.01	-0.08	-92.81	-94.75
ca6	-91.96	-91.96	0.00	-91.88	-93.77
ca7	-90.98	-90.68	0.30	-90.92	-92.81
ca8	-89.93	-89.64	0.29	-89.97	-91.83
aa5	-	-55.64	-	-55.64	-57.58
a6	74.500	74.165	-0.335	74.16	74.16

Table 5.4: Analyser angles as scanned and their set-point values. Also tabulated is the McStas simulated, fitted optimum positions of the analyser blades in position 1 where  $\Omega_A = -55.64$  and position 2 where  $\Omega_A = -57.58$ .

distance (dsa) is 1.207m and analyser to detector (dad) is 0.339m, which is slightly different than the values we measured by a ruler (dsa=1.195 dsa=0.363

<sup>5</sup>notice that window 2 is at high x-values and window 8 at low x-values in McStas due to the orientation of the coordinate system. Each PSD monitor of the detector has been rotated 180 degrees around the vertical y-axis in order to get the the pixel-enumeration as in the physical RITA-II

including the distance to the detector wires inside the detector case). Therefore the  $aa5 = \Omega_A = -55.64$  is slightly off the calculated optimal value of  $\Omega_A = -57.58$ . Using one or the other  $\Omega_A$  in the simulation does not change the widths of the scans significantly as can be seen from the plot of the data in Figure 5.12 and 5.13 and I will use the optimal position  $A5 = \Omega_A = -57.58$  in the following virtual experiments.

The simulated scans are generally wider (4-20%) than the measured ones indicating that the mosaicity might be up to 20% overestimated in the simulations. This is probably due to the alterations to the analyser in 2006 as described in 5.10 which are not implemented in the present V-RITA-II.

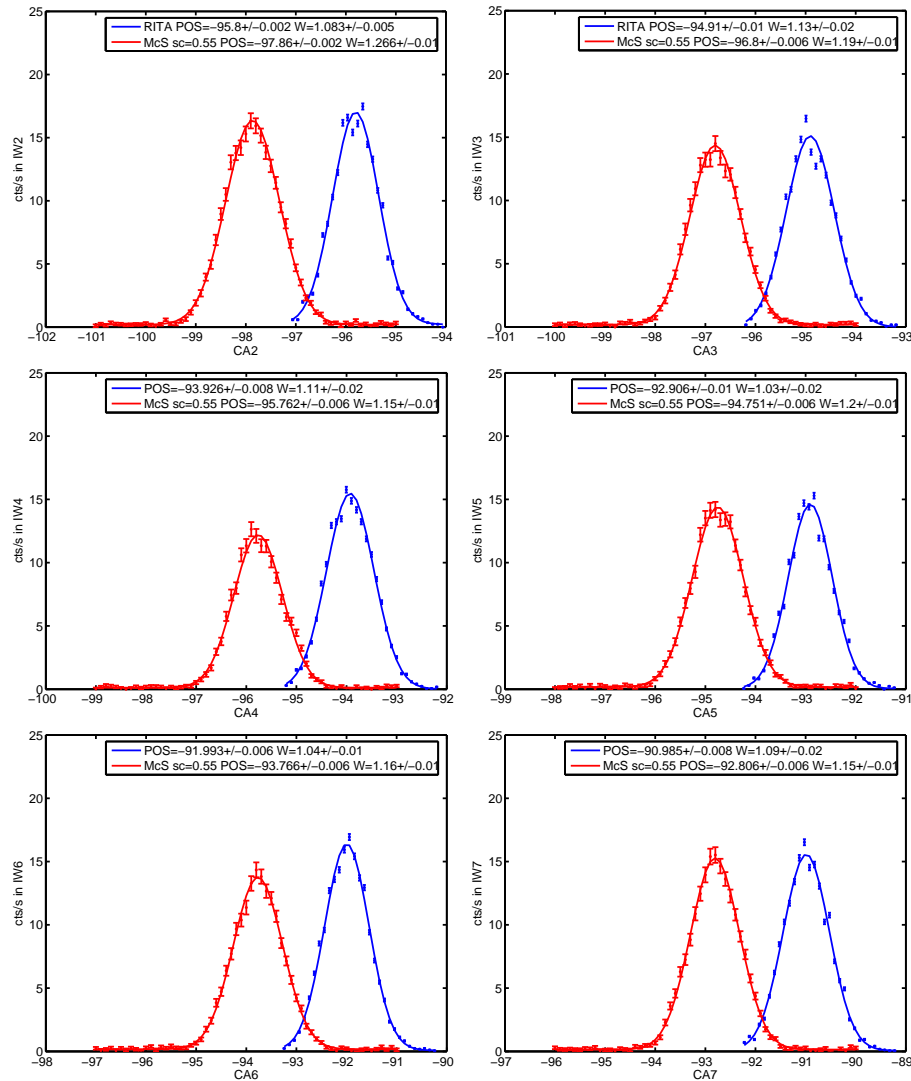


Figure 5.12: Simulated and measured scans of the blade angles. Intensities are counts in the appropriate electronic windows and  $\Omega_A = -57.58$  in the simulation.

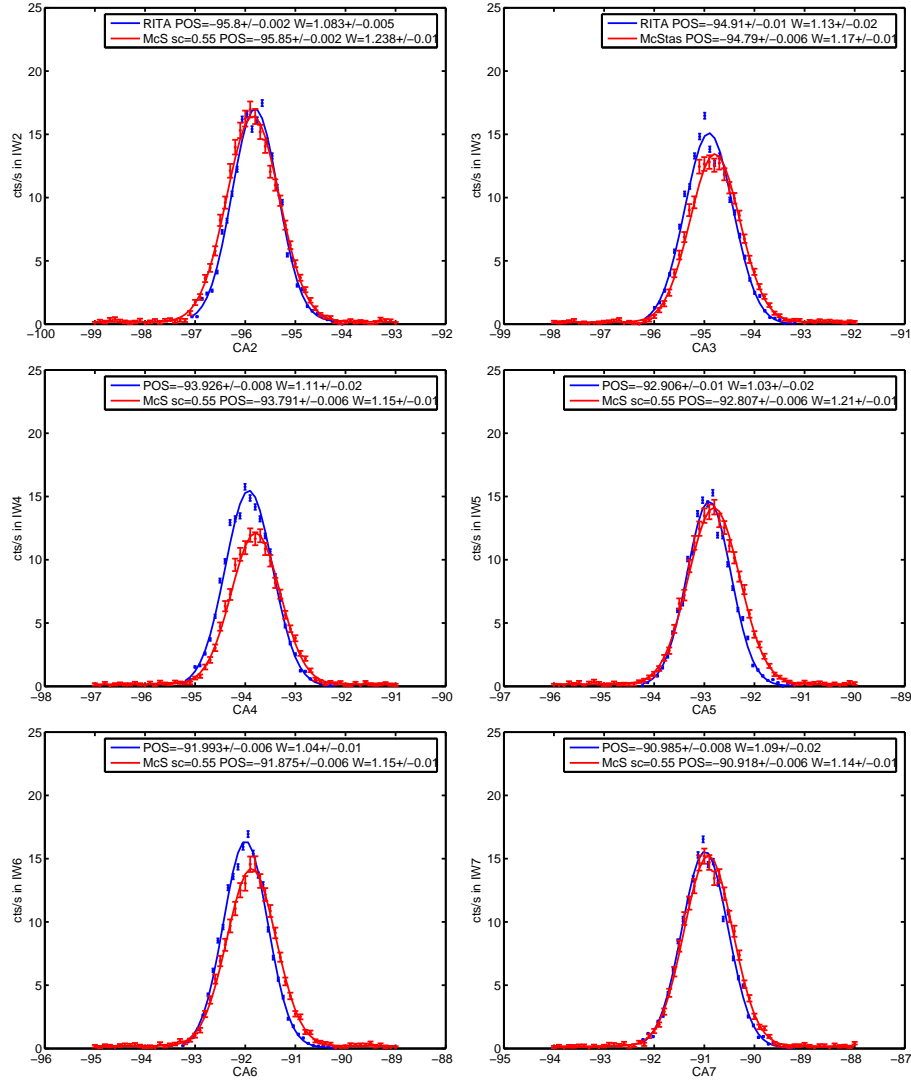


Figure 5.13: Simulated and measured scans of the blade angles. Intensities are counts in the appropriate electronic windows and  $\Omega_A = -55.64$  in the simulation.

### 5.13.2 Setting electronic windows

The V-RITA-II was used in 3-axis mode and with the same setup as described in Section 5.13.1. As in the physical set-up we use vanadium as a sample and put a4 to -85<sup>6</sup>. With the calculated value of aa5=-57.58, each analyser blade angle ca2-ca8 is scanned and, fitted by a Gaussian and each ca-motor set to the fitted ca-value of maximum intensity. The detector collimator (RC & LC) is scanned, the LC positions of maximum intensity in electronic window 2 is noted and the RC positions of maximum intensity in electronic window 8 is noted. The RC and LC values is used henceforth and the ca-motors scanned again and the RC

<sup>6</sup>we did not set a4=-90 as in the physical experiment since some of the non-scattered neutrons will then never be able to propagate to the plane of the next component after the sample which gives 'negative time' warnings

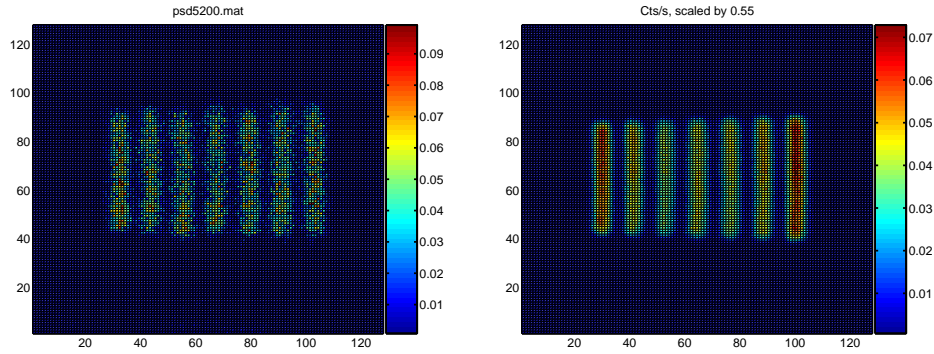


Figure 5.14: PSD image at the detector in monochromatic imaging mode using Vanadium as a sample. Left is measured and right is simulated with (V-)RITA-II in monochromatic imaging mode.

and LC scanned again. Using the optimal values the instrument is finally run with a source with  $\lambda$  distribution from  $3.84\text{\AA}$  to  $4.25\text{\AA}$ <sup>7</sup>,  $10^{10}$  rays. The 2D PSD intensity shown in Figure 5.14 is then summed vertically compared to the similar one measured at RITA-II, see Figure 5.15.

In the first iterations the simulated pattern was wider than the measured one, suggesting that the active area of the PSD is smaller than 0.30 m in the technical drawings. Through some iterations the active area was set to 0.275 m (a value which was supported by recent unpublished measurements by Jari í Hjöllum) and the optimisation procedure described above repeated. Finally the vertically summed simulated PSD picture is compared to the measured one in Figure 5.15. From this the optimal values of the electronic windows are set as to cut off anything below 0.5 cts/s in the summed intensity plot.

In the monochromatic imaging mode of the virtual experiments the detector is hence irradiated by the isotropic incoherent elastic scatterer from pixel 24 to 95 along x and pixel 39 to 91 along y corresponding to an image 0.153 m wide and 0.112 m high. The individual electronic window settings match the ones typically obtained in the corresponding physical experiment. The rest of the detector would in the physical experiment record the background intensity.

---

<sup>7</sup>second and third order scattering from the monochromator will anyhow be removed by the filter after the sample

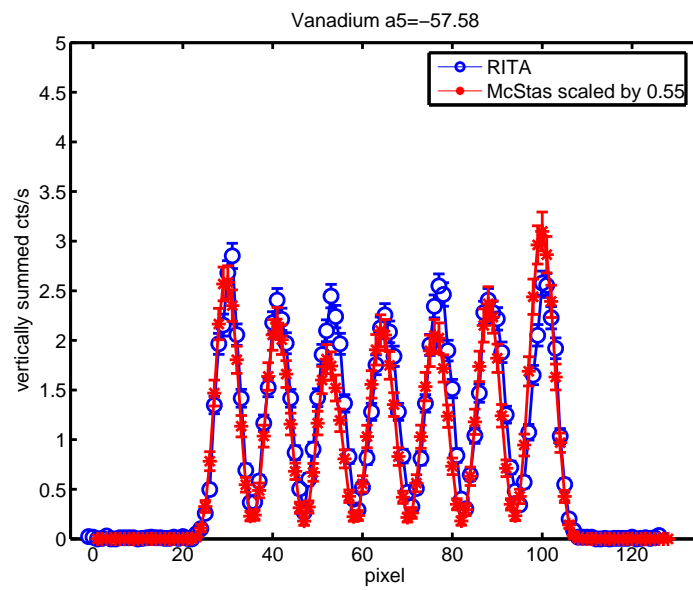


Figure 5.15: The vertically summed PSD image (Figure 5.14) in monochromatic imaging mode using Vanadium as a sample. The simulated data are plotted by  $\bullet$  and the measured by  $\circ$ . The lines are guides to the eye.

## 5.14 Testing the collimators

Setup was MV(5meV)-10'-mon-8.8mmplexi-D-TestColl-D-open-AF-PSD. RITA-II was used in '1-axis mode' by writing 'tasub const elastic' and driving aa5=-90 and a4=a6=0 so we were shooting directly through a flat analyser ca2-ca8=0 (not using the analyser). The diaphragm slits were set to MSL=5 MSR=5 MST=22 MSB=15 and SSL=5 SSR=5 SST=25 SSB=25.

Each test collimator (20',40',80') of width×height×length=0.04m×0.15m×0.20m was placed on the sample table and rotated in an a3 scan as shown in Figure 5.16. In the figure the simulated data are also shown using collimation as to fit the measured data, the central electronic window has been used in order to filter out background.

The data points seem somehow over-determined and hence the errors on the fit unreasonably small. In addition the physically measured data show some flattening in the top which might be due to saturation of the detector. Using a bandpass of 0.1-1.05 corresponding to  $\lambda$  between 0.40 and 4.25 a scaling of 0.1 on the simulated data gives the same intensity as the measured ones, see Figure 5.16.

In Table 5.5 the effective collimation of the physical and virtual experiments are determined from fits of two convoluted triangles to the a3 scans is listed along with the geometrically determined collimation found from the expression  $\tan^{-1} \frac{w \cdot 180 \cdot 60}{\pi \cdot n \cdot l}$  where  $w, l, n$  is the width, length and number of blades in the collimator.

As is shown on Figure 5.17 the beam probes the central part of the collimator, but unfortunately we could not measure the beam profile at the sample position and hence cannot be completely sure how large a part of the collimator was probed, but the beam size at the sample position is roughly 2cm×2cm. The size of the beam spot on the PSD corresponds to 2.4cm×10cm.

Collimator	Geometrical coll.[min]	Effective coll.[min]	McStas coll. [min]
10	9.7	-	9.7
20 checked 2008/11/05	18.6	20.37	19.6
40 after mono	37.2	38.98	39.0
80 after mono	76.3	79.40	79.2

Table 5.5: Collimator parameters, measured and simulated. The first column shown the 'name' of the collimator, the second their geometrically determined collimation and the third column shows the collimation as fitted from measured data at RITA-II. The fourth column is the McStas input parameter to `Collimator_linear` which in the virtual experiment gives the same effective collimation as listed in the third column within errors. All collimations are listed in arc minutes. The lines are fits to two convoluted triangles of the same height where the width of one is kept fixed at the nominal value of the monochromator collimator (9.7').

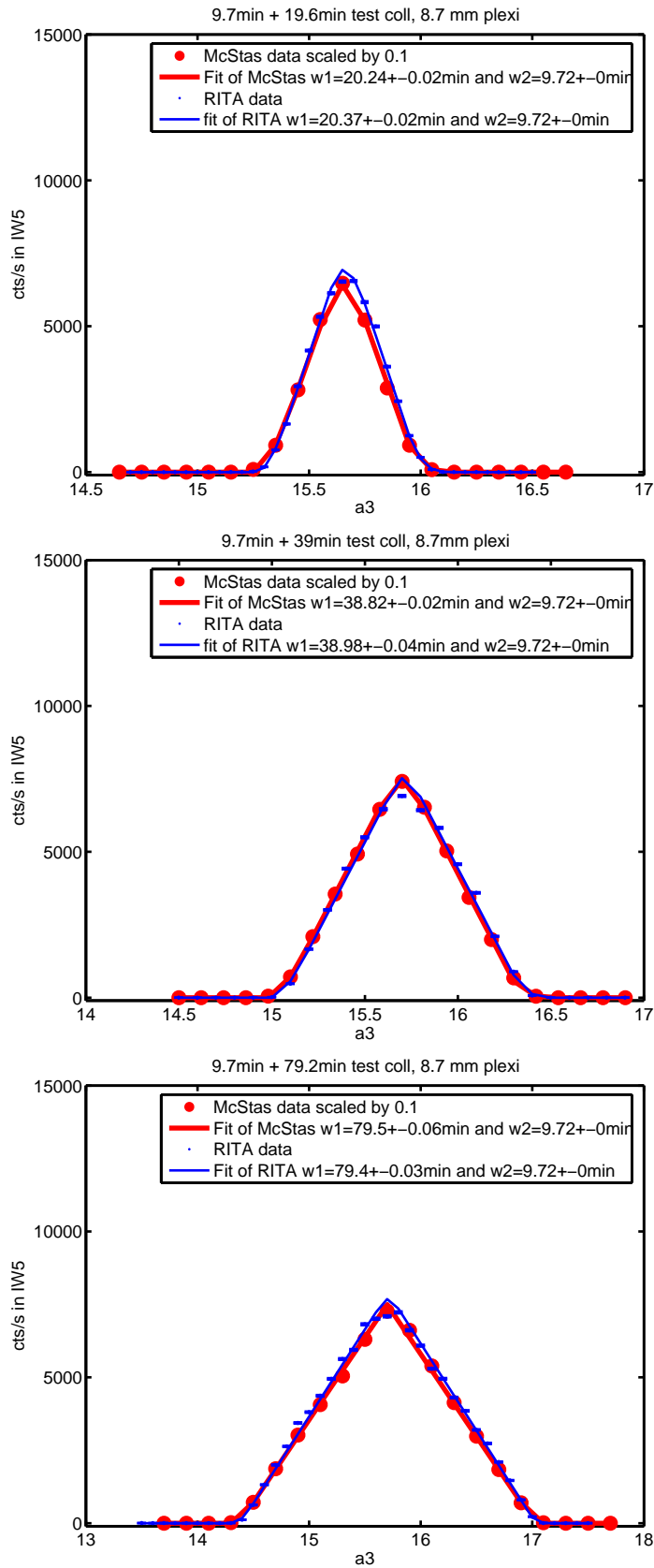


Figure 5.16: Test of collimators. (Top) Both RITA-II and V-RITA-II 20' coll. (Centre) RITA-II 40' coll and V-RITA-II 38.5' coll. (Bottom) RITA-II 80' and V-RITA-II 79' coll

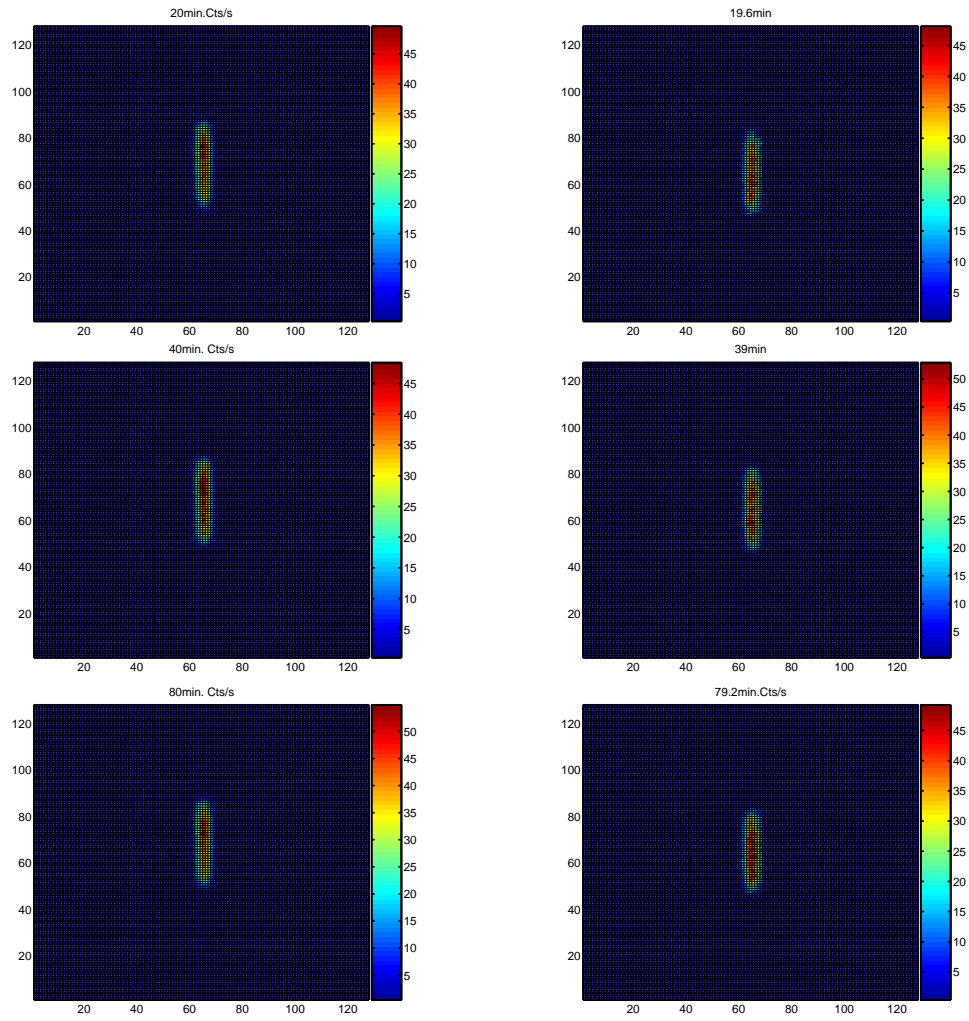


Figure 5.17: The PSD images at the optimal intensity position of the three collimators which were used as samples in a '1-axis' setup. The left column is from physical RITA-II measurements, the right column is produced by McStas.

## 5.15 Q-resolution in 2-axis mode

A powder sample was used to test the V-RITA-II without the analyser. One test compares the absolute value of the measured and simulated diffraction energy and different collimations in Section 5.15.1. Another compares the widths and intensities of several diffraction peaks at positive and negative scattering angles in Section 5.15.2.

### 5.15.1 Finding zero-point of a4 and the absolute energy

In the physical experiment we used a sapphire pressed powder sample ( $\text{Al}_2\text{O}_3$ ) to find the zero-point of the scattering angle and the absolute energy of the beam at a particular monochromator setting. The setup was MV(5meV)-coll-mon-D-Al2O3-open-AF-PSD.

RITA-II was used in 2-axis mode by writing 'tasub const elastic' and driving aa5=-90 and a4=a6=0 so we were shooting directly through the flat analyser ca1-ca9=0 (i.e. not using it). The diaphragm slits were set to MSL=10, MSR=10, MST=25, MSB=25, SSL=10, SSR=10, SST=25 and SSB=25.

For each of the collimators (labelled 20',40',80') the a4 position of the (1 0 -2)  $\text{Al}_2\text{O}_3$  powder peak was measured, data shown in Figure 5.18 along with the simulated ones which used as input the values of Table 5.5. The central value of the positive/negative peak position can be used as a zero-point of a4 for the particular collimator and the average scattering angle to find the absolute energy. The results are tabulated in Table 5.6.

The McStas simulations used a source with wavelength interval 3.84 - 4.25Å ( $\pm 5\%$  bandpass) and an ideal  $\text{Al}_2\text{O}_3$  PowderN sample with the following parameters: radius = 0.0068 , h = 0.015, pack = 1 , vc = 254.52, sigma\_abs = 0.4625 , sigma\_inc = 0.0188, deltad.d=0. The simulated results are shown in Table 5.7.

It is seen that there is a systematic shift of the peak position towards the positive a4 in both the simulated and the measured data which is probably due to an effect of scattering relatively more neutrons from the front of the sample than the backside. The shift is the same for all collimators within errors but the shift is larger in the measured data, indicating a small misalignment of a4 at the RITA physical instrument. The correction to the zero-point as indicated in Table 5.6 was implemented as a new zero-point for a specific collimator in the following physical experiments. The centre of the absolute energy distribution is 5.00 meV within errors for all collimations the virtual experiments. In the physical experiments the average measured energy is however 5.01 meV which suggests an error in the alignment giving 0.2% higher energy.

The line width is produced for all collimators within 2%, and the scaling is 0.55 which is the same as in the 3-axis imaging mode using Vanadium as sample ( see Section 5.13.2).

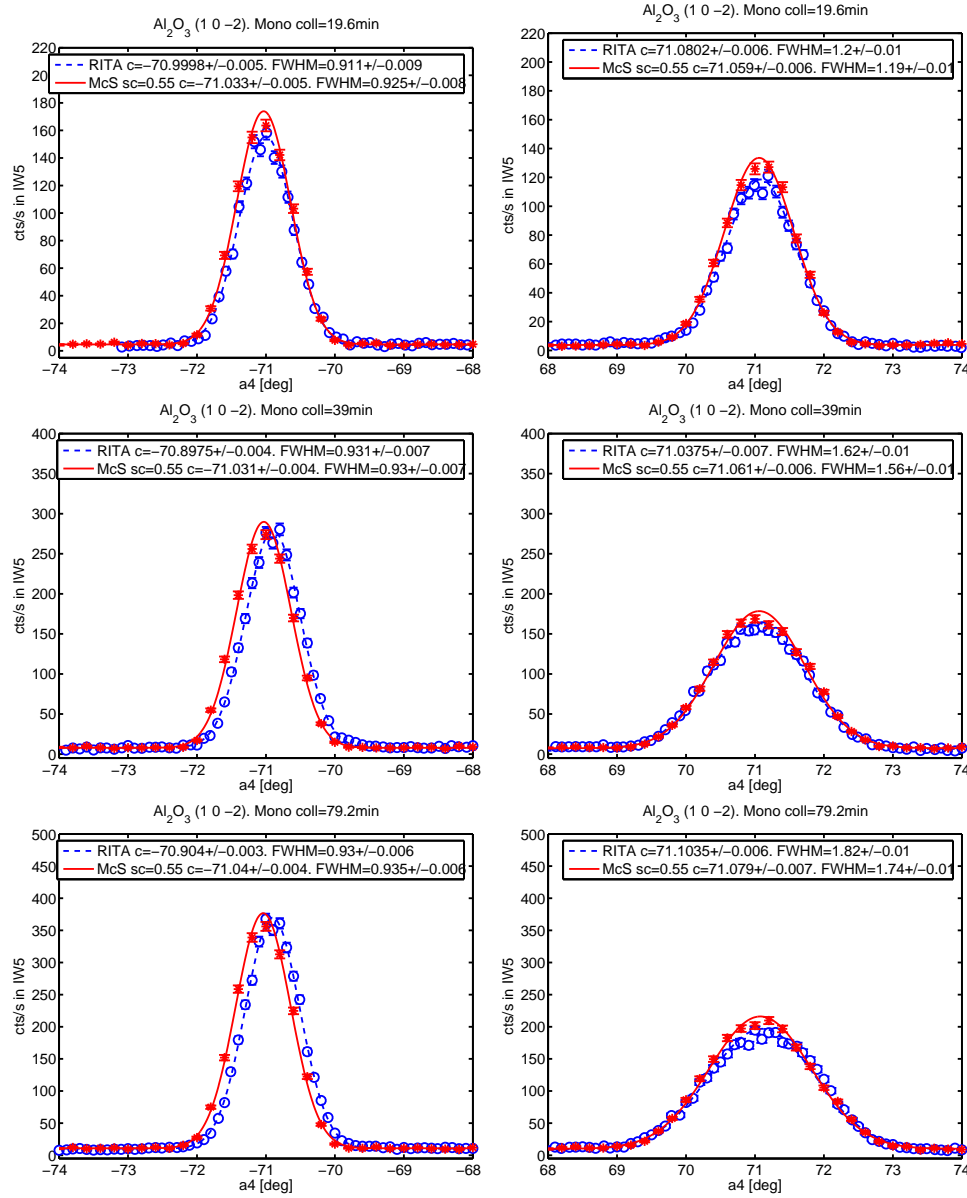


Figure 5.18: A4 positions of the (10-2)  $\text{Al}_2\text{O}_3$  powder peak using different collimators. The simulations and measurement were performed in 2-axis mode and the data from electronic window 5 are shown in the figure.

collimator	20 min	40 min	80 min
a4 offset	$0.080 \pm 0.007$	$0.070 \pm 0.008$	$0.100 \pm 0.007$
$\langle \theta \rangle$	$35.500 \pm 0.004$	$35.483 \pm 0.004$	$35.5019 \pm 0.004$
$\lambda = 2 * 3.4808 * \sin(\theta)$	$4.0426 \pm 0.0004$	$4.0410 \pm 0.0004$	$4.0428 \pm 0.0004$
energy = $\frac{81.8042}{\lambda^2}$	$5.0056 \pm 0.0009$	$5.0095 \pm 0.0009$	$5.0051 \pm 0.0009$

Table 5.6: Measured A4 zero-point and absolute energy calculated from d-spacing =  $3.4808 \text{ \AA}$  of  $\text{Al}_2\text{O}_3$  (1 0 -2).

collimator	19.6 min	39 min	79.2 min
a4 offset	$0.017 \pm 0.008$	$0.015 \pm 0.007$	$0.017 \pm 0.008$
$\langle \theta \rangle$	$35.525 \pm 0.004$	$35.525 \pm 0.004$	$35.526 \pm 0.004$
$\lambda = 2 * 3.4808 * \sin(\theta)$	$4.0451 \pm 0.0004$	$4.0451 \pm 0.0004$	$4.0452 \pm 0.0004$
energy= $\frac{81.8042}{\lambda^2}$	$4.9993 \pm 0.0009$	$4.9991 \pm 0.0009$	$4.9991 \pm 0.0010$

Table 5.7: Simulated A4 zero-point and absolute energy calculated from d-spacing=3.4808Å of Al<sub>2</sub>O<sub>3</sub> (1 0 -2). Data from electronic window 5.

### 5.15.2 Comparing scans of several PowderN reflections to Al<sub>2</sub>O<sub>3</sub>

Using the 19.6' collimator and the setup otherwise as in Section 5.15.1 we wanted to compare virtual experiments with physical experiments using a powder sample. In Figure 5.19 the intensity in the electronic windows of an a4 scan through the Al<sub>2</sub>O<sub>3</sub> (10-2) powder cone is shown. As is seen the positions and widths of the simulated and measured peaks are very close in all windows. As mentioned in Section 5.15.1 a scaling of 0.55 of the McStas simulated data is needed to compare to the measured data on blade 5. This scaling factor is the same as found in the 3-axis simulations in Section 5.13.2. As is seen on the lower intensity in windows away from the central one, the beam to the other blades than the central one is partially or completely blocked by the sample slit. Hence this experiment should be repeated with a more relaxed slit setting in order to confirm that the scattering from all blades have the same scaling factor. When setting the slits to SSR=SSL=10 only the central 88 mm of the detector are irradiated in the two-axis setting which in the McStas simulations completely cuts off the beam in the two outmost windows. In the physical experiment on blade 6 and 7 the intensities are lower than the simulated ones. This can be explained by actual slits settings being a little off-centred and smaller than their nominal value. This situation can easily happen since the slit motors are not encoded.

The other peaks reachable by 5 meV neutrons were also measured and virtual experiments performed as shown in Figure 5.20. The peak positions are the same within 0.05° and the widths of the simulated peaks are within two error-bars (2%) of the measured.

The grain size and distribution in the sample will affect the line width, but it seems from the comparison above that the virtual sample with idealised parameters of  $\Delta d/d = 0$  and packing factor of one is a good representation of the physical sample.

The virtual experiments used a source with wavelength interval 3.843 - 4.247Å using 1e8 neutrons and no SPLIT repetition.

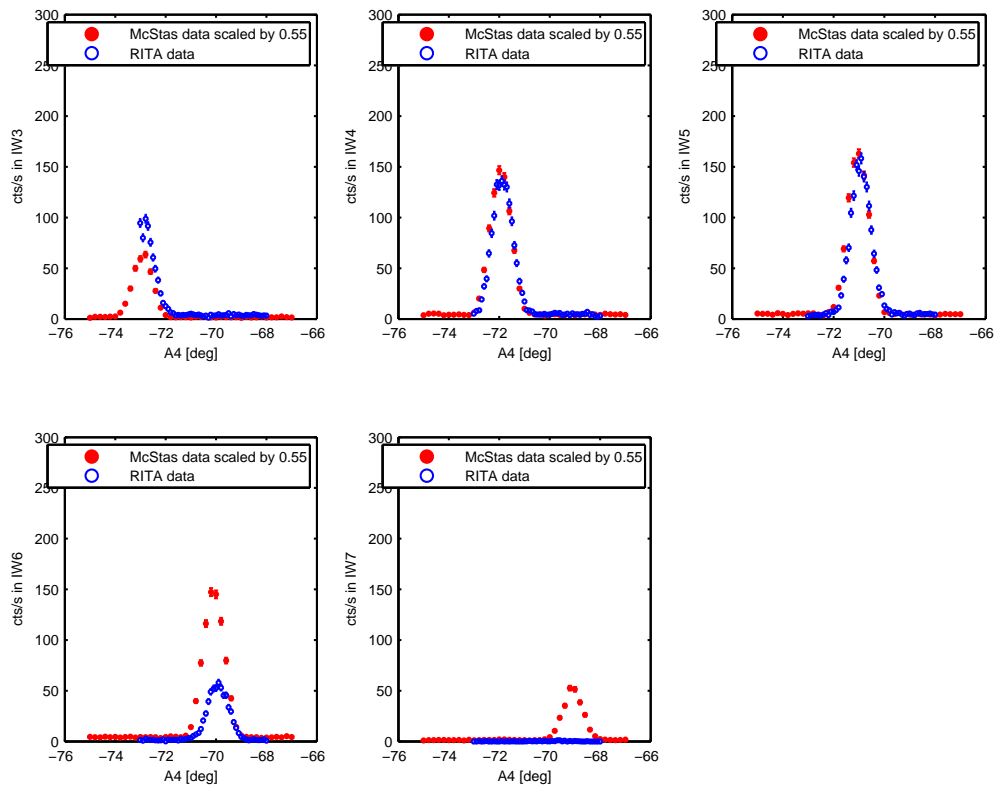


Figure 5.19: A4 scan of  $\text{Al}_2\text{O}_3$  (10-2) powder peak in different electronic windows, simulated and measured in 2-axis mode.

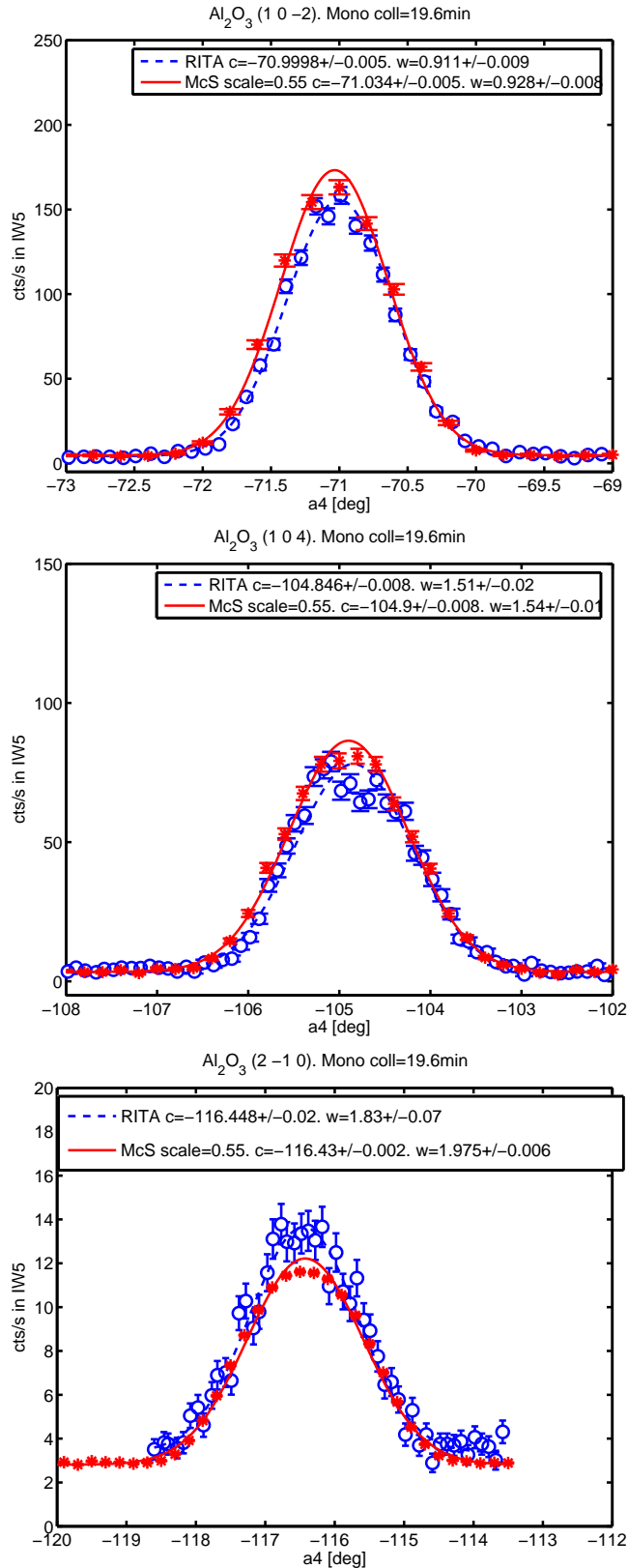


Figure 5.20: A4 positions of the  $\text{Al}_2\text{O}_3$  powder peaks. The simulated and measured data shown are from the central electronic window 5 and (V-)RITA-II was in 2-axis mode. The scaling factor of the simulated data with respect to the measured is the same in all three figures.

## 5.16 Q-resolution in 3-axis mode

Physical and corresponding virtual experiments on two different Ge single crystals were performed to study the Q-resolution of RITA-II in 3-axis mode, i.e. including the analyser. One Ge crystal was previously used as a monochromator and had a finite and known mosaicity and the (111) reflection is studied in Section 5.16.1. The same reflection was studied in Section 5.16.2 for the other Ge crystal which was a wafer i.e. a perfect crystal for which multiple scattering and extinction becomes important.

### 5.16.1 Ge single crystal

A large single crystal (oval slab 57mm\*52mm\*7mm) which was previously used as a monochromator in another neutron spectrometer was used as a sample. The setup was MF(5meV)-40min-mon-D-Ge-D-radBe-AI(5meV)-PSD. The slits were set to MSL=MSR=10 MST=MSB=20 and SSL=25 SSR=30 SST=SSB=40. In the physical experiment 6.6 mm Plexiglass was used to attenuate the beam before the sample. This was also simulated using `V_sample` with `v0=1 sig_a=0.019` and `sig_i=4.7` and `zthick=6.6mm` as perspex attenuator. As is seen in the longitudinal scan of Figure 5.21 the simulated intensity fits well after the overall scaling of 0.55 (which was also used in the other virtual experiments using powder and vanadium samples). The transversal scan in the same figure has higher intensity since the corresponding goniometer was adjusted slightly after the longitudinal scan.

It is seen that using mosaicity=13' and  $\Delta d/d = 8 \cdot 10^{-4}$  gives the correct width of the transversal and longitudinal scans when fitted to a Gaussian. This value of the mosaicity matches the previously measured which is denoted by a marker as 12-13' on one side of the crystal. Since no other reflection were possible to reach at this energy it was however not possible to check the settings at another reflection.

### 5.16.2 Ge wafer

The (111) Bragg peak of a Ge wafer was investigated in the setup MF(5meV)-40min-mon-D-Ge wafer-D-radBe-AI(5meV)-PSD. The diaphragm slits were set to MSL=MSR=15 MST=MSB=25 and SSL=25 SSR=30 SST=SSB=40. The  $a_3$  scan of the wafer measured on RITA-II is fitted to a Gaussian with FWHM=0.323(3) $^\circ$  corresponding to Gaussian standard deviation  $\sigma_m = \frac{0.323(3)^\circ}{\sqrt{8 \ln 2}} * 60 = 8.2'$ . In this case  $\sigma_m$  can however not be interpreted as the mosaicity  $\eta$  since the resolution of the spectrometer sets the lower limit of the width of the scan. The wafer is a perfect thick<sup>8</sup> crystal so the kinematic approximation no longer applies and dynamical diffraction has to be considered. If the wafer is rotated (rocked) by  $\theta$  there is total reflection within the angular range  $[-\Delta\theta_D; \Delta\theta_D]$  where  $\Delta\theta_D$  is the angular Darwin width [142]

<sup>8</sup>relative to the distance between crystal planes

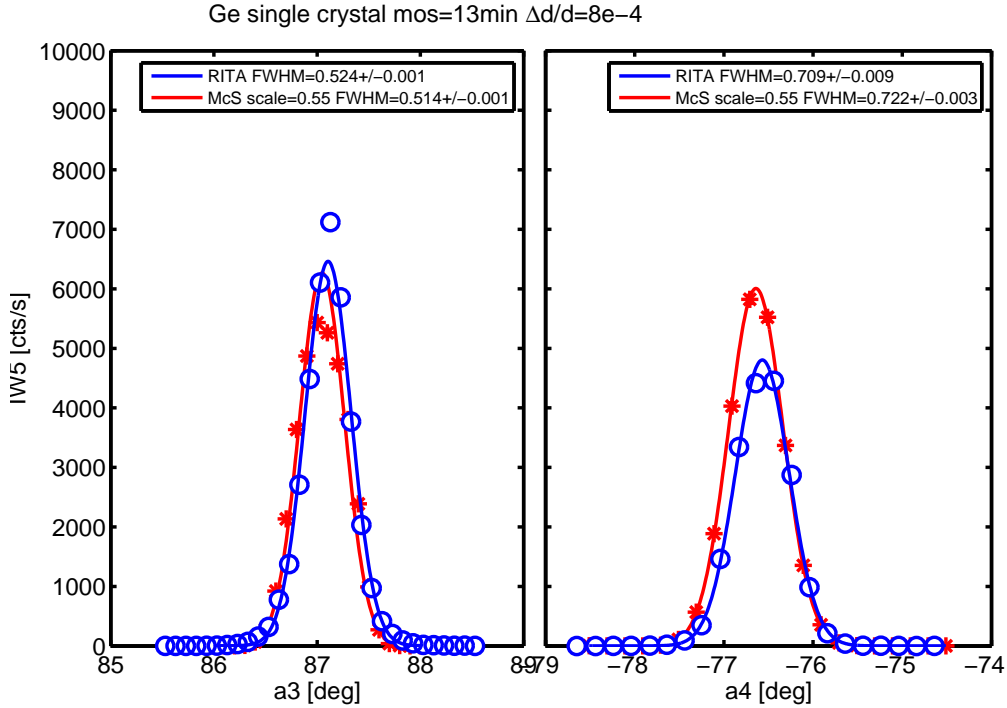


Figure 5.21: Transversal (left) and longitudinal (right) scans through the (111) Bragg reflection of a Ge single crystal with (V-)RITA-II in monochromatic imaging mode. Data shown from electronic window 5. In the longitudinal scan the crystal was not completely aligned on the (111) reflection, hence the maximum intensity here is a little lower than the transversal scan for which the reflection was aligned.

$$\Delta\theta_D = \frac{e^{-W} F(HKL)\lambda^2}{V_0\pi \sin 2\theta} \quad (5.7)$$

where  $e^{-W}$  is the Debye-Waller factor at the particular temperature,  $F(HKL)$  is the structure factor and  $2\theta$  the scattering angle of the  $(HKL)$  reflection<sup>9</sup>. For Ge (111) at 292K and  $\lambda = 4.045\text{\AA}$ ,  $2\theta = 76.6^\circ$ ,  $W = B_{292} \left(\frac{\sin 2\theta}{\lambda}\right)^2 = 0.0099[143]$ ,  $F(111) = 46.30 \cdot 10^{-15} \text{ m}$  and  $V_0 = 181.0\text{\AA}^3$ . Hence  $\Delta\theta_D = 1.37\text{rad} = 0.047'$ . If the incident beam is perfectly monochromatic the FWHM of the reflectivity curve is given by the Darwin width as  $w_D^{\text{FWHM}} = \frac{3}{2\sqrt{2}} 2\Delta\theta_D = 0.0999'[86]$ .

In the experiment the rocking curve is fitted to  $\text{FWHM} = 0.323^\circ = 19.38'$  and the longitudinal scan to  $\text{FWHM } w = 0.653^\circ = 39.2'$  which reflects the resolution of the spectrometer, not characteristics of the wafer, see Figure 5.22. The `Single_crystal` component models dynamical scattering. Hence in the simulations, besides the structure factors, absorption and incoherent cross-sections, the scattered intensity is sensitive to the  $\Delta d/d$  and mosaicity parameters within the range  $\Delta d/d > 10^{-5}$  and mosaicity  $< 15'$  for the (111) reflection. The lower

<sup>9</sup>The expression is slightly different than [142] in order to relate to the definition of the structure factor in Section 3.1.1

limit at which changing mosaicity no longer changes intensity depends on  $\Delta d/d$ . For mosaicity=0.05' the intensity is maximal for  $\Delta d/d \leq 10^{-4}$ . The Darwin width cannot be directly related to the mosaicity or  $\Delta d/d$  parameter separately using just a single reflection so several solutions yielding the correct intensity are possible. Using mosaicity=0.3' and  $\Delta d/d = 10^{-5}$  or mosaicity=0.05' and  $\Delta d/d = 10^{-4}$  in the `Single_crystal` component, the simulated intensity is comparable to the measured when scaling by the overall factor 0.55 which was also used for the powder and vanadium virtual experiments. If the mosaicity parameter is assumed to be the dominant parameter of the virtual sample deciding the width of the rocking curve the most appropriate value is  $\sigma_D = \frac{w_D^{\text{FWHM}}}{\sqrt{8 \ln 2}} \sim 0.05'$ . Transversal and longitudinal scans through the (111) reflection using mosaicity=0.05' and  $\Delta d/d = 10^{-4}$  are shown in Figure 5.22. Although increasing the mosaicity increases the intensity it does not change the width of a transversal scan within 10% up to mosaicity=5'.

A scan of a4 which moves the Bragg peak over the 7 analyser blades is shown in Figure 5.23 together with its virtual experiment counterpart for one set of parameters. Most of the a4 widths are very similar, however the simulated width is 14% larger than the measured at blade 5. This is probably due to the changes made to the analyser blade in 2006 as described in Section 5.10 so the present blade 5 in the physical RITA-II has lower mosaicity than the one used in the V-RITA-II model (see 5.10.2).

In general scans of more than one reflection is needed in order to fix the mosaicity and  $\Delta d/d$  values of the single crystal component. This is done in Chapter 6.

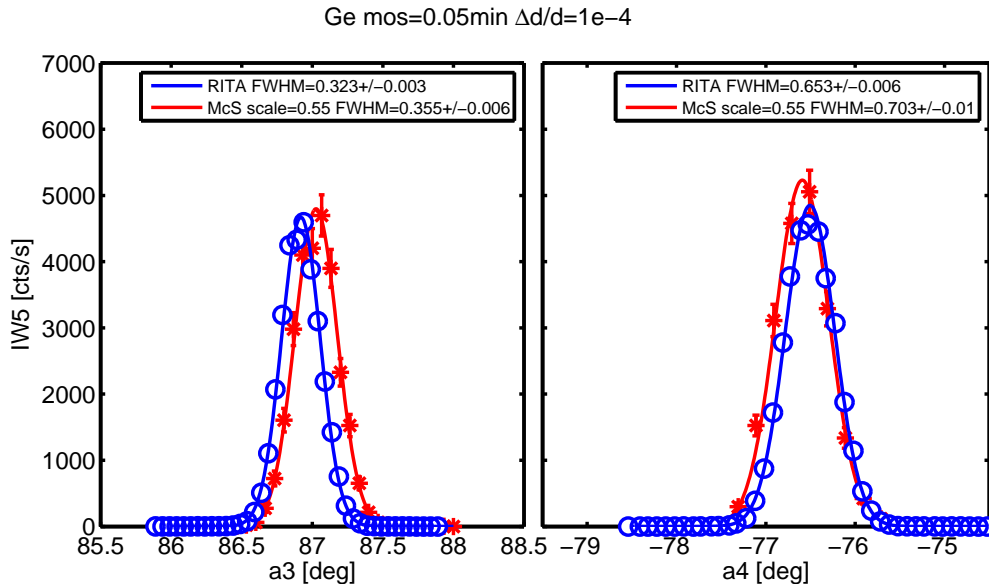


Figure 5.22: Transversal (left) and longitudinal (right) scans through the (111) Bragg reflection of a Ge wafer. (V-)RITA-II was in monochromatic imaging mode and data from electronic window 5 are shown.

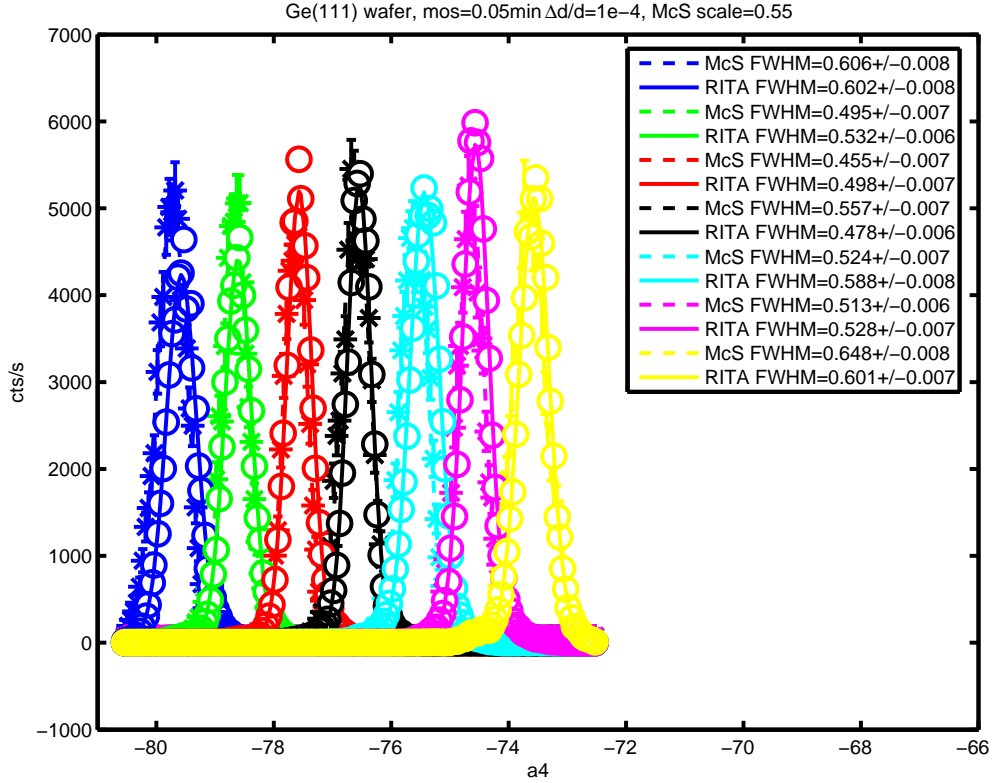


Figure 5.23: Simulated and measured  $a_4$  scan of Germanium wafer with the instrument in monochromatic imaging mode. Open symbols are simulated data, stars are measured data. Full lines are fits to simulated data, dashed line fits to measured data.

## 5.17 Elastic energy resolution

The setup of the physical and virtual experiment was MV(5meV)-40min-mon-D-Vanadium-D-open-AI-PSD(5meV). In order to avoid most airscattering we moved  $a_4=-90$ .

The diaphragm slits were set to MSL=12 MSR=12 MST=25 MSB=25 and SSL=25 SSR=30 SST=40 SSB=40.

Vanadium scatters elastically incoherent and almost isotropically. As is seen from Figure 5.24 and the corresponding Table 5.8 the elastic energy resolution is simulated accurately within the error bar for all blades except 2 and 8 which in the simulations are 4% and 8% wider respectively, probably due to the mosaicity of the particular analyser blade being too large. Another explanation of the measured energy width being slightly smaller than the simulated in the outer blades could be if the beam was slightly cut off in the physical experiment thus effectively allowing a smaller incoming divergence of the beam.

A theoretical estimate for the energy width of a constant  $Q$  scan through a dissipation-less surface at  $E_i = E_f = 5$  meV is  $\Delta E = 0.16$  meV if all horizontal

collimations and mosaicities are the same and equal to  $40'$  as shown in Section 3.1.4. This is 25-30% less than the measured and simulated value for all analyser blades of RITA-II.

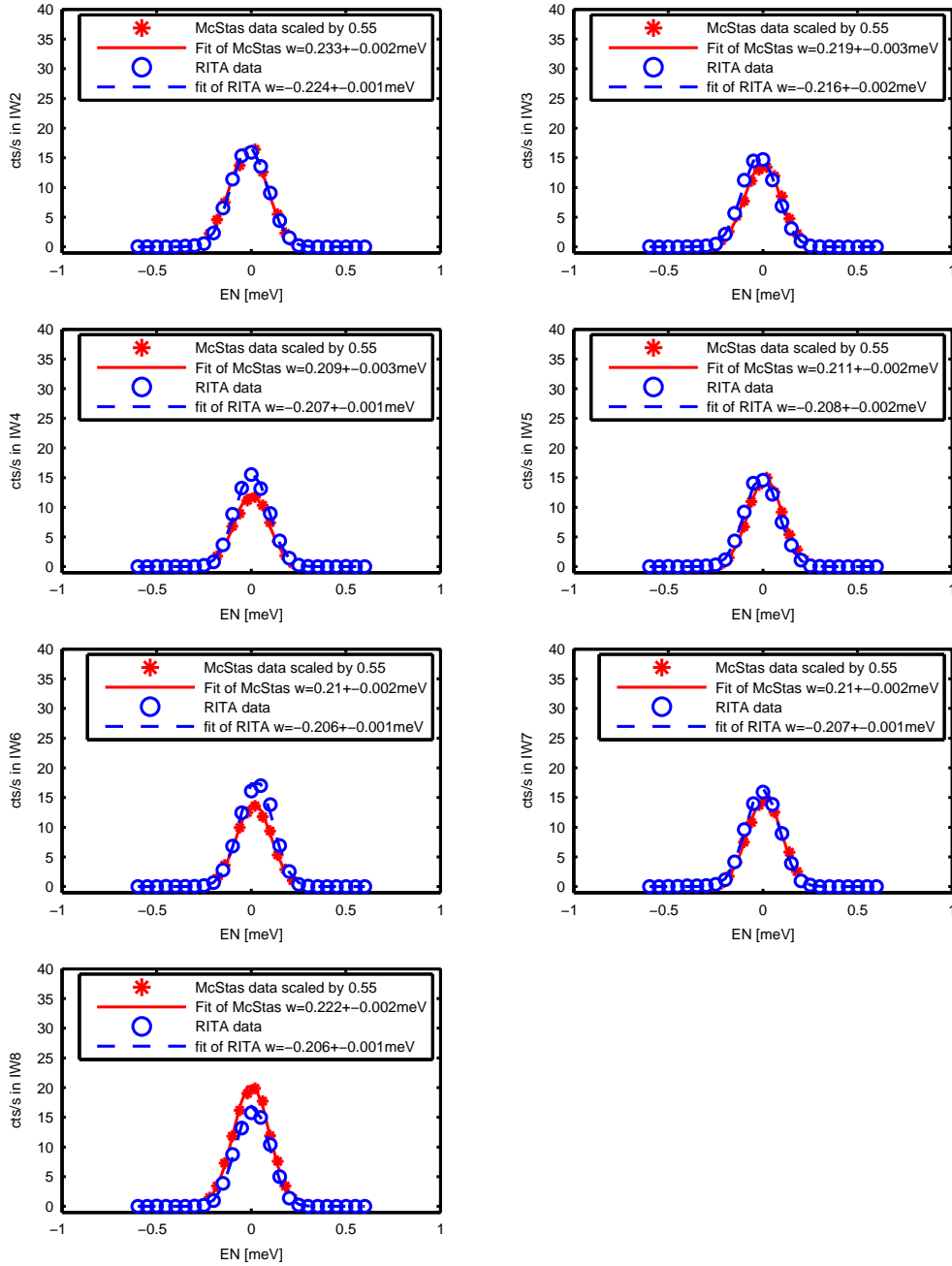


Figure 5.24: The elastic energy resolution in each electronic window measured and simulated in monochromatic imaging mode using Vanadium as sample.

Blade #	bl 2	bl 3	bl 4	bl 5	bl 6	bl 7	bl 8
$\Delta E^{meas}$ [meV]	0.224(1)	0.216(2)	0.217(1)	0.208(2)	0.206(1)	0.207(1)	0.206(1)
$\Delta E^{sim}$ [meV]	0.232(3)	0.217(3)	0.210(3)	0.210(3)	0.210(2)	0.210(3)	0.223(2)

Table 5.8: Measured and simulated values of the energy resolution for each analyser blade scattering 5 meV at  $q = 1.87325\text{\AA}^{-1}$ . Vanadium was used as sample.

## 5.18 Summary and discussion of the virtual testing experiments

In this section the results of the validation of the V-RITA-II by comparison of virtual experiments against measured data is discussed. An overview of the test cases is presented in Table 5.9. In general I conclude that the resolution of RITA-II is very precisely simulated by the V-RITA-II.

### 5.18.1 Line width

The effective collimations of the collimators with nominal values 20', 40' and 80' (used between the monochromator and sample position) have been measured and simulated. The appropriate collimation parameters to use in the virtual experiment for a perfect match were very close to the nominal values, 19.6', 39' and 79.2' in V-RITA-II, respectively.

An  $\text{Al}_2\text{O}_3$  pressed powder sample was used to test the reproducibility of measured data by the finely tuned virtual instrument in 2-axis mode, i.e. without the analyser. It was also used to find the absolute energy of the instrument for different collimator settings.

The width of the simulated powder diffraction peaks matched within 5% of the measured ones including both positive and negative scattering angles. The absolute energy of the simulations was within 0.2% of the measured one for three different collimator settings. The average position in the positive and negative measured diffraction angle was used to correct a small offset in a4 for each of the three collimators.

Using the 19.6' collimator before the sample, simulations and measurements of the intensity through several powder cones were performed by a4 scans in 2-axis mode. The positions of the peaks matched within 0.05% and the intensity within 5% of the measured values.

The properties of the analyser was investigated for use of the V-RITA-II in the 3-axis mode. The mosaicity of the analyser blades varied by up to 50% but it was possible to tune each mosaicity explicitly by McStas in the `Monochromator_flat` component to match the rocking curve of each analyser blade. However, since the physical experiment was done in 2006 and alterations have been done to several of the the analyser blades later on, it would be advisable for future use of V-RITA-II to repeat the experiment in Section 5.10.2 and adjust the mosaicity in the V-RITA-II analyser blades accordingly. The simulations should include the full bandwidth from the monochromator and include the Plexiglass attenuator in the beam.

Using the finely tuned V-RITA-II in (3-axis) monochromatic imaging mode, the elastic energy resolution measured by energy scans of the incoherent scattering from vanadium was simulated within 8% of the measured value. The correspondence between the simulated and measured experiment was however extraordinarily good in the central analyser blades as the energy resolution was simulated within 2% which is within the error bars.

Still in monochromatic imaging mode, the width of a transversal scan through the (111) reflection of a Ge single crystal with a known mosaicity was reproduced within error bars using the same mosaicity in the virtual crystal. In general more than one fundamental reflection is however needed to adjust both the mosaicity and the  $\Delta d/d$  parameter.

### 5.18.2 Intensity

The flux before the monochromator was simulated within 2% of the previously measured and simulated value meaning that the absolute intensity of the source in V-RITA-II is validated. The flux at the sample position was simulated within 3% compared to Au foil measurements in 2001[133].

At the PSD detector an overall scaling of 0.55 between the intensity in the V-RITA-II and the physical experiments was generally employed for elastic scattering at 5 meV. Some of this factor is due to the efficiency of the detector being only 80% at 5 meV, whereas the simulated efficiency is 100%. Taking this into account the scaling factor would be  $0.55 \cdot 0.8 = 0.66$ . Measurements of the present flux at the sample position for a filtered monochromatised beam are scheduled in the near future and the remaining 50% lower intensity at the physical RITA-II compared to V-RITA-II might be explained after these measurements.

The overall scaling of 0.55 was also reproduced in a virtual experiment using a Ge wafer in which multiple scattering and extinction occurs. In the simulations the mosaicity parameter was set to the Darwin width and the uncertainty in the lattice parameter was set to a value so small that total reflection was achieved.

There are however a couple of exceptions to the 0.55 scaling factor as the experiments labelled #1 & #3 in Table 5.9 which have scaling factors of 0.2 and 0.1 respectively. They both use the 'direct beam' meaning that higher order scattering from the monochromator passes to the detector. A source of the factor 2-5 overestimated intensity is the handling of reflectivity in the `Monochromator_flat` component. The reflectivity is assigned as a scalar appropriate to the scattered energy. The reflectivity for 5 meV neutrons is set to 0.8 whereas the appropriate value for first order scattering of 20 meV neutrons is 0.6<sup>10</sup> but this is not automatically implemented in V-RITA-II. Using this correction the intensity of scattered neutrons off the monochromator and analyser blades is 25% less at 20meV than 5 meV. However this correction does not account for the difference in a couple of orders of magnitude on the intensity in the experiments which passes higher order neutrons to the PSD. There seems to be a another source of error in `Monochromator_flat` which is substantiated by the fact that scaling is accumulative when second order scattering from the

<sup>10</sup>according to the reflection list for PG at [134]

monochromator is scattered at the sample and passed a second time through the component in the analyser before reaching the detector as in experiment #13 with scaling 0.03 in Table 6.1 of Chapter 6. The source of the overestimated intensity of the higher order scattered neutrons might be the assumption of an infinitely thin crystal with  $\Delta d/d = 0$  in the `Monochromator_flat` component. It might also be that the reflectivity is assumed to be independent of the order of the reflection. Future virtual experiments and corresponding physical experiments will clarify this issue.

#	Experiment	Year	Scale	Int	Linewidth
1	Analyser mosaicity (direct beam)	2006	0.2	20%	5%
2	Analyser mosaicity (V sample in sec. 5.13.1)	2008	0.55	20%	4-20%
3	Collimators 19.6'/39'/79.2'	2008	0.1	5%	4%
4	PowderN collimators 19.6'/39'/79.2'	2008	0.55	10%	2%
5	PowderN reflections (10-2)/(104)/(2-10)	2008	0.55	10%	2%
6	Elastic energy resolution (V sample)	2008	0.55	10%	2% (8%)
7	Ge single crystal	2008	0.55	10%	2 %
8	Ge wafer (perfect single crystal)	2008	0.55	10%	10%

Table 5.9: The various VE which have been performed in order to adjust and test V-RITA-II. The second column lists the type of experiment, the third the year the corresponding physical measurements were done and the fourth the overall scaling of the VE to the physical experimental data in electronic window 5. The second to last and last columns list the accuracy within which the VE reproduces the intensity and line width after the overall scaling of the particular experiment.



## Chapter 6

# Analysis of LSCO+O diffraction data by virtual experiments

In this chapter it is shown how virtual experiments can be used in data analysis of diffraction data from single crystals containing finite size domain structures. The finely tuned V-RITA-II was used with a single crystal virtual sample which matches the physically measured LSCO+O crystals as closely as possible apart from the finite size domains. The `Single_crystal` component takes a Bragg reflection list generated from `Crystallographica`. However the excess oxygen was not taken into account. Instead the *Bmab* structure of LSCO with the appropriate amount of Sr and lattice parameters as measured in the physical experiments of LSCO+O was used in the virtual crystal.

The idea is to adjust the mosaicity and  $\frac{\Delta d}{d}$  parameter of each of the four virtual single crystals on two orthogonal basic Bragg reflections. This is done by comparing to physically measured transversal and longitudinal scans of Bragg reflections of the four LSCO+O samples. Preferably the 'adjusting reflections' should be far apart in  $2\theta$  to separate the influence of the mosaicity and  $\Delta d/d$  parameters but since the virtual experiments were performed post-experimentally the only choice of Bragg reflections were the ones used to align the crystal in the experiment.

The mosaicity and  $\frac{\Delta d}{d}$  parameters of the present version of `Single_crystal` component are isotropic. Hence if the mosaicity and  $\frac{\Delta d}{d}$  differ on the two fundamental Bragg reflections in a particular scattering plane of a specific crystal an interpolated value is used to simulate the other reflections of that crystal in that plane.

Once the parameters have been set for each virtual single crystal it can be used to predict the line width of any scan of the particular crystal in case there is no finite size broadening. All data presented in this section is from the central electronic window 5 of the PSD, corresponding to scattering from the central blade of the seven blade analyser.

## 6.1 LSCO+O $x=0$

In Crystallographica a reflection list for the structural peaks was generated for LSCO  $x=0$  in the  $Bmab$  phase but with the measure lattice parameters of LCO+O. This list of reflections and their structure factors was used in the virtual crystal along with the calculated absorption- and incoherent cross-sections. The sample (sLSCOc.0) has an irregular shape which was approximated by a box with dimensions  $2.65\text{mm} \times 2.65\text{mm} \times 0.5\text{mm}$ .

The fundamental Bragg peaks at (020) and (002) were simulated with -n 5e8 and REP=1 using BP=0.45-1.05. As shown in Figure 6.1 the physical LCO+O crystal is twinned but this is not simulated. An overall scaling of the simulated data of 0.3 is appropriate when comparing to the measured intensity, as seen in the scans through (002) in the bottom of Figure 6.1. The small misalignment of a3 in the scan though (002) was later corrected in the experiment. The simulated scans though (020) in the top of the same figure seem to need a scaling which is a factor two smaller, but this is due to the twinning being so large that only two of four domains is caught by the resolution in the rocking curve through (020). The other two domains can be seen in the second peak in the longitudinal scan through (020). The domain areas are of approximately equal size giving an overall instrumental scaling factor of 0.3.

The most optimal value of the mosaicity through (020) is 16' whereas it is 12' through (002) but the  $\Delta d/d = 4 \cdot 10^{-3}$  is optimal for both. However putting mosaicity to 14' reproduces three of the widths within 1% and the last within 5%. The (014) peak in Figure 6.2 was simulated with -n 5e8 and REP=8 using BP=0.95-1.05, mosaicity=14' and  $\Delta d/d = 4 \cdot 10^{-3}$ . The simulated data are shown together with the corresponding measured data at low temperatures. From comparison of the width of the measured data with the simulated it is seen that the Bmab peak is resolution limited along L as the width is the same as the simulated L scan through (014) within errors. It was checked that using a bandpass of BP=0.45-1.05 which includes the second order scattering (20 meV) from the monochromator does not change the intensity or width of the simulated peak.

If we assume the expected intensity of the (014) peak to have the same scaling factor as the fundamental reflections in the virtual experiment, it is seen that the measured scattered intensity of (014) is a factor of  $\frac{0.3}{0.12} \sim 2.5$  lower than expected if the sample was described by a pure  $Bmab$  phase of LCO. If the integrated area of the (014) plus the staging peaks is however taken into account this sum is close to the expected for a pure  $Bmab$  phase. It is therefore possible that the real LCO+O sample has a part which is  $Bmab$  and another part which is staged and perhaps described within the  $Fmmm$  setting.

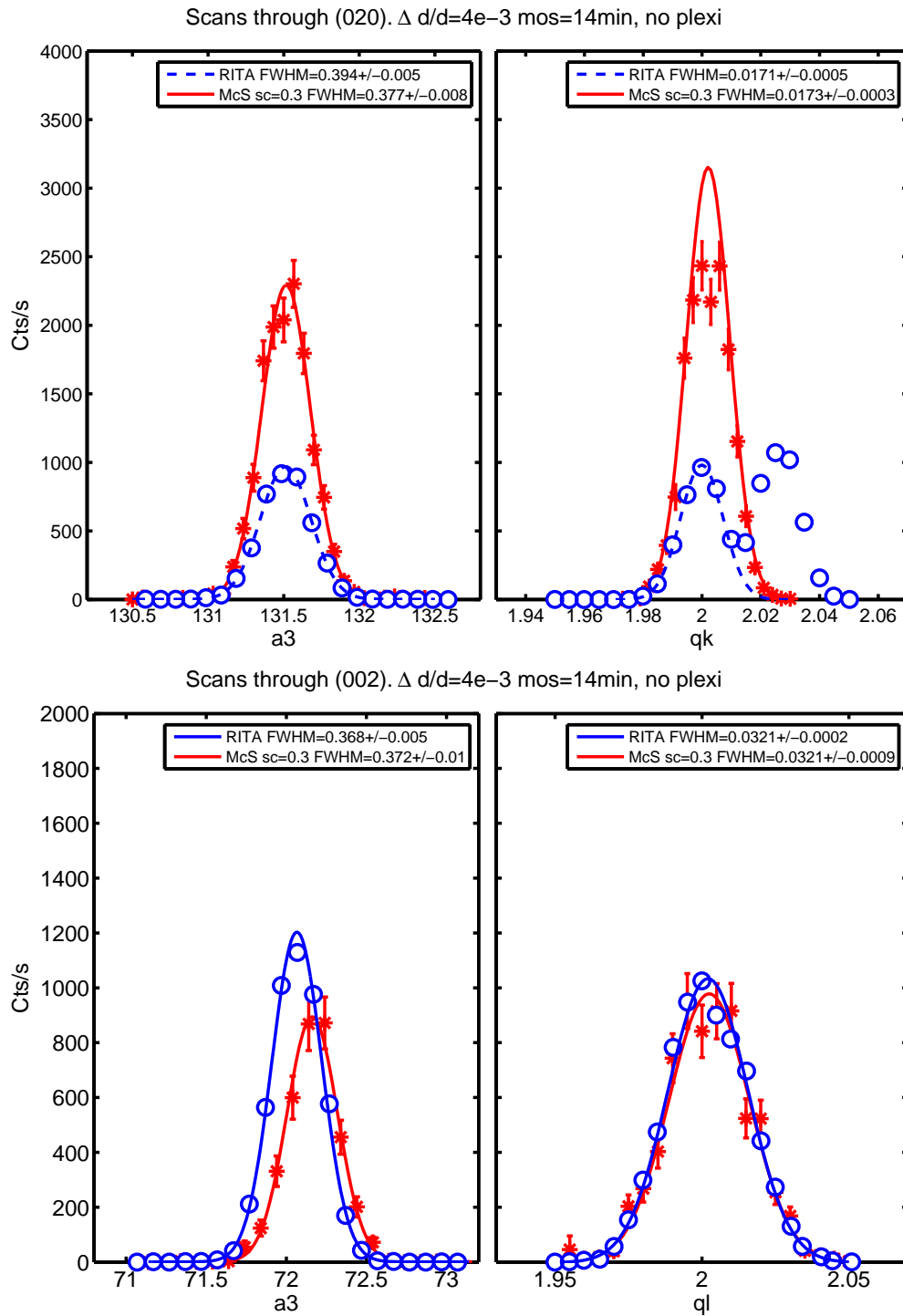


Figure 6.1: Scans through basic reflections of LCO+O  $x=0$ . In the top figure transversal and longitudinal scans through (020) are shown and the bottom similar scans through (002) are shown.

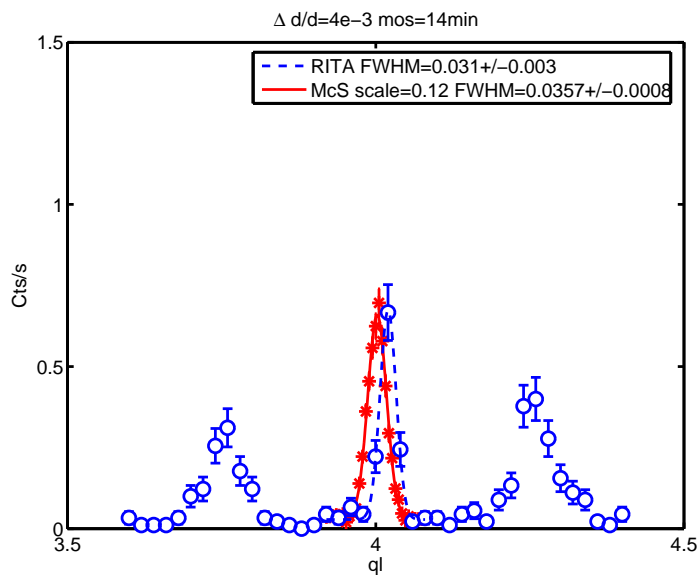


Figure 6.2: Scans showing staging of LSCO+O  $x=0$ . The simulation is of the (014) peak in  $B_{mab}$  LCO.

## 6.2 LSCO+O $x=0.04$

In Crystallographica a reflection list for the structural peaks was generated for LSCO  $x=0.04$  in the  $Bmab$  phase but using the lattice parameters measured in LSCO+O  $x=0.04$ . This list of reflections and their structure factors was used in the virtual crystal along with the calculated absorption- and incoherent cross-sections. The sample (sLSCO\_4A-C) had an irregular shape which was approximated by a box with dimensions  $2.1\text{mm}\times 2.1\text{mm}\times 2.1\text{mm}$ . The fundamental Bragg peaks were simulated with  $-n\ 5e8$  and  $\text{REP}=1$  using  $\text{BP}=0.45-1.05$ . Most of the widths of the transversal and longitudinal scans through (020) and (002) were simulated within 3%, and all are simulated within 5% of the measured value by setting mosaicity to  $16'$  and  $\Delta d/d = 4 \cdot 10^{-3}$ . The measured and simulated data and their fits are shown in Figure 6.3, and it is seen that an overall scaling of the simulated data by 0.4 is appropriate. The splitting of (020) is visible in the longitudinal scan but not quite resolved hence the factor two scaling of the simulated data which was necessary in LCO+O between the scans through (020) and (002) are not employed here. The small  $0.3^\circ$  misalignment of  $a_3$  in the scan through (002) was later corrected in the experiment and the value of the intensity is a bit different than the longitudinal scan since the transversal scan was taken at slightly different position.

The (014) peak was simulated with  $-n\ 5e8$  and  $\text{REP}=8$  using  $\text{BP}=0.95-1.05$  and the simulated data are shown with the corresponding measured data at low temperature in Figure 6.4. Comparing the width of the measured peak with the simulated it is seen that the measured  $Bmab$  peak is not resolution limited. Let us assume that the expected scaling factor on the simulations of the (014) peak is the same as the scaling factor of the fundamental peaks ( $=0.4$ ). Then it is seen from the actual scaling factor of 0.15 in Figure 6.4 that the intensity at the peak position is approximately a factor of  $\frac{0.4}{0.15} \sim 2.5$  lower than expected for a pure  $Bmab$  phase. However, if the integrated intensity of the measure broadened (014) peak (dashed blue line in Figure 6.4) is compared to the resolution limited simulation, the intensity corresponds to the expected if the sample had been LSCO  $x = 0.04$  with a pure  $Bmab$  phase.

Considering the integrated area of both the (014) and the staging satellites together, the intensity is a factor of 3 larger than the simulated integrated area of the  $Bmab$  (014) peak in LSCO  $x=0.04$  after the simulation has been scaled by the overall factor 0.4 in this experiment. Thus the scattering cannot simply be attributed to part of the sample being in the  $Bmab$  phase while the other part is a staged phase described by the  $Fmmm$  setting.

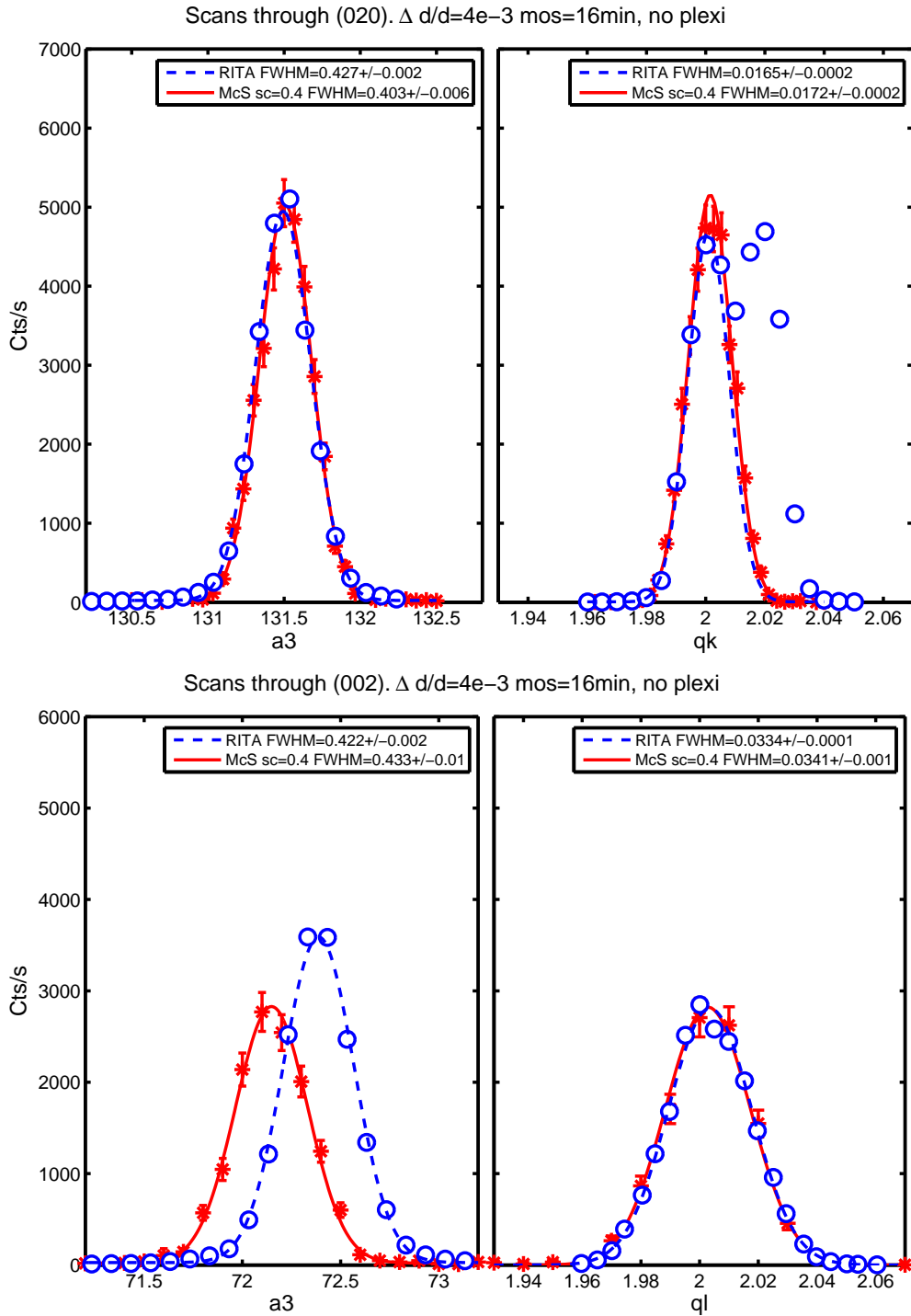


Figure 6.3: Scans through basic reflections of LSCO+O  $x=0.04$ . In the top figure transversal and longitudinal scans through (020) are shown, and at the bottom similar scans through (002) are shown. The peak position in the rocking curve was renormalized to the nominal value matching the value in the McStas scan. Also the scan was taken slightly off the centre of the longitudinal scan.

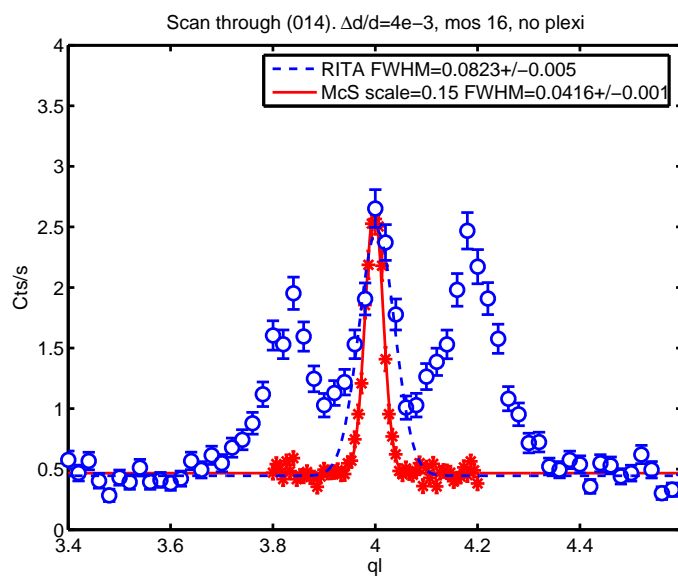


Figure 6.4: Scans showing staging of LSCO+O  $x=0.04$ . The simulation is of the (014) peak in *Bmab* LSCO with  $x=0.04$ .

### 6.3 LSCO+O $x=0.065$

In Crystallographica a reflection list for the structural peaks was generated for LSCO  $x=0.065$  in the  $Bmab$  phase but using the lattice parameters measured in LSCO+O  $x=0.065$ . This list of reflections and their structure factors was used in the virtual crystal along with the calculated absorption- and incoherent cross-sections. The sample (sLSCO\_0.065A-B) had an irregular shape which was approximated by a box with dimensions  $2.8\text{mm}\times 2.8\text{mm}\times 2.8\text{mm}$ . The simulations of the scans through the fundamental Bragg peaks in Figure 6.5 were performed using `-n 5e8 end REP=1`. As is seen from the figure the mosaicity is quite large and unevenly distributed, however I have chosen to perform a simple Gaussian fit and use this as a guide to the setting of the mosaicity in the simulations. The mosaicity and lattice spacing variation used to make the simulation match the measured width are slightly different for the (020) and (004) reflections as seen in Figure 6.5. However using an interpolated value of mosaicity=51' and  $\Delta d/d = 4 \cdot 10^{-3}$  reproduces the measured width of the narrow Gaussian (014) peak within errors. The simulations used `-n 5e8 and BP=0.95-1.05`. The broad Gaussian underneath the resolution resolved one might result from some 'disordered tilt' pattern due to random distribution of the excess oxygen making the octahedra tilt in no particular pattern along  $L$ .

The intensity is however larger than expected based on the following argument: Let us assume that the expected scaling factor on the simulations of the (014) peak is the same as the scaling factor of the fundamental peaks (=0.55). The actual scaling factor of the simulated (014) peak is 1.65 which can be interpreted as the structure factor of the (014) reflection of LSCO+O  $x=0.065$  being 3 times larger than for the same reflection of LSCO  $x=0.065$  in the  $Bmab$  phase.

Including the area of the broad Gaussian at the (014) position too, the integrated intensity of the measured peak is 9 times larger than the simulated. Although there might be an effect of the irregular shape of the sample which is not simulated, the large intensity can not be attributed a part of the physical sample being in  $Bmab$  phase similar to the one of LSCO  $x=0.065$  and another part having disordered tilts. The virtual experiments suggest that the  $F_{(014)}^2 = 0.0442$  barns calculated from LSCO  $x=0.065$  in the  $Bmab$  phase is underestimated when the crystal is superoxygenated.

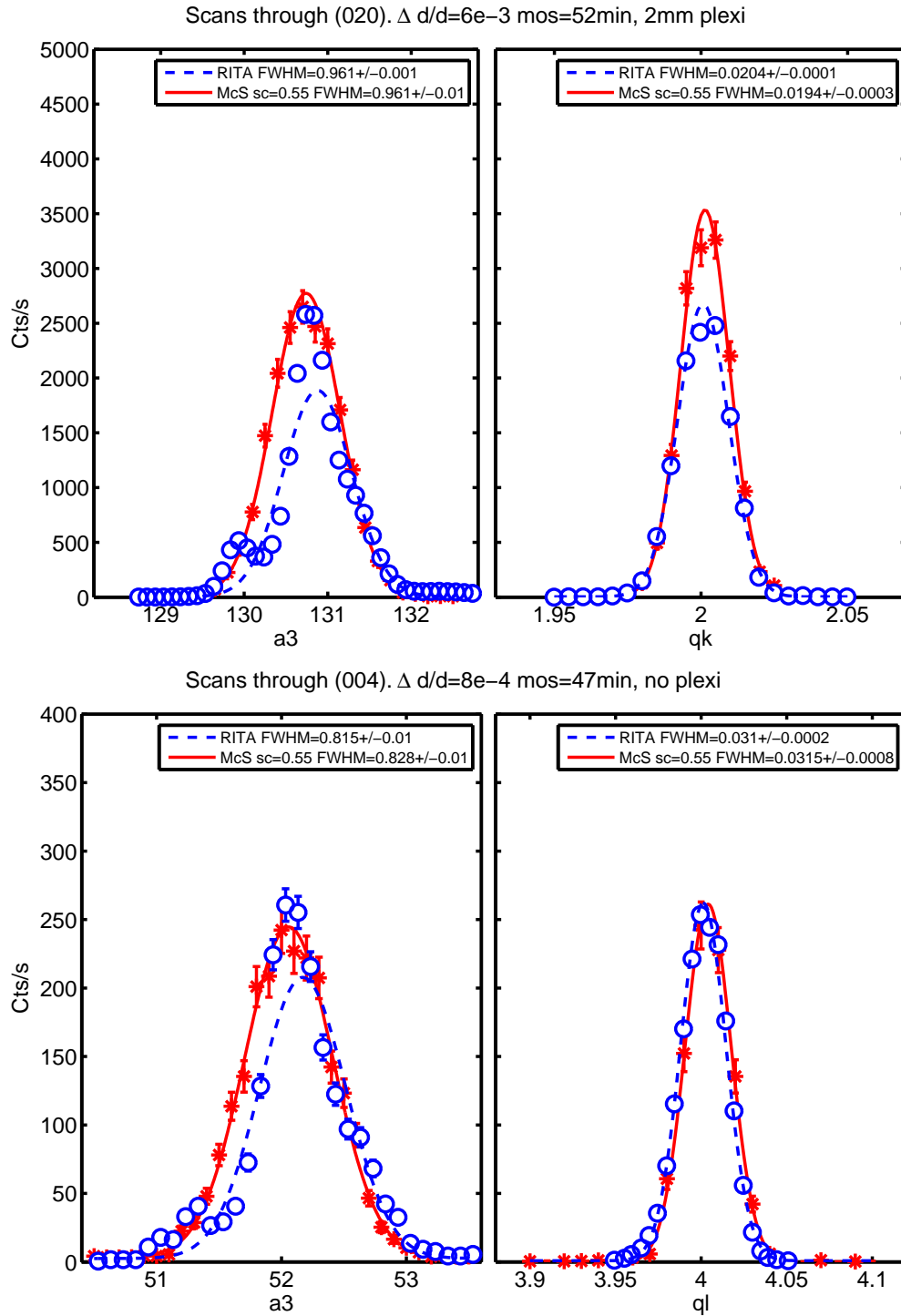


Figure 6.5: Scans through basic reflections of LSCO+O  $x=0.065$ . In the top figure transversal and longitudinal scans through (020) are shown and the bottom similar scans through (004) are shown.

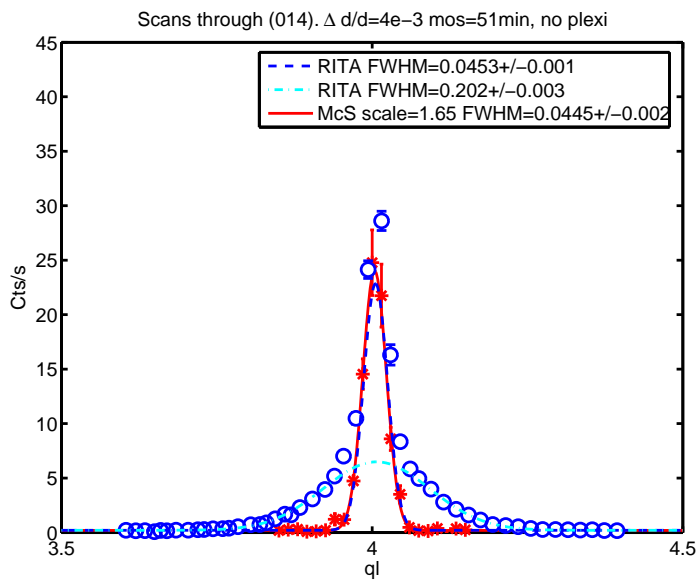


Figure 6.6: Scans along L through (014) of LSCO+O  $x=0.065$ . The simulation is of the (014) peak in *Bmab* LSCO with  $x=0.065$ .

## 6.4 LSCO+O $x=0.09$

In Crystallographica a reflection list for the structural peaks was generated for LSCO  $x=0.09$  in the  $Bmab$  phase but using the lattice parameters as measured in LSCO+O  $x = 0.09$ . This list of reflections and their structure factors was used in the virtual crystal along with the calculated absorption- and incoherent cross-sections. The sample (sLSCO\_0.09) has an irregular shape which was approximated by a box with dimensions  $4.5\text{mm} \times 4.5\text{mm} \times 3\text{mm}$ .

The optimal value for the mosaicity parameter in order to reproduce the peak width of a3 scans through (020) and (-200) is  $31.5'$  and  $33'$  respectively. However using isotropic mosaicity of  $32'$  and  $\Delta d/d = 7e-3$  reproduces the peak widths of transversal and longitudinal scans through basic Bragg reflections in the  $(H, K)$  plane within 5% as seen from figure 6.7. These scans actually cover the splitting of each Bragg peak in four unresolved peaks due to twinning as part of the mosaicity and  $\Delta d/d$  parameters.

The second order scattering peak from 20meV neutrons off (-200) is shown in figure 6.4. In McStas it was generated by a source with bandpass 0.45-1.05 corresponding to 4.54-24.69meV. By setting the instrument to scatter 5meV neutrons elastically at the (-100) reflection and taking out the filter, the peak is scanned just as in the physical experiment. The width of the simulated peak is 0.0111(2) rlu and agrees within 7% of the measured one but there is a scaling of 0.01 on the simulated data. Some of this downscaling is due to the decreased reflectivity of 0.63 of PG(002) at 20meV compared to the value of 0.81 at 5meV. This gives a downscaling of the intensity reflected from the monochromator and analyser of  $(0.63/0.81)^2 = 0.6$  on top of the overall instrumental scaling of 0.7, in total a factor of 0.4. However the additional factor of 0.07 to get totally  $0.03 * 0.6 * 0.7 = 0.03$  is unaccounted for at this point. Since the other experiments where second order scattering passes to the detector also have a low scaling factor I believe the description of the monochromator\_flat might be too simple at this point to simulate the intensity correctly as discussed in Section 5.6. The detector efficiency also depends on the energy and accounting for this would give a lower count-rate if the beam contains higher order (faster) neutrons scattered from the monochromator. Finally the crystal might be partially shielded by the Cd-foil covering the holder in the physical experiment.

The IC AFM peak position is close to (-100), and since the instrumentally resolved line width at this position was simulated within 7%, I assume that the instrumentally resolved line width at the IC AFM position too can be predicted by the virtual experiment within 7%.

The structure factor of the magnetic peak was put arbitrarily to  $F^2 = 0.01$  which gives reasonable runtime for a scan with -n 5e8 (1 min using 32 processors). The scattering from this peak in McStas needs to be scaled arbitrarily by 0.002 in order to match the physically measured intensity as shown in figure 6.9. Is it seen that using the mosaicity and  $\Delta d/d$  found by adjusting the McStas single crystal on the Bragg reflections gives a simulated resolution limited peak at  $(-0.885, 0.123, 0)$  with FWHM  $w_r^G = 0.0098(2)$  r.l.u. which is slightly less than the measured  $w_m^G = 0.013(1)$  r.l.u. along  $K$ . If this extra width is taken to be a signature of finite size broadening it is

$$w_b^G = \frac{2\pi}{5.337\text{\AA}} \sqrt{0.0130^2 - 0.0098^2} = 0.010(2)\text{\AA}^{-1} \quad (6.1)$$

which is the same as the estimated intrinsic width of the IC AFM peak in 4.8.4. The estimate of the correlation length can be either  $2\pi/w_b^G = 620 \pm 150\text{\AA}$  or by the Scherrer formula  $\frac{K\lambda}{B \cos \theta} = \frac{0.9 \cdot 4.045}{0.010 \cdot \cos(-39.8/2)} = 380\text{\AA}$  with  $B = 2 \tan^{-1} \frac{\sigma}{2q_{IC}}$ . However the simplest model for the correlation length is exponentially decaying in real-space which would give a Lorentzian line shape in reciprocal space. When convoluted with the Gaussian instrumental resolution the resulting line shape is a Voigt. Keeping the Gaussian width from the McStas simulations, the Lorentzian FWHM of the Voigt fit is  $w_b^L = 0.005(2) \text{ rlu} = 0.006(2) \text{\AA}^{-1}$  giving correlation length of  $2/w_b^L = 340 \pm 120 \text{\AA}^{-1}$ .

The mosaicity in the K,L plane seems to be much smaller than in the H,K, plane as seen in Figure 6.10. As is seen from the figure one set of mosaicity and  $\frac{\delta_d}{d}$  parameters cannot even be matched within the K,L plane on two orthogonal reflections. It is therefore also difficult to predict the line width of the (014) peak by interpolation as seen in Figure 6.11(top). At the bottom of the same figure, a McStas simulation is shown with the same line width as the measured but using a different set of parameters. The highly anisotropic mosaicity might be the source of this discrepancy. Hence it would be a good next step to develop the single crystal component to cover cases of anisotropic mosaicity in the future.

We can still, however, conclude qualitative on the virtual experiments even in this scattering plane. If we assume that the scaling factor (1.5) of the fundamental Bragg peaks is expected to apply to the (014) peak, the measured intensity of the (014) peak in LSCO+O is a factor of 10 too large compared to the expected of a pure  $Bmab$  phase in LSCO  $x=0.065$ . As in the case of LSCO+O with  $x=0.04$  and  $x=0.065$  it seems that the structure factor of the (014) is much larger than the structure factor of the pure  $Bmab$  phase in the corresponding non-superoxygenated compound.

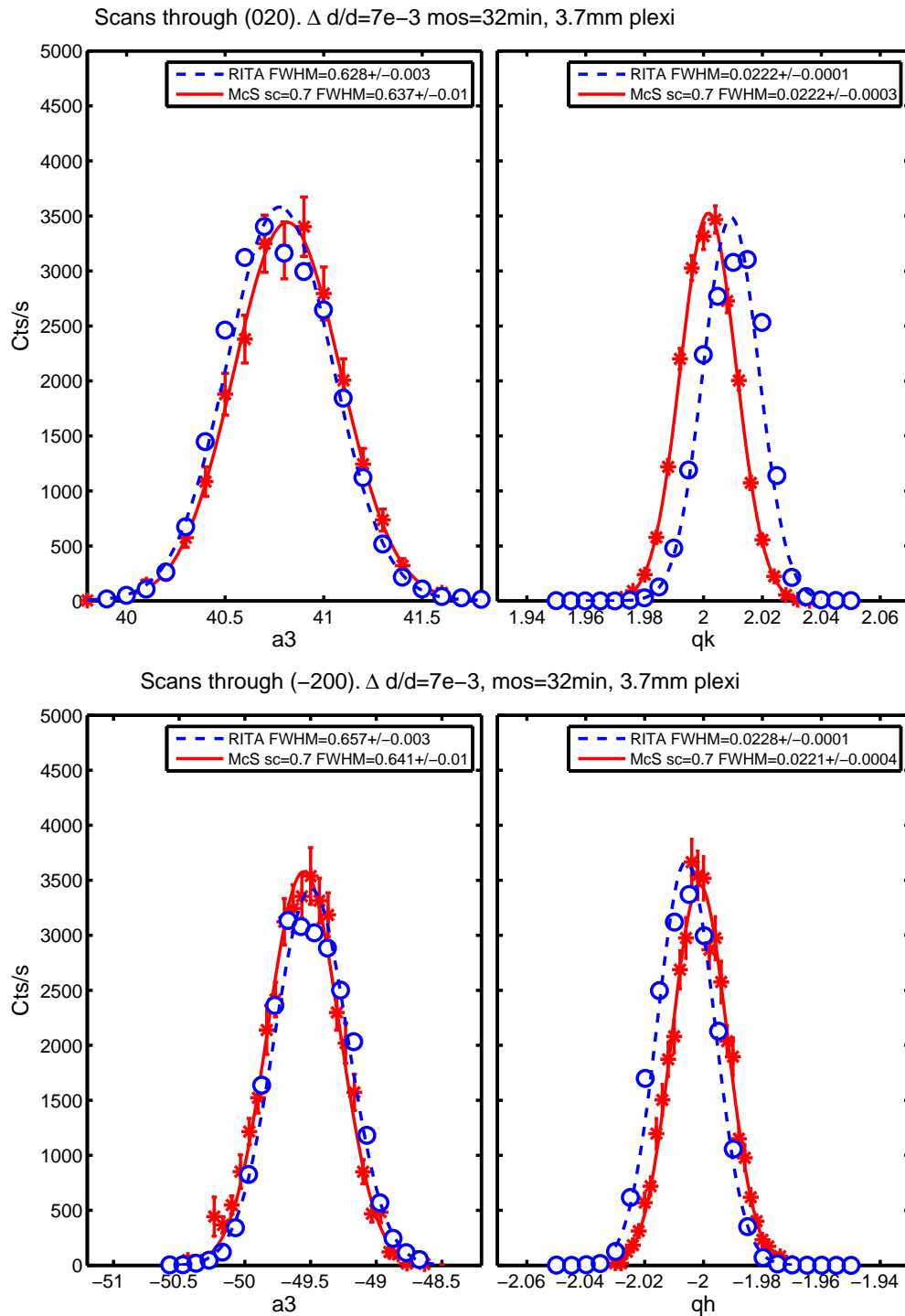


Figure 6.7: Scans through basic reflections of LSCO+O  $x=0.09$ . In the top figure transversal and longitudinal scans through (020) are shown and the bottom similar scans through (-200) are shown.

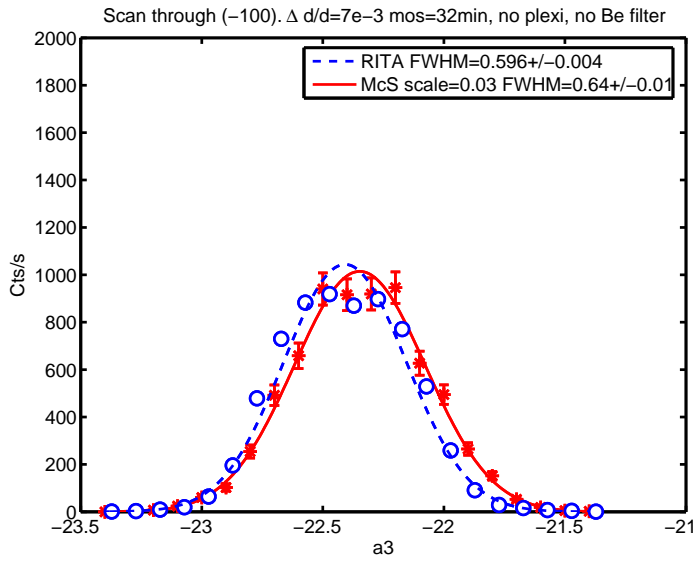


Figure 6.8: Measured and simulated scan through the (-100) position of LSCO+O  $x=0.09$ . The intensity comes from second order scattering off (-200).

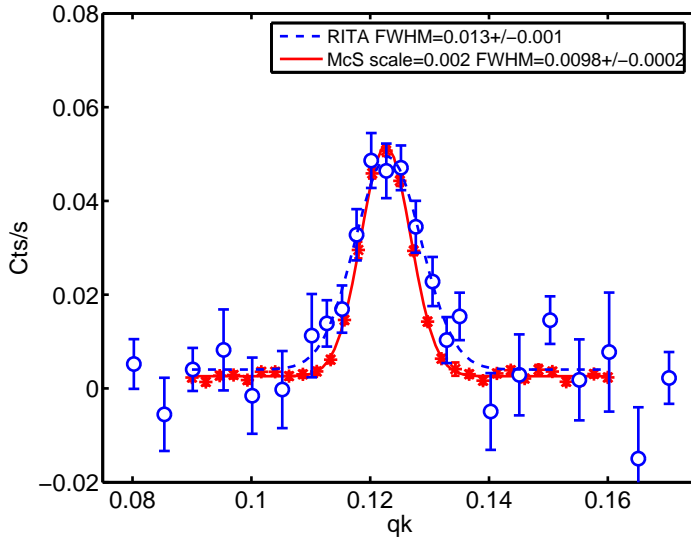


Figure 6.9:  $K$  scan through the IC AFM position at (-0.885, 0.123, 0) of LSCO+O  $x=0.09$  using same mosaicity as the scans through the nuclear Bragg peaks. The RITA-II data in the figure were measured at  $T=2$  K but are have been subtracted a fitted sloping background found from the same scan at  $T=40$ K.

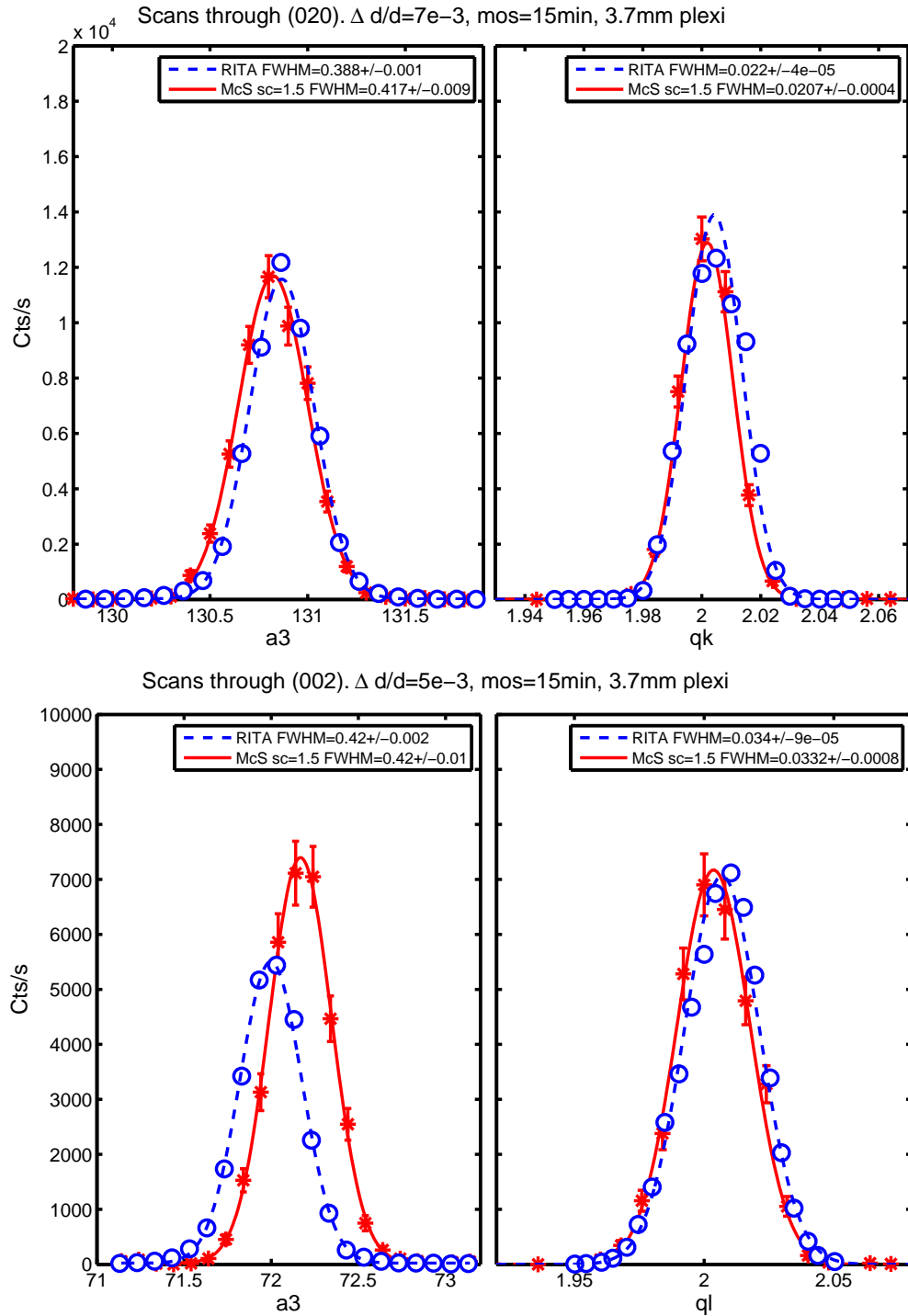


Figure 6.10: Scans through basic reflections of LSCO+O  $x=0.09$  in the (0KL) plane. In the top figure transversal and longitudinal scans through (020) are shown and the bottom similar scans through (002) are shown.

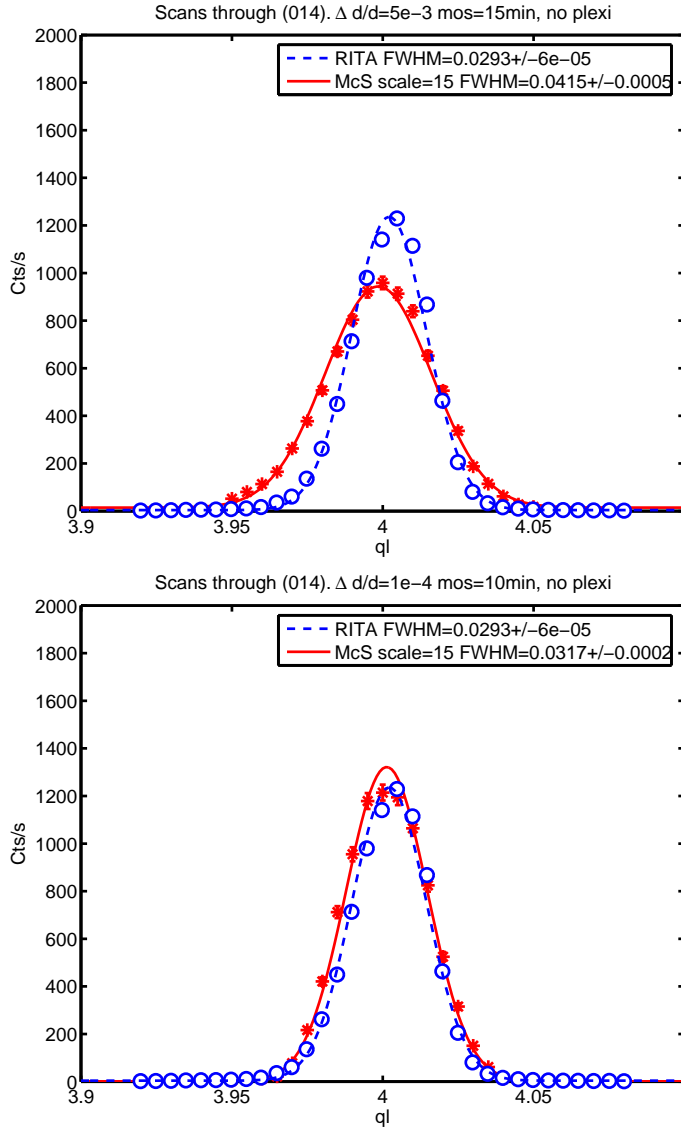


Figure 6.11: Scans along L through (014) of LSCO+O  $x=0.09$ . The simulation is of the (014) peak in  $Bmab$  LSCO with  $x=0.09$ . The top scan is using mosaicity=15 and  $\Delta d/d = 5 \cdot 10^{-3}$  which are the expected values of the simulated crystal. The bottom simulation uses mosaicity=10 and  $\Delta d/d = 10^{-4}$  (as discussed in the text) which gives a simulated width close to the measured one.

## 6.5 Summary and discussion of the virtual data analysis experiments

In this section the virtual experiments of LSCO+O are discussed. A comprehensive table of the simulations of the fundamental Bragg peaks is shown in Table 6.1. The interpretation of the broadened *Bmab* and staging peaks have been presented in Chapter 4 and will not be repeated here.

### 6.5.1 Line width

The line width of the fundamental Bragg peaks could be simulated within errors of the measured value. However the optimal mosaicity and  $\Delta d/d$  parameter set of each of the two fundamental 'adjustment' reflections in the same scattering plane were slightly different, reflecting anisotropic mosaicity of the samples. In most cases however it was possible to use an interpolated parameter set which reproduced the fundamental peaks within 1-5%. The interpolated parameter set was used to predict the instrumentally resolved line width of other reflections in the scattering plane.

The simulated line width of homogeneous (*Bmab*) virtual LSCO samples revealed in comparison to the measured values for phase separated LSCO+O samples that the (014) peaks were instrumentally resolved for  $x=0$ , 0.065 and 0.09, but was broadened in the  $x=0.04$  sample. Likewise a small broadening of the IC AFM peak for  $x=0.09$  was identified.

To simulate the width of the peaks even better, an anisotropic mosaicity and variance in lattice distance should be incorporated in the `Single_crystal` component, and we are currently work on this aspect. Specifically, the mosaicity of  $x=0.065$  and  $x=0.09$  samples turned out to be highly anisotropic. However in the case of the  $x=0.065$  sample, interpolating between the values of the mosaicity and  $\frac{\Delta d}{d}$  parameters from the (020) and (004) reflections respectively, gave a simulated peak width at (014) very close to the width of the physically measured (014) peak. This indicates that even if the mosaicity is anisotropic the line width can still be predicted using the present method under certain circumstances. On the other hand, in the  $x=0.09$  sample, the simulated peak at (014) using interpolated values of the parameters from (020) and (002) was 30% wider than the measured peak. This however, does not change the conclusion that the (014) peak is instrumentally resolved for  $x=0.09$  since the peak width is overestimated by McStas, not underestimated.

### 6.5.2 Intensity

In some of the experiments on LSCO+O the scaling is slightly different from the factor of 0.55 found as a universal scaling by the virtual test experiments in Chapter 5. In most cases this can however be explained by the shape of the sample which is approximated by a box (of appropriate volume) but is in reality rather some fragment of a cylinder. Experiment #14 of Table 6.1 however has a scaling of 1.5 which could be due to an underestimation of the structure factors of (020) and (002) in LSCO+O  $x=0.09$  as compared to *Bmab* LSCO with  $x=0.09$  which was simulated.

Curiously the measured intensity of the (014) peak in the LSCO+O single-crystals with  $x=0.065$  and  $x=0.09$  was larger than the expected from the simulations of the corresponding non-oxygenated virtual samples which assumed all of the sample to be in the  $Bmab$  phase. Even more interesting is the fact that the integrated area of the (014) + satellites seems to grow exponentially with Sr doping  $x$ . This is very unexpected since the intensity should decrease with decreasing tilt angle. And from the splitting due to twinning we know that the orthorhombicity, and presumably thereby the tilt angle, decreases with increasing  $x$ . Therefore the intensity of the  $Bmab$  peaks should *decrease* with increasing  $x$ , not *increase*. Structural refinements of LSCO+O powder exist [52, 113], but they predict decreasing intensity of the (014) peak upon superoxygenation. Thus the increase in the intensity of the (014) peak in our data remains an open question.

In order to explain this phenomenon, further measurements of the peaks at the  $Bmab$  positions and the staging satellites in several scattering planes through each reflection need to be performed.

#	Experiment	Year	Scale	Int	Line width
9	LSCO+O $x=0$ (fund. $KL$ reflections)	2008	0.3	20%	5%
10	LSCO+O $x=0.04$ (fund. $KL$ reflections)	2005	0.4	5%	5%
11	LSCO+O $x=0.065$ (fund. $KL$ reflections)	2005	0.55	20%	5%
12	LSCO+O $x=0.09$ (fund. $HK$ reflections)	2005	0.7	10%	5%
13	LSCO+O $x=0.09$ (2. order scattering)	2005	0.03	5%	7%
14	LSCO+O $x=0.09$ (fund. $KL$ reflections)	2005	1.5	10%	5%

Table 6.1: The precision of the performed virtual experiments on fundamental reflections of LSCO+O. The second column lists the type of experiment, the third column the year the corresponding physical measurements were performed and the fourth the overall scaling of the VE to the physical experimental data. The second to last and last columns list the accuracy within which the VE reproduces the intensity and line width after the overall scaling of the particular experiment.

## Chapter 7

# Conclusion

In this chapter I will summarise some of the conclusions which were drawn from the experiments, data analysis and discussions in the previous chapters of the thesis. In order to improve the readability the conclusion has been divided into sections. Some ideas of the next steps to be taken after this thesis work in order to close some of the open questions are given in Section 7.6.

### 7.1 Virtual test experiments

It was possible to build a virtual instrument matching an actual physical neutron TAS with very high precision in the line width of particular scans on both a powder sample, an incoherent scatterer and a single crystal sample used as test cases. The precision of the scattering vector line width was typically within 1-2 % and always within 5% for fundamental reflections and finite mosaicity which was close to isotropic. The simulated elastic energy resolution using a vanadium sample was simulated within 2% for the central analyser blades and within 8% on the outer analyser blades. The precision in the reproduction of the line widths of this broad range of experiments proves that the simulations qualify as virtual experiments. In order for the intensity to be comparable to the physically measured, a universal scaling factor of 0.55 was applied to the simulation data in these elastic, monochromatic test scattering experiments, regardless of the sample type. The source of this universal scaling factor is being sought out by gold foil measurements at RITA-II PSI in the moment of writing. From the preliminary gold foil measurements it seems that the intensity at the sample position is actually a factor of approximately two lower at the sample position than expected which would explain why I have to scale my simulated data by a factor of roughly 0.5. It is therefore concluded that virtual experiments can be performed which reproduce measured data quite accurately both in terms of line width and intensity.

### 7.2 Resolution line width by virtual experiments

The virtual experiments were used to de-convolute the intrinsic width and thereby the correlation length of superstructures of LSCO+O. This was done by adjusting the single crystal sample in McStas (the virtual sample) on two

Bragg peaks within the scattering plane of interest. Interpolated values from these adjustments were used as isotropic mosaicity and variance of the lattice parameter in the subsequent virtual experiments. The virtual sample was after the adjustment considered a homogeneous version of the real crystal and any broadening of other measured peaks considered due to finite size effects in the real crystal. By this method the instrumental resolution of a peak at the IC AFM position of  $x = 0.09$  was determined and the resolution width along  $K$  found to be  $w_r^G = 0.0098(2)$  rlu. The same value within errors was found by scanning the (-200) Bragg peak at the close-by (-100) position (by second order neutrons) in the physical experiment. Likewise the simulated resolution limited width of the (014) peak along the  $L$  direction was found to match the physically measured width for  $x = 0$  and 0.065. This proves the validity of the virtual experiment by virtual sample method to reproduce the instrumentally resolved line width of particular scans of single crystals, at least in crystals close to isotropic conditions of mosaicity and variance in lattice parameter within the scattering plane.

### 7.3 Intrinsic line width and transition temperatures

By de-convolution of the measured peaks using the resolution width found by virtual experiments, the intrinsic line width broadening was determined for the IC AFM peak of LSCO+O  $x = 0.09$ . Depending on the model the measured fitted intrinsic broadening of the IC AFM peak including one standard deviation in both models, corresponds to an in-plane domain size between 200 Å and 800 Å. The magnetic correlation is concluded to extend over 50-200 pseudo-tetragonal unit cells in the in-plane  $b$ -direction. As the magnetic peaks of the other crystals were measured on IN14 for which no virtual instrument replica had been made, no virtual experiments could be performed at present. It was however estimated from the width of Bragg peaks that the IC AFM peaks of  $x=0$ , 0.04 and 0.065 were not finite size broadened. I conclude that the correlation length of the IC AFM is long for all  $x$ , exceeding 200Å. In addition, for  $x = 0.09$  the detailed data analysis showed that the correlation length is at most 800 Å.

The transition temperature of the (014) peak and the onset of staging was measured by neutron and hard x-ray diffraction, an overview is shown in Figure 7.1. It was discussed whether the (014) peak was due to magnetic scattering from an un-doped impurity phase, but since the transition temperature of the (014) peak in LCO+O is higher than the expected  $T_N$  for the undoped compound ( $x = 0$  and  $y \sim 0$ ) and no sign of a commensurate AFM phase was detected by  $\mu$ SR, it was concluded that (014) most likely belonged to the structural  $Bmab$  phase. In some of the crystals satellites (staging) corresponding to an additional tilting order of the  $\text{CuO}_6$  octahedra were however also observed around the  $Bmab$  positions. The resolution widths of the  $L$  scans though the (014) and staging peaks of LSCO+O were also investigated by the virtual experiment method. The (014) peak was instrumentally resolved for all  $x$  except  $x = 0.04$ . It can therefore be concluded that the  $Bmab$  structure is long-range ordered in most cases. The staging was finite-size broadened along  $L$  with a width corresponding to the correlation length along  $c$  being the size of the super-

structure unit cell itself. Future investigation of the in-plane correlation length of both the (014) and staging peaks will add to this picture and further clarify the morphology of the staged inclusions and if they are related to the  $Bmab$  phase or not. The periodicity of the staging increased with  $x$  which could be explained by a decreasing amount of intercalated oxygen. Direct measurement of the oxygen content by e.g. TGA analysis is however needed to clarify this question.

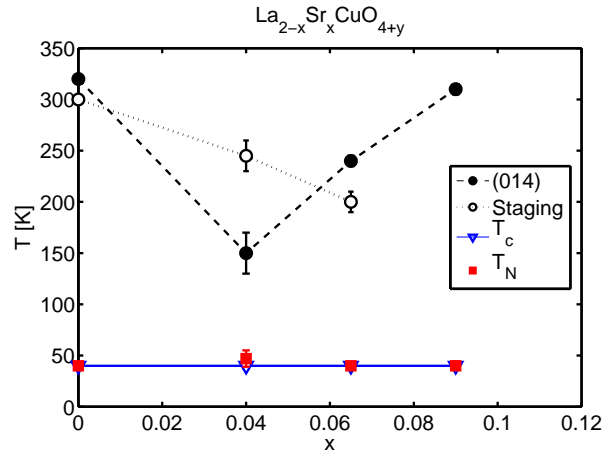


Figure 7.1: Transition temperature of in LSCO+O. The lines are guides to the eye. For  $x = 0$  the transition temperature of (014) for  $x = 0$  could not be reached by the available cryostat sample environment but the highest temperature at which we have measured it is marked in the figure. The transition temperatures of the IC AFM phase are measured by neutron diffraction in this work and the superconducting  $T_c$  is measured by bulk susceptibility in [112].

## 7.4 Structure

The IC AFM peaks positions in zero applied field could be explained by a stripe model similar to the model of LBCO and LNSCO with an IC AFM periodicity of 8 along the Cu-O bonds. Furthermore their relative intensities at zero applied field agreed with a simple model of two layers of stripes, the stripes in one layer being orthogonal to the other.

An enhancement of the IC AFM peak by application of a magnetic field was observed in LSCO+O for  $x = 0$  but not for  $x = 0.09$ . It has previously been discovered that a similar enhancement could be produced in a  $x = 0$  sample with similar staging to ours by fast cooling[108]. The conclusion of [108] was that when LCO+O is cooled too fast for the excess oxygen to order, the samples show an enhanced IC AFM signal similar to the effect of an applied field.

An explanation of the field effect could be that the oxygen ordering facilitates itinerant doped holes thereby favouring SC in a mechanism similar to that of YBCO. For  $x = 0.09$  the oxygen is not ordered indicated by the lack

of staging peaks and the lack of 'direct oxygen' peaks. According to the mechanism described above, SC is therefore not particularly favoured even at zero applied field in the Sr/O codoped LSCO+O system ( $x > 0$ ) and no field effect is observed of the IC AFM peaks.

The integrated intensity of the (014)+staging peaks was found to grow exponentially with increasing  $x$ . Furthermore, the intensity in samples with  $x > 0$  was larger than expected from virtual experiments on corresponding samples in the  $Bmab$  phase. This phenomenon cannot be explained by increasing structure factor with increasing tilt angle of the  $\text{CuO}_6$  octahedra, since tilting is expected to decrease with increasing  $x$ . Further measurements are needed to clarify the mechanism behind this interesting property and produce an accurate model of the crystal structure in superoxygenated LSCO+O single crystals.

## 7.5 Phase separation

The LSCO+O is a 'clean' HTSC system in the respect that it contains just one SC phase and just one static magnetic phase. The transition temperatures of these two phases are coinciding  $T_c \sim T_N = 40$  K just above the optimally doped superconducting transition temperature. It was concluded that even if parts of the LSCO+O samples were not oxygen-enriched or even oxygen-poor, they were not hole poor, and there are strong indications that the phase separation is electronic in nature such that the static magnetic phase has hole-doping  $n_h = 1/8$  and the SC phase has a hole doping  $n_h \sim 0.16$  in the SC phase. The IC AFM is long-range ordered within the  $(a, b)$  plane and probably only correlates over two stripe ( $\text{CuO}_2$ ) layers along  $c$ . Likewise the domain size of the staging regions (which are probably oxygen-enriched) only extends over one or two superstructure unit-cells along  $c$ . It therefore seems that the electronic phase-separation is mainly governed by in-plane correlations. From the occurrence in LBCO, LNSCO and as strongly suggested in this work also in LSCO+O, it seems that the  $1/8$  state<sup>1</sup> is somehow especially stable in the La-based cuprates. In LSCO+O it even exists without the stabilising transition to an LTT phase which occurs in LBCO and LNSCO. Since the  $1/8$  state coexists with 'optimal' superconductivity in the LSCO+O samples, LSCO+O acts as a model system of the co-existence or competition between IC AFM and SC order in HTSC. In this respect the LSCO+O system might provide the long-sought key to the secret of HTSC.

The interplay between IC AFM and SC is believed to be central to the understanding of HTSC in general and the present study has provided a small piece to the puzzle as well as proved the concept of virtual experiments by virtual samples which will be useful in further studies of the morphology in HTSC (and other) systems.

## 7.6 Outlook

An experiment has been scheduled IN14 in which I will measure if there is a field effect of the IC AFM in the staged Sr/O co-doped LSCO+O  $x = 0.04$

<sup>1</sup>here denoted by the lack of field effect in the spin stripe(-like) IC AFM

sample. This is very important in relation to the conclusions of the influence of oxygen order on the formation of the SC and IC AFM phases.

In order to clarify the rôle of the oxygen and/or staging ordering with respect to the field dependence of the magnetism it would also be very interesting to study the morphology of the magnetic structure along the  $c$ -axis direction and the staging structure along the  $a$  and  $b$  directions respectively to complete the picture. Studying magnetic correlation in the small crystals demands a high-flux cold neutron TAS like IN14, particularly since the correlations are expected to be short along  $c$  and intensity is therefore lost if  $c$  is in the scattering plane and not along the relaxed vertical direction of the TAS. The in-plane correlations of the staging structures could be studied at RITA-II where the possibility to de-convolute the peak widths by virtual experiments is readily available. Some effort will have to be made though to measure superstructures in all directions without a four-circle to scan in odd directions.

It is still somewhat unclear if staging is directly related to the oxygen content and direct measurement by TGA should be performed on pieces of each sample.

The quartet of IC AFM peaks of LCO+O should be measured both around the (100) and (010) point without an applied field. It will be interesting to see if the relative intensity between peaks at high- $Q$  and low- $Q$  positions redistribute without an applied field, perhaps to have the same distribution as LSCO+O with  $x=0.04$  and  $x=0.065$ .

In order to relate the magnetism and magnetic excitations of LSCO to superoxygenated LSCO+O, the spin excitation spectrum should be measured in LSCO+O. Highly oxygenated ( $T_c \geq 40$  K) LCO+O crystals with  $m \geq 1$  g have already been produced and inelastic neutron diffraction experiments similar to those of Figure 2.8 should be performed. These experiments could be performed at IN14 or at PANDA where preliminary results on a LCO+O crystal with  $T_c=30$  K (plus a lesser phase with  $T_c=15$ ) have been obtained.

With respect to the virtual experiments of RITA-II the source of the overestimation of the intensity when higher order scattered neutrons are allowed passage to the detector in V-RITA-II should be investigated. A measurement from RITA-II of the intensity at the monitor (after the monochromator) as function of the primary monochromator energy  $E_i = \frac{\hbar^2 k_i^2}{2m_n}$  is shown in Figure 7.6. The proton current to the target was stable in the measurement period and the data are corrected for the efficiency of the monitor which scales with  $\frac{1}{k_i}$ . Qualitatively the (interpolated) ratio of the intensities at 5 meV and 20 meV appear to match the ratio of the integrated intensity at the same energies just after the monochromator (the energy distribution is shown in Figure 5.5). The overestimated higher order contribution in the virtual experiments as compared to the physical measurements could either be due to the description of the source, the guide system or the monochromator\_flat component. Further virtual experiments tested against physical experiments are needed to clarify this issue.

The `Single_crystal` component should be developed to describe highly anisotropic mosaicity in a sample. A new prototype has very recently been developed based on the work and conclusions of this thesis and is at the moment of writing ready for testing.

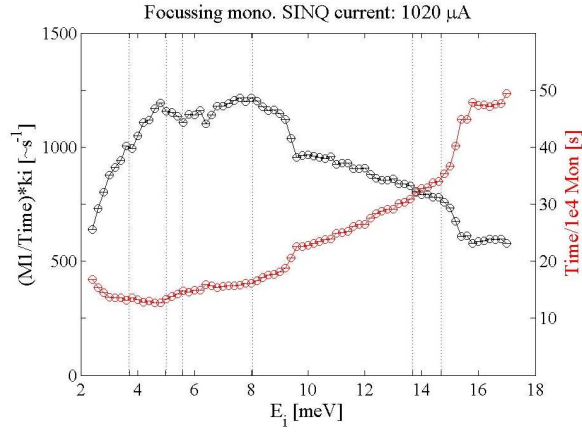


Figure 7.2: The intensity at the monitor position of RITA-II as function of energy (black). The proton current to the target was stable in the measurement period (red) and the data are corrected for the efficiency of the monitor which scales with the wave vector of the neutrons as  $\frac{1}{k_i}$ .

We also plan to perform virtual experiments of the inelastic energy resolution and compare the results to measurements of phonons in different types of materials.

# Appendix A

## BW5 hard x-ray experiments on $\text{La}_{2-x}\text{Sr}_x\text{CuO}_{4+\delta}$ $x=0,0.04,0.09$

Linda Udby (RISØ DTU), Niels H. Andersen (RISØ DTU),  
Thomas B. S. Jensen (RISØ DTU),  
Martin von Zimmermann (HASYLAB)

This document serves merely as a short resumé of the data acquired October 3rd to October 10th 2008, hence the 'data treatment' presented here is very crude and preliminary, and references to papers on the topic missing.

Energy=100.000 keV. Monochromator/analyser crystals are Si/Ge gradient crystals.

Displex and 4-circle used, in-pile aperture 1\*1 mm<sup>2</sup>. All lattice references are to the Bmab setting. During the beamtime we experienced a lot of problems with the heater not being able to maintain the temperature og to heat/cool at given rate.

### 0% Sr doped sample m=0.025g (sLCO)

This was the same piece of sample used in the June 2008 RITA-II beamrun. The sample was glued with GE-varnish in the  $(a + b, c)$ -plane on a Cu holder. Low temperature crystal parameters used:  $a = b = 5.326 \text{ \AA}$   $c = 13.233 \text{ \AA}$ .

The orthorhombic splitting of the (020) peak is shown in the first plot of in figure A.1 and the mosaicity is also seen to be small, about 0.2°. There is surprisingly a peak at (110) as seen in figure A.2 corresponding to a minority of the sample being in the P4<sub>2</sub>/ncm (LTT) or Pccn (LTO2) phase, since (110) is forbidden in the Bmab (LTO1) phase but allowed in the other two phases. A similar peak with same intensity was found at (330) (not shown). However these peaks persist to 300K, which remains to be understood. There is no peak increase of the peak at (010) which has previously been speculated to signal a

phasetransition from LTO to LTT in LNSCO by Chang[3].

The staging along  $qz$  was measured at various Bmab allowed positions as seen in figure A.3, and contrary to the earlier measurements on the 4% Sr sample with x-rays[119] no staging peaks are observed around (010), but intensity around (032) is clearly largest, in agreement with the 4% Sr sample. Rocking curves and longitudinal scan have been performed on each peak in order to compare intensities(not shown). A grid showing the broadening of the staging with respect to the Bmab peak in the  $qy, qz$  plane is shown in figure A.4 along with some scans along  $qx$  and  $qy$  likewise showing a (Lorentzian) broadening along this direction. The temperature dependence was followed for the staging peaks around (014) in figure A.5 and it is seen that the low staging at  $\Delta qx = 0.5$  and  $\Delta qx = 0.3$  disappear at  $T=190K$ , whereas the high staging number at  $\Delta qx = 0.2$  remains up to  $T=280K$ . The central Bmab peak seems also to have a sudden decrease at  $T=190K$  even after normalisation to the integrated peak intensity of (004).

Before heating, we also searched for charge ordering around Bragg positions  $(2\ 2\ qz)$  and  $(2\ 4\ qz)$ . The second position was chosen since this was reported to have the largest intensity in LBCO by Kim[144]. We found peaks at integer  $qz$  values for  $qx = 1.335$   $qy = 2$  and 4, but none at the expected charge-order positions  $(1.75\ 1.75\ qz)$ . It was checked that peaks at  $(1.335\ 2\ qz)$  were localised for  $qz=0,2,3$  and 4 but the ones at  $qz=1$  and 5 were not localised.

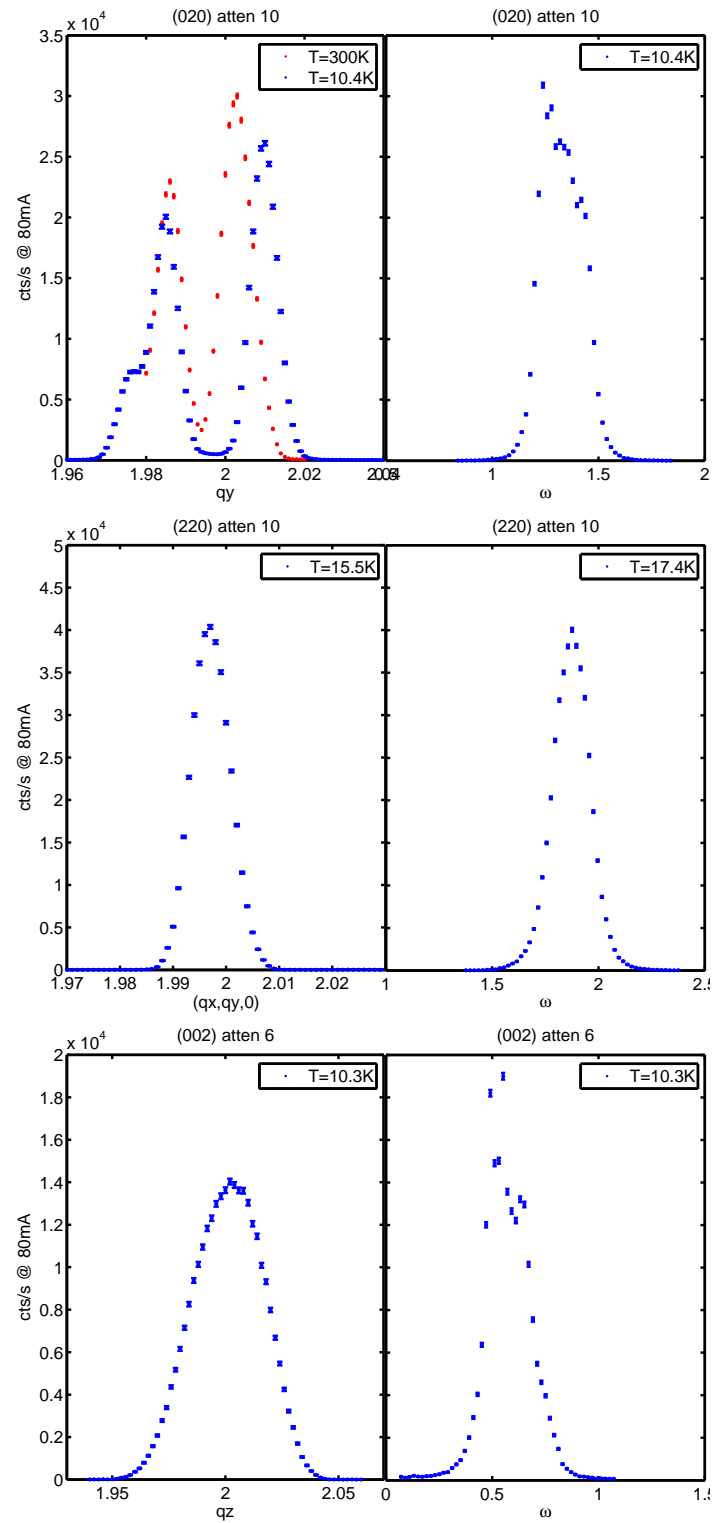


Figure A.1: **sLCO**: Longitudinal scans and rocking curves of Bragg peaks in sLCO. The longitudinal splitting of (020) increases with decreasing temperature)

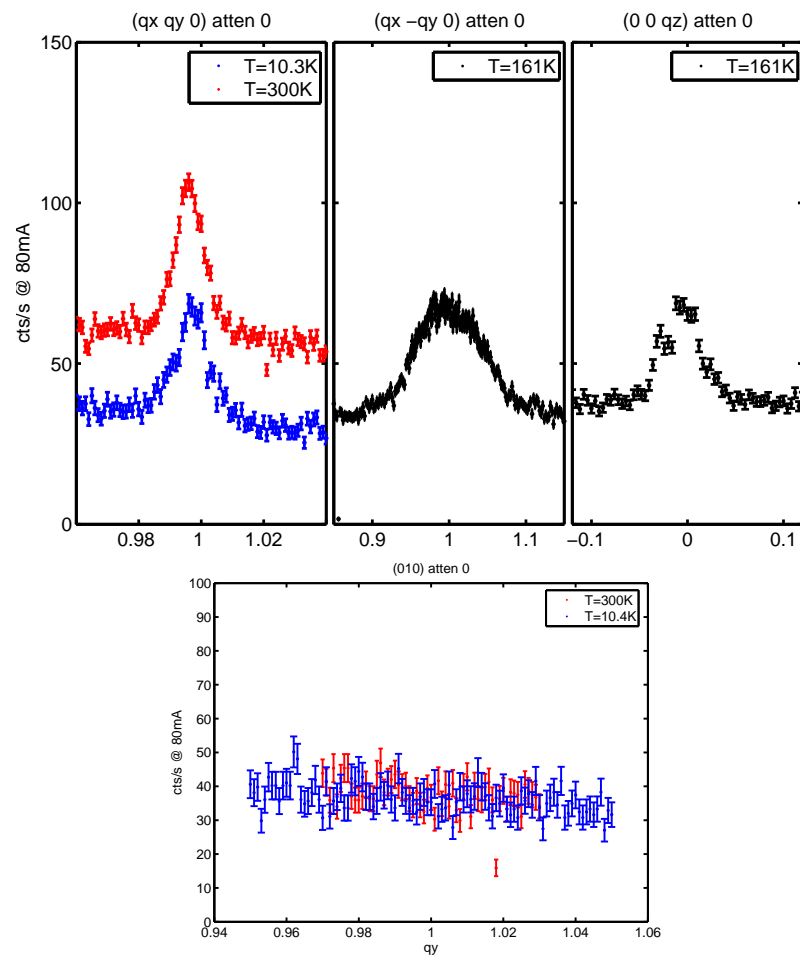


Figure A.2: sLCO: The peak at (110) and no peak at (010)

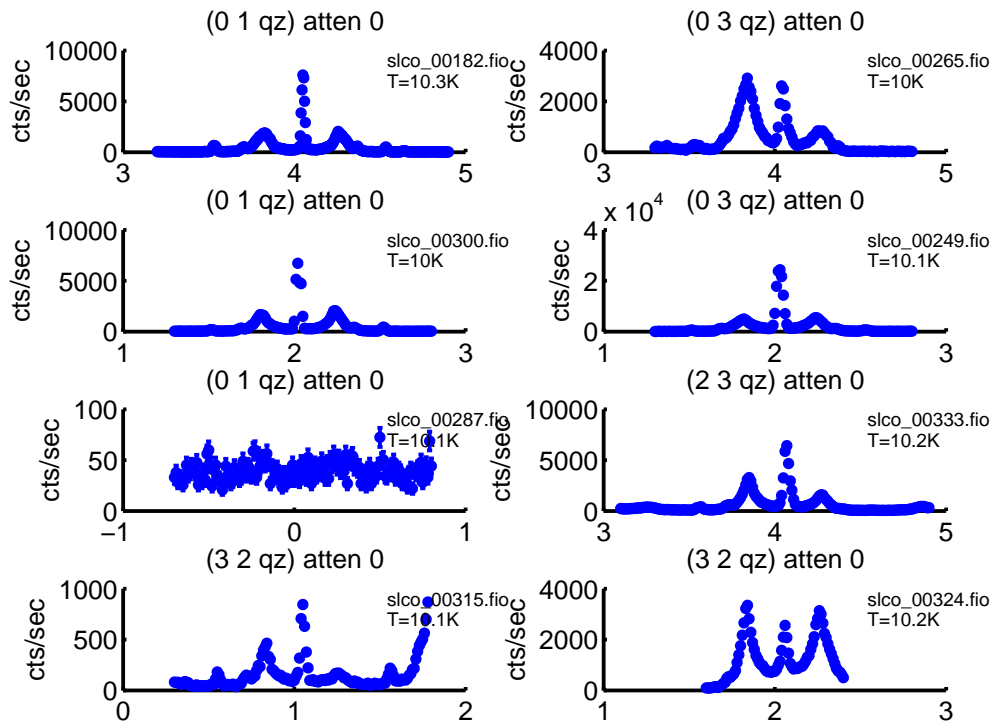


Figure A.3: **sLCO**: Staging peaks along  $qz$ . The (010) and (322) peaks are not allowed in the Bmab phase, hence there is no staging around (010). However there seems to be staging around (322) but we suspect that the scattering at this position is actually from the (232) of the twin domain which IS allowed in Bmab. All scans except (0 1  $qz$ ) lined up on central peak.

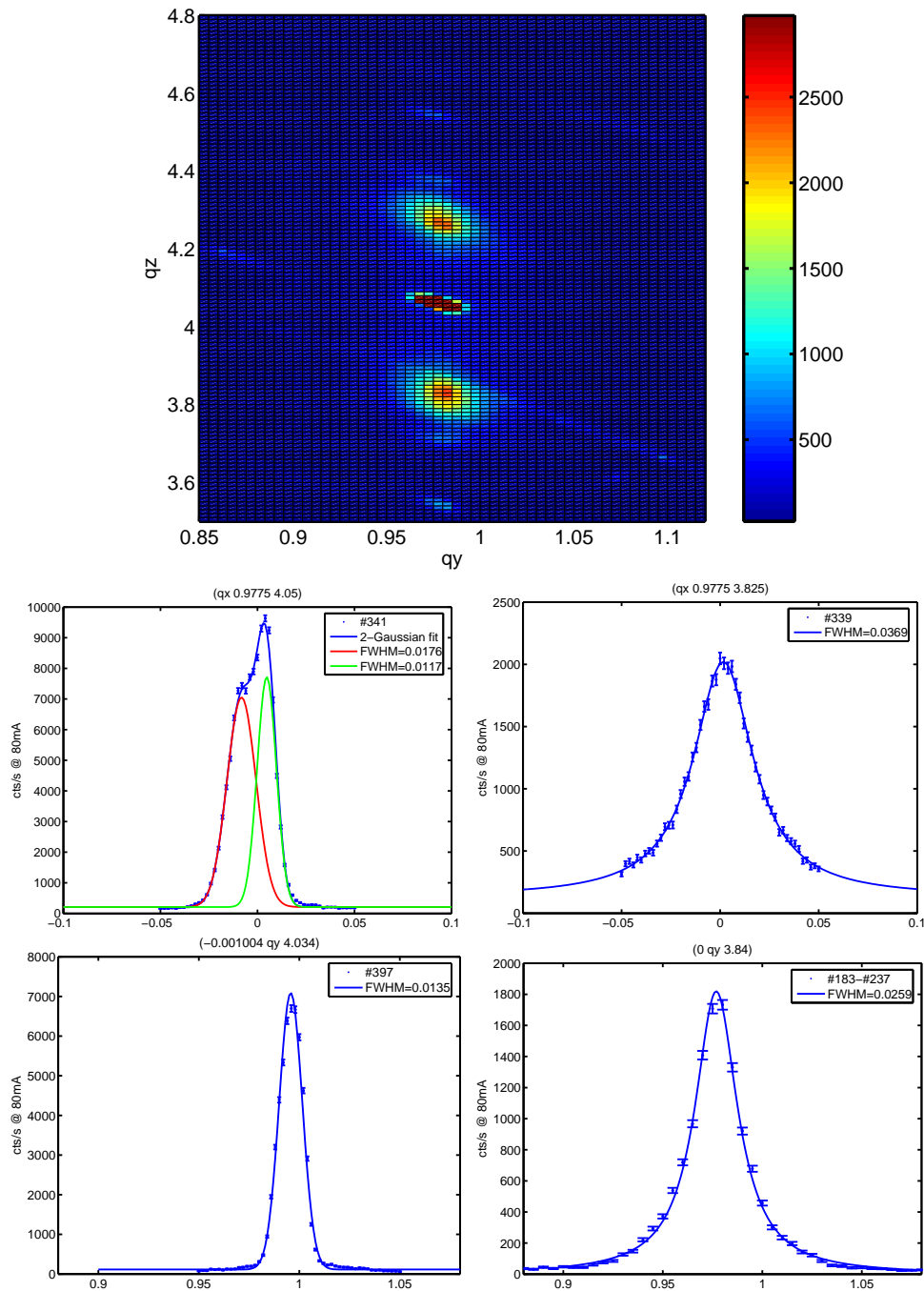


Figure A.4: **sLCO**: Top: In-plane grid around (014) showing the instrumental resolution of the central peak and the almost circular broadening of the staging peaks. The ratio of the axis is approximately correct. Some powderlines are also visible. Centre row:  $q_x$ -scan through the central peak (left) and a side-peak (right). The fits to the central peak are Gaussian whereas the fit to the side (staging-) peak is Lorentzian and widened with respect to each Gaussian fit to the central peak. Bottom row:  $q_y$ -scan through the central peak (left) and a side-peak (right). The fits to the central peak is Gaussian whereas the fit to the side (staging-) peak is Lorentzian and widened with respect to the Gaussian fit to the central peak.

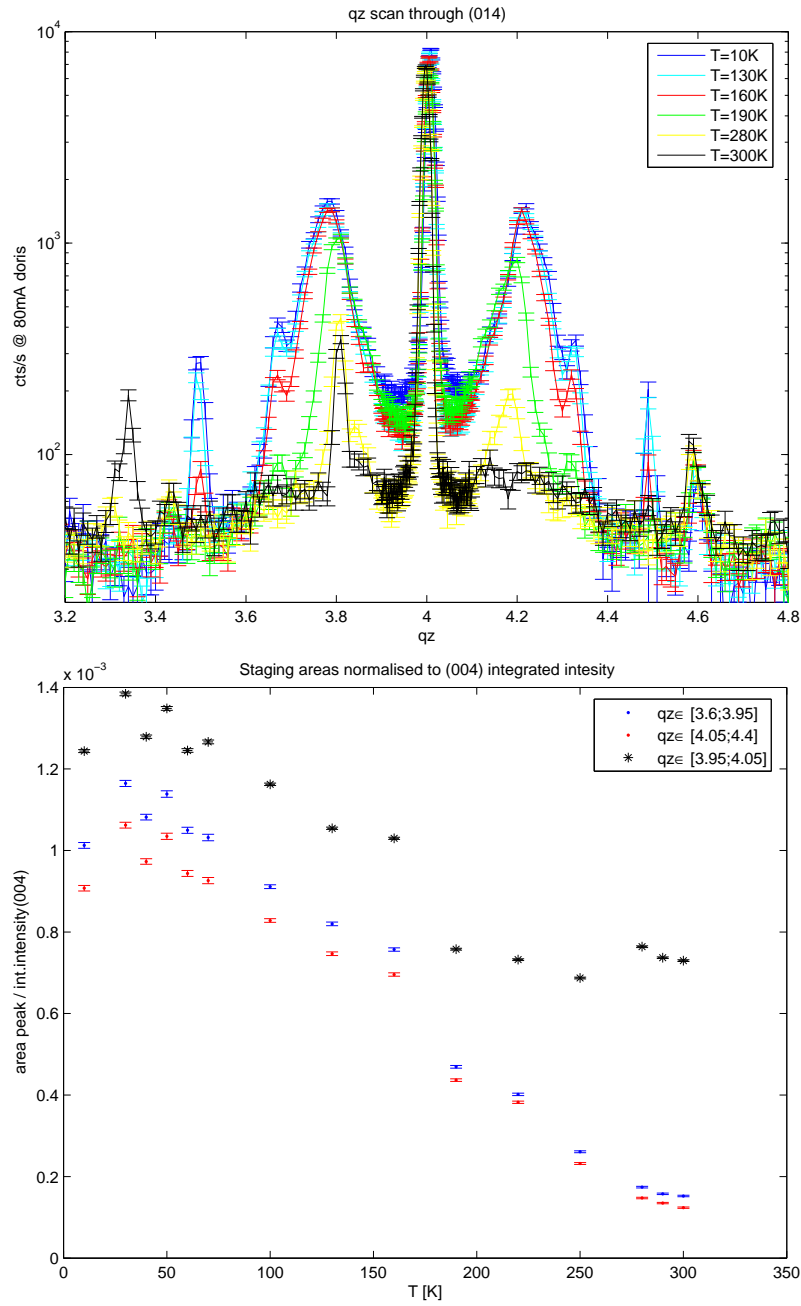


Figure A.5: **sLCO**: Top: A  $q_z$  scan through (014) at various temperatures on logarithmic scale. Bottom: Summed areas of the staging peaks, and Bmab peak at (014), all normalised to the product of summed areas of rocking curves and longitudinal scans of the (004) peak at the respective temperatures

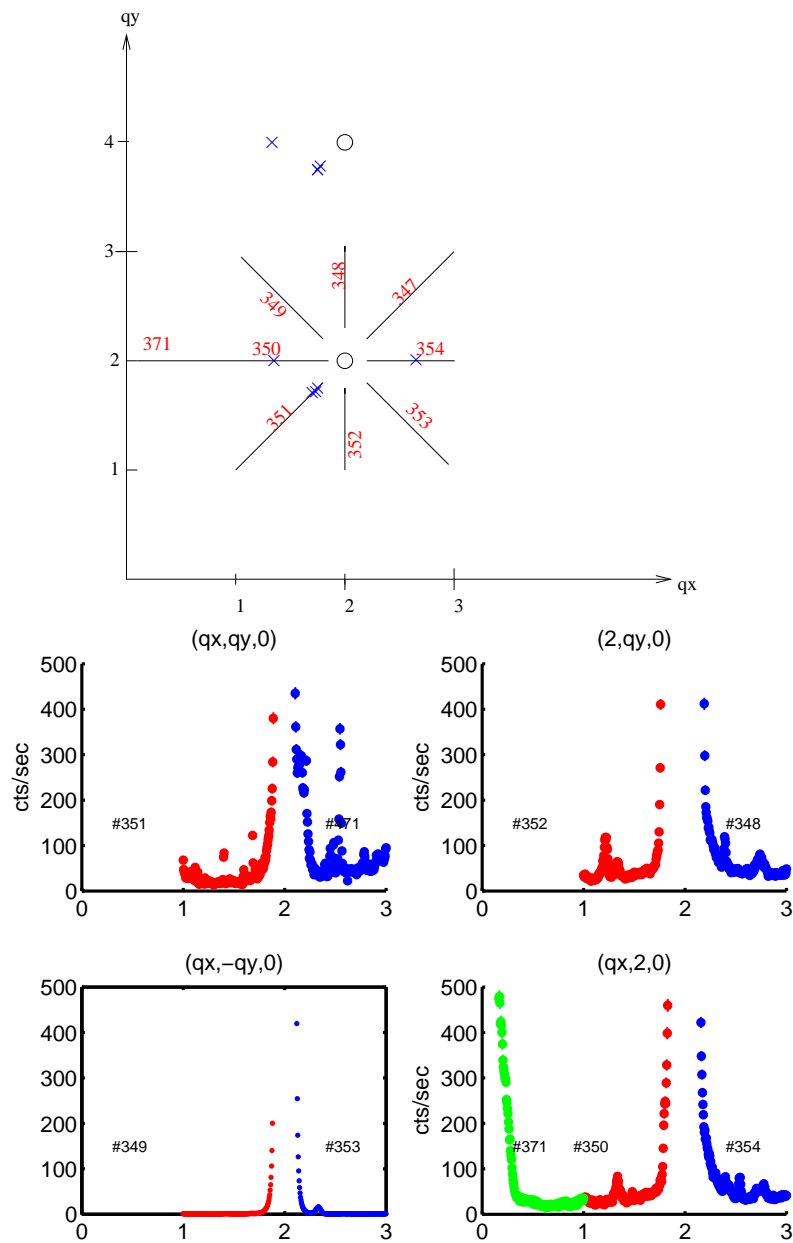


Figure A.6: **sLCO**: Top: A schematic drawing of the scans searching for charge order. The blue crosses mark the positions where scans along  $q_z$  were performed and the red numbers are the filenames of the in-plane scans. Bottom: The measured scans at the positions marked in the schematic drawing above.

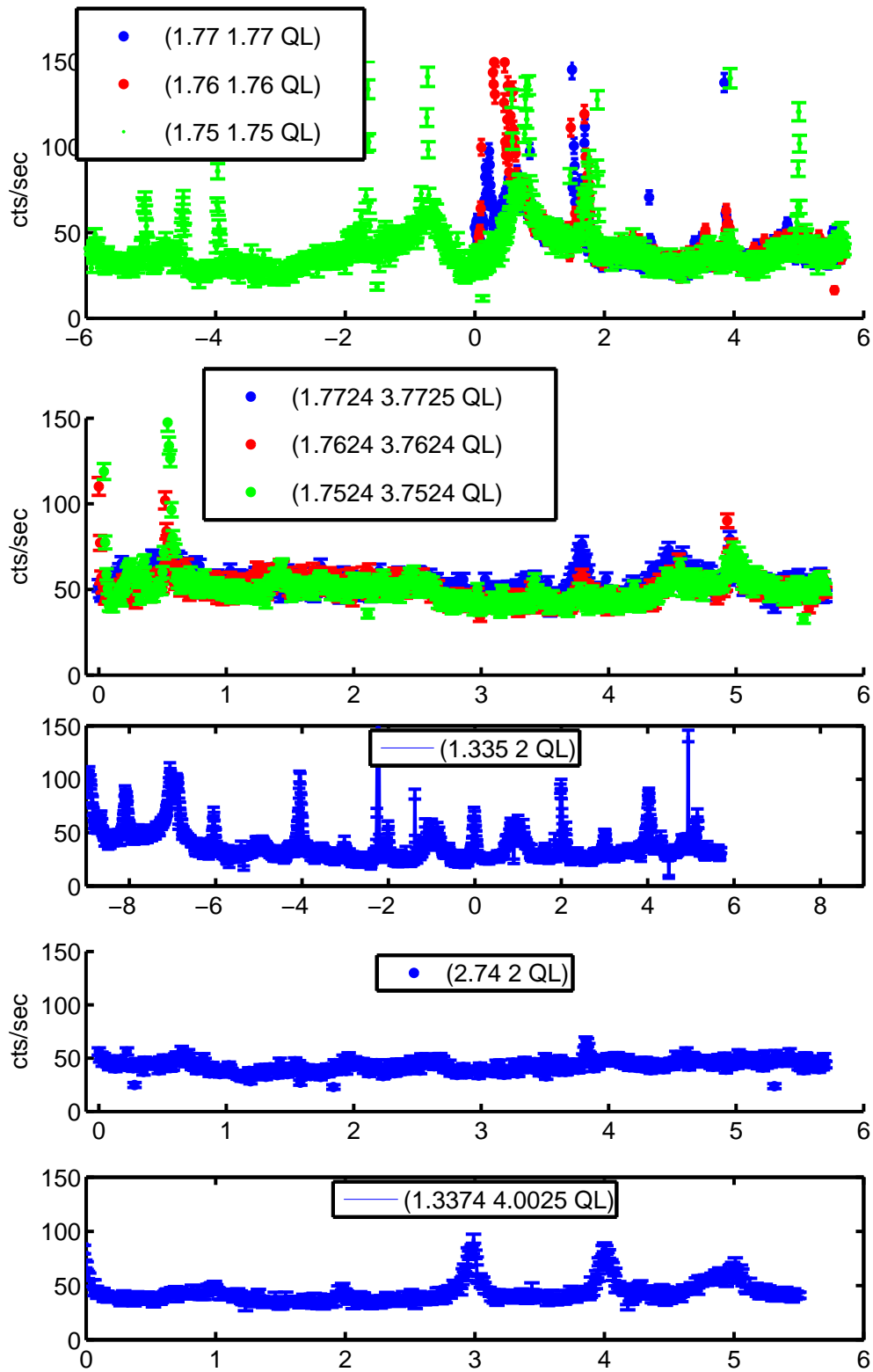


Figure A.7: *sLCO*: $qz$ -Scans through suspected charge-order peaks. There are peaks at integer  $qz$  for  $q_x = 1.335$  and  $q_y = 2$  and  $4$

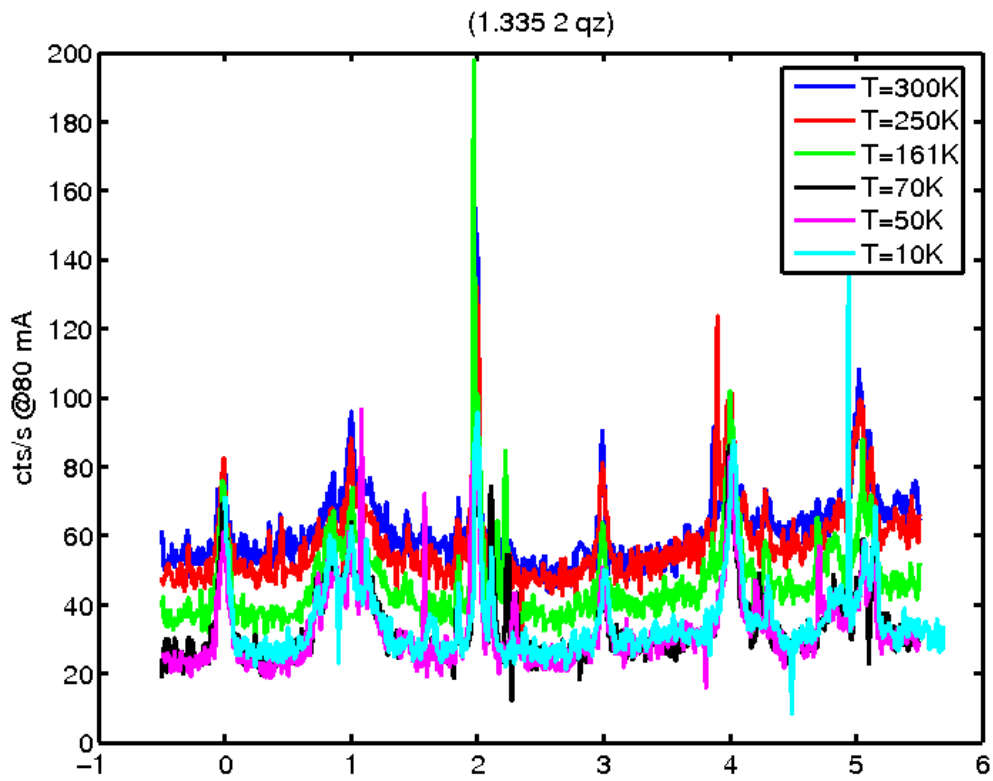


Figure A.8: *sLCO*:*qz*-Scans through suspected charge-order peaks, as a function of temperature. They are seen to persist unchanged to  $T=300\text{K}$  except for increasing background.

## 4% Sr doped sample m=0.019g (sLSCO4)

This was the same piece of sample used in the June 2008 RITA-II beamrun. The sample was glued with GE-varnish roughly in the  $(a, b)$ -plane on a Cu holder.

Crystal parameters used:  $a = b = 5.326 \text{ \AA}$   $c = 13.233 \text{ \AA}$ .

Some alignment scans are shown in figure A.9, and the  $\omega$  scans are seen to be broad, especially across (220), although this might be 3 peaks due to twinning. From measurements at RITA-II in June this year the mosaicity FWHM was  $0.4^\circ$  across (020) and (002), which is comparable to the present value.

In figure A.10 the staging pattern is shown around (014). The staging number is similar to the one measured previously at bw5 and RITA, but whereas the central peak was very weak as seen with hard xrays in the other piece of this crystal [119] the relative intensity between the central and staging peaks in the present piece of the sample seems to be similar to the one measured in both pieces of sample by neutrons [145, 146]. The transition temperature of staging is 230K in all experiments whereas the transition temperature of the central peak is 150K - much lower than that of the staging which seems odd thinking that staging is a superstructure of Bmab. In addition, the (220) peak remains split up to RT, indicating the sample is still twinned and thus orthorhombic even when the (014) peak is gone, and it seems this peak cannot be used as an indicator of the Bmab phase. In figure A.11 both the central peak (first row in figure) and the staging peaks (second row) are broadened along  $qx$  and  $qy$  with respect to the (020) and (004) Bragg peaks in the third and fourth rows.

We looked for chargeorder along the diagonal close to (220), and as seen in figure A.12 there are peaks at  $(2.15 \ 2.15 \ qz)$  for even  $qz$ , but these peak persist to RT.

We checked for signs of the LTT phase at base temperature, but found no localised peaks at (110), (330) or (130) after counting 5s/pt.

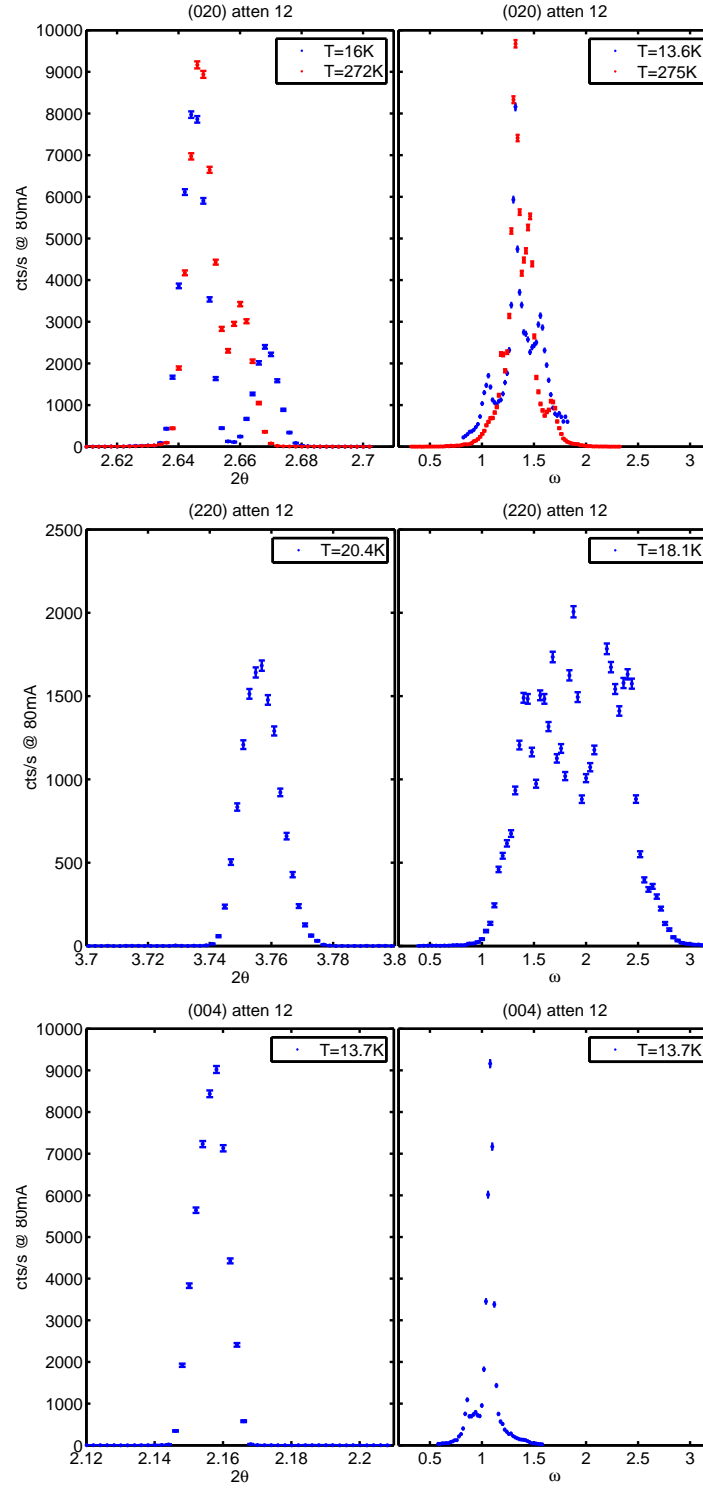


Figure A.9: [sLSCO4](#): Longitudinal scans and rocking curves of Bragg peaks in sLSCO4. The longitudinal splitting of (020 increases with decreasing temperature), the low temperature splitting corresponds to  $\Delta q = 2 \cdot k \cdot \sin \frac{\Delta 2\theta}{2} = 0.33 \text{ \AA}^{-1} = 0.28 \text{ r.l.u.}$

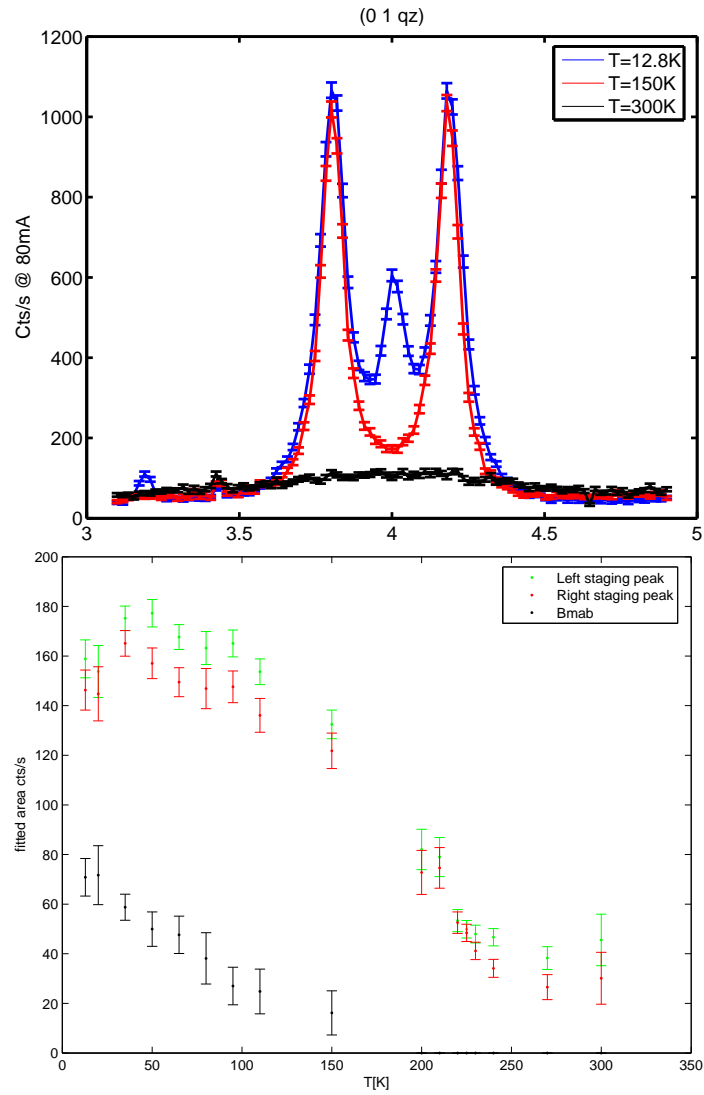
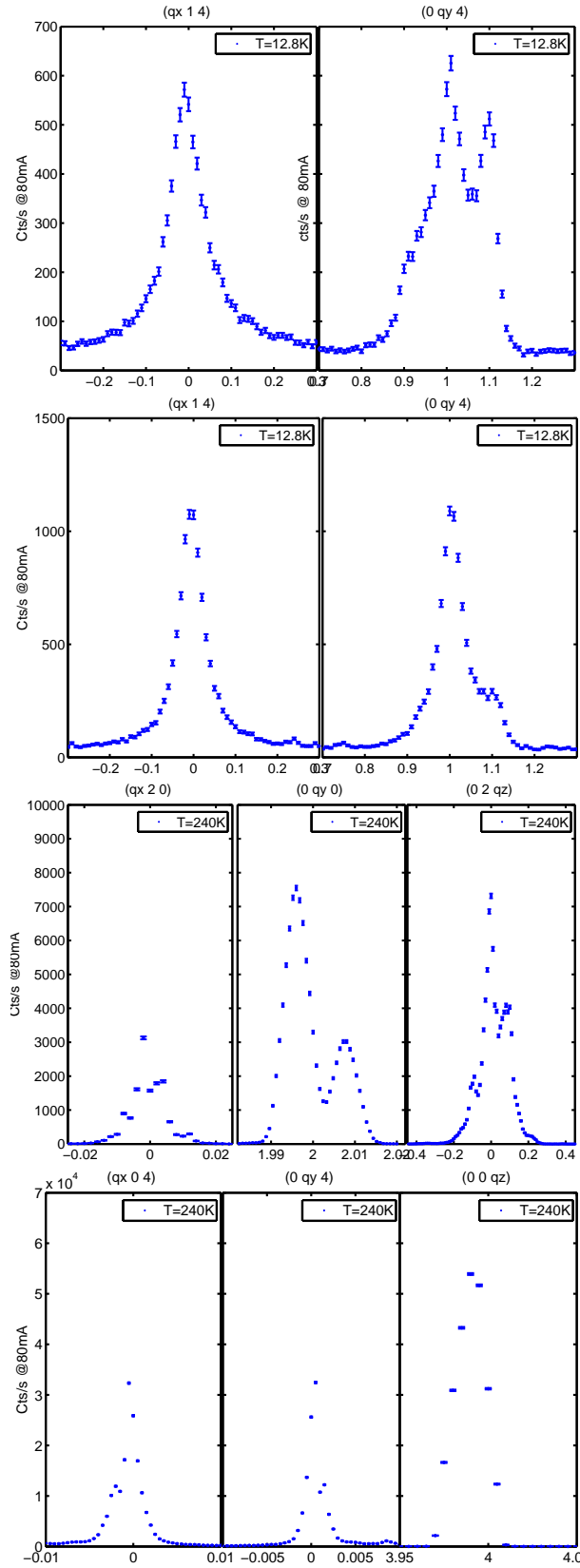


Figure A.10:  $s\text{LSCO4}$ : The staging peaks seen by  $qz$  through (014) at selected temperatures is seen in the top plot and the Lorentzian fitted areas of the central and staging peaks as function of temperature is seen in the bottom plot.

Figure A.11:  $sLSCO_4$ :  $qx$ ,  $qy$  and  $qz$  Scans through staging and Bragg peaks

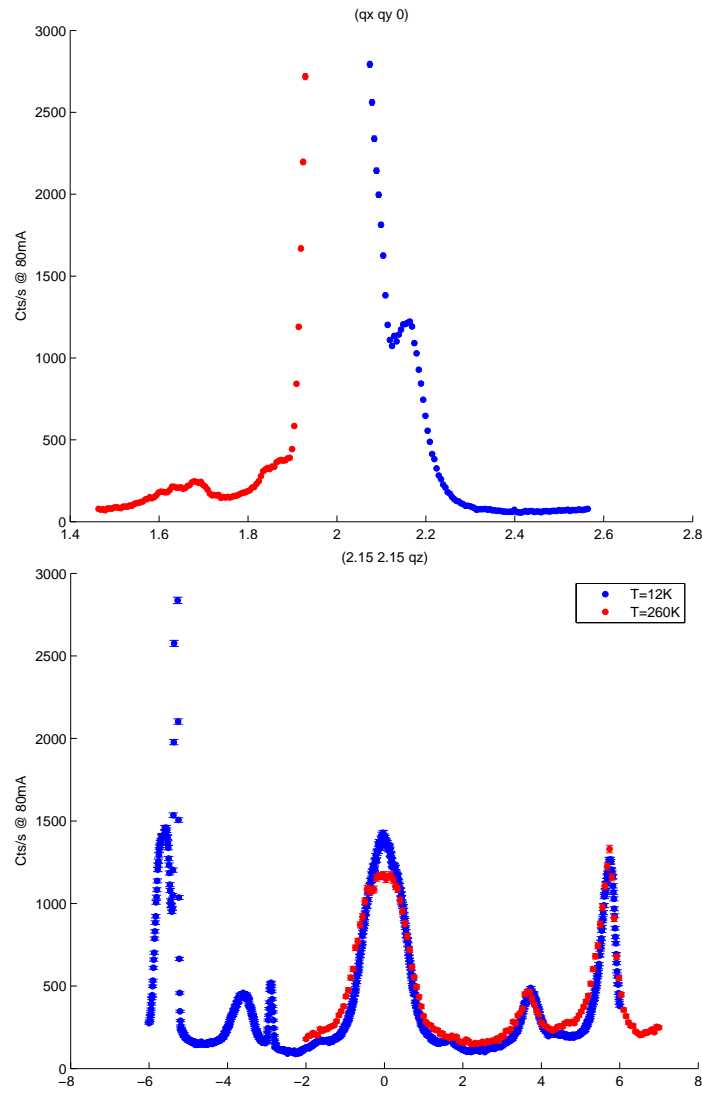


Figure A.12: [sLSCO4](#): The top figure shows scans along  $qx = qy$  close to  $(220)$  showing a candidate for charge order at  $(2.15\ 2.15\ 0)$  which has been scanned along  $Q_z$  in the bottom figure. It is seen that there is intensity at even values of  $Q_z$ , but this intensity persists to RT.

## 9% Sr doped sample $m=0.419\text{g}$ (sLSCO9)

The last night we had a quick check of the 9% Sr sample. The sample was glued with GE-varnish roughly in the  $(a, b)$ -plane on a Cu holder.

Crystal parameters used:  $a = b = 5.326 \text{ \AA}$   $c = 13.233 \text{ \AA}$ .

From the line-up scans figure A.13 it is seen that the rocking curve of of (020) and especially (220) is very broad, and the width along  $qz$  of this peak is also extremely large - maybe due to unresolved staging ? The (020) peak is split at base temperature but not at RT, indicating the sample to be in the HTT phase at RT. In accordance with this, the (014) peak has transition temperature at approximately 300K as seen in previous [128] measurements .

Bmab peaks at (014) and (032) were present, but contrary to sLCO and sLSCO4 the intensity of (032) is smaller than (014).

There was no sign of a an LTT peak at (110).

A peak was observed at  $(2.09 \ 2.09 \ 0)$  as seen before [118] but unfortunately we were not able to pursue this before the end of the beamtime due to difficulties with the heater and beam instabilities.

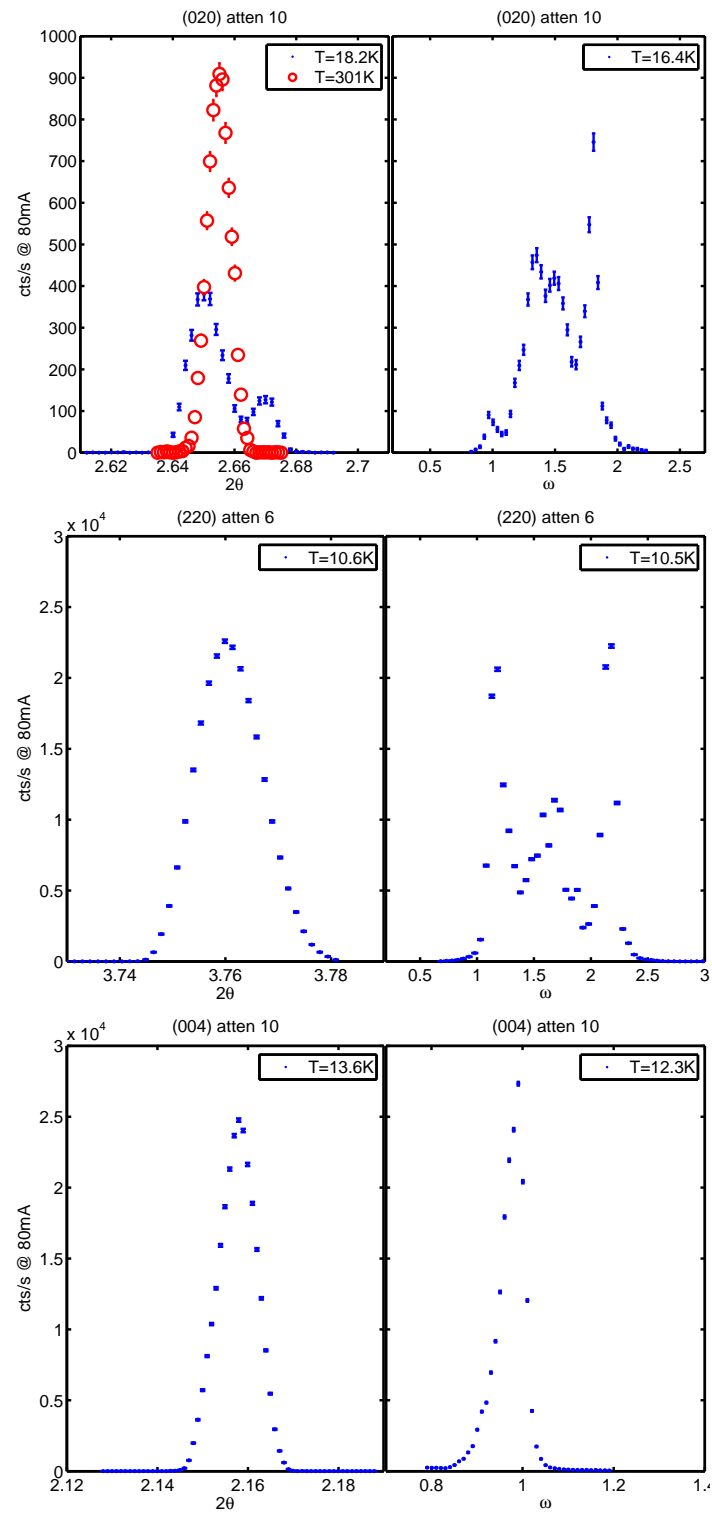


Figure A.13: sLSCO9: Longitudinal scans and rocking curves of Bragg peaks.

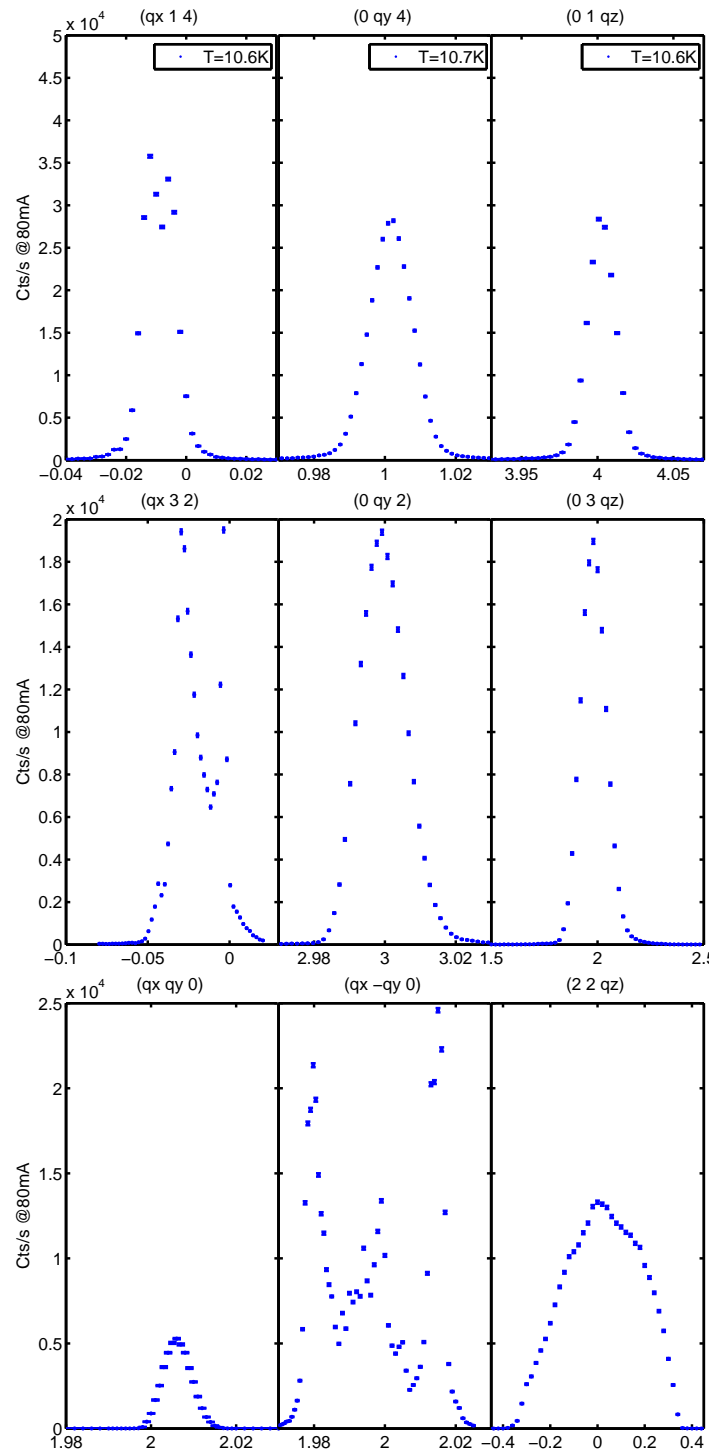


Figure A.14: **sLSCO9**:  $q$ -scans of (014) (top), (320) (centre) and (220) (bottom) showing unusual broadness of transversal and  $qz$  scans of (220). The  $qz$  width of (014) corresponds to the  $qz$  width of (004) in figure A.13

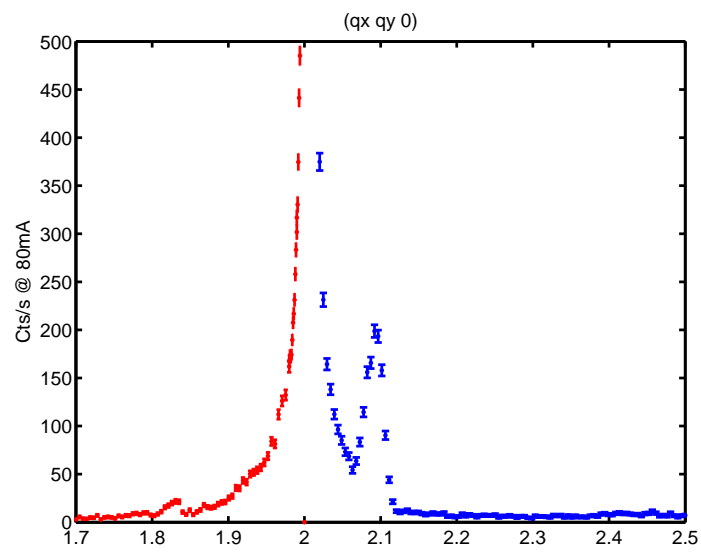


Figure A.15: **sLSCO9**. Scans along  $Q_x = Q_y$  close to (220) showing a candidate for chargeorder at (2.15 2.15 0)

## Conclusion and outlook

Searching for charge order, we found some incommensurate structures along the orthorhombic axis in sLCO and along the Cu-O bonds in sLSCO4 which peaked at integer values of  $qz$ , but they were not temperature dependent up to RT. To date the best candidate for charge ordering is the  $(2.09\ 2.09\ 0)$  of sLCO9, which has previously [118] been shown to disappear above 170K. In future beamtime this peak should be measured along  $qz$  and also checked at  $(2.09, 4.09, qz)$ .

Curiously transversal scans of the  $(220)$  peak were very broad for the co-doped samples. In sLCO there were signs of a minority LTT phase from peaks at  $(110)$  and  $(330)$  however, these peaks remained unchanged up to RT. In the co-doped samples there were no signs of LTT peaks.

It was confirmed that the  $(014)$  of sLSCO4 has transition temperature of 150K, much lower than the staging satellites transition temperature of 230K. Since the orthorhombic splitting persists to RT in this sample, it is likely that the peak at  $(014)$  is not a Bmab signature, but what else it might be remains to be understood.

The staging of sLCO seems to be comprised of several staging levels whereof the highest staging numbers persist to the highest temperatures.

## Appendix B

# TriCS experiments on a large $\text{La}_2\text{CuO}_{4+\delta}$ crystal

Linda Udby, Jürg Schefer, Christof Niedermayer

This document is a short resumé of the data acquired June 29th to July 5th 2008.

### 0% Sr doped sample $m=0.545$ g

For this beamtime, which I luckily got hold of with a few days warning, we used one ( $m=0.545\text{g}$ ) of two pieces of a superoxygenated LCO+O crystal. The other piece ( $m \approx 0.8\text{g}$ ) has been measured at NIST, having IC AFM phase with transition  $T_m = 40\text{K}$  occupying 30% of the volume (measured by muons at PSI) coinciding with the superconducting phase transition of  $T_c = 40\text{K}$ . Since this particular piece had been fast-cooled - and maybe oxygen-disordered hereby - at the  $\mu\text{SR}$  experiment just before the TriCS beamtime I decided to use the other piece of the original crystal.

The setup of TriCS was 40'h/20'v-Sample-80'-SingleDet. Sample parameters used for the ub-matrix were  $a=5.32\text{\AA}$ ,  $b=5.40\text{\AA}$ ,  $c=13.18\text{\AA}$ .

The staging[53] of the crystal is shown in L-scans though the Bmab positions ( $0KL$ ) for  $K = -3$  and  $K = -1$  in figure B.1 to be mostly stage 2 and a minor phase with stage 4. I chose to follow the temperature dependence of the staging peaks around  $(0 -3 2)$  since they had the largest and most symmetric intensity, although the abrupt 'edge' of the peak at  $L=2.5$  before the temperature dependent 'shoulder' seems somewhat strange. The fitted areas of the Bmab, stage 4 and stage 2 from L-scans are plotted in figure B.2. Some H-scans through the stage 2 and stage 4 peaks at different temperatures are also shown, from which it is seen that there is no apparent broadening along this direction during the transition.

As can be seen from figure B.2 the Bmab and stage 2 peaks decrease slowly

above 100K. The transition temperature for the stage 4 is 280K and for the stage 2 an extrapolated transition temperature is somewhere between 350K and 450K. Both transitions are very broad. The staging numbers do not change with temperature.

The B<sub>mab</sub> transition is probably at higher temperatures than the stage 2 transition, as expected. After fast cooling from 320K to 13K in 1 hour the intensity of the stage 2 and stage 4 peaks fully recovers, the only change is perhaps a slight decrease of the B<sub>mab</sub> peak. This is in contrast to what we have previously seen with hard x-rays on another La<sub>2</sub>CuO<sub>4+δ</sub> crystal which however was most predominantly stage 4 (with similar transition temperature to the stage 4 of the present crystal) and not stage 2 like the present crystal. It seems that the higher oxygenation level of the present crystal stabilises the staging eliminating the need for slow cooling. The present crystal is hence similar to the 4% Sr-doped superoxygenated crystal in the way that intensity of the staging peaks recovers after fast-cool.

We found structural peaks at  $\Delta_1 = 0.04, \Delta_2 = 0.27, \Delta L = 0.5$ , and it was checked for  $L=5.5$  that the eight peaks  $(\pm\Delta_1, \pm\Delta_2, 5.5)$  and  $(\pm\Delta_2, \pm\Delta_1, 5.5)$  were present. The peak was also confirmed at  $(\Delta_1, \Delta_2, -\Delta L)$ , but at much lower intensity, see figure B.3. The position of the peak  $(\Delta_1, \Delta_2, 5.5)$  and the satellite at  $(0.08, 0.25, 5.5)$  is quite close to the position of Lee [108] which he claims to be due to direct oxygen. An L-scan through the peak and the small satellite next to it is shown in figure B.4 and it is seen that the L-dependence of the direct oxygen peaks is the same as for the 'stage 2' peaks, i.e. peaking at  $L \pm 0.5$  for even  $L$ , although intensity is vanishing for small  $L$ . In the gridplots of figure B.3 it is seen that the satellite cannot be resolved from the main peak in the  $H > 0, K < 0$  and the  $H < 0, K > 0$  quadrants due to the direction of the resolution ellipsoid. In the bottom of figure B.3 an  $H$ -linescan through these peaks (at  $K=0.27$ , which is the centre of the main peak but slightly off the centre of the satellite) is shown at base temperature, at 320K and at base temperature after cooling from 320K in 1 hour (fast-cool): It appears that the satellite at  $H=0.106$  loses some intensity on heating which does not recover after a fast-cool supporting the interpretation that this peak is due to direct oxygen ordering. The peak at  $H=-0.055$  contains both the main peak and the satellite which can be seen on from the gridplot and also on the fitted width which is significantly larger than the width of the peak at  $H=0.037$ . It is hence expected that intensity of this peak does not recover upon fast cooling but the decrease is too small to observe on the larger main peak. Based on the observation of Lee[108] that the 'direct oxygen peak' at  $(0.09, 0.24, 5.5)$  disappears at 330K and has approximately half intensity at 320K, our 'satellite peak' at approximately  $(0.11, 0.25, 5.5)$  probably corresponds to the direct oxygen peak whereas the main peak at  $(0.04, 0.27, 5.5)$  is probably structural. A second harmonic of this peak was found at  $(0.08, 0.55, 5.00)$  with intensity a factor 2.5 lower than the main peak.

In addition we also found peaks at  $H = K = 0$  and  $L$  odd, indicating some periodicity between adjacent CuO<sub>2</sub> layers but without in-plane structure, see figure B.5. It was checked that these peaks, and the other mentioned above, are not due to a second order effect by momentary use of a Ge(311) monochromator.

We might use as structural scaling reference in future x-ray experiments the Fmmm/Bmab allowed peak at  $(-3 -1 1)$  with  $2\theta = 87.7^\circ$ . It was measured to have max peak intensity of 270 cts/2e5 mon. Position  $(0 -3 2)$  has  $2\theta = 84.1^\circ$ .

The crystal was left at the PSI after the experiment.

## Outlook

It would be interesting to measure a piece of this particular crystal with hard x-rays to see if these 'direct oxygen' peaks are visible or not. I guess if they are not it would be the strongest evidence presented that they do actually stem from direct oxygen.

We could also apply for more beamtime at TriCS but to get the transition temperature for the peaks at  $(\Delta_1, \Delta_2, \Delta_L)$  and the satellite would require using an oven. At TriCS there is also a possibility of using a cryo which heats to 380K but I fear this will not be sufficient. We have to ask around if anyone has an oven which could be mounted on TriCS. It would also be very interesting to look for this peaks in our 4% Sr co-doped crystal. We could try this on TriCS if we could get the beamtime, but the experiment is going to be much harder since the crystal is a factor of 10 smaller than the one used in this report. If it is possible to see anything on this particular crystal at TriCS we could also try to figure out what the peak at (0 -1 4) which seems not to be a B<sub>mab</sub> peak really is.

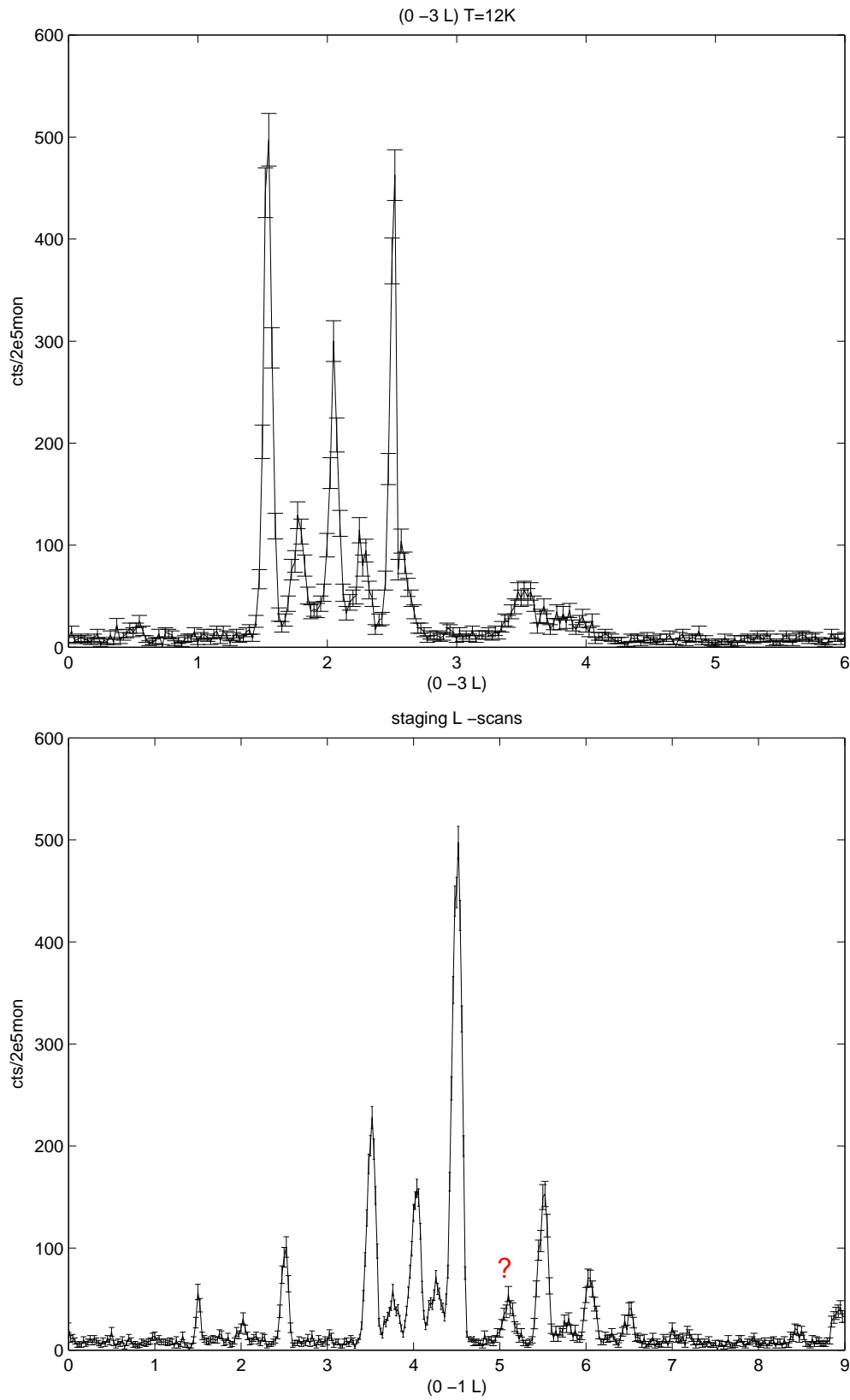


Figure B.1: Top: L-scans through (0 -3 L). Bottom: L-scans through (0 -1 L)

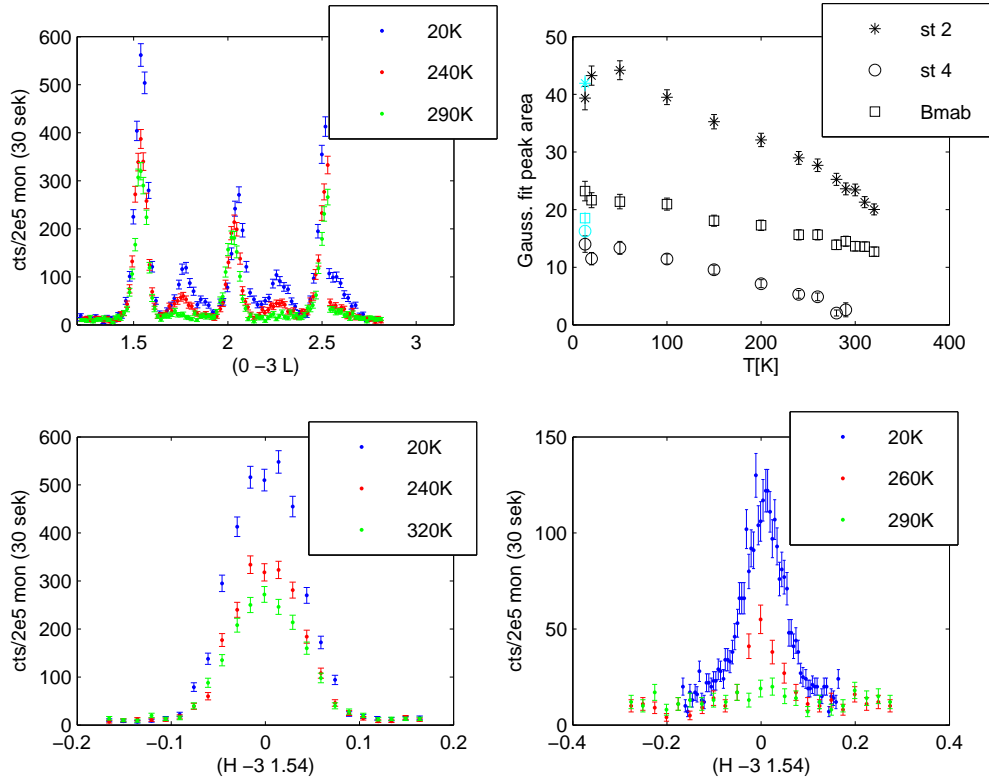


Figure B.2: Top: (Right)  $L$ -scans through (0 -3 L), (left) Gaussian areas of  $L$ -scans at st2=(0 -3 1.54), st4=(0 -3 1.78) and Bmab=(0 -3 2.05) as funktion of temperature. Cyan markers are the areas after fast-cooling. Bottom:  $H$ -scans through stage 2 (left) and stage 4 (right).

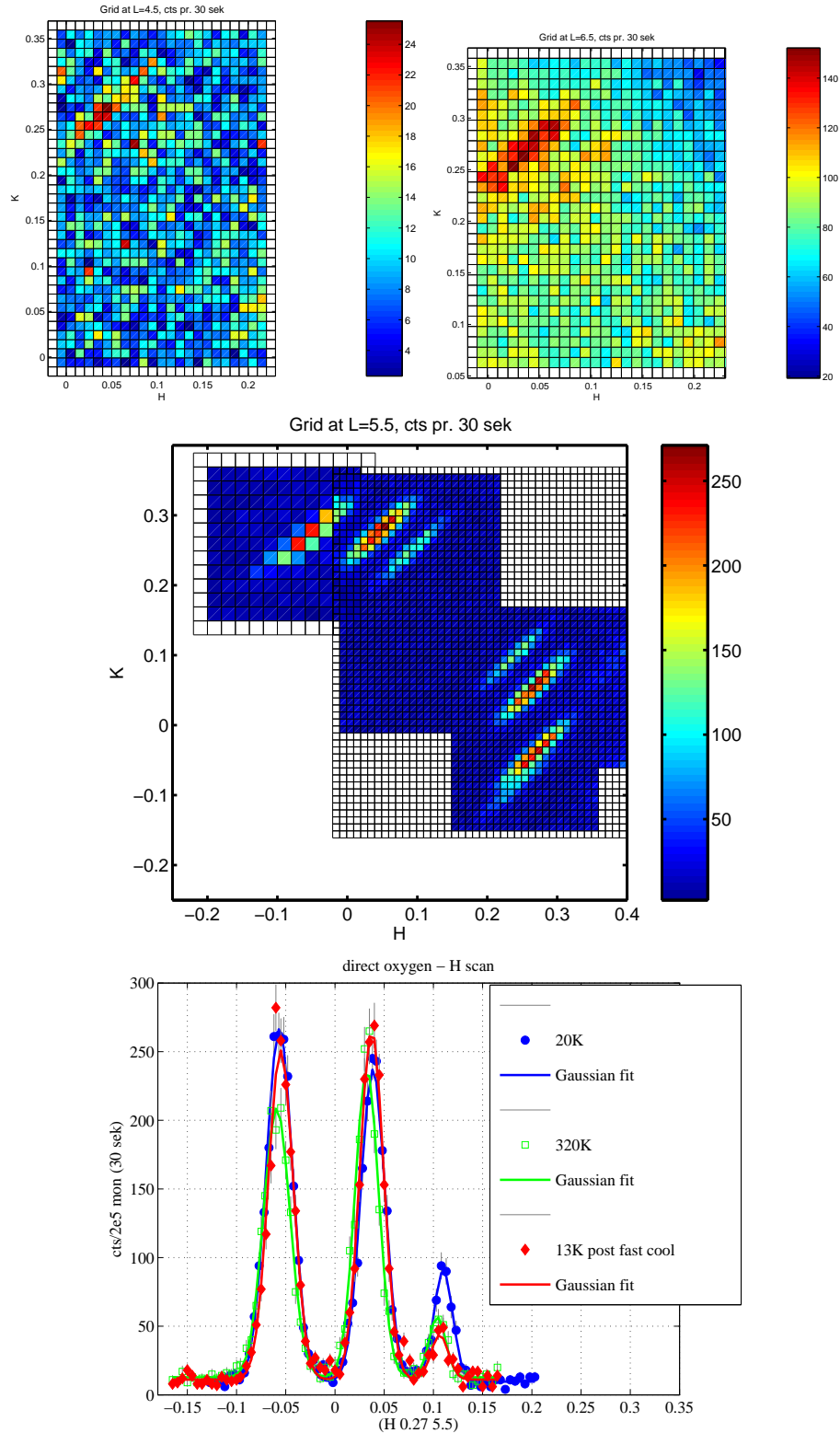


Figure B.3: Peaks at the acclaimed direct oxygen positions. Top:  $HK$ -grid at  $L=4.5$  (left) and  $L=6.5$ (right). Centre:  $HK$ -grid at  $L=5.5$  Bottom: Temperature dependence of the direct oxygen and its satellite.

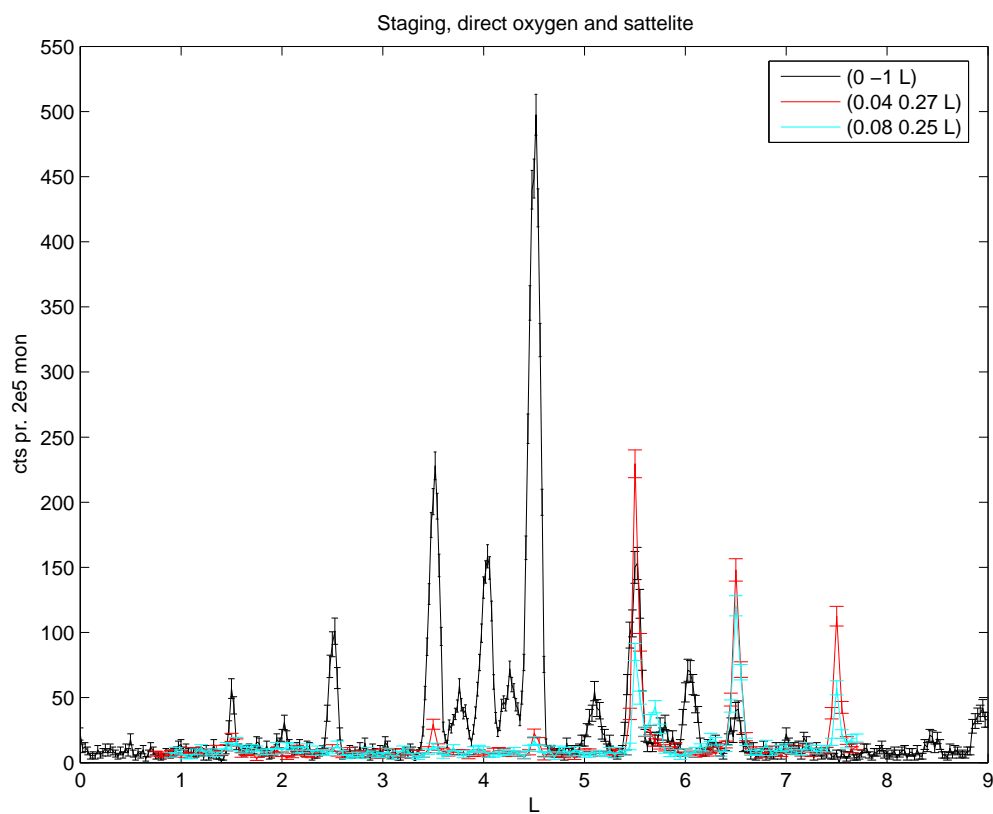


Figure B.4: Overlaid  $L$ -dependence of the peak at  $(0 -1 L)$ , the direct oxygen peak and its satellite at base temperature

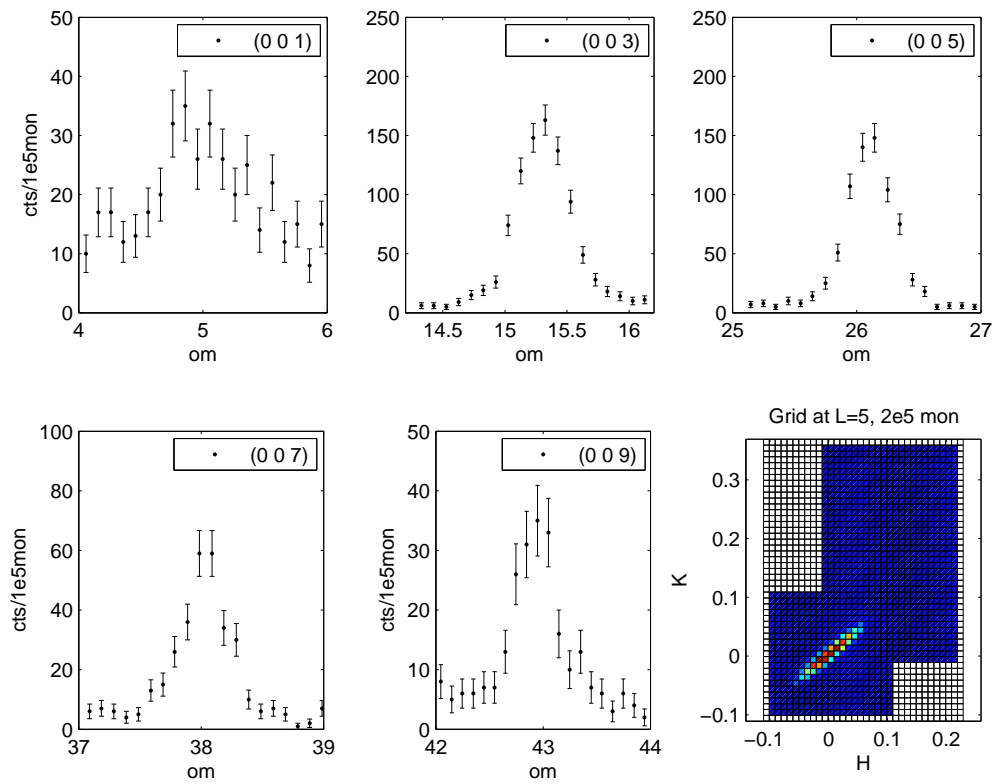


Figure B.5: Peaks at  $(0\ 0\ L)$  for  $L$  odd. These peaks are forbidden in the Bmab structure





```

* verbose: print TAS configuration. 0 to be quiet [1]
* MST: Monochromator TOP slit [m]
* MSB: Monochromator BOTTOM slit [m]
* MSR: Monochromator RIGHT slit [m]
* MSL: Monochromator LEFT slit [m]
* SST: Sample TOP slit [m]
* SSB: Sample BOTTOM slit [m]
* SSR: Sample RIGHT slit [m]
* SSL: Sample LEFT slit [m]
* SM:
* SS: Scattering configuration signs. 'W' is SM=1,SS=-1,SA=1 [1]
* SA:
* FILTER: Flag to indicate if filter is in or out [1]
* COARSE: Flag to indicate if Detector collimator is in or out [1]
* dmv: Mono-virtual source dist [m]
* dvs: virtual source - sample dist. dms=dmv+dvs [m]
* REP: Repetition factor of virtual_input [1]
* ANA_MOS_H: Analyzer, horizontal mosaicity [min]
* ANA_MOS_V: Analyzer, vertical mosaicity [min]
* MONO_MOS_H: Monochromator, horizontal mosaicity [min]
* MONO_MOS_V: Monochromator, vertical mosaicity [min]
* LC: Detector-collimator angle of the leftmost blade [deg]
* RC: Detector-collimator angle of the rightmost blade [deg]
* U: Monochromator curvature. If 0 then flat, else the value is calculated[1]
* PERSPEX: Flag to indicate if perspex attenuator is in or out [1]
* PTHICK: Thickness of perspex attenuator [m]
*****
* Sample parameters:
*****
* SAMPLE: 1 is incoherent scatterer, 2 is powder, 3 is single crystal.[1]
* SAMPLEFILE: Name of samplefile (with reflectionlist etc) [string]
* XW: sample thickness across downstream direction [m]
* YH: sample vertical height [m]
* ZT: sample thickness along downstream direction [m]
* MOS: Isotropic 'mosaicity' of single crystal
* DD_D: spead of lattice parameter
* AS: Sample lattice parameter A [Angs]
* BS: Sample lattice parameter B [Angs]
* CS: Sample lattice parameter C [Angs]
* AA: Angle between lattice vectors B,C [deg]
* BB: Angle between lattice vectors C,A [deg]
* CC: Angle between lattice vectors A,B [deg]
* AH: First reciprocal lattice vector in scattering plane, X [rlu]
* AK: First reciprocal lattice vector in scattering plane, Y [rlu]
* AL: First reciprocal lattice vector in scattering plane, Z [rlu]
* BH: Second reciprocal lattice vector in scattering plane, X [rlu]
* BK: Second reciprocal lattice vector in scattering plane, Y [rlu]
* BL: Second reciprocal lattice vector in scattering plane, Z [rlu]
* AAX:
* AAY: Orientation vector of unit cell, single_crystal
* AAZ:
* BBX:
* BBY: Orientation vector of unit cell, single_crystal
* BBZ:
* CCX:
* CCY: Orientation vector of unit cell, single_crystal
* CCZ:
*****
DEFINE INSTRUMENT RITA_II(PTHICK=1e-3,PERSPEX=0,
string SOURCEFILE="Vin_default.dat",
MONO_N=1,MONOFORCE=0,MONO_MOS_H=37, MONO_MOS_V=37,COLL_MS=40, BPL=0.0001,BPH=10,
EI=0, EF=0,
QH=0, QK=0, QL=0,
EN=0, QM=0,
AS=5.3241, BS=5.3241, CS=13.1821,
AA=90, BB=90, CC=90,
AH=0, AK=0, AL=0,
BH=0, BK=0, BL=0,
verbose=1,
AAX=0, AAY=0, AAZ=0, BBX=0, BBY=0, BBZ=0, CCX=0, CCY=0, CCZ=0,
A1=0,A2=0,A3=0,A4=0,A5=0,A6=0,SM=1,SS=-1,SA=1,
MST=40, MSB=40, MSL=40, MSR=40,
SAMPLE, string SAMPLEFILE="default",MOS=100,DD_D=1e-3, XW=0.01, YH=0.01, ZT=0.01,
SST=40, SSB=40, SSL=40, SSR=40,
FILTER=1, string FILTERFILE="Be.trm",
CA2=0, CA3=0, CA4=0, CA5=0, CA6=0, CA7=0, CA8=0,
ANA_MOS_H=40, ANA_MOS_V=40, COARSE=1,
REP=1, TILT=0, COLL=40, LC=6, RC=4,U=1,ANAMOSCORR=0)

DECLARE
%{
/* Declarations for 'Coarse Collimator' at the PSD detector surface */
int EntrySlit;
int ExitSlit;
int AnaBlade;
double BladeThickness = 0.007;// detector coll after 2006, from drawings
double WindowSize = 0.025;
double BladeLength = 0.179;// detector coll after 2006, from drawings
double BladeHeight = 0.272;// detector coll after 2006, from drawings
//double BladeThickness = 0.002;// detector coll before 2006
//double WindowSize = 0.025;
//double BladeLength = 0.180;// detector coll before 2006

```

```

//double BladeHeight = 0.250;// detector coll before 2006
double FirstWindowSizeL;
double FirstWindowSizeR;
double deltaL;
int coarse;
int monoforce;

struct sample_struct {
    double as, bs, cs; // Lattice parameters
    double aa, bb, cc; // Lattice angles
    double ax, ay, az; // First scattering plane vector
    double bx, by, bz; // Second scattering plane vector
} sample;

struct machine_hkl_struct {
    double dm, da; // Mono and ana d-spacings
    double sm, ss, sa; // Mono, sample, ana angle signs
    double ki, kf, ei, ef; // Initial and Final wavevectors and energies
    double qh, qk, ql, en; // Momentum transfer and energy transfer in sample
} machine_hkl;

struct machine_real_struct {
    double a1,a2,a3,a4,a5,a6;
    double rmh, rmv, rah, rav;
    double qm, qs, qt[3];
    char message[256];
} machine_real;

struct machine_real_struct qhkl2angles(
    struct sample_struct sample,
    struct machine_hkl_struct machine_hkl,
    struct machine_real_struct machine_real) {

    /* code from TASMAD/t_rlp.F:SETRLP */
    double qhkl[3];
    double alpha[3];
    double a[3];
    double aspv[3][2];
    double cosa[3], sina[3];
    double cosb[3], sinb[3];
    double b[3], c[3], s[4][4];
    double vv[3][3], bb[3][3];
    double arg, cc;
    int i,j,k,l,m,n;
    char liquid_case=1;
    /* transfered parameters to local arrays */
    qhkl[0] = machine_hkl.qh; /* HKL target */
    qhkl[1] = machine_hkl.qk;
    qhkl[2] = machine_hkl.ql;
    alpha[0] = sample.aa; /* cell angles */
    alpha[1] = sample.bb;
    alpha[2] = sample.cc;
    a[0] = sample.as; /* cell parameters */
    a[1] = sample.bs;
    a[2] = sample.cs;
    aspv[0][0]= sample.ax; /* cell axis A */
    aspv[1][0]= sample.ay;
    aspv[2][0]= sample.az;
    aspv[0][1]= sample.bx; /* cell axis B */
    aspv[1][1]= sample.by;
    aspv[2][1]= sample.bz;

    /* default return values */
    strcpy(machine_real.message, "");
    machine_real.a3 = machine_real.a4 = 0;
    machine_real.a1 = machine_real.a5 = 0;

    /* if using HKL positioning in crystal (QM = 0) */
    if (machine_real.qm <= 0) {
        liquid_case = 0;
        /* compute reciprocal cell */
        for (i=0; i< 3; i++)
            if (a[i] <=0) sprintf(machine_real.message, "Lattice parameters a[%i]=%g", i, a[i]);
            else {
                a[i] /= 2*PI;
                alpha[i]*= DEG2RAD;
                cosa[i] = cos(alpha[i]);
                sina[i] = sin(alpha[i]);
            }
        cc = cosa[0]*cosa[0]+cosa[1]*cosa[1]+cosa[2]*cosa[2]; /* nprm */
        cc = 1 + 2*cosa[0]*cosa[1]*cosa[2] - cc;
        if (cc <= 0) sprintf(machine_real.message, "Lattice angles (AA,BB,CC) cc=%g", cc);
        else cc = sqrt(cc);

        if (strlen(machine_real.message)) return machine_real;

        /* compute bb */
        j=1; k=2;
        for (i=0; i<3; i++) {
            b[i] = sina[i]/(a[i]*cc);
            cosb[i] = (cosa[j]*cosa[k] - cosa[i])/(sina[j]*sina[k]);
            sinb[i] = sqrt(1 - cosb[i]*cosb[i]);
        }
    }
}

```

```

    j=k; k=i;
}

bb[0][0] = b[0];
bb[1][0] = 0;
bb[2][0] = 0;
bb[0][1] = b[1]*cosb[2];
bb[1][1] = b[1]*sinb[2];
bb[2][1] = 0;
bb[0][2] = b[2]*cosb[1];
bb[1][2] = -b[2]*sinb[1]*cosa[0];
bb[2][2] = 1/a[2];

/* compute vv */
for (k=0; k< 3; k++)
    for (i=0; i< 3; i++) vv[k][i] = 0;

for (k=0; k< 2; k++)
    for (i=0; i< 3; i++)
        for (j=0; j< 3; j++)
            vv[k][i] += bb[i][j]*aspv[j][k];

for (m=2; m>=1; m--)
    for (n=0; n<3; n++) {
        i = (int)fmod(m+1,3); j= (int)fmod(m+2,3);
        k = (int)fmod(n+1,3); l= (int)fmod(n+2,3);
        vv[m][n]=vv[i][k]*vv[j][l]-vv[i][l]*vv[j][k];
    }

for (i=0; i< 3; i++) { /* compute norm(vv) */
    c[i]=0;
    for (j=0; j< 3; j++)
        c[i] += vv[i][j]*vv[i][j];
    if (c[i]>0) c[i] = sqrt(c[i]);
    else {
        sprintf(machine_real.message, "Vectors A and B, c[%i]=%g", i, c[i]);
        return machine_real;
    }
}

for (i=0; i< 3; i++) /* normalize vv */
    for (j=0; j< 3; j++)
        vv[j][i] /= c[j];

for (i=0; i< 3; i++) /* compute S */
    for (j=0; j< 3; j++) {
        s[i][j] = 0;
        for (k=0; k< 3; k++)
            s[i][j] += vv[i][k]*bb[k][j];
    }
s[3][3]=1;
for (i=0; i< 3; i++) s[3][i]=s[i][3]=0;

/* compute q modulus and transverse component */
machine_real.qs = 0;
for (i=0; i< 3; i++) {
    machine_real.qt[i] = 0;
    for (j=0; j< 3; j++) machine_real.qt[i] += qhkl[j]*s[i][j];
    machine_real.qs += machine_real.qt[i]*machine_real.qt[i];
}
if (machine_real.qs > 0) machine_real.qm = sqrt(machine_real.qs);
else sprintf(machine_real.message, "Q modulus too small QM^2=%g", machine_real.qs);
} else {
    machine_real.qs = machine_real.qm*machine_real.qm;
}
/* end if qm <= 0 ***** */

/* positioning of monochromator and analyser */
arg = PI/machine_hkl.dm/machine_hkl.ki;
if (fabs(arg > 1))
    sprintf(machine_real.message, "Monochromator can not reach this KI. arg=%g", arg);
else {
    if (machine_hkl.dm <= 0 || machine_hkl.ki <= 0)
        strcpy(machine_real.message, "Monochromator DM=0 or KI=0.");
    else
        machine_real.a1 = asin(arg)*RAD2DEG;
    machine_real.a1 *= machine_hkl.sm;
}
machine_real.a2=2*machine_real.a1;

arg = PI/machine_hkl.da/machine_hkl.kf;
if (fabs(arg > 1))
    sprintf(machine_real.message, "Analyzer can not reach this KF. arg=%g",arg);
else {
    if (machine_hkl.da <= 0 || machine_hkl.kf <= 0)
        strcpy(machine_real.message, "Analyzer DA=0 or KF=0.");
    else
        machine_real.a5 = asin(arg)*RAD2DEG;
    machine_real.a5 *= machine_hkl.sa;
}
machine_real.a6=2*machine_real.a5;
if (strlen(machine_real.message)) return machine_real;

```

```

/* code from TASMAD/t_conv.F:SAM_CASE */
arg = (machine_hkl.ki*machine_hkl.ki + machine_hkl.kf*machine_hkl.kf - machine_real.qs)
/ (2*machine_hkl.ki*machine_hkl.kf);
if (fabs(arg) < 1)
machine_real.a4 = RAD2DEG*acos(arg);
else
sprintf(machine_real.message, "Q modulus too big. Can not close triangle. arg=%g", arg);
machine_real.a4 *= machine_hkl.ss;

if (!liquid_case) { /* compute a3 in crystals */
machine_real.a3 =
-atan2(machine_real.qt[1],machine_real.qt[0])
-acos( (machine_hkl.kf*machine_hkl.kf-machine_real.qs-machine_hkl.ki*machine_hkl.ki)
/((-2*machine_real.qm*machine_hkl.ki) ));
machine_real.a3 *= RAD2DEG*(machine_real.a4 > 0 ? 1 : -1 );
//machine_real.a3 = machine_real.a3 -90;// Add by PW & LU
}

return machine_real;
}
/* The following is from RITA2front, Kim Lefmann / Linda Udby */

/* Static values... */
double l0,lmin,lmax;
double emin,emax;
double KI,KF;
/* Guide element parameters*/
double angleGuideCurved;
double R = 0.88;
double R0 = 0.995;
double Qc = 0.0217;
double W = 1/334;
double M= 2.15;
double alpha;
/* Monochromator material parameters */
double mono_q = 1.87325;
double mono_r0 = 0.8;
double DM; /*d-spacing monochromator*/
double mono_mosaic_h;
double mono_mosaic_v;
/* Monochromator curvature parmeters */
double u,v;
double dms; /* Target vector for focusing */
double tx,tz; /* Target vector for focusing */
double sintm,sinta;
int i;
double mrot[5+1];
/* Monochromator geometrical parameters */
/* Size of monochromator blades are hard-coded in the component*/
double mono_d = 0.026; /* Distance between mono blades. From drawings */
double dmc; /* Distance monochromator to front of collimator. Was 0.32 from Stine */
double rmh = 0.58; /* Radius of monohousing. Measured 2008/11/05 */
double lc = 0.198; /*Length of monocollimator. Measured 2008/11/05*/
/* Sample parameters */
double d_sample_slit = 0.35; /* Measured 2008/11/05, was 25 cm from Stine */
double d_sample_filter = 0.51; /*To centre of filter. Measured 2008/11/05, was to filter front 25 cm from Stine */
double dsa = 1.195; /* distance sample-analyzer (m). Was 1.256 from Stine */
double dmv = 1.00; /* distance monochromator to virtual out */
//double dvs = 0.67; /* distance virtual in to sample. dmv+dvs=1.67=rmh+1.09. Mal5 setting */
double dvs = 0.54; /* distance virtual in to sample. dmv+dvs=1.54=rmh+1.09 */
/* Analyser material parameters*/
double ana_mosaic_h;
double ana_mosaic_v;
double ana_q = 1.87325;
double ana_r0 = 0.8;
double DA; /* d-spacing analyser*/
/*Analyser geometrical parameters */
double ana_d = 0.025; /* Width of analyser blades. From drawings */
double ana_h = 0.15; /* Height of analyser blades. From drawings */
double dad = 0.338; /* distance analyzer-detector (m) */
double wan = 0.024; /* width of analyzer blades , by ruler (m) */
/* Detector parameters */
//double det_width = 0.2735; /* was 0.3 from Stine*/
double det_width = 0.275;
double det_height =0.5;
double PSF = 0.0074/2.35;// FWHM=0.0074m, measured by C. Bahl NIMB 246, 452.
/* Random number pr. neutron event for incoherent V scattering */
double is_incoh;
/* Filenames for the sample comps: */
char *PowderFile;
char *SingleXFile;
/* Window positions */
int XwinMin[9];
int YwinMin[9];
int XwinMax[9];
int YwinMax[9];
int BinX;
int BinY;

%}

```

```

/* end of DECLARE */

INITIALIZE
%{
/* calculate mirror reflectivity slope */
alpha=(R0-R)/(Qc*(M-1));
printf(" * ALPHA=%g [AA]\n", alpha);

double Vi, Vf;
double tmp=0;
char Qmode = 0;
DM = 2*PI/mono_q;
DA = 2*PI/ana_q;

machine_real.a1 = A1;
machine_real.a2 = A2;
machine_real.a3 = A3;
machine_real.a4 = A4;
machine_real.a5 = A5;
machine_real.a6 = A6;

/* energy conservation */
if (EI && EF) {
    EN = EI - EF;
    fprintf(stderr,"%s WARNING: EN is now set to %g since you provided both EI=%g (KI) and EF=%g (KF)\n", NAME_CURRENT_COMP, EN, EI, EF);
} else if (EI && !EF){
    EF = EI - EN;
    fprintf(stderr,"%s WARNING: EF is now set to %g since you provided both EI=%g (KI) and EN=%g\n", NAME_CURRENT_COMP, EF, EI, EN);
} else if (EF && !EI) {
    EI = EF + EN;
    fprintf(stderr,"%s WARNING: EI is now set to %g since you provided both EF=%g (KF) and EN=%g\n", NAME_CURRENT_COMP, EI, EF, EN);
} else {
    fprintf(stderr,"%s WARNING: Neither EI, EF nor EN defined: Energies are set from user angle input:\n", NAME_CURRENT_COMP);
    l0 = 2 * DM * sin(DEG2RAD*A2/2)/MONO_N;
    EI = 9.045/l0;
    EI = EI*EI;
    fprintf(stderr,"%s: WARNING: EI has been adjusted to %g[meV] (A2 = %g[deg])\n", NAME_CURRENT_COMP, EI, A2);
    l0 = 2 * DA * sin(DEG2RAD*A6/2)/MONO_N;
    EF= 9.045/l0;
    EF = EF*EF;
    fprintf(stderr,"%s: WARNING: EF has been adjusted to %g[meV] (A6 = %g[deg])\n", NAME_CURRENT_COMP, EF, A2);
}
/* determine remaining neutron energies */
Vi = SE2V*sqrt(EI);
KI = V2K*Vi;
Vf = SE2V*sqrt(EF);
KF = V2K*Vf;

/* transfered sample parameters */
sample.aa = AA;
sample.bb = BB;
sample.cc = CC;
sample.as = AS;
sample.bs = BS;
sample.cs = CS;
sample.ax = AH;
sample.ay = AK;
sample.az = AL;
sample.bx = BH;
sample.by = BK;
sample.bz = BL;

/* transfered target parameters */
machine_hkl.ki = KI;
machine_hkl.kf = KF;
machine_hkl.ei = EI;
machine_hkl.ef = EF;
machine_hkl.qh = QH;
machine_hkl.qk = QK;
machine_hkl.ql = QL;
machine_hkl.en = EN;
machine_real.qm = QM;

if (QM || QH || QK || QL) {
    Qmode=1;
    fprintf(stderr,"%s: Running in HKL mode\n", NAME_CURRENT_COMP);
} else {
    fprintf(stderr,"%s: Running in angle mode\n", NAME_CURRENT_COMP);
}

if (verbose && Qmode) {
    printf("%s: Detailed TAS configuration\n", NAME_CURRENT_COMP);
    printf(" * Incoming beam: EI=%.4g [meV] KI=%.4g [Angs-1] Vi=%g [m/s]\n", EI, KI, Vi);
    printf(" * Outgoing beam: EF=%.4g [meV] KF=%.4g [Angs-1] Vf=%g [m/s]\n", EF, KF, Vf);
}

/* transfered machine parameters */
/* For W configuration of TAS: */
machine_hkl.sm = SM;
machine_hkl.ss = SS;
machine_hkl.sa = SA;

```

```

/* These two are actually constants, see top of INITIALIZE */
machine_hkl.dm = DM;
machine_hkl.da = DA;

if (Qmode) {
  machine_real = qhkl2angles(sample, machine_hkl, machine_real);
  if (strlen(machine_real.message)) {
    exit(fprintf(stderr, "%s: ERROR: %s [qhkl2angles]\n", NAME_CURRENT_COMP, machine_real.message));
  }
}

if (A1 && (machine_real.a1 != A1)) {
  printf("Warning, resetting A1 from calculated %g to user provided %g\n", machine_real.a1, A1);
  machine_real.a1 = A1;
}
if (A2 && (machine_real.a2 != A2)) {
  printf("Warning, resetting A2 from calculated %g to user provided %g\n", machine_real.a2, A2);
  machine_real.a2 = A2;
}
if (A3 && (machine_real.a3 != A3)) {
  printf("Warning, resetting A3 from calculated %g to user provided %g\n", machine_real.a3, A3);
  machine_real.a3 = A3;
}
if (A4 && (machine_real.a4 != A4)) {
  printf("Warning, resetting A4 from calculated %g to user provided %g\n", machine_real.a4, A4);
  machine_real.a4 = A4;
}
if (A5 && (machine_real.a5 != A5)) {
  printf("Warning, resetting A5 from calculated %g to user provided %g\n", machine_real.a5, A5);
  machine_real.a5 = A5;
}
if (A6 && (machine_real.a6 != A6)) {
  printf("Warning, resetting A6 from calculated %g to user provided %g\n", machine_real.a6, A6);
  machine_real.a6 = A6;
}

if (verbose) {
  printf(" * Transferred: EN=%g [meV] QM=%g [Angs-1]\n", EN, machine_real.qm);
  printf("Angles: A1=%.4g A2=%.4g A3=%.4g A4=%.4g A5=%.4g A6=%.4g [deg]\n",
    machine_real.a1, machine_real.a2,
    machine_real.a3, machine_real.a4,
    machine_real.a5, machine_real.a6);
  printf("(RITA Analyzer Angles: CA2=%.4g CA3=%.4g CA4=%.4g CA5=%.4g CA6=%.4g CA7=%.4g CA8=%.4g [deg]\n",
    CA2, CA3, CA4, CA5, CA6, CA7, CA8);
}

/* The following is from RITA2front, Kim Lefmann / Linda Udby */
mono_mosaic_h = MONO_MOS_H; /* MON_MOSAIC; */
mono_mosaic_v = MONO_MOS_V; /* MON_MOSAIC; */
ana_mosaic_h = ANA_MOS_H; /* ANA_MOSAIC; */
ana_mosaic_v = ANA_MOS_V; /* ANA_MOSAIC; */
angleGuideCurved=20.0/2408.0;
/* fix 08/02/2009 by LU */
/* Forcing monochromator to set value */
if (MONOFORCE) {monoforce = 1;}
else {monoforce = 0;}
/* fix 20/02/2008 by LU */
u=U;
dms = dm+dv; /* Distance between mono and sample */
v= atan(mono_d/dms);
if (u && !monoforce){
  u = asin(KI/mono_q*sin(v))*RAD2DEG;
}
printf("Monochromator curvature parameters:dms=%g [m] KI=%g[Ang^-1] v=%g [rad] u=%g [deg]\n", dms,KI,v,u);

dmc = rmh-lc; /*distance monochromator to front of monocollimator*/

for (i=1; i<=5; i++) {
  /* GM removed below, could be included for completeness */
  /* Calibration constants from linear fit, get CUM in degrees */
  /* mrot[i]=(3-i)*(0.04275+CUM*0.05056); */
  // mrot[i]=(3-i)*0.95;// CUM is optimal (by scan) at 0.95 degrees which is 15.066 Rita-units for 5meV neutrons
  mrot[i]=(3-i)*u;
}

/* Set min and max wavelength for source */
l0=9.045/sqrt(EI);
lmin=BPL*10/MONO_N; /* MONO_N is the order of the reflection */
lmax=BPH*10/MONO_N;
printf("Source wavelength interval=%.4g - %.4g[Ang] \n",lmin, lmax);

/* Calculate min and max energy for source to use with energy monitors */
emin=(9.045*9.045)/(lmax*lmax);
emax=(9.045*9.045)/(lmin*lmin);
printf("Source energy interval=%.4g - %.4g[meV] \n",emin, emax);

if (SAMPLE == 2){
  /* Powder sample, relevant WHEN below */
  if (!strcmp(SAMPLEFILE,"default")) {
    PowderFile="Al2O3_102.lau";
  } else {

```

```

    PowderFile=SAMPLEFILE;
  }
  SingleXFile="";
} else if (SAMPLE == 3) {
/* Single crystal sample, relevant WHEN below */
if (!strcmp(SAMPLEFILE,"default")) {
  SingleXFile="current.lst";
} else {
  SingleXFile=SAMPLEFILE;
}
PowderFile="";
} else {
/* Purely incoherent scatterer, relevant WHEN below */
SingleXFile="";
PowderFile="";
}

/* Coarse collimator */
if (COARSE) {coarse = 1;}
else {coarse = 0;}

/* Opening slits of coarse collimator depends on analyzer settings: */
deltaL = 2 * WindowSize * cos(DEG2RAD*machine_real.a6 + fabs(DEG2RAD*machine_real.a5));
FirstWindowSizeL = WindowSize * (dad-BladeLength-deltaL+BladeLength*sin(DEG2RAD*machine_real.a6 + fabs(DEG2RAD*machine_real.a5)))/(dad-
FirstWindowSizeR = WindowSize * (dad-BladeLength+deltaL+BladeLength*sin(DEG2RAD*machine_real.a6 + fabs(DEG2RAD*machine_real.a5)))/(dad+

/* Window positions */
XwinMin[0] = 0;
XwinMin[1] = 0;
XwinMin[2] = 24;
XwinMin[3] = 36;
XwinMin[4] = 48;
XwinMin[5] = 60;
XwinMin[6] = 72;
XwinMin[7] = 84;
XwinMin[8] = 95;

XwinMax[0] = 0;
XwinMax[1] = 0;
XwinMax[2] = 33;
XwinMax[3] = 45;
XwinMax[4] = 57;
XwinMax[5] = 69;
XwinMax[6] = 81;
XwinMax[7] = 93;
XwinMax[8] = 104;

YwinMin[0] = 0;
YwinMin[1] = 0;
YwinMin[2] = 39;
YwinMin[3] = 39;
YwinMin[4] = 39;
YwinMin[5] = 39;
YwinMin[6] = 39;
YwinMin[7] = 39;
YwinMin[8] = 39;

YwinMax[0] = 0;
YwinMax[1] = 0;
YwinMax[2] = 91;
YwinMax[3] = 91;
YwinMax[4] = 91;
YwinMax[5] = 91;
YwinMax[6] = 91;
YwinMax[7] = 91;
YwinMax[8] = 91;

%}

/* end of INITIALIZE */

TRACE

/* PRIMARY START */

/* Source description */
COMPONENT armSource = Progress_bar()
  AT (0,0,0) ABSOLUTE

  /*COMPONENT source = Source_Maxwell_3(
height = 0.135, width = 0.08, xw = 0.030, yh = 0.120, dist = 1.465,
  l_low = lmin, l_high = lmax,
  //T1 = 150.42, T2 = 38.74, T3 = 14.84, I1 = 3.67E11, I2 = 3.64E11, I3 = 0.95E11 // source 1996
T1 = 150.42, T2 = 38.74, T3 = 14.84, I1 = 5.1E11, I2 = 5.1E11, I3 = 1.3E11 // source 2005
  )
AT (0,0,0) RELATIVE armSource*/

COMPONENT source = Source_gen4 (
  h = 0.135, w = 0.08, xw = 0.03, yh = 0.12,
  dist = 1.465, Lmin=lmin, Lmax=lmax, /*Lmin=0.1 LMax=10*/
  T1=301.287, I1=(1.27e13/4/PI),

```

```

T2=105.655,I2=(3.818e12/4/PI),
T3=25.379,I3=(2.331e12/4/PI),
HETailA=8.306e11/4/PI, HETailL0=-0.398)
AT (0,0,0) RELATIVE armSource ROTATED (0,0,0) RELATIVE armSource

COMPONENT slitGuideBegin = Slit(
  xmin = -0.015, xmax = 0.015,
  ymin = -0.06, ymax = 0.06)
AT (0,0,1.464999) RELATIVE armSource

/*COMPONENT emon_guide_start = E_monitor(
  nchan = 1000, filename = "emon_guide_start.dat", xmin = -0.02,
  xmax = 0.02, ymin = -0.075, ymax = 0.075, Emin = EMIN, Emax = EMAX, restore_neutron = 1)
AT (0, 0, 1.4649991) RELATIVE armSource */

/*COMPONENT lmon_guide_start = L_monitor(
  nchan = 1000, filename = "lmon_guide_start.dat", xmin = -0.02, xmax = 0.02,
  ymin = -0.075, ymax = 0.075, Lmin = lmin, Lmax = lmax, restore_neutron = 1)
AT (0, 0, 1.4649992 ) RELATIVE armSource */

COMPONENT guideStraight = Guide(
  w1 = 0.03, h1 = 0.12, w2 = 0.03, h2 = 0.12, l = 4.628,
  R0 = R0, Qc = Qc, alpha = alpha, m = M, W = W)
AT (0, 0, 1.465) RELATIVE armSource

/* 0.035m gap*/

COMPONENT guideCurved1 = Guide(
  w1 = 0.03, h1 = 0.12, w2 = 0.03, h2 = 0.12, l = 0.499995,
  R0 = R0, Qc = Qc, alpha = alpha, m = M, W = W)
AT (0, 0, 4.663) RELATIVE guideStraight
ROTATED (0,angleGuideCurved,0) RELATIVE guideStraight

COMPONENT guideCurved2 = Guide(
  w1 = 0.03, h1 = 0.12, w2 = 0.03, h2 = 0.12, l = 0.499995,
  R0 = R0, Qc = Qc, alpha = alpha, m = M, W = W)
AT (0, 0, 0.5) RELATIVE guideCurved1
ROTATED (0,angleGuideCurved,0) RELATIVE guideCurved1

COMPONENT guideCurved3 = Guide(
  w1 = 0.03, h1 = 0.12, w2 = 0.03, h2 = 0.12, l = 0.499995,
  R0 = R0, Qc = Qc, alpha = alpha, m = M, W = W)
AT (0, 0, 0.5) RELATIVE guideCurved2
ROTATED (0,angleGuideCurved,0) RELATIVE guideCurved2

COMPONENT guideCurved4 = Guide(
  w1 = 0.03, h1 = 0.12, w2 = 0.03, h2 = 0.12, l = 0.499995,
  R0 = R0, Qc = Qc, alpha = alpha, m = M, W = W)
AT (0, 0, 0.5) RELATIVE guideCurved3
ROTATED (0,angleGuideCurved,0) RELATIVE guideCurved3

COMPONENT guideCurved5 = Guide(
  w1 = 0.03, h1 = 0.12, w2 = 0.03, h2 = 0.12, l = 0.499995,
  R0 = R0, Qc = Qc, alpha = alpha, m = M, W = W)
AT (0, 0, 0.5) RELATIVE guideCurved4
ROTATED (0,angleGuideCurved,0) RELATIVE guideCurved4

COMPONENT guideCurved6 = Guide(
  w1 = 0.03, h1 = 0.12, w2 = 0.03, h2 = 0.12, l = 0.499995,
  R0 = R0, Qc = Qc, alpha = alpha, m = M, W = W)
AT (0, 0, 0.5) RELATIVE guideCurved5
ROTATED (0,angleGuideCurved,0) RELATIVE guideCurved5

COMPONENT guideCurved7 = Guide(
  w1 = 0.03, h1 = 0.12, w2 = 0.03, h2 = 0.12, l = 0.499995,
  R0 = R0, Qc = Qc, alpha = alpha, m = M, W = W)
AT (0, 0, 0.5) RELATIVE guideCurved6
ROTATED (0,angleGuideCurved,0) RELATIVE guideCurved6

COMPONENT guideCurved8 = Guide(
  w1 = 0.03, h1 = 0.12, w2 = 0.03, h2 = 0.12, l = 0.499995,
  R0 = R0, Qc = Qc, alpha = alpha, m = M, W = W)
AT (0, 0, 0.5) RELATIVE guideCurved7
ROTATED (0,angleGuideCurved,0) RELATIVE guideCurved7

COMPONENT guideCurved9 = Guide(
  w1 = 0.03, h1 = 0.12, w2 = 0.03, h2 = 0.12, l = 0.499995,
  R0 = R0, Qc = Qc, alpha = alpha, m = M, W = W)
AT (0, 0, 0.5) RELATIVE guideCurved8
ROTATED (0,angleGuideCurved,0) RELATIVE guideCurved8

COMPONENT guideCurved10 = Guide(
  w1 = 0.03, h1 = 0.12, w2 = 0.03, h2 = 0.12, l = 0.499995,
  R0 = R0, Qc = Qc, alpha = alpha, m = M, W = W)
AT (0, 0, 0.5) RELATIVE guideCurved9
ROTATED (0,angleGuideCurved,0) RELATIVE guideCurved9

COMPONENT guideCurved11 = Guide(
  w1 = 0.03, h1 = 0.12, w2 = 0.03, h2 = 0.12, l = 0.499995,
  R0 = R0, Qc = Qc, alpha = alpha, m = M, W = W)
AT (0, 0, 0.5) RELATIVE guideCurved10

```



```
COMPONENT guideCurved27 = Guide(
  w1 = 0.03, h1 = 0.12, w2 = 0.03, h2 = 0.12, l = 0.499995,
  R0 = R0, Qc = Qc, alpha = alpha, m = M, W = W)
  AT (0, 0, 0.5) RELATIVE guideCurved26
  ROTATED (0,angleGuideCurved,0) RELATIVE guideCurved26

COMPONENT guideCurved28 = Guide(
  w1 = 0.03, h1 = 0.12, w2 = 0.03, h2 = 0.12, l = 0.499995,
  R0 = R0, Qc = Qc, alpha = alpha, m = M, W = W)
  AT (0, 0, 0.5) RELATIVE guideCurved27
  ROTATED (0,angleGuideCurved,0) RELATIVE guideCurved27

COMPONENT guideCurved29 = Guide(
  w1 = 0.03, h1 = 0.12, w2 = 0.03, h2 = 0.12, l = 0.499995,
  R0 = R0, Qc = Qc, alpha = alpha, m = M, W = W)
  AT (0, 0, 0.5) RELATIVE guideCurved28
  ROTATED (0,angleGuideCurved,0) RELATIVE guideCurved28

COMPONENT guideCurved30 = Guide(
  w1 = 0.03, h1 = 0.12, w2 = 0.03, h2 = 0.12, l = 0.499995,
  R0 = R0, Qc = Qc, alpha = alpha, m = M, W = W)
  AT (0, 0, 0.5) RELATIVE guideCurved29
  ROTATED (0,angleGuideCurved,0) RELATIVE guideCurved29

COMPONENT guideCurved31 = Guide(
  w1 = 0.03, h1 = 0.12, w2 = 0.03, h2 = 0.12, l = 0.499995,
  R0 = R0, Qc = Qc, alpha = alpha, m = M, W = W)
  AT (0, 0, 0.5) RELATIVE guideCurved30
  ROTATED (0,angleGuideCurved,0) RELATIVE guideCurved30

COMPONENT guideCurved32 = Guide(
  w1 = 0.03, h1 = 0.12, w2 = 0.03, h2 = 0.12, l = 0.499995,
  R0 = R0, Qc = Qc, alpha = alpha, m = M, W = W)
  AT (0, 0, 0.5) RELATIVE guideCurved31
  ROTATED (0,angleGuideCurved,0) RELATIVE guideCurved31

COMPONENT guideCurved33 = Guide(
  w1 = 0.03, h1 = 0.12, w2 = 0.03, h2 = 0.12, l = 0.499995,
  R0 = R0, Qc = Qc, alpha = alpha, m = M, W = W)
  AT (0, 0, 0.5) RELATIVE guideCurved32
  ROTATED (0,angleGuideCurved,0) RELATIVE guideCurved32

COMPONENT guideCurved34 = Guide(
  w1 = 0.03, h1 = 0.12, w2 = 0.03, h2 = 0.12, l = 0.499995,
  R0 = R0, Qc = Qc, alpha = alpha, m = M, W = W)
  AT (0, 0, 0.5) RELATIVE guideCurved33
  ROTATED (0,angleGuideCurved,0) RELATIVE guideCurved33

COMPONENT guideCurved35 = Guide(
  w1 = 0.03, h1 = 0.12, w2 = 0.03, h2 = 0.12, l = 0.499995,
  R0 = R0, Qc = Qc, alpha = alpha, m = M, W = W)
  AT (0, 0, 0.5) RELATIVE guideCurved34
  ROTATED (0,angleGuideCurved,0) RELATIVE guideCurved34

COMPONENT guideCurved36 = Guide(
  w1 = 0.03, h1 = 0.12, w2 = 0.03, h2 = 0.12, l = 0.499995,
  R0 = R0, Qc = Qc, alpha = alpha, m = M, W = W)
  AT (0, 0, 0.5) RELATIVE guideCurved35
  ROTATED (0,angleGuideCurved,0) RELATIVE guideCurved35

COMPONENT guideCurved37 = Guide(
  w1 = 0.03, h1 = 0.12, w2 = 0.03, h2 = 0.12, l = 0.499995,
  R0 = R0, Qc = Qc, alpha = alpha, m = M, W = W)
  AT (0, 0, 0.5) RELATIVE guideCurved36
  ROTATED (0,angleGuideCurved,0) RELATIVE guideCurved36

COMPONENT guideCurved38 = Guide(
  w1 = 0.03, h1 = 0.12, w2 = 0.03, h2 = 0.12, l = 0.499995,
  R0 = R0, Qc = Qc, alpha = alpha, m = M, W = W)
  AT (0, 0, 0.5) RELATIVE guideCurved37
  ROTATED (0,angleGuideCurved,0) RELATIVE guideCurved37

COMPONENT guideCurved39 = Guide(
  w1 = 0.03, h1 = 0.12, w2 = 0.03, h2 = 0.12, l = 0.499995,
  R0 = R0, Qc = Qc, alpha = alpha, m = M, W = W)
  AT (0, 0, 0.5) RELATIVE guideCurved38
  ROTATED (0,angleGuideCurved,0) RELATIVE guideCurved38

COMPONENT guideCurved40 = Guide(
  w1 = 0.03, h1 = 0.12, w2 = 0.03, h2 = 0.12, l = 0.499995,
  R0 = R0, Qc = Qc, alpha = alpha, m = M, W = W)
  AT (0, 0, 0.5) RELATIVE guideCurved39
  ROTATED (0,angleGuideCurved,0) RELATIVE guideCurved39

/* bunker wall, m=2, 3.0 m */
COMPONENT bunker = Guide(w1= 0.03, h1=0.12, w2=0.03, h2=0.12,
  l=3.45, R0 = R0, Qc = Qc, alpha = alpha, m = M, W = W)
  AT (0,0,0.5) RELATIVE guideCurved40

/*15cm space for main shutter*/
```

```

/* guide segment 3, m=2, 1.3 m */
COMPONENT guide3 = Guide(w1=0.03, h1=0.12, w2=0.03, h2=0.12,
    l=5.2, R0 = R0, Qc = Qc, alpha = alpha, m = M, W = W)
    AT (0,0,3.6) RELATIVE bunker

COMPONENT slitGuideEnd = Slit(
    xmin = -0.016, xmax = 0.016,
    ymin = -0.061, ymax = 0.061)
    AT (0,0,5.2001) RELATIVE guide3

COMPONENT psd_guide_end = PSD_monitor(
    xmin = -0.020, xmax = 0.020, ymin = -0.075, ymax = 0.075,
    nx=64, ny=64, filename="psd_guide_end.dat", restore_neutron = 1)
    AT (0, 0, 0.04) RELATIVE slitGuideEnd

/*COMPONENT emon_guide_end = E_monitor(
    nchan = 1000, filename = "emon_guide_end.dat", xmin = -0.02,
    xmax = 0.02, ymin = -0.075, ymax = 0.075, Emin =EMIN, Emax = EMAX, restore_neutron = 1)
    AT (0, 0, 0.5) RELATIVE slitGuideEnd*/

COMPONENT lmon_guide_end = L_monitor(
    nchan = 100, filename = "lmon_guide_end.dat", xmin = -0.02, xmax = 0.02,
    ymin = -0.07, ymax = 0.07, Lmin = lmin, Lmax = lmax, restore_neutron = 1)
    AT (0, 0, 0.06) RELATIVE slitGuideEnd

COMPONENT divmon_guide_end = Divergence_monitor(
    nh = 128, nv = 128, filename = "divmon_guide_end.dat",
    restore_neutron = 1, xwidth = 0.04, yheight = 0.14,
    h_maxdiv = 2, v_maxdiv = 2, restore_neutron = 1)
    AT (0, 0, 0.07) RELATIVE slitGuideEnd

COMPONENT focus_mono = Arm()
    AT (0, 0, 0.15) RELATIVE slitGuideEnd
    ROTATED (0, machine_real.a1, 0) RELATIVE slitGuideEnd

COMPONENT m1= Monochromator_flat(
    zmin=-0.075, zmax=0.075, ymin=-0.0125, ymax=0.0125,
    mosaich=mono_mosaic_h, mosaicv=mono_mosaic_v,
    r0=mono_r0, Q=mono_q)
    AT (0, -2*mono_d, 0) RELATIVE focus_mono
    ROTATED (0, 0, mrot[1]) RELATIVE focus_mono

COMPONENT m2= Monochromator_flat(
    zmin=-0.075, zmax=0.075, ymin=-0.0125, ymax=0.0125,
    mosaich=mono_mosaic_h, mosaicv=mono_mosaic_v,
    r0=mono_r0, Q=mono_q)
    AT (0, -mono_d, 0) RELATIVE focus_mono
    ROTATED (0, 0, mrot[2]) RELATIVE focus_mono

COMPONENT m3= Monochromator_flat(
    zmin=-0.075, zmax=0.075, ymin=-0.0125, ymax=0.0125,
    mosaich=mono_mosaic_h, mosaicv=mono_mosaic_v,
    r0=mono_r0, Q=mono_q)
    AT (0, 0, 0) RELATIVE focus_mono
    ROTATED (0, 0, mrot[3]) RELATIVE focus_mono

COMPONENT m4= Monochromator_flat(
    zmin=-0.075, zmax=0.075, ymin=-0.0125, ymax=0.0125,
    mosaich=mono_mosaic_h, mosaicv=mono_mosaic_v,
    r0=mono_r0, Q=mono_q)
    AT (0, mono_d, 0) RELATIVE focus_mono
    ROTATED (0, 0, mrot[4]) RELATIVE focus_mono

COMPONENT m5= Monochromator_flat(
    zmin=-0.075, zmax=0.075, ymin=-0.0125, ymax=0.0125,
    mosaich=mono_mosaic_h, mosaicv=mono_mosaic_v,
    r0=mono_r0, Q=mono_q)
    AT (0, 2*mono_d, 0) RELATIVE focus_mono
    ROTATED (0, 0, mrot[5]) RELATIVE focus_mono

COMPONENT a2 = Arm()
    AT (0,0,0) RELATIVE focus_mono
    ROTATED (0, machine_real.a2, 0) RELATIVE slitGuideEnd

COMPONENT Lmon_primary_after_mono = L_monitor(
    nchan = 100, filename = "Lmon_primary_after_mono.dat",xwidth = 0.20, yheight = 0.20, Lmin = lmin, Lmax = lmax, restore_neutron=1)
    AT (0, 0, 0.19) RELATIVE a2

COMPONENT slitShutter = Slit(
    xmin = -0.02, xmax = 0.02,
    ymin = -0.075, ymax = 0.075)
    AT (0, 0, 0.2) RELATIVE a2
    ROTATED (0,0,0) RELATIVE a2

COMPONENT MSCollimator = Collimator_linear(
    xmin = -0.02, xmax = 0.02, ymin = -0.075, ymax = 0.075,
    len = 0.20, divergence = COLL_MS)
    AT (0, 0, dmc) RELATIVE a2

```

```

/* COMPONENT MSCollimator = Soller( */
/*   xmin = -0.02, xmax = 0.02, ymin = -0.075, ymax = 0.075, len = 0.20 , */
/*   divergence = COLL_MS ) */
/*   AT (0, 0, 0.32) RELATIVE a2 */

COMPONENT Lmon_primary_after_mono_coll = L_monitor(
  nchan = 100, filename = "Lmon_primary_after_mono_coll.dat",xwidth = 0.10, yheight = 0.10, Lmin = lmin, Lmax = lmax, restore_neutron=1)
  AT (0, 0, 0.201) RELATIVE MSCollimator

COMPONENT psd_virt = PSD_monitor(
  nx=128, ny=128, filename="psd_virt.dat", xwidth = 0.10, yheight = 0.10 )
  AT (0, 0, dmv-0.01) RELATIVE a2

COMPONENT emon_virt = E_monitor(
  nchan=128, filename="emon_virt.dat",xwidth = 0.06, yheight = 0.10, Emin=emin, Emax=emax, restore_neutron=1)
  AT (0, 0, dmv-0.005) RELATIVE a2

COMPONENT lmon_virt = L_monitor(
  nchan = 100, filename = "lmon_virt.dat", xwidth=0.06, yheight=0.10,//the size of the beam
  Lmin = lmin, Lmax = lmax, restore_neutron=1)
  AT (0, 0, dmv) RELATIVE a2 // Needs to be here in order to propagate virtual_out to dmv

/* /\* This virtual output should ONLY be used if secondary spectrometer IS NOT present *\/*
/* /\* Otherwise sensible to do a SPLIT on aa2 below! *\/*
/* /\* COMPONENT virtualsource = Virtual_output(file=SOURCEFILE, bufsize=0) *\/*
/* /\* AT (0, 0, dmv) RELATIVE a2 *\/*

/*PRIMARY END */

/* CONFIG STUFF HERE!!! */

/* SECONDARY START */

/* This arm should be used in case of primary spectrometer present */
SPLIT REP COMPONENT aa2 = Arm()
  AT (0,0,dmv) RELATIVE a2

/* /\*This arm and Virtual_input should be used in case of primary spectrometer NOT present*\/*
/* COMPONENT aa2 = Progress_bar() */
/* AT (0,0,0) ABSOLUTE */

/* COMPONENT virtualsource = Virtual_input(file=SOURCEFILE, verbose=1, repeat_count=REP) */
/* AT (0,0,0) RELATIVE aa2 */

COMPONENT monitor = PSD_monitor(
  xwidth = 0.040, yheight=0.080,
  nx=64, ny=64, filename="monitor.dat",restore_neutron=1)
  AT (0, 0, 0.170) RELATIVE aa2

COMPONENT slitMonochromator = Slit(
  xmin = -MSL/1000.0, xmax = MSR/1000.0,
  ymin = -MSB/1000.0, ymax = MST/1000.0)
  AT (0, 0, 0.285) RELATIVE aa2

COMPONENT Perspex = V_sample(V0=1,sig_a=0.019,sig_i=4.7, xwidth = 0.1, yheight = 0.1, zthick = PTHICK, frac=1e-2)
  WHEN (PERSPEX>0) AT (0, 0, 0.3) RELATIVE aa2

COMPONENT emon_before_sample = E_monitor(
  nchan=128, filename="emon_before_sample.dat",xwidth = 0.02, yheight = 0.04, Emin=emin, Emax=emax, restore_neutron=1)
  AT (0, 0, dvs-0.05) RELATIVE aa2

COMPONENT emon_before_sample_size = E_monitor(
  nchan=128, filename="emon_before_sample_size.dat",xwidth=0.0201, yheight=0.0187, Emin=emin, Emax=emax, restore_neutron=1)
  AT (0, 0, dvs-0.045) RELATIVE aa2

COMPONENT psd_before_sample = PSD_monitor(
  nx=128, ny=128, filename="psd_before_sample.dat", xwidth = 0.1, yheight = 0.1,restore_neutron=1 )
  AT (0, 0, dvs-0.04) RELATIVE aa2

COMPONENT divmon_before_sample = Divergence_monitor(
  nh = 128, nv = 128, filename = "divmon_before_sample",
  xwidth = 0.02, yheight = 0.04, h_maxdiv = 3, v_maxdiv = 3, restore_neutron=1)
  AT (0, 0, dvs-0.03) RELATIVE aa2

/* This should be removed when sample is present*/
/* COMPONENT psd_samplepos = PSD_monitor( */
/*   nx=128, ny=128, filename="psd_samplepos.dat", xwidth = 0.02, yheight = 0.06, restore_neutron=1) */
/* AT (0, 0, dvs) RELATIVE aa2 */

COMPONENT a3 = Arm()
  AT (0,0,dvs) RELATIVE aa2
  ROTATED (0, machine_real.a3, 0) RELATIVE aa2

COMPONENT aa3 = Arm()
  AT (0,0,0) RELATIVE a3
  ROTATED (TILT, 0, 0) RELATIVE a3

COMPONENT Collimator = Collimator_linear(
  xmin = -0.02, xmax = 0.02, ymin = -0.075, ymax = 0.075,

```

```

    len = 0.20, divergence = COLL)
WHEN (SAMPLE==4)
AT (0, 0, -0.1) RELATIVE a3
ROTATED (0, 0, 0) RELATIVE a3

COMPONENT incohSample = V_sample(
/*      V0=1,sig_a=0,sig_i=4.70,radius_i=0, radius_o=0.0025, h=0.068,target_index=10, // perspex sample */
      V0=13.827,sig_a=5.08,sig_i=5.08,radius_i=0.0149/2, radius_o=0.0201/2, h=0.0187,target_index=13, // vanadium sample
      focus_r=0.5) // focus on emon before ana. Square focusing gives neg. int. for |a3|<90
//WHEN ((SAMPLE==2 || SAMPLE==3 || SAMPLE==4))
WHEN (SAMPLE==1)
AT (0, 0, 0) RELATIVE a3
/*EXTEND %{
printf("x %g y %g z %g vx %g vy %g vz %g\n",x,y,z,vx,vy,vz);
%}*/

COMPONENT powderSample = PowderN(
  reflections=PowderFile, format=Crystallographica, d_phi = 12, radius = 0.0068, h = 0.015, pack = 1, Vc = 254.52, sigma_abs = 0.46,
  sigma_inc = 0.0188, frac = 0, barns=0)
WHEN (SAMPLE==2)
AT (0, 0, 0) RELATIVE a3

COMPONENT crystalSample = Single_crystal(//order=1, p_transmit=0,
  reflections = SingleXFile, mosaic=MOS, xwidth = XW, yheight = YH,zthick = ZT, delta_d=DD_D,
  ax =AAX, ay = AAY, az =AAZ, bx =BBX, by =BBY, bz =BBZ, cx =CCX, cy =CCY, cz =CCZ)
WHEN (SAMPLE==3)
AT (0, 0, 0) RELATIVE aa3

/*COMPONENT Sphere = PSD_monitor_4PI(radius=d_sample_slit/2-0.003, filename="sphere.dat", restore_neutron=1)
AT (0,0,0) RELATIVE a3 */

COMPONENT a4 = Arm()
AT (0, 0, 0) RELATIVE a3
ROTATED (0, machine_real.a4, 0) RELATIVE aa2

COMPONENT psd_after_sample0= PSD_monitor(
  nx=128, ny=128, filename="psd_after_sample0.dat", xmin =-SSL/1000.0, xmax =SSR/1000.0,
  ymin = -SSB/1000.0, ymax =SST/1000.0, restore_neutron=1)
AT (0, 0,d_sample_slit/2-0.002) RELATIVE a4

COMPONENT psd_after_sample= PSD_monitor(
  nx=128, ny=128, filename="psd_after_sample.dat", xmin = -0.01, xmax = 0.01,
  ymin = -0.03, ymax = 0.03, restore_neutron=1)
AT (0, 0,d_sample_slit/2-0.001) RELATIVE a4

COMPONENT emon_after_sample = E_monitor(
  nchan=128, filename="emon_after_sample.dat", xmin =-SSL/1000.0, xmax =SSR/1000.0,
  ymin = -SSB/1000.0, ymax =SST/1000.0, Emin=emin, Emax=emax, restore_neutron=1)
AT (0, 0,d_sample_slit/2) RELATIVE a4

COMPONENT slitSample = Slit(
  xmin = -SSL/1000.0, xmax = SSR/1000.0,
  ymin = -SSB/1000.0, ymax = SST/1000.0)
AT (0, 0, d_sample_slit) RELATIVE a4
ROTATED (0,0,0) RELATIVE a4

COMPONENT emon_after_sample_slit = E_monitor(
  nchan=128, filename="emon_after_sample_slit.dat", xmin =-SSL/1000.0, xmax =SSR/1000.0,
  ymin = -SSB/1000.0, ymax =SST/1000.0, Emin=emin, Emax=emax, restore_neutron=1)
AT (0, 0, 0.001) RELATIVE slitSample

COMPONENT filter_coll=Exact_radial_coll_fix(
  in_radius=0.4525, channels=9, foil_thick=0.000125,verbose=1,h_in=0.2,h_out=0.2,length=0.0988,theta_mini=-10.26/2,theta_maxi=10.26/2
)
WHEN (FILTER>0)
AT (0, 0, d_sample_filter-0.4525-0.0988/2) RELATIVE a4

COMPONENT filter = Filter_gen(
  xmin = -0.1, xmax = 0.1, ymin = -0.1, ymax = 0.1, options="wavevector multiply", file=FILTERFILE)
WHEN (FILTER>0)
AT (0, 0,0.4525+0.0988+0.0001) RELATIVE filter_coll

COMPONENT psd_after_filter= PSD_monitor(
  nx=128, ny=128, filename="psd_after_filter.dat", xmin = -0.01, xmax = 0.01,
  ymin = -0.03, ymax = 0.03, restore_neutron=1)
AT (0, 0, 0.0001) RELATIVE filter

COMPONENT psd_anaslit= PSD_monitor(
  nx=128, ny=128, filename="psd_anaslit.dat", xmin = -0.01, xmax = 0.01,
  ymin = -0.03, ymax = 0.03, restore_neutron=1)
AT (0, 0, d_sample_filter+0.13) RELATIVE a4

COMPONENT ana_slit1 = Slit(
  xmin = -0.158/2, xmax = 0.158/2, //xmin = -0.06, xmax = 0.06,
  ymin = -0.08/2, ymax = 0.08/2) //ymin = -0.085, ymax = 0.085)
AT (0, 0, d_sample_filter+0.13) RELATIVE a4
ROTATED (0,0,0) RELATIVE a4

```

```

COMPONENT ana_slit2 = Slit(
xmin = -0.158/2, xmax = 0.158/2, //xmin = -0.06, xmax = 0.06,
ymin = -0.103/2, ymax = 0.103/2 //ymin = -0.085, ymax = 0.085)
  AT (0, 0, d_sample_filter+0.33) RELATIVE a4
  ROTATED (0,0,0) RELATIVE a4

COMPONENT emon_before_ana = E_monitor(
xmin = -0.060, xmax = 0.060, ymin = -0.085, ymax = 0.085,
Emin=emin, Emax=emax, nchan=128, filename="emon_before_ana.dat", restore_neutron=1)
  AT (0, 0, dsa-5*ana_d) RELATIVE a4

COMPONENT psd_before_ana = PSD_monitor(
  nx = 128, ny = 128, filename = "psd_before_ana.dat",
  //xmin = -0.1, xmax = 0.1, ymin = -0.1, ymax = 0.1)
  xmin = -0.060, xmax = 0.060, ymin = -0.085, ymax = 0.085)
  AT (0, 0, dsa-5*ana_d+0.001) RELATIVE a4

COMPONENT divmon_before_ana = Divergence_monitor(
  nh = 128, nv = 128, filename = "divmon_before_ana",
  xwidth = 0.02, yheight = 0.17, h_maxdiv = 1, v_maxdiv = 1, restore_neutron = 1)
  AT (0, 0, dsa-5*ana_d+0.002) RELATIVE a4

COMPONENT focus_ana = Arm()
  AT (0, 0, dsa) RELATIVE a4
  ROTATED (0, machine_real.a5, 0) RELATIVE a4
EXTEND %{
  AnaBlade=0;
  %}

COMPONENT an2l= Monochromator_flat(
zmin=-wan/2.0, zmax=wan/2.0, ymin=-ana_h/2.0, ymax=0,
mosaich=38.7-ANAMOSCRR, mosaicv=38.7-ANAMOSCRR,
r0=ana_r0, Q=ana_q)
  AT (0, 0, -3*ana_d) RELATIVE focus_ana
  ROTATED (0, -CA2, 0) RELATIVE focus_ana
//GROUP ANA
EXTEND %{
  if(SCATTERED) AnaBlade = 2;
  %}

COMPONENT an2u= Monochromator_flat(
zmin=-wan/2.0, zmax=wan/2.0, ymin=0, ymax=ana_h/2.0,
mosaich=43.0-ANAMOSCRR, mosaicv=43.0-ANAMOSCRR,
r0=ana_r0, Q=ana_q)
  AT (0, 0, -3*ana_d) RELATIVE focus_ana
  ROTATED (0, -CA2, 0) RELATIVE focus_ana
//GROUP ANA
EXTEND %{
  if(SCATTERED) AnaBlade = 2;
  %}

COMPONENT an3l= Monochromator_flat(
zmin=-wan/2.0, zmax=wan/2.0, ymin=-ana_h/2.0, ymax=0,
mosaich=31.1-ANAMOSCRR, mosaicv=31.1-ANAMOSCRR,
r0=ana_r0, Q=ana_q)
  AT (0, 0, -2*ana_d) RELATIVE focus_ana
  ROTATED (0, -CA3, 0) RELATIVE focus_ana
//GROUP ANA
EXTEND %{
  if(SCATTERED) AnaBlade = 3;
  %}

COMPONENT an3u= Monochromator_flat(
zmin=-wan/2.0, zmax=wan/2.0, ymin=0, ymax=ana_h/2.0,
mosaich=35.5-ANAMOSCRR, mosaicv=35.5-ANAMOSCRR,
r0=ana_r0, Q=ana_q)
  AT (0, 0, -2*ana_d) RELATIVE focus_ana
  ROTATED (0, -CA3, 0) RELATIVE focus_ana
//GROUP ANA
EXTEND %{
  if(SCATTERED) AnaBlade = 3;
  %}

COMPONENT an4l= Monochromator_flat(
zmin=-wan/2.0, zmax=wan/2.0, ymin=-ana_h/2.0, ymax=0,
mosaich=27.2-ANAMOSCRR, mosaicv=27.2-ANAMOSCRR,
r0=ana_r0, Q=ana_q)
  AT (0, 0, -1*ana_d) RELATIVE focus_ana
  ROTATED (0, -CA4, 0) RELATIVE focus_ana
//GROUP ANA
EXTEND %{
  if(SCATTERED) AnaBlade = 4;
  %}

COMPONENT an4u= Monochromator_flat(
zmin=-wan/2.0, zmax=wan/2.0, ymin=0, ymax=ana_h/2.0,
mosaich=30.4-ANAMOSCRR, mosaicv=30.4-ANAMOSCRR,
r0=ana_r0, Q=ana_q)
  AT (0, 0, -1*ana_d) RELATIVE focus_ana

```

```
    ROTATED (0, -CA4, 0) RELATIVE focus_ana
//GROUP ANA
EXTEND %{
    if(SCATTERED) AnaBlade = 4;
%}

COMPONENT an5l= Monochromator_flat(
zmin=-wan/2.0, zmax=wan/2.0, ymin=-ana_h/2.0, ymax=0,
mosaich=36.6-ANAMOSCRR, mosaicv=36.6-ANAMOSCRR,
r0=ana_r0, Q=ana_q)
    AT (0, 0, 0) RELATIVE focus_ana
    ROTATED (0, -CA5, 0) RELATIVE focus_ana
//GROUP ANA
EXTEND %{
    if(SCATTERED) AnaBlade = 5;
%}

COMPONENT an5u= Monochromator_flat(
zmin=-wan/2.0, zmax=wan/2.0, ymin=0, ymax=ana_h/2.0,
mosaich=35.9-ANAMOSCRR, mosaicv=35.9-ANAMOSCRR,
r0=ana_r0, Q=ana_q)
    AT (0, 0, 0) RELATIVE focus_ana
    ROTATED (0, -CA5, 0) RELATIVE focus_ana
//GROUP ANA
EXTEND %{
    if(SCATTERED) AnaBlade = 5;
%}

COMPONENT an6l= Monochromator_flat(
zmin=-wan/2.0, zmax=wan/2.0, ymin=-ana_h/2.0, ymax=0,
mosaich=31.5-ANAMOSCRR, mosaicv=31.5-ANAMOSCRR,
r0=ana_r0, Q=ana_q)
    AT (0, 0, ana_d) RELATIVE focus_ana
    ROTATED (0, -CA6, 0) RELATIVE focus_ana
//GROUP ANA
EXTEND %{
    if(SCATTERED) AnaBlade = 6;
%}

COMPONENT an6u= Monochromator_flat(
zmin=-wan/2.0, zmax=wan/2.0, ymin=0, ymax=ana_h/2.0,
mosaich=36.1-ANAMOSCRR, mosaicv=36.1-ANAMOSCRR,
r0=ana_r0, Q=ana_q)
    AT (0, 0, ana_d) RELATIVE focus_ana
    ROTATED (0, -CA6, 0) RELATIVE focus_ana
//GROUP ANA
EXTEND %{
    if(SCATTERED) AnaBlade = 6;
%}

COMPONENT an7l= Monochromator_flat(
zmin=-wan/2.0, zmax=wan/2.0, ymin=-ana_h/2.0, ymax=0,
mosaich=33.1-ANAMOSCRR, mosaicv=33.1-ANAMOSCRR,
r0=ana_r0, Q=ana_q)
    AT (0, 0, 2*ana_d) RELATIVE focus_ana
    ROTATED (0, -CA7, 0) RELATIVE focus_ana
//GROUP ANA
EXTEND %{
    if(SCATTERED) AnaBlade = 7;
%}

COMPONENT an7u= Monochromator_flat(
zmin=-wan/2.0, zmax=wan/2.0, ymin=0, ymax=ana_h/2.0,
mosaich=37.2-ANAMOSCRR, mosaicv=37.2-ANAMOSCRR,
r0=ana_r0, Q=ana_q)
    AT (0, 0, 2*ana_d) RELATIVE focus_ana
    ROTATED (0, -CA7, 0) RELATIVE focus_ana
//GROUP ANA
EXTEND %{
    if(SCATTERED) AnaBlade = 7;
%}

COMPONENT an8l= Monochromator_flat(
zmin=-wan/2.0, zmax=wan/2.0, ymin=-ana_h/2.0, ymax=0,
mosaich=46.8-ANAMOSCRR, mosaicv=46.8-ANAMOSCRR,
r0=ana_r0, Q=ana_q)
    AT (0, 0, 3*ana_d) RELATIVE focus_ana
    ROTATED (0, -CA8, 0) RELATIVE focus_ana
//GROUP ANA
EXTEND %{
    if(SCATTERED) AnaBlade = 8;
%}

COMPONENT an8u= Monochromator_flat(
zmin=-wan/2.0, zmax=wan/2.0, ymin=0, ymax=ana_h/2.0,
mosaich=51.3-ANAMOSCRR, mosaicv=51.3-ANAMOSCRR,
r0=ana_r0, Q=ana_q)
    AT (0, 0, 3*ana_d) RELATIVE focus_ana
    ROTATED (0, -CA8, 0) RELATIVE focus_ana
//GROUP ANA
EXTEND %{
```

```

if (SCATTERED) AnaBlade = 8;
%}

COMPONENT a6 = Arm()
  AT (0,0,0) RELATIVE focus_ana
  ROTATED (0, machine_real.a6, 0) RELATIVE a4

COMPONENT emon_before_coarse = E_monitor(
  nchan=128, filename = "emon_before_coarse.dat", Emin=emin, Emax=emax,
  xmin = -0.01, xmax = 0.01, ymin = -0.15, ymax = 0.15, restore_neutron=1)
  //xmin = -0.060, xmax = 0.060, ymin = -0.085, ymax = 0.085, restore_neutron=1)
  AT (0, 0, dad-BladeLength-0.02) RELATIVE a6

COMPONENT psd_before_coarse = PSD_monitor(
  nx = 128, ny = 128, filename = "psd_before_coarse.dat",
  xmin = -0.15, xmax = 0.15, ymin = -0.15, ymax = 0.15, restore_neutron=1)
  //xmin = -0.060, xmax = 0.060, ymin = -0.085, ymax = 0.085, restore_neutron=1)
  AT (0, 0, dad-BladeLength-0.01) RELATIVE a6

COMPONENT ArmR1 = Arm()
  AT (-WindowSize/2,0,dad-0.005) RELATIVE a6
  ROTATED (0,-RC/9,0) RELATIVE a6

COMPONENT BladeR1 = Absorber(xmin=-BladeThickness/2, xmax=BladeThickness/2,
  ymin=-BladeHeight/2, ymax=BladeHeight/2,
  zmin=-BladeLength,zmax=0)
  WHEN (COARSE>0) AT (0,0,0) RELATIVE ArmR1
  EXTEND %{
  if (SCATTERED) printf("Absorption in R1\n");
  %}

COMPONENT ArmR2 = Arm()
  AT (-3*WindowSize/2,0,dad-0.005) RELATIVE a6
  ROTATED (0,-3*RC/9,0) RELATIVE a6

COMPONENT BladeR2 = Absorber(xmin=-BladeThickness/2, xmax=BladeThickness/2,
  ymin=-BladeHeight/2, ymax=BladeHeight/2,
  zmin=-BladeLength,zmax=0)
  WHEN (COARSE>0) AT (0,0,0) RELATIVE ArmR2

COMPONENT ArmR3 = Arm()
  AT (-5*WindowSize/2,0,dad-0.005) RELATIVE a6
  ROTATED (0,-5*RC/9,0) RELATIVE a6

COMPONENT BladeR3 = Absorber(xmin=-BladeThickness/2, xmax=BladeThickness/2,
  ymin=-BladeHeight/2, ymax=BladeHeight/2,
  zmin=-BladeLength,zmax=0)
  WHEN (COARSE>0) AT (0,0,0) RELATIVE ArmR3

COMPONENT ArmR4 = Arm()
  AT (-7*WindowSize/2,0,dad-0.005) RELATIVE a6
  ROTATED (0,-7*RC/9,0) RELATIVE a6

COMPONENT BladeR4 = Absorber(xmin=-BladeThickness/2, xmax=BladeThickness/2,
  ymin=-BladeHeight/2, ymax=BladeHeight/2,
  zmin=-BladeLength,zmax=0)
  WHEN (COARSE>0) AT (0,0,0) RELATIVE ArmR4

COMPONENT ArmR5 = Arm()
  AT (-9*WindowSize/2,0,dad-0.005) RELATIVE a6
  ROTATED (0,-9*RC/9,0) RELATIVE a6

COMPONENT BladeR5 = Absorber(xmin=-BladeThickness/2, xmax=BladeThickness/2,
  ymin=-BladeHeight/2, ymax=BladeHeight/2,
  zmin=-BladeLength,zmax=0)
  WHEN (COARSE>0) AT (0,0,0) RELATIVE ArmR5

COMPONENT ArmL1 = Arm()
  AT (WindowSize/2,0,dad-0.005) RELATIVE a6
  ROTATED (0,LC/9,0) RELATIVE a6

COMPONENT BladeL1 = Absorber(xmin=-BladeThickness/2, xmax=BladeThickness/2,
  ymin=-BladeHeight/2, ymax=BladeHeight/2,
  zmin=-BladeLength,zmax=0)
  WHEN (COARSE>0) AT (0,0,0) RELATIVE ArmL1

COMPONENT ArmL2 = Arm()
  AT (3*WindowSize/2,0,dad-0.005) RELATIVE a6
  ROTATED (0,3*LC/9,0) RELATIVE a6

COMPONENT BladeL2 = Absorber(xmin=-BladeThickness/2, xmax=BladeThickness/2,
  ymin=-BladeHeight/2, ymax=BladeHeight/2,
  zmin=-BladeLength,zmax=0)
  WHEN (COARSE>0) AT (0,0,0) RELATIVE ArmL2

COMPONENT ArmL3 = Arm()
  AT (5*WindowSize/2,0,dad-0.005) RELATIVE a6

```

```

ROTATED (0,5*LC/9,0) RELATIVE a6

COMPONENT BladeL3 = Absorber(xmin=-BladeThickness/2, xmax=BladeThickness/2,
  ymin=-BladeHeight/2, ymax=BladeHeight/2,
  zmin=-BladeLength,zmax=0)
  WHEN (COARSE>0) AT (0,0,0) RELATIVE ArmL3

COMPONENT ArmL4 = Arm()
  AT (7*WindowSize/2,0,dad-0.005) RELATIVE a6
ROTATED (0,7*LC/9,0) RELATIVE a6

COMPONENT BladeL4 = Absorber(xmin=-BladeThickness/2, xmax=BladeThickness/2,
  ymin=-BladeHeight/2, ymax=BladeHeight/2,
  zmin=-BladeLength,zmax=0)
  WHEN (COARSE>0) AT (0,0,0) RELATIVE ArmL4

COMPONENT ArmL5 = Arm()
  AT (9*WindowSize/2,0,dad-0.005) RELATIVE a6
ROTATED (0,9*LC/9,0) RELATIVE a6
EXTEND %{
  BinX = 0; BinY=0;
%}

COMPONENT BladeL5 = Absorber(xmin=-BladeThickness/2, xmax=BladeThickness/2,
  ymin=-BladeHeight/2, ymax=BladeHeight/2,
  zmin=-BladeLength,zmax=0)
  WHEN (COARSE>0) AT (0,0,0) RELATIVE ArmL5

COMPONENT psd_detector = PSD_monitor_psf(
  xmin = -det_width/2.0, xmax = det_width/2.0, ymin = -det_height/2.0,
  ymax = det_height/2.0, nx = 128, ny = 128, psf = PSF, filename = "psd_detector.dat",restore_neutron=0)
// restore_neutron needs to be 0 to propagate the neutrons in use for EXTEND section
  AT (0, 0, dad+0.0215) RELATIVE a6
  ROTATED (0,180,0) RELATIVE a6
EXTEND %{
  BinX = floor((x - xmin)*nx/(xmax - xmin)); BinY = floor((y - ymin)*ny/(ymax - ymin));
%}

COMPONENT emon_detector = E_monitor(
  nchan=128, filename="detector.dat", xwidth =det_width , yheight=det_height, Emin=0, Emax=1e3,restore_neutron=1)
  AT (0, 0, dad+0.0215) RELATIVE a6
ROTATED (0,180,0) RELATIVE a6

COMPONENT psd2_detector = PSD_monitor_psf(
  xmin = -det_width/2.0, xmax = det_width/2.0, ymin = -det_height/2.0,
  ymax = det_height/2.0, nx = 128, ny = 128, psf = PSF, filename = "psd2_detector.dat",restore_neutron=1)
WHEN ((BinX >= XwinMin[2] && BinX <= XwinMax[2] && BinY >= YwinMin[2] && BinY <= YwinMax[2])) AT (0, 0, dad+0.0215) RELATIVE a6
  ROTATED (0,180,0) RELATIVE a6

COMPONENT emon2_detector = E_monitor(
  nchan = 128, filename="detector2.dat", xwidth =det_width , yheight=det_height, Emin=emin, Emax=emax,restore_neutron=1)
WHEN ((BinX >= XwinMin[2] && BinX <= XwinMax[2] && BinY >= YwinMin[2] && BinY <= YwinMax[2])) AT (0, 0, dad+0.0215) RELATIVE a6
  ROTATED (0,180,0) RELATIVE a6

COMPONENT psd3_detector = PSD_monitor_psf(
  xmin = -det_width/2.0, xmax = det_width/2.0, ymin = -det_height/2.0,
  ymax = det_height/2.0, nx = 128, ny = 128, psf = PSF, filename = "psd3_detector.dat",restore_neutron=1)
WHEN ((BinX >= XwinMin[3] && BinX <= XwinMax[3] && BinY >= YwinMin[3] && BinY <= YwinMax[3])) AT (0, 0, dad+0.0215) RELATIVE a6
  ROTATED (0,180,0) RELATIVE a6

COMPONENT emon3_detector = E_monitor(
  nchan = 128, filename="detector3.dat", xwidth =det_width , yheight=det_height, Emin=emin, Emax=emax,restore_neutron=1)
WHEN ((BinX >= XwinMin[3] && BinX <= XwinMax[3] && BinY >= YwinMin[3] && BinY <= YwinMax[3])) AT (0, 0, dad+0.0215+0.0008) RELATIVE a6
  ROTATED (0,180,0) RELATIVE a6

COMPONENT psd4_detector = PSD_monitor_psf(
  xmin = -det_width/2.0, xmax = det_width/2.0, ymin = -det_height/2.0,
  ymax = det_height/2.0, nx = 128, ny = 128, psf = PSF, filename = "psd4_detector.dat",restore_neutron=1)
WHEN ((BinX >= XwinMin[4] && BinX <= XwinMax[4] && BinY >= YwinMin[4] && BinY <= YwinMax[4])) AT (0, 0, dad+0.0215) RELATIVE a6
  ROTATED (0,180,0) RELATIVE a6

COMPONENT emon4_detector = E_monitor(
  nchan = 128, filename="detector4.dat", xwidth =det_width , yheight=det_height, Emin=emin, Emax=emax,restore_neutron=1)
WHEN ((BinX >= XwinMin[4] && BinX <= XwinMax[4] && BinY >= YwinMin[4] && BinY <= YwinMax[4])) AT (0, 0, dad+0.0215) RELATIVE a6
  ROTATED (0,180,0) RELATIVE a6

COMPONENT psd5_detector = PSD_monitor_psf(
  xmin = -det_width/2.0, xmax = det_width/2.0, ymin = -det_height/2.0,
  ymax = det_height/2.0, nx = 128, ny = 128, psf = PSF, filename = "psd5_detector.dat",restore_neutron=1)
WHEN ((BinX >= XwinMin[5] && BinX <= XwinMax[5] && BinY >= YwinMin[5] && BinY <= YwinMax[5])) AT (0, 0, dad+0.0215) RELATIVE a6
  ROTATED (0,180,0) RELATIVE a6

COMPONENT emon5_detector = E_monitor(
  nchan = 128, filename="detector5.dat", xwidth =det_width , yheight=det_height, Emin=emin, Emax=emax,restore_neutron=1)
WHEN ((BinX >= XwinMin[5] && BinX <= XwinMax[5] && BinY >= YwinMin[5] && BinY <= YwinMax[5])) AT (0, 0, dad+0.0215) RELATIVE a6
  ROTATED (0,180,0) RELATIVE a6

```

```
COMPONENT psd6_detector = PSD_monitor_psf(
  xmin = -det_width/2.0, xmax = det_width/2.0, ymin = -det_height/2.0,
  ymax = det_height/2.0, nx = 128, ny = 128, psf = PSF, filename = "psd6_detector.dat", restore_neutron=1)
WHEN ((BinX >= XwinMin[6] && BinX <= XwinMax[6] && BinY >= YwinMin[6] && BinY <= YwinMax[6])) AT (0, 0, dad+0.0215) RELATIVE a6
  ROTATED (0,180,0) RELATIVE a6

COMPONENT emon6_detector = E_monitor(
  nchan = 128, filename="detector6.dat", xwidth =det_width , yheight=det_height, Emin=emin, Emax=emax,restore_neutron=1)
WHEN ((BinX >= XwinMin[6] && BinX <= XwinMax[6] && BinY >= YwinMin[6] && BinY <= YwinMax[6])) AT (0, 0, dad+0.0215) RELATIVE a6
  ROTATED (0,180,0) RELATIVE a6

COMPONENT psd7_detector = PSD_monitor_psf(
  xmin = -det_width/2.0, xmax = det_width/2.0, ymin = -det_height/2.0,
  ymax = det_height/2.0, nx = 128, ny = 128, psf = PSF, filename = "psd7_detector.dat", restore_neutron=1)
WHEN ((BinX >= XwinMin[7] && BinX <= XwinMax[7] && BinY >= YwinMin[7] && BinY <= YwinMax[7])) AT (0, 0, dad+0.0215) RELATIVE a6
  ROTATED (0,180,0) RELATIVE a6

COMPONENT emon7_detector = E_monitor(
  nchan = 128, filename="detector7.dat", xwidth =det_width , yheight=det_height, Emin=emin, Emax=emax,restore_neutron=1)
WHEN ((BinX >= XwinMin[7] && BinX <= XwinMax[7] && BinY >= YwinMin[7] && BinY <= YwinMax[7])) AT (0, 0, dad+0.0215) RELATIVE a6
  ROTATED (0,180,0) RELATIVE a6

COMPONENT psd8_detector = PSD_monitor_psf(
  xmin = -det_width/2.0, xmax = det_width/2.0, ymin = -det_height/2.0,
  ymax = det_height/2.0, nx = 128, ny = 128, psf = PSF, filename = "psd8_detector.dat", restore_neutron=1)
WHEN ((BinX >= XwinMin[8] && BinX <= XwinMax[8] && BinY >= YwinMin[8] && BinY <= YwinMax[8])) AT (0, 0, dad+0.0215) RELATIVE a6
  ROTATED (0,180,0) RELATIVE a6

COMPONENT emon8_detector = E_monitor(
  nchan = 128, filename="detector8.dat", xwidth =det_width , yheight=det_height, Emin=emin, Emax=emax,restore_neutron=1)
WHEN ((BinX >= XwinMin[8] && BinX <= XwinMax[8] && BinY >= YwinMin[8] && BinY <= YwinMax[8])) AT (0, 0, dad+0.0215) RELATIVE a6
  ROTATED (0,180,0) RELATIVE a6

/* SECONDARY END */

END
```



## Appendix D

# Recent publications by L. Udby

For convenience of the reader, three scientific papers which I have published during my PhD study, are reprinted in this appendix.

The topic of the first paper, which is accepted for publication in Physical Review B, is the (lack of) field effect of the SDW signal in LSCO+O  $x=0.09$ . I have planned and participated in all the neutron scattering experiments which provided the data to the paper as well performing the data analysis and writing the main part of the text.

The second paper was the first paper to introduce the electronic phase-separation of LSCO+O and was published in Nature Materials volume 5 in 2006. I have provided supplementary neutron scattering data which were important for the conclusion that the magnetic phase is correlated over long distances. An observation which could not be directly deduced from the  $\mu$ SR technique which was the primary experimental technique of investigation of the magnetic phase in this paper.

The topic of the third paper is real-space modelling of stripe systems and it was published in Physical Review B volume 73 in 2006. I have developed the real-space recursion method to model STM/STS data of HTSCs and provided the main part of the simulated data in the paper. I have also contributed in writing the manuscript.

Magnetic ordering in electronically phase separated Sr/O co-doped  $\text{La}_{2-x}\text{Sr}_x\text{CuO}_{4+y}$ 

L. Udby,<sup>1</sup> N.H. Andersen,<sup>1</sup> F.C. Chou,<sup>2</sup> N.B. Christensen,<sup>1,3,4</sup> S.B. Emery,<sup>5</sup>  
K. Lefmann,<sup>1,6,7</sup> J.W. Lynn,<sup>8</sup> H.E. Mohottala,<sup>5</sup> Ch. Niedermayer,<sup>3</sup> and B.O. Wells<sup>5</sup>

<sup>1</sup>Materials Research Division, Risø DTU, Technical University of Denmark, DK-4000 Roskilde, Denmark

<sup>2</sup>Center for Condensed Matter Sciences, National Taiwan University, Taipei 10617, Taiwan

<sup>3</sup>Laboratory for Neutron Scattering, ETHZ & PSI, CH-5232 Villigen PSI, Switzerland

<sup>4</sup>Nanoscience Center, Niels Bohr Institute, University of Copenhagen, DK-2100 Copenhagen, Denmark

<sup>5</sup>Department of Physics, University of Connecticut U-3046,

2152 Hillside Road, Storrs, Connecticut 06269-3046, USA

<sup>6</sup>Nanoscience Center, Niels Bohr Institute, University of Copenhagen, DK-2100 Copenhagen, Denmark

<sup>7</sup>ESS-Scandinavia, University of Lund, Stora Algatan 4, 22350 Lund, Sweden

<sup>8</sup>NIST Center for Neutron Research, Gaithersburg, MD 20899, USA

(Dated: June 8, 2009)

We present results of magnetic neutron diffraction experiments on the co-doped super-oxygenated  $\text{La}_{2-x}\text{Sr}_x\text{CuO}_{4+y}$  ( $\text{LSCO}_{+O}$ ) system with  $x = 0.09$ . The spin-density wave has been studied and we find long-range incommensurate antiferromagnetic order below  $T_N$  coinciding with the superconducting ordering temperature  $T_c = 40$  K. The incommensurability value is consistent with a hole-doping of  $n_h \approx \frac{1}{8}$ , but in contrast to non-superoxygenated  $\text{La}_{2-x}\text{Sr}_x\text{CuO}_4$  with hole-doping close to  $n_h \approx \frac{1}{8}$  the magnetic order parameter is not field-dependent. We attribute this to the magnetic order being fully developed in  $\text{LSCO}_{+O}$  as in the other striped lanthanum-cuprate systems.

PACS numbers: 74.25.Ha, 74.72.Dn, 75.25.+z

## I. INTRODUCTION

The presence of an inhomogeneous charge concentration in cuprate superconductors has become increasingly obvious in recent years. The most dramatic experiments showing local density of state variations have been performed using Scanning Tunneling Microscopy/Spectroscopy [1–3]. There has also been an increasing number of other experiments that are best explained by invoking an inhomogeneous electronic structure [4–7]. For most of these experiments the charge variations appear to be short ranged, associated with a length scale of only a few nanometers at most. However, for the special cases of oxygen doped  $\text{La}_2\text{CuO}_{4+y}$  ( $\text{LCO}_{+O}$ ) or oxygen co-doped  $\text{La}_{2-x}\text{Sr}_x\text{CuO}_{4+y}$  ( $\text{LSCO}_{+O}$ ), muon and superconducting quantum interference techniques suggest that the electronic inhomogeneity moves beyond such local variations to form fully phase separated regions [8, 9]. For both cases, with hole concentrations ( $n_h$ ) between 0.125 and 0.16 per Cu site, samples at low temperatures spontaneously form separate regions of a magnetic phase consistent with  $n_h=1/8$  that is not superconducting and an optimally doped superconductor with  $n_h=0.16$  that is not magnetically ordered. The driving force for this phase separation appears to be interactions between the doped holes themselves rather than any specific O or Sr chemistry[9].

The full implications of this complete phase separation are still to be determined both theoretically and empirically. One area where phase separation should certainly be important is for effects associated with competing order parameters. A pronounced case of such an effect is the large magnetic field enhancement of the

ordered moment in underdoped  $\text{La}_{2-x}\text{Sr}_x\text{CuO}_4$  ( $\text{LSCO}$ ) superconductors as measured by neutron diffraction. A series of experiments have shown that samples with  $x < 1/8$  have an incommensurate (IC) antiferromagnetic (AFM) elastic diffraction peak that grows substantially with the application of a magnetic field [10, 11]. Samples with  $x \gtrsim 0.14$  have no elastic magnetic peak in zero applied field, but such a peak appears at a critical field,  $H_c$ , and then grows in intensity as the field increases above that [10, 12]. For samples doped very close to  $x = 1/8$ , and for which suppression of the superconducting  $T_c$  is also observed, a strong magnetic peak exists at zero field with less enhancement from the application of a field. Samples of  $\text{La}_{1.88}\text{Sr}_{0.12}\text{CuO}_4$  still show a small field enhancement [13], while samples of  $\text{La}_{1.48}\text{Nd}_{0.4}\text{Sr}_{0.12}\text{CuO}_4$  ( $\text{LNSCO}$ ) and  $\text{La}_{7/8}\text{Ba}_{1/8}\text{CuO}_4$  ( $\text{LBCO}$ ) have a fully developed magnetic moment and no - or very small - field enhancement [10, 14, 15]. We will hereafter refer to samples with fully developed magnetic order and no field enhancement within 13.5 T applied field as true 1/8 samples.

A widely used theory for the intensity enhancement by application of an external field has been developed by Demler, Sachdev, and Zhang [16]. This theory (DSZ) describes the cuprates as having coexisting but competing magnetic and superconducting order parameters. The functional form for the magnetic peak intensity versus field appears to fit existing data well and the predicted phase diagram appears to qualitatively match measurements for samples which are not true 1/8. However, the observation that true 1/8 samples have no field enhancement does not match the predictions of the DSZ paper. Of natural interest is how this theory

of competing but coexisting order parameters might be adapted for related samples which appear to have fully separated order parameters that do not coexist at the same location in the sample.

In the present work we study the details of the elastic magnetic scattering of a  $\text{LSCO}_{+O}$  single crystal by neutron diffraction. The phase separation, phase fractions, zero field ordered moment, and flux pinning have been carefully measured previously using muon spin resonance ( $\mu\text{SR}$ ) and bulk susceptibility measurements [9, 17]. Here we establish that the magnetic phase is IC AFM and long-range ordered with the same incommensurability as the true  $1/8$  samples of  $\text{LNSCO}$  and  $\text{LBCO}$ . This is surprising since the superconducting transition temperature is not suppressed in our sample but instead is very high ( $T_c = 40$  K) and coinciding with the ordering temperature of the IC AFM. Field and temperature dependence of the IC AFM peak intensity is also presented. We discuss the field dependence in relation to the DSZ model, pointing out that some development is necessary to account for samples where the magnetic and superconducting phases fully separate rather than coexist.

## II. METHODS

Our sample is a co-doped single-crystal with Sr content  $x = 0.09$  ( $\text{LSCO}_{+O}^{x=0.09}$ ). It has mass  $m = 0.429$  g. It was grown by the travelling solvent floating zone method in a mirror furnace. Additional oxygen was introduced using wet electrochemical methods as presented previously [18]. Previous studies of this particular crystal showed onset for both superconductivity and magnetism at 40 K [9]. Only one superconducting and one magnetic phase were detected, and each of these two phases occupy close to 50% of the volume as measured by  $\mu\text{SR}$ .

The neutron diffraction measurements were performed at the cold neutron triple-axis spectrometers RITA-II at PSI and SPINS at NIST. In both experiments we used 5 meV neutrons, 40' collimation before the sample and Be filter before the analyzer. Error bars in this manuscript are statistical in nature and represent one standard deviation.

RITA-II has the special feature of a seven blade PG(002) analyzer making it possible to monitor seven different reciprocal space points at the same time and energy-transfer, the so-called monochromatic imaging mode [19–21]. This enables simultaneous measurements of peak and background, which have proven very useful since the weak magnetic signal requires very long counting times of the order of hours. The size of the sample and the width of the analyzer blades result in an effective horizontal collimation of 40' between the sample and each analyzer blade.

The LSCO system is subject to twinning when in the low temperature orthorhombic (LTO) state. In terms of the  $F4/mmm$  unit cell for the high temperature tetrag-

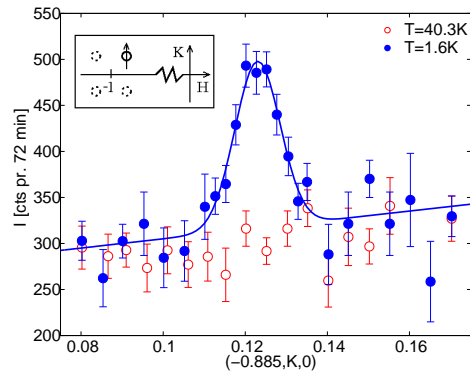


FIG. 1: (Color online) Scans in reciprocal space through  $(-0.885, 0.123, 0)$  along the  $K$ -direction. Scans are taken above and below  $T_N$  in zero applied field, the solid line is a fit to the data as explained in section IV. The inset shows the peak position and scan direction.

onal (HTT) structure the twinning is along  $(110)$  and  $(\bar{1}\bar{1}0)$ . The orthorhombic axes are almost parallel to the  $F4/mmm$  axes and the twinning gives up to four peaks in the LTO phase for each peak in the high temperature tetragonal (HTT) phase [22]. In our crystal even at low temperatures in the LTO state [23], the difference between lattice constants  $a = 5.318(4)\text{\AA}$  and  $b = 5.337(6)\text{\AA}$  gives rise to only a tiny transversal splitting of  $\alpha = 0.10(4)^\circ$  across the  $H$  and  $K$  axes.

All references to crystallography are in the LTO  $Bmab$  notation unless explicitly stated otherwise.

## III. RESULTS

Previous  $\mu\text{SR}$  studies [9] of our  $\text{LSCO}_{+O}^{x=0.09}$  crystal have shown a strongly damped oscillatory behavior with  $\nu = 3.33(8)\text{MHz}$ . This corresponds to an internal field of 24.7 mT which is about  $2/3$  of the value observed in the undoped compound  $\text{La}_2\text{CuO}_4$  (LCO) [24].

Our neutron diffraction studies find IC AFM elastic peaks at the same scattering vectors as in superoxygenated  $\text{LCO}_{+O}$  crystals [25, 26]. Scans through the incommensurate point are shown in Fig. 1 at base temperature and just above the magnetic transition temperature  $T_N$ . The peak incommensurability is  $\delta_H = 0.1150(18)$  r.l.u. and  $\delta_K = 0.1230(5)$  r.l.u., respectively, which gives a distance  $\delta = 0.198(3)\text{\AA}^{-1}$  from the AFM point. This corresponds to an incommensurability of  $\delta_T = 0.119(2)$  r.l.u. in pseudo-tetragonal notation [37], which is consistent with a hole-doping of  $n_h \approx 1/8$  according to the Yamada-plot [27] and consistent with the  $\delta \approx 0.12$  of  $\text{LBCO}$  [28] and  $\text{LNSCO}$  [10]. The incommensurate peaks are similar to or sharper than the previously reported

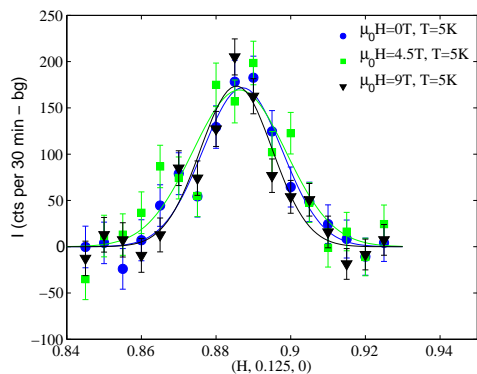


FIG. 2: (Color online) H-scans through the IC peak position at various fields. The experimental data have been fit to a Gaussian on sloping background. In the figure the data points and their Gaussian fits (solid lines) are shown after subtracting their sloping background (940 cts/30 min at the peak position). All fitted Gaussian parameters are the same within error bars for the different fields.

instrumentally resolved ones in  $\text{LCO}_{+0}$  [25, 26, 29, 30].

It has been checked by multiple tests that the peak width, position and amplitude do not depend on cooling rate or cycle.

As is shown in Fig. 2, application of a field does not shift or broaden the IC peak within the error bars, making it possible to monitor the intensity as a function of applied field in few-point scans. In imaging mode at RITA-II the central blade is used for measuring the peak amplitude whereas the other blades measure the background which is found to be field independent. Data for applied fields up to 13.5 T are shown in Fig. 3. Simply fitting the peak intensity to a constant describes our data quite accurately meaning that we observe no field effect within this field range. This is similar to the anomalous behavior of the other true 1/8 samples such as LNSCO and LBCO. In addition, the  $\text{LSCO}_{+0}$  system also has the same  $\mu\text{SR}$  response as LBCO and LNSCO, which is a strongly damped oscillatory behavior with a frequency  $\nu \approx 3.5$  MHz corresponding to a local ordered moment of  $\sim 0.35\mu_B$  [9, 10, 31]. The neutron scattering data are proportional to the ordered spin moment squared. Therefore, in order to compare with  $\mu\text{SR}$  results, our data have been presented after taking the square root of the background subtracted measured intensities and scaling to LNSCO muon data in [10].

The temperature dependence of the IC spin density wave (SDW) peak intensity is shown in Fig. 4 for both 0 T and 13.5 T applied field. From a linear mean-field fit we find a magnetic ordering temperature of  $T_N = 40(4)$  K for both the 0 T and 13.5 T data. The magnetic transition temperature is well within the experimental uncertainties of the measured bulk superconducting transition

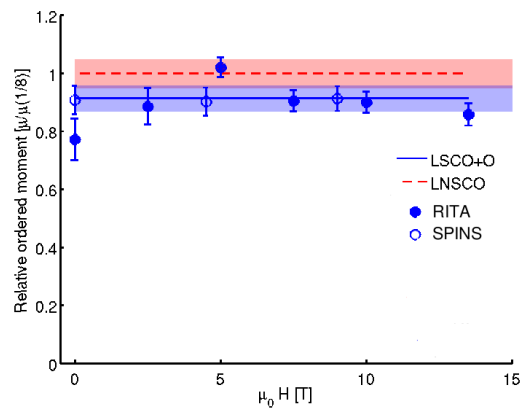


FIG. 3: (Color online) Internal magnetic moment (square root of SDW peak intensities) as a function of applied field. Closed symbols are data from RITA-II (measuring one point at the peak position) and open symbols are from SPINS (full momentum scan fitted to a Gaussian) scaled to weighted average of RITA-II data. A constant fit to the data (solid line) is shown relative to the internal moment of LNSCO from [10] (dashed line). Shaded areas indicate the error related to the determination of the local ordered moment from  $\mu\text{SR}$ .

temperature.

#### IV. DISCUSSION

We first consider the IC AFM peak of Fig. 1. We find that the peak has  $FWHM_{IC} = 0.0130(14)$  r.l.u. by a simple Gaussian fit on sloping background, which is slightly broader than the resolution at the  $(-1, 0, 0)$  position having  $FWHM_{res} = 0.0101(1)$  r.l.u. [38]. However, even if we take the small excess width with respect to the resolution width to be due to finite-size broadening, the SDW correlation length will still exceed  $400\text{\AA}$  [39]. Hence it is reasonable to conclude that the IC peak is close to resolution limited and expressing long range SDW order. The unconvoluted width of our IC AFM peak is the same as the width of the IC AFM peak of LSCO  $x = 0.12$  and LNSCO [10] which are resolution limited. Thus the correlation length is maximum at  $x \sim 1/8$  whereas it decreases in LSCO when doping departs from  $x = 1/8$  [10, 32].

Imposing a field does not change the intensity, correlation length, incommensurability or transition temperature of the magnetic phase and it is hence reasonable to conclude that the magnetic state in the part of the sample with  $n_h = 1/8$  is already fully developed in zero field.

This is in contrast to LSCO  $x = 0.12$  for which neutron diffraction studies have shown that the field enhancement matches the functional form of the DSZ theory. In this

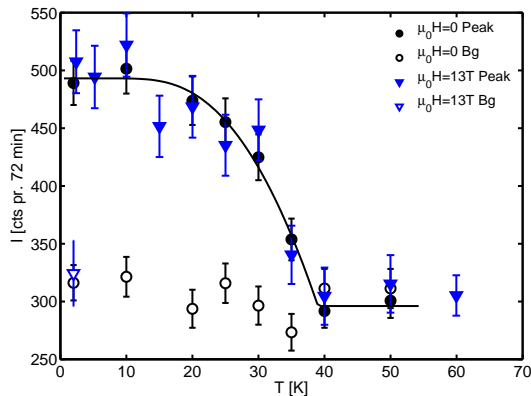


FIG. 4: (Color online) Temperature dependence of the IC SDW peak intensity at  $\mu_0 H = 0$  (in cryostat) and  $\mu_0 H = 13.5$  T (in magnet, after field-cooling) respectively. The  $\mu_0 H = 13.5$  T data are scaled (from the ratio of Bragg peak intensity in the cryostat and magnet respectively) and subtracted a constant background. The solid curve is a guide to the eye.

case SC and the SDW coexist but the local ordered magnetic moment is not fully developed in zero applied field. Imposing a field, however, pushes it towards the local ordered moment of the true  $1/8$  state[10].

Enhancement up to a factor of two of the elastic IC AFM peak at moderate fields ( $< 8$  T) has also been observed by neutron diffraction in non-Sr doped  $\text{LCO}_{+O}$  crystals when they were cooled slowly enough for the excess oxygen to order[26]. The oxygen ordering is observable by the concomitant staging superstructure. At the time of writing the authors of [26] did not consider their crystal to be macroscopically phase separated. Given more recent developments, and the fact that the reported magnetic and superconducting properties of that crystal are very similar to ours, it seems likely that the sample used in that report was indeed phase separated in a manner similar to the sample we present here. Hence in the following discussion we will assume that this is the case. It is however important to bear in mind that the value of the magnetic volume fraction of otherwise similar  $\text{LCO}_{+O}$  crystals can vary alot [40].

One possible explanation for the increase in the magnetic signal in [26] could be that the local magnetic moment in this sample was not saturated in zero field and after slow cooling. However, from our previous  $\mu\text{SR}$  work we know that highly oxygenated  $\text{LCO}_{+O}$  crystals have a fully developed local magnetic moment at zero applied field[9], so the field effect of  $\text{LCO}_{+O}$  is probably not explained by an unsaturated magnetic moment. We speculate instead that it is due to the ability of  $\text{LCO}_{+O}$  to convert SC regions into SDW in the case where the excess oxygen is ordered. The mechanism behind this might be similar to what is found in  $\text{YBa}_2\text{Cu}_3\text{O}_{6+x}$  (YBCO).

In YBCO [33, 34] oxygen ordering facilitates itinerant doped holes thereby favoring SC, whereas oxygen disorder does not favor SC. In this scenario SC would be favored in slowly cooled oxygen ordered  $\text{LCO}_{+O}$  at least at zero applied field. Applying moderate fields hereafter allows SDW regions to grow to a plateau volume. In  $\text{LCO}_{+O}$  oxygen disorder can be introduced by fast cooling. In  $\text{LSCO}_{+O}$ , which can be viewed as doping  $\text{LCO}_{+O}$  with Sr, the homogeneously distributed Sr anticorrelates to the excess oxygen, creating an increasingly disordered oxygen distribution with increasing Sr content [23]. Thus following this scenario, in  $\text{LSCO}_{+O}^{x=0.09}$  and fast-cooled  $\text{LCO}_{+O}$ , SC regions are not particularly favored over SDW regions even at zero applied field. This can explain why we see little or no enhancement of the magnetic signal by application of a field in the  $\text{LSCO}_{+O}$  system.

Let us now consider the volume of our sample with  $n_h = 0.16$  separately and treat it within the DSZ frame. Then keeping our high  $T_c$  of 40 K in mind, probably the critical field needed to actually enhance the magnetic signal in  $\text{LSCO}_{+O}$  would be at least as large as that of  $\text{LSCO } x = 0.16$  (optimally doped). According to the DSZ phase diagramme, the critical field increases rapidly with increasing  $x$ . The fact that the critical field of  $x = 0.145$  is already 7 T [10], suggests that the critical field for  $x = 0.16$  would not be within our experimental reach.

The total outcome considering both phases would be that neither of them would show significant field enhancement of the magnetic signal in moderate fields, which is indeed what we observe.

There was no evidence in our co-doped  $\text{LSCO}_{+O}$  crystal of any superconducting phase with  $T_c$  different from 40 K[9], nor did we observe any signs of the Néel antiferromagnetic order observed in  $\text{LCO}$ [24] as well as in the hole-poor phase of non-Sr-doped  $\text{LCO}_{+O}$ [35]. This is corroborating evidence for the suggestion[9] that in the region of the  $\text{LSCO}+O$  phase diagram to which our sample belongs, there exist only two stable ground states: The optimally doped superconducting phase and the "true  $1/8$ " magnetically ordered SDW phase.

## V. CONCLUSION

We conclude that the magnetic phase in our  $\text{LSCO}_{+O}$  crystal consists of fully developed long-range SDW order corresponding to the SDW of the  $1/8$  compounds  $\text{LBCO}$  and  $\text{LNSCO}$  with the same incommensurability  $\delta \approx 0.12$ , local  $\text{Cu}^{2+}$  moment  $\sim 0.35\mu_B$  and lack of field effect. The regions occupied by the SDW are large, at least 400 Å, meaning that below 40 K large SDW islands (or patches correlated over large distances) form simultaneously with the optimally doped SC in the rest of the sample.

Since there is no enhancement of the IC AFM peak with application of external field, we conclude that the  $\text{LSCO}_{+O}$  system has a fully developed magnetic phase which cannot be expanded at least below 13.5 T applied

field. In the slow-cooled highly oxygen-doped  $\text{LCO}_{+\text{O}}$  system with the same magnetic structure there is clearly a (large) enhancement of the SDW peak with field. We speculate that the discrepancy with respect to our system is due to the ability of the (slow-cooled)  $\text{LCO}_{+\text{O}}$  system to convert SC volume into SDW volume by application of an external field. This ability might be related to the degree of oxygen ordering in the sample.

Our neutron scattering measurements support that co-doping facilitates long-range electronic phase separation below  $T_N = T_c = 40\text{K}$  in two phases, 40 K SC and true 1/8 SDW, whose relative amounts are only determined by the total hole content.

### Acknowledgments

We would like to thank Brian M. Andersen for many helpful discussions. This work was supported by the

Danish Agency for Science Technology and Innovation under the Framework Programme on Superconductivity and the Danish Research Council FNU through the instrument center DANSCATT. Work at the University of Connecticut was supported by the U.S. Department of Energy under Contract No. DE-FG02-00ER45801. Part of this work was performed at the Swiss Spallation Neutron Source, Paul Scherrer Institute, Villigen, Switzerland. Work on SPINS is supported in part by the National Science Foundation under Agreement No. DMR-0454672.

- 
- [1] K. M. Lang, V. Madhavan, J. E. Hoffman, E. W. Hudson, H. Eisaki, S. Uchida, and J. C. Davis, *Nature* **415**, 412 (2002).
- [2] C. Howald, P. Fournier, and A. Kapitulnik, *Phys. Rev. B* **64**, 100504(R) (2001).
- [3] Y. Kohsaka, C. Taylor, K. Fujita, A. Schmidt, C. Lupien, T. Hanaguri, M. Azuma, M. Takano, H. Eisaki, H. Takagi, et al., *Science* **315**, 1380 (2007).
- [4] M. v. Zimmermann, A. Vigilante, T. Niemöller, N. Ichikawa, T. Frello, J. Madsen, P. Wochner, S. Uchida, N. H. Andersen, J. Tranquada, et al., *Europhys. Lett.* **41**, 629 (1998).
- [5] S. V. Dordevic, S. Komiya, Y. Ando, and D. N. Basov, *Phys. Rev. Lett.* **91**, 167401 (2003).
- [6] P. M. Singer, A. W. Hunt, and T. Imai, *Phys. Rev. Lett.* **88**, 047602 (2002).
- [7] S. Wakimoto, K. Yamada, J. M. Tranquada, C. D. Frost, R. J. Birgeneau, and H. Zhang, *Phys. Rev. Lett.* **98**, 247003 (2007).
- [8] A. T. Savici, Y. Fudamoto, I. M. Gat, T. Ito, M. I. Larkin, Y. J. Uemura, G. M. Luke, K. M. Kojima, Y. S. Lee, M. A. Kastner, et al., *Phys. Rev. B* **66**, 014524 (2002).
- [9] H. E. Mohottala, B. O. Wells, J. I. Budnick, W. A. Hines, C. Niedermayer, L. Udby, C. Bernhard, A. R. Moodenbaugh, and F. C. Chou, *Nature Mat.* **5**, 377 (2006).
- [10] J. Chang, C. Niedermayer, R. Gilardi, N. B. Christensen, H. Rønnow, D. F. McMorrow, M. Ay, J. Stahn, O. Sobolev, A. Hiess, et al., *Phys. Rev. B* **78**, 104525 (2008).
- [11] B. Lake, H. M. Rønnow, N. B. Christensen, G. Aeppli, K. Lefmann, D. F. McMorrow, P. Vorderwisch, P. Smeibild, N. Mangkorntong, T. Sasagawa, et al., *Nature* **415**, 299 (2002).
- [12] B. Khaykovich, S. Wakimoto, R. J. Birgeneau, M. A. Kastner, Y. S. Lee, P. Smeibild, P. Vorderwisch, and K. Yamada, *Phys. Rev. B* **71**, 220508(R) (2005).
- [13] S. Katano, M. Sato, K. Yamada, T. Suzuki, and T. Fukase, *Phys. Rev. B* **62**, R14677 (2000).
- [14] M. Fujita, M. Matsuda, H. Goka, T. Adachi, Y. Koike, and K. Yamada, *J. of Phys. Conf. Series* **51**, 510 (2006).
- [15] J. Wen, Z. Xu, G. Xu, J. M. Tranquada, G. Gu, S. Chang, and H. J. Kang, *Phys. Rev. B* **78**, 212506 (2008).
- [16] E. Demler, S. Sachdev, and Y. Zhang, *Phys. Rev. Lett.* **87**, 067202 (2001).
- [17] H. E. Mohottala, B. O. Wells, J. I. Budnick, W. A. Hines, C. Niedermayer, and F. C. Chou, *Phys. Rev. B* **78**, 064504 (2008).
- [18] B. O. Wells, R. J. Birgeneau, F. C. Chou, Y. Endoh, D. C. Johnston, M. A. Kastner, Y. S. Lee, G. Shirane, and J. M. Tranquada, *Z. Phys. B* **100**, 535 (1996).
- [19] K. Lefmann, D. F. McMorrow, H. M. Rønnow, K. Nielsen, K. N. Clausen, B. Lake, and G. Aeppli, *Physica B* **283**, 343 (2000).
- [20] C. R. H. Bahl, P. Andersen, S. N. Clausen, and K. Lefmann, *Nucl. Instr. and Meth. B* **226**, 667 (2004).
- [21] C. R. H. Bahl, K. Lefmann, A. B. Abrahamsen, H. M. Rønnow, F. Saxild, T. B. S. Jensen, L. Udby, N. H. Andersen, N. B. Christensen, H. S. Jacobsen, et al., *Nucl. Instr. and Meth. B* **246**, 452 (2006).
- [22] M. Braden, G. Heger, P. Schweiss, Z. Fisk, K. Gamayunov, I. Tanaka, and H. Kojima, *Phys. C* **191**, 455 (1992).
- [23] L. Udby *et al.*, *Neutron- and hard x-ray studies of the staging structure in co-doped  $\text{La}_{2-x}\text{Sr}_x\text{CuO}_{4+y}$* , in preparation (2009).
- [24] J. I. Budnick, B. Chamberland, D. P. Yang, C. Niedermayer, A. Golnik, E. Recknagel, M. Rossmannith, and A. Weidinger, *Europhys. Lett.* **5** (7), 651 (1988).
- [25] Y. S. Lee, R. J. Birgeneau, M. A. Kastner, Y. Endoh, S. Wakimoto, K. Yamada, R. W. Erwin, S. H. Lee, and G. Shirane, *Phys. Rev. B* **60**, 3643 (1999).
- [26] Y. S. Lee, F. C. Chou, A. Tewary, M. A. Kastner, S. H. Lee, and R. J. Birgeneau, *Phys. Rev. B* **69**, 020502(R) (2004).
- [27] K. Yamada, C. H. Lee, K. Kurahashi, J. Wada, S. Waki-

- moto, S. Ueki, H. Kimura, Y. Endoh, S. Hosoya, G. Shirane, et al., Phys. Rev. B **57**, 6165 (1998).
- [28] M. Fujita, H. Goka, K. Yamada, J. M. Tranquada, and L. P. Regnault, Phys. Rev. B **70**, 104517 (2004).
- [29] B. Khaykovich, Y. S. Lee, R. W. Erwin, S.-H. Lee, S. Wakimoto, K. J. Thomas, M. A. Kastner, and R. J. Birgeneau, Phys. Rev. B **66**, 014528 (2002).
- [30] B. Khaykovich, R. J. Birgeneau, F. C. Chou, R. W. Erwin, M. A. Kastner, S.-H. Lee, Y. S. Lee, P. Smeibidl, P. Vorderwisch, and S. Wakimoto, Phys. Rev. B **67**, 054501 (2003).
- [31] B. Nachumi, Y. Fudamoto, A. Keren, K. M. Kojima, M. Larkin, G. M. Luke, J. Merrin, O. Tchernyshyov, Y. J. Uemura, N. Ichikawa, et al., Phys. Rev. B **58**, 8760 (1998).
- [32] M. Fujita, K. Yamada, H. Hiraka, P. M. Gehring, S. H. Lee, S. Wakimoto, and G. Shirane, Phys. Rev. B **65**, 064505 (2002).
- [33] M. v. Zimmermann, J. R. Schneider, T. Frello, N. H. Andersen, J. Madsen, M. Käll, H. F. Poulsen, R. Liang, P. Dosanjh, and W. N. Hardy, Phys. Rev. B **68**, 104515 (2003).
- [34] G. Uimin, Phys. Rev. B **50**, 9531 (1994).
- [35] E. J. Ansaldo, J. H. Brewer, T. M. Riseman, J. E. Schirber, E. L. Venturini, B. Morosin, D. S. Ginley, and B. Sternlieb, Phys. Rev. B **40**, 2555 (1989).
- [36] S. B. Emery *et al.*, in preparation (2009).
- [37]  $a_T = b_T = \frac{a+b}{2\sqrt{2}} = \frac{5.328(4)}{\sqrt{2}} = 3.767(3)\text{\AA}$
- [38] This was measured by 2. order scattering off the structural  $(-2, 0, 0)$  peak (without Be filter) but the resolution is similar in angular space
- [39] If the peak is fitted to a Gaussian the combined width is the sum of the internal width  $\sigma$  and the resolution in quadrature giving  $\sigma = \sqrt{(0.0130 * \frac{2\pi}{5.318})^2 - (0.0101 * \frac{2\pi}{5.337})^2} = 0.00972 \text{ \AA}^{-1}$ . The estimate of the correlation length can be either  $2\pi/\sigma = 646\text{\AA}$  or by the Scherrer formula  $\frac{K\lambda}{B \cos \theta} = \frac{0.9 \cdot 4.045}{0.00972 \cdot 0.9404} = 414\text{\AA}$  with  $B = 2 \tan^{-1} \frac{\sigma}{2qIC}$ . The Scherrer dimensionless constant  $K$  is dependent on domain-geometry but the value of 0.9 used here is correct within 10% error. The error on the Lorentzian width on fitting to a Voigt is as large as the value itself, hence it has not been considered fitting to a Voigt in the main text.
- [40] As an example the LCO<sub>+O</sub> crystals of [9] and [36] were prepared by a similar electrochemical method and both have  $T_c = T_M = 40$  K but the first had magnetic volume fraction of 66(5)% whereas the second only had 30(5)% measured in zero applied field and by the same  $\mu$ SR method after similar cooling conditions. We should mention that the first crystal is very small ( $m=0.025$  g) and hence no attempt has been made so far to measure the field dependence of the magnetic signal.

# Phase separation in superoxygenated $\text{La}_{2-x}\text{Sr}_x\text{CuO}_{4+y}$

HASHINI E. MOHOTTALA<sup>1</sup>, BARRETT O. WELLS<sup>1\*</sup>, JOSEPH I. BUDNICK<sup>1</sup>, WILLIAM A. HINES<sup>1</sup>, CHRISTOF NIEDERMAYER<sup>2</sup>, LINDA UDBY<sup>3</sup>, CHRISTIAN BERNHARD<sup>4</sup>, ARNOLD R. MOODENBAUGH<sup>5</sup> AND FANG-CHENG CHOU<sup>6</sup>

<sup>1</sup>University of Connecticut U-3046, 2152 Hillside Road, Storrs, Connecticut 06269-3046, USA

<sup>2</sup>Laboratory for Neutron Scattering, ETHZ & PSI, CH-5232 Villigen PSI, Switzerland

<sup>3</sup>Department of Material Research, Risoe National Laboratory, DK-4000 Roskilde, Denmark

<sup>4</sup>Max-Planck-Institut fuer Festkoerperforschung, Heisenbergstrasse 1, D-70569 Stuttgart, Germany

<sup>5</sup>Materials Science Department, Brookhaven National Laboratory, Upton, New York 11973, USA

<sup>6</sup>Center for Condensed Matter Sciences, National Taiwan University, Taipei 106, Taiwan

\*e-mail: wells@phys.uconn.edu

Published online: 16 April 2006; doi:10.1038/nmat1633

The complex interplay between superconducting and magnetic phases remains poorly understood. Here, we report on the phase separation of doped holes into separate magnetic and superconducting regions in superoxygenated  $\text{La}_{2-x}\text{Sr}_x\text{CuO}_{4+y}$ , with various Sr contents. Irrespective of Sr-doping, excess oxygen raises the superconducting onset to 40 K with a coexisting magnetic spin-density wave that also orders near 40 K in each of our samples. The magnetic region is closely related to the anomalous, 1/8-hole-doped magnetic versions of  $\text{La}_2\text{CuO}_4$ , whereas the superconducting region is optimally doped. The two phases are probably the only truly stable ground states in this region of the phase diagram. This simple two-component system is a candidate for electronic phase separation in cuprate superconductors, and a key to understanding seemingly conflicting experimental observations.

From the beginning of research into copper-oxide-based superconductors, the consensus phase diagram featured insulating magnetic phases that border generally poorly conducting, but superconducting phases. The relationship between these states has been a focus of intense research and debate. Soon after the discovery of high-temperature superconductivity in hole-doped cuprate compounds there were calculations showing that spin-only holes in a Mott insulator background would phase-separate into hole-rich and hole-poor regions<sup>1-3</sup>. A realization of this tendency has been thought to be the formation of charge and spin stripe-ordered states. Another view is that magnetism and superconductivity are coupled, with a continuous transition between the magnetic and superconducting phases. This would allow coexistence, in the same domains, of at least short-range ordered magnetism and superconductivity. Such coexistence leads naturally to consideration of a magnetic mechanism for the formation of Cooper pairs<sup>4</sup>. More recent developments have shown that the difference between a fully phase-separated material and one with some coexistence of magnetism and superconductivity might not be fundamental but might depend on the degree of disorder<sup>5</sup>. Nevertheless, it remains crucial to understand the underlying tendencies. The experimental data reported here are new evidence for the segregation of a cuprate material into separate magnetic and superconducting phases, probably with different hole concentrations. In this case, the magnetic state is not the undoped Néel phase but a spin-density wave connected to the unique behaviour of samples doped near 1/8 hole per copper site. We discuss whether the primary force driving this phase separation is more likely to be the interaction of the holes themselves or the specific chemistry of oxygen in this structure. The data are primarily from muon-spin-rotation ( $\mu\text{SR}$ ) and magnetization studies of Sr and O co-doped samples of  $\text{La}_{2-x}\text{Sr}_x\text{CuO}_{4+y}$ , with supporting evidence from neutron scattering.

## ARTICLES

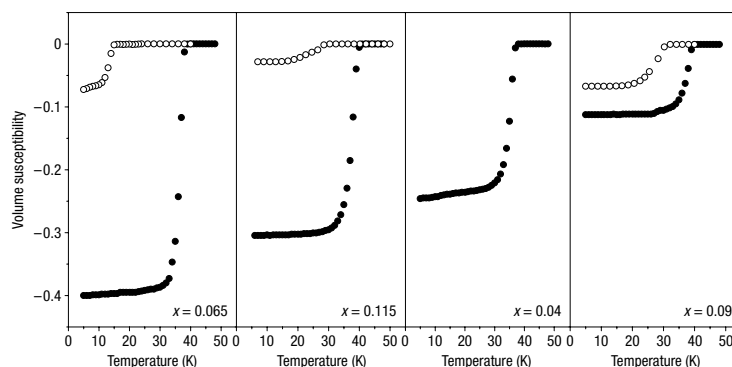


**Figure 1** Field-cooled d.c. magnetization (Meissner fraction) in a field of 10 G versus temperature for  $\text{La}_{2-x}\text{Sr}_x\text{CuO}_{4+y}$ . Open (filled) circles represent the sample before (after) oxidation. The  $x = 0.04$  does not show a superconducting Meissner effect before oxidation<sup>38</sup>. After oxidation all of the samples show a  $T_c \approx 40$  K. The panels are arranged in order of decreasing post-oxidation Meissner fraction.

Two systems of particular interest with regard to the interplay of superconductivity and magnetism are substitutional cation and interstitial anion-doped versions of the insulating parent compound  $\text{La}_2\text{CuO}_4$ . Materials with a hole concentration of  $n_h \approx 1/8$  in structures such as  $\text{La}_{1.875}\text{Ba}_{0.125}\text{CuO}_4$  (ref. 6) or  $(\text{LaNd})_{1.875}\text{Sr}_{0.125}\text{CuO}_4$  (ref. 7) show a surprising suppression of the superconducting state with a concomitant appearance of a static, spin-density wave. Somewhat different behaviour was observed in superoxygenated  $\text{La}_2\text{CuO}_{4.11}$ . This system has a very robust superconducting state with a transition temperature  $T_c > 40$  K, which is higher than that for the optimally doped sample  $\text{La}_{1.85}\text{Sr}_{0.15}\text{CuO}_4$  ( $T_c = 38$  K maximum). However, neutron scattering and  $\mu\text{SR}$  measurements both reveal static magnetism with an ordering temperature,  $T_M$ , very close to  $T_c$  (refs 8–12). Thus, in some manner, magnetism and superconductivity coexist within a  $\text{La}_2\text{CuO}_{4+y}$  sample.

The term superoxygenated has been used for samples of  $\text{La}_2\text{CuO}_4$  or  $\text{La}_{2-x}\text{Sr}_x\text{CuO}_4$  that are then loaded with excess oxygen through wet-chemical techniques. The addition of oxygen serves to hole-dope the materials. Regardless of the amount of Sr, most oxygenated samples have a superconducting  $T_c$  at 40 K or above, significantly higher than for samples doped with Sr alone<sup>13,14</sup>. However, these materials are difficult to synthesize, and there are fewer studies of them than there are of more familiar cuprate superconductors. Most work is on samples without Sr. Uniform oxidation of single crystals requires weeks to months in an electrochemical cell at elevated temperatures, and becomes more difficult when Sr is present. Some interesting results have been achieved on  $\text{La}_2\text{CuO}_{4+y}$ . Initial studies identified a miscibility gap between an insulating phase that incorporates very little oxygen and a superconducting, oxygen-rich phase<sup>15</sup>. A muon study of  $\text{La}_2\text{CuO}_{4+y}$  in this miscibility gap was carried out<sup>16</sup> to explore the magnetic properties of the system. The excess oxygen was found to intercalate between layers in a manner reminiscent of staging in graphite, ordering near room temperature<sup>17</sup>. These same interstitial oxygen ions were found to further order into a three-dimensional superlattice at a temperature near 200 K (ref. 18). A phase diagram has been proposed to account for the structural phases observed<sup>19</sup>. In the present report, we describe a set of  $\mu\text{SR}$  and magnetization measurements on a series of samples of  $\text{La}_{2-x}\text{Sr}_x\text{CuO}_{4+y}$ . The phase separation we discuss here is not directly related to the previously

reported oxygen miscibility gap, but occurs in a more hole-rich region of the phase diagram.

A series of single crystals and powders of  $\text{La}_{2-x}\text{Sr}_x\text{CuO}_4$  (with  $x = 0, 0.04, 0.055, 0.065, 0.09, 0.115, 0.14$ ) was studied. According to the phase diagram, none of the Sr-doped samples are magnetically ordered for temperatures above about 10 K (ref. 20), whereas  $\text{La}_2\text{CuO}_4$  is antiferromagnetic up to 325 K. After oxidation, all of the samples developed a Meissner response (field-cooled diamagnetic fraction) indicating a bulk-superconducting phase with  $T_c$  near 40 K. Over time the transitions became sharp. Examples of the field-cooled (Meissner) magnetization response for several samples are shown in Fig. 1. All of the samples had essentially identical magnetic response, except for the magnitude of the low-temperature signal. We conclude that the superconducting phase in each sample is identical because after oxidation all of the samples measured have a sharp Meissner transition near 40 K, a large Meissner fraction, and there is no evidence for any additional diamagnetic signal at any other temperature.

Structural characterization of these samples was carried out by X-ray and neutron scattering. All of the samples were orthorhombic at low temperatures. A non-destructive indication of the oxygen level in the samples is the staging structure. Those with the most oxygen will have the lowest staging number—less distance between oxygen layers; lower oxygen levels lead to a higher stage number, and even less oxygen leads to no staging at all. We have collected staging information for four samples as shown in Table 1. The samples have different staging configurations ranging from stage 4 for a sample with no Sr to no staging at all for a sample with 9% Sr. This indicates considerably different amounts of oxygen incorporated into the crystals, as expected for samples with different Sr content but roughly similar total hole content.

Zero-field (ZF) and weak-transverse-field (WTF) muon spectra were taken to investigate the static magnetic order. In this paper, we focus on the ZF results because the interpretation of these results is more intuitive. The WTF results are entirely consistent. In ZF, each sample except that with  $x = 0.14$  shows similar oscillations with onset below 40 K. This indicates the presence of a static internal field and an ordered magnetic state. Typical muon histograms, above and below the magnetic-ordering temperature, are shown in Fig. 2. We fit the oscillating signals to a Bessel function as described in the Supplementary Information. Figure 3a

**Table 1** Different staging configurations obtained for some of our superoxygenated samples. The staging number is reflective of the amount of doped oxygen in each sample. Samples with more Sr have less O, thus there is a progression from low to higher staging numbers, then to vanishing of the staging process altogether as the amount of O decreases.

Sample	Staging	Magnetic fraction (ZF- $\mu$ SR)
$\text{La}_2\text{CuO}_{4+y}$ (0% Sr)	Stage 4	66
$\text{La}_{1.96}\text{Sr}_{0.04}\text{CuO}_{4+y}$ (4% Sr)	Near stage 6	42
$\text{La}_{1.935}\text{Sr}_{0.065}\text{CuO}_{4+y}$ (6.5% Sr)	No peaks, some related diffuse scattering	19
$\text{La}_{1.91}\text{Sr}_{0.09}\text{CuO}_{4+y}$ (9% Sr)	No staging	51

shows the low-temperature ZF- $\mu$ SR spectra for some of our superoxygenated samples, and Fig. 3b shows the resultant low-temperature frequency for each sample studied, as well as an additional data point from a previous study<sup>9</sup>. The frequencies are identical within the error bars, with an average value of 3.33(8) MHz, corresponding to an internal field of 247 G. As all of the measured samples (except the  $x = 0.14$  sample) have a magnetic phase with the same  $T_M$ , all fit by a Bessel function, and all with the same internal fields, we conclude that the magnetic phase in all of the samples is identical.

Our data also allow us to measure the fraction of the sample that shows static magnetism. The amplitude of the oscillating portion of the ZF- $\mu$ SR spectra, corrected for geometry, gives the fraction of the sample that is magnetic. The third column of Table 1 lists the magnetic volume fractions for the samples for which we also measured oxygen staging. Similarly, the magnetic fraction appears in the WTF- $\mu$ SR signals as a signal loss due to quick damping. For all of our samples, the magnetic fraction determined by each method agrees to within a few per cent. A completely independent measure of the superconducting volume fraction can be derived from the magnitude of the Meissner signals reported in Fig. 1. The superconducting volume fraction can also be derived from high transverse field (HTF)  $\mu$ SR with consistent results, as described in the Supplementary Information. Figure 4 shows the Meissner superconducting volume fraction versus the ZF- $\mu$ SR-derived magnetic volume fraction. The two values have a negative linear relationship. The sum of the two phases is constant, although less than one. This is probably an artefact caused by an underestimation of the superconducting phase fraction by the Meissner signal due to flux trapping and flux penetration into small superconducting regions.

The characteristic parameters of the superconducting and magnetic phases are virtually identical for all of our superoxygenated samples. Only their relative volume fractions are changing. This change is a negative linear correlation between the superconducting and magnetic volume fractions and shows no trend with Sr or O content. The combined trends strongly argue against a homogeneous hole distribution. Instead they suggest a scenario of a phase separation between magnetic (hole poor) and superconducting (hole rich) regions.

We estimate the hole concentration and the nature of the magnetic phase by comparing our  $\mu$ SR results to those from samples of magnetic and weakly superconducting  $\text{La}_{1.875}\text{Ba}_{0.125}\text{CuO}_4$  or  $(\text{La}, \text{Nd})_{1.875}\text{Sr}_{0.125}\text{CuO}_4$ . The former sample has a magnetic ordering temperature near 35 K. The time evolution of the muon-spin polarization is best described by a Bessel function, and the ZF frequency is found to be 3.5 MHz (ref. 21). In all cases these values are very close to the results for our oxygenated samples, and we conclude that the magnetic phases measured are similar. The major difference in the ZF- $\mu$ SR is that

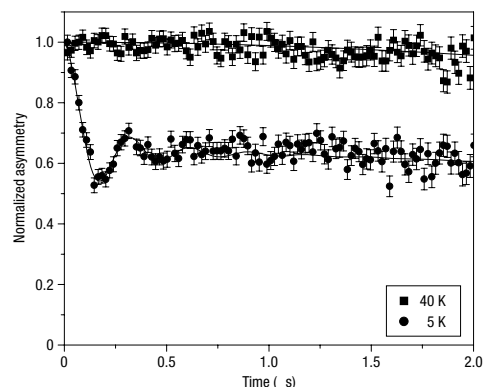


**Figure 2** ZF- $\mu$ SR spectra for  $\text{La}_{1.91}\text{Sr}_{0.09}\text{CuO}_{4+y}$  obtained at 5 K and at 40 K. The line represents the best fit to the data as described in the text. The fit gives values for the frequency from which we find the magnitude of the local field, and the asymmetry from which we derive the magnetic volume fraction. The error bars represent statistical counting errors from the  $\mu$ SR raw data.

for  $\text{La}_{1.875}\text{Ba}_{0.125}\text{CuO}_4$  and  $(\text{La}, \text{Nd})_{1.875}\text{Sr}_{0.125}\text{CuO}_4$ , the oscillatory signal accounts for the full asymmetry of the muon signal. Thus, these compounds seem to be fully magnetic, whereas only a fraction of the oxygenated samples are magnetic. Further support for this identification arises from the incommensurability of the magnetic diffraction peaks. Neutron-scattering studies<sup>8,11,12</sup> on samples of superoxygenated  $\text{La}_2\text{CuO}_{4+y}$  (no Sr) found elastic magnetic peaks with an incommensurability of  $\delta = 0.123$  (with reference to the pseudo-tetragonal unit cell). Our preliminary neutron-scattering studies of the oxygenated  $x = 0.09$  sample find magnetic peaks at exactly the same incommensurability. This value is consistent with a hole-doping of  $n_h \approx 0.125$  according to the well known Yamada plot<sup>22</sup>.

The hole content of the superconducting phase is harder to identify. Given the high  $T_C$  and robust nature of the superconducting phase, we assume it represents the optimally doped material with  $n_h \approx 0.16$ .

To test the hypothesis that the magnetic state corresponds to  $n_h \approx 1/8$  we studied another sample with greater Sr content,  $x = 0.14$ . In such a sample, the movement of holes associated with oxygen dopants could not lead to the formation of a phase with  $n_h = 1/8$ . The expectation was that oxygenating this sample should not produce any region with an ordered magnetic state. Indeed, after oxygenation this sample did not show two-phase coexistence. It was superconducting with  $T_C \approx 40$  K, had the largest Meissner signal of any of the samples studied, and showed no ZF- $\mu$ SR oscillations at low temperatures as shown in Fig. 3a, thus there is no evidence of an ordered magnetic phase.

Figure 5 is a phase diagram that summarizes our findings for superoxygenated  $\text{La}_{2-x}\text{Sr}_x\text{CuO}_4$  and  $\text{La}_2\text{CuO}_{4+y}$ . Different colours have been used to highlight different states in the system, and the cross-hatched regions indicate miscibility gaps. The light and dark arc regions represent the superconducting ( $n_h = 0.16$ ) and magnetic ( $n_h = 0.125$ ) line phases respectively. Much of the three-dimensional space remains blank as it remains unstudied—a rare unexplored phase region in the high- $T_C$  cuprates.

There are some aspects of our data that indicate that phase separation depends on the nature of the dopant ions present.

## ARTICLES

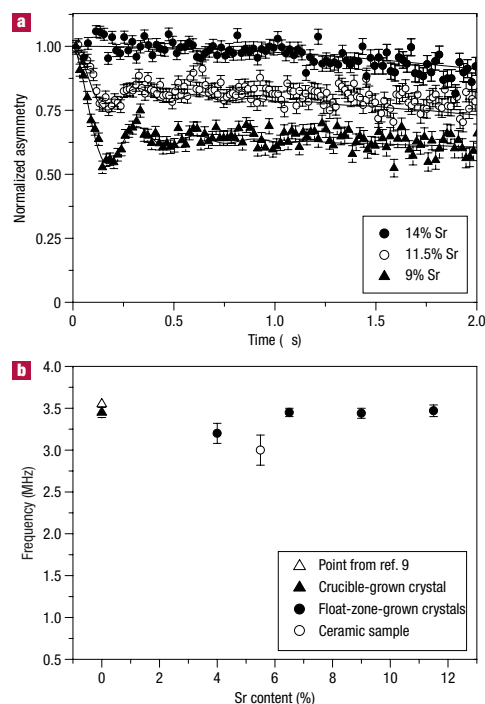


**Figure 3** ZF- $\mu$ SR spectra obtained for some of our superoxygenated samples at 5 K and the frequencies obtained at the same temperature. **a**, ZF- $\mu$ SR spectra for  $\text{La}_{1.91}\text{Sr}_{0.09}\text{CuO}_{4+y}$ ,  $\text{La}_{1.895}\text{Sr}_{0.115}\text{CuO}_{4+y}$  and  $\text{La}_{1.86}\text{Sr}_{0.14}\text{CuO}_{4+y}$  samples. The lines represent the best fit to the data. Oscillating signals were fitted as described in the text. The non-oscillating signal ( $\text{La}_{1.86}\text{Sr}_{0.14}\text{CuO}_{4+y}$ ) was fitted using a Kubo-Gauss function. **b**, ZF frequency obtained at 5 K versus Sr concentration for all  $\text{La}_{2-x}\text{Sr}_x\text{CuO}_{4+y}$  (except  $\text{La}_{1.86}\text{Sr}_{0.14}\text{CuO}_{4+y}$ ). The frequency is constant within the error indicated. The error bars obtained from  $\mu$ SR data fittings are included.

Most obviously, the complete phase separation we report here apparently does not exist for  $\text{La}_{2-x}\text{Sr}_x\text{CuO}_4$  without excess oxygen. Furthermore, we do not detect such phase separation when the Sr content  $x$  is greater than  $1/8$ . Some difference between the nature of interstitial O ions and substitutional Sr ions is crucial, probably the excess mobility of the O ions. Nevertheless, there is evidence that a key driving force is the interaction of the doped holes themselves. The evidence is threefold. First, the persistent stable phases seem to be characterized by special hole concentrations, rather than any particular O or Sr concentration. Second, the relative amount of the magnetic versus superconducting phase is not described by a simple, monotonic relationship with either the O or Sr concentration. Presumably it is determined by a combination of the two, or the total hole concentration. On both the first and second points this differs from the phase separation seen in the related compound  $\text{La}_{2-x}\text{Sr}_x\text{NiO}_{4+d}$ , where a series of miscibility gaps are clearly related to oxygen concentration<sup>23</sup>. However, we cannot measure the average hole concentration directly, and thus cannot confirm that it sets the relative phase fractions. In addition, we cannot rule out the possibility of a complicated dependence of the phase fractions on O or Sr concentration. Third, we have not found any structural modulation associated with the phase

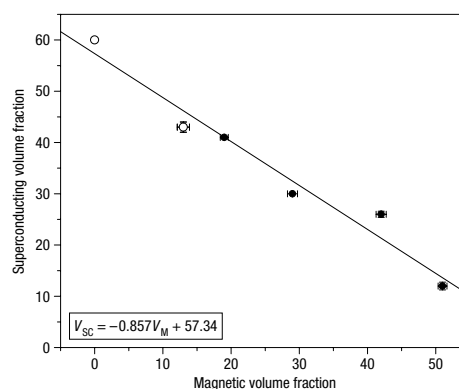


**Figure 4** Superconducting volume fraction (Meissner fraction) versus magnetic volume fraction for  $\text{La}_{2-x}\text{Sr}_x\text{CuO}_{4+y}$ . The open circles represent the two ceramic samples. The graph indicates a negative linear relationship between the two fractions. The line represents the best fit, and the equation for the fitting line is shown in the box. Both  $x$  (from ZF- $\mu$ SR) and  $y$  (from superconducting quantum interference device magnetometry) error bars from the fittings are shown.

separation, and specifically find no connection to the presence or lack of O ion staging. Taken together, we believe these attributes make a plausible case that the electronic interaction of the doped holes is the primary driver of the phase separation rather than the specific chemistry of O or Sr in this compound.

The overall morphology of the various regions is an important issue that will require further study. Most claims of phase separation in other cuprate superconductors have been for regions that are small, with a characteristic size of a few nanometres. In our case, the phase-separated regions must be large in at least some dimensions. The fact that we detect a Meissner state at all indicates that the superconducting regions must be of the order of the penetration depth, generally believed to be over 100 nm for these compounds. The best indication of the size of the magnetic regions is the width of the peaks in neutron diffraction. A careful analysis of the magnetic peaks in  $\text{La}_2\text{CuO}_{4+y}$  was carried out in ref. 8 and gave an in-plane correlation length of at least 40 nm, but only about 1.3 nm perpendicular to the planes. Our preliminary neutron results on the Sr  $x = 0.09$  sample are consistent with those values.

The anomalous behaviour of the  $n_h = 1/8$  phases has sometimes been regarded as a phenomenon that is not central to the high- $T_C$  problem and the physics of cuprates. This is because it was only seen to appear in a small subset of high- $T_C$  samples, those that also show the low-temperature tetragonal (space group  $P4_2/nm$ ) version of the 214 structure<sup>24</sup>. However, in our studies we see the same anomalous  $1/8$  behaviour in a sample that does not seem to show the low-temperature tetragonal phase on the basis of our X-ray and neutron diffraction results. Previous studies of the structure of  $\text{La}_2\text{CuO}_{4.11}$  (ref. 7) have shown this material to be orthorhombic with space group  $Bmab$ , known as the low-temperature orthorhombic (LTO) phase. Our own initial X-ray diffraction studies and neutron-scattering studies have also shown the system that we discuss here to be orthorhombic.

The idea of inherent phase separation of doped holes in the cuprates has long been discussed, with imperfect empirical evidence for its existence. Nuclear magnetic resonance studies of  $\text{La}_{2-x}\text{Sr}_x\text{CuO}_4$  appear to indicate the presence of two separated phases on very short length and timescales,

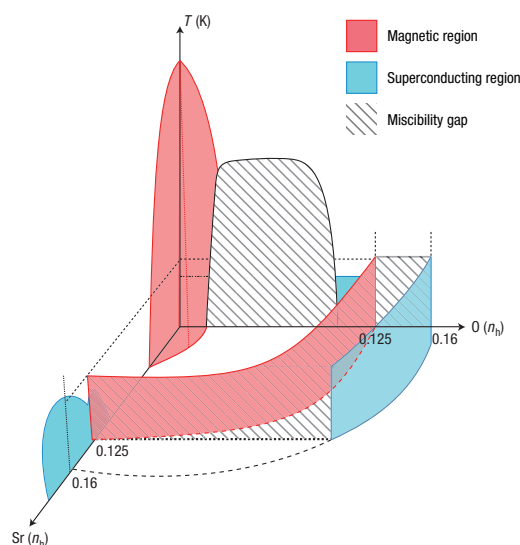


**Figure 5** Three-dimensional, Sr–O–temperature phase diagram for  $\text{La}_{2-x}\text{Sr}_x\text{CuO}_{4+y}$ . Actual data points and some details of the lowest doping regions are omitted for clarity. The Sr (out of the page) and O (horizontal) axes are both labelled in terms of the hole content,  $n_h$ . Thus paths with constant hole concentration are circular arcs in the Sr–O plane. The red regions represent the magnetically ordered states, whereas the blue regions represent superconducting states. The hatched areas represent miscibility gaps. All of the oxygenated samples described in this paper, except for the one with Sr  $x = 0.14$ , fall into the arc-shaped, miscibility gap between  $n_h = 1/8$  and  $n_h = 0.16$ . The arc-shaped region is cut off at a Sr concentration of  $1/8$  to indicate that samples with  $x \geq 1/8$  do not show phase separation at length- and timescales measurable in this study. A dashed line that continues past this cut-off indicates optimal doping.

essentially a frustrated phase separation<sup>25</sup>. Tunnelling spectroscopy experiments on  $\text{Bi}_2\text{Sr}_2\text{CaCu}_2\text{O}_8$  indicate inhomogeneity on the surface. In particular, some measurements indicate granular superconductivity with either the superconducting<sup>26</sup> or insulating<sup>27</sup> phases being of the order of 3 nm. In those experiments, the magnetic nature of the non-superconducting regions is not addressed. A two-phase model has been suggested for samples doped near  $1/8$  hole per copper site. Infrared measurements of the Josephson plasma resonance indicate an inhomogeneous superconducting state near  $1/8$  doping with the coexistence of non-superconducting and superconducting regions<sup>28</sup>. Several notable experiments have determined that magnetic fields induce or enhance static magnetism in cuprate superconductors, particularly for those doped near  $1/8$  hole per copper site<sup>12,29–33</sup>. Recently, both Raman<sup>34</sup> and  $\mu\text{SR}$ <sup>35</sup> reports on similar samples have argued that this magnetic-field effect is due to the coexistence of separate magnetic and superconducting regions, with the magnetic field stabilizing the magnetic phase at the expense of the superconducting phase. In these magnetic-field experiments, the nature of the two phases is not specified. Comparing those results with ours suggests that the application of a magnetic field somehow mimics a change in doping, thus promoting the magnetic phase over the superconducting phase. How that occurs remains to be understood.

Inherent electronic phase separation has been discussed generally as a major influence on the physics of materials with

strong electron–electron interactions. Although the presence of such a process has not previously been clearly demonstrated for the cuprate superconductors, intrinsic phase separation has been accepted as central to the physics of the manganite compounds with colossal magnetoresistance<sup>36</sup>. In some manganites there is evidence that metallic- and charge-ordered insulating phases coexist on a mesoscopic scale. The data we report here might be consistent with a similar model for the cuprates with superconducting and magnetically ordered phases. A recent Landau free-energy analysis explores the type of phase separation we have measured, and also its relation to Sr-doped compounds<sup>37</sup>. The phase diagrams described in that work seem consistent with the results reported here.

Our experiments point towards a model for the underdoped cuprates with only a few inherently stable phases. The underlying tendency is to form separate magnetic and superconducting regions with a direct transition between them. For superoxygenated  $\text{La}_{2-x}\text{Sr}_x\text{CuO}_{4+y}$ , the mobility of the intercalated oxygen dopant ions seems to be the key element that allows phase separation over length and timescales long enough to measure easily. For other compounds, such phase separation is suppressed, but may exist over short length and timescales. It may be that the presence of highly mobile oxygen dopants has provided a key to help unlock the inherent physics of holes in a copper oxide plane.

## METHODS

All of our samples were oxidized using electrochemical methods as discussed previously<sup>17</sup>. The magnetic responses of each sample were measured before and after oxidation on a Quantum Design superconducting quantum interference device magnetometer. The field-cooled diamagnetic signal (Meissner signal) measured with an applied field of 10 G was used to determine  $T_C$  and as a relative measurement of the superconducting volume fraction.  $T_C$  was taken as the temperature at which the Meissner signal reached 1% of the low-temperature value. The superconducting volume fraction was taken as the value of  $4\pi\chi$  at 5 K, we also used HTF muon scans as an alternative measure of the superconducting volume fraction (see the Supplementary Information).

The  $\mu\text{SR}$  experiments were carried out at the Paul Scherrer Institute (PSI) using the surface muon beam facility with an incident muon momentum of  $28 \text{ MeV c}^{-1}$ . As well as the ZF- $\mu\text{SR}$  measurements, we obtained supporting evidence from WTF- $\mu\text{SR}$  and HTF- $\mu\text{SR}$  measurements. Previous studies have indicated a single muon site in this type of crystal, simplifying the interpretation of  $\mu\text{SR}$  results. We fit the ZF data with a strategy that basically follows the procedures outlined by Savici *et al.*<sup>10</sup>, with a correction to account for the fact that the muon spins can only be flipped by  $60^\circ$  at PSI. More details on ZF data analysis are discussed in the Supplementary Information.

In an applied external field,  $H_{\text{ext}}$ , the amplitude of the muon signal precessing at a frequency corresponding to  $H_{\text{ext}}$  reflects the volume fraction of the sample, which is not ordered magnetically. Muons stopping in the antiferromagnetically ordered regions will experience a broader field distribution, which leads to a rapid decay of the muon-spin asymmetry at early times, and these two fractions can easily be separated. Thus, we analysed the low-temperature WTF- $\mu\text{SR}$  data by fitting it to a two-term mathematical function. Both terms include a cosine oscillating signal and a damping term. More details are given in the Supplementary Information.

Thermogravimetric analysis (TGA) measurements were carried out on one of our samples to estimate the oxygen content. The experiments were carried out at the PSI. A superconducting sample with 6.5% Sr, a separate crystal from those used for  $\mu\text{SR}$  experiments was used. Similarly to the other samples, the sample was superconducting after oxidation with  $T_C$  of 40 K. The Meissner fraction,  $4\pi\chi$ , for this sample was 10%. The TGA was carried out in a hydrogen reduction atmosphere so that the known end products are  $\text{La}_2\text{O}_3$ , SrO, and Cu metal. The measurement detected a 4.23% oxygen loss beginning near  $200^\circ\text{C}$  and primarily occurring near  $500^\circ\text{C}$ . This corresponds to an initial total amount of oxygen in the sample of 4.032, or  $y = 0.032$ . This value seems to be consistent with our model of phase separation between a magnetic phase with  $n_h = 0.125$  and a superconducting phase with  $n_h = 0.16$ . If we assume one doped hole per Sr and two holes per excess oxygen, then this particular sample

## ARTICLES

has a hole content of 0.1284. Using a lever rule to calculate the relative amount of the magnetic phase ( $n_h = 0.125$ ) and the superconducting phase ( $n_h = 0.16$ ) gives a superconducting fraction of 10%, roughly matching that determined by the Meissner signal.

Our preliminary neutron data were taken on the triple-axis spectrometer RITA2 at the spallation neutron source SINQ at the PSI. We measured elastic diffraction from the well known magnetic peaks at  $q$ -space positions  $((1/2) \pm \delta, 1/2, 0)$  and  $(1/2, (1/2) \pm \delta, 0)$  in pseudo-tetragonal notation using 5 meV neutrons.

Received 16 May 2005; accepted 8 March 2006; published 16 April 2006.

## References

- Zaenen, J. & Gunnarsson, O. Charge magnetic domain lines and the magnetism of high- $T_c$  oxides. *Phys. Rev. B* **40**, 7391–7394 (1989).
- Emery, V. J., Kivelson, S. A. & Lin, H. Q. Phase-separation in the T-J model. *Phys. Rev. Lett.* **64**, 475–478 (1990).
- Hellberg, C. S. & Manoussakis, E. Phase separation at all interaction strengths in the t-J model. *Phys. Rev. Lett.* **78**, 4609–4612 (1997).
- Chubukov, A. V., Pines, D. & Schmalian, J. A. in *Spin Fluctuation Model for d-wave Superconductivity in The Physics of Conventional and Unconventional Superconductors* (eds Bennemann, K. H. & Ketterer, J. B.) Ch. 7, 495–579 (Springer, Berlin, 2004).
- Demler, E., Sachdev, S. & Ying, Z. Spin-ordering quantum transitions of superconductors in magnetic field. *Phys. Rev. Lett.* **87**, 067202 (2001).
- Moodenbaugh, A. R., Xu, Y., Suenaga, M., Folkerts, T. J. & Shelton, R. N. Superconducting properties of  $\text{La}_{2-x}\text{Ba}_x\text{CuO}_4$ . *Phys. Rev. B* **38**, 4596–4600 (1988).
- Nachumi, B. et al. Muon spin relaxation study of the stripe phase order in  $\text{La}_{1-x}\text{Nd}_x\text{Sr}_x\text{CuO}_4$  and related 214 cuprates. *Phys. Rev. B* **58**, 8760–8772 (1998).
- Lee, Y. S. et al. Neutron-scattering study of spin-density wave order in the superconducting state of excess-oxygen-doped  $\text{La}_2\text{CuO}_{4+x}$ . *Phys. Rev. B* **60**, 3643–3654 (1999).
- Savici, A. et al. Muon spin relaxation studies of incommensurate magnetism and superconductivity in stage-4  $\text{La}_2\text{CuO}_{11}$  and  $\text{La}_{10}\text{Sr}_{10}\text{CuO}_{11}$ . *Phys. Rev. B* **66**, 014524 (2002).
- Savici, A. et al. Static magnetism in superconducting stage-4  $\text{La}_2\text{CuO}_{11}$  ( $y = 0.12$ ). *Physica B* **289–290**, 338–342 (2000).
- Lee, Y. S. et al. Neutron scattering study of the effects of dopant disorder on the superconductivity and magnetic order in stage-4  $\text{La}_2\text{CuO}_{11}$ . *Phys. Rev. B* **69**, 020502 (2004).
- Khaykovich, B. et al. Enhancement of long-range magnetic order by magnetic field in superconducting  $\text{La}_2\text{CuO}_{11}$ . *Phys. Rev. B* **66**, 014528 (2002).
- Johnston, D. C. et al. Phase separation and doped hole segregation in  $\text{La}_2\text{CuO}_{4+x}$  and  $\text{La}_{2-x}\text{Sr}_x\text{CuO}_{4+x}$ . *Physica C* **235–240**, 257–260 (1994).
- Rial, C., Morán, E., Alario-Franco, M. A., Amado, U. & Anderson, N. H. Structural and superconducting properties of  $\text{La}_{2-x}\text{Sr}_x\text{CuO}_{4+x}$  ( $0 < x < 0.15$ ) prepared by room temperature chemical oxidation. *Physica C* **254**, 233–248 (1995).
- Jorgensen, J. D., Dabrowski, B., Pei, S., Hinks, D. G. & Soderholm, L. Superconducting phase of  $\text{La}_2\text{CuO}_{4+x}$ : A superconducting composition resulting from phase separation. *Phys. Rev. B* **38**, 11337–11345 (1988).
- Ansaldo, E. J. et al. Magnetic properties of the superconducting 'superoxide'  $\text{La}_2\text{CuO}_{4.4}$ . *Phys. Rev. B* **40**, 2555–2557 (1989).
- Wells, B. O. et al. Intercalation and staging behaviour in super-oxygenated  $\text{La}_2\text{CuO}_{4+x}$ . *Z. Phys. B* **100**, 535–545 (1996).
- Xiong, X. et al. Evidence of in-plane superstructure formation in phase separated and staged single crystal  $\text{La}_2\text{CuO}_{4+x}$ . *Phys. Rev. Lett.* **76**, 2997–3000 (1996).
- Wells, B. O. et al. Incommensurate spin fluctuations in high-transition temperature superconductors. *Science* **277**, 1067–1071 (1997).
- Niedermayer, Ch. et al. Common phase diagram for antiferromagnetism in  $\text{La}_{2-x}\text{Sr}_x\text{CuO}_4$  and  $\text{Y}_{1-x}\text{Ca}_x\text{Ba}_2\text{Cu}_3\text{O}_7$  as seen by muon spin rotation. *Phys. Rev. Lett.* **80**, 3843–3846 (1998).
- Luke, G. M. et al. Static magnetic order in  $\text{La}_{1.875}\text{Ba}_{0.125}\text{CuO}_4$ . *Physica C* **185–189**, 1175–1176 (1991).
- Yamada, K. et al. Doping dependence of the spatially modulated dynamical spin correlations and the superconducting-transition temperature in  $\text{La}_{2-x}\text{Sr}_x\text{CuO}_4$ . *Phys. Rev. B* **57**, 6165–6172 (1998).
- Hucker, M. et al. Oxygen and strontium codoping of  $\text{La}_2\text{NiO}_7$ : room-temperature phase diagrams. *Phys. Rev. B* **70**, 064105 (2004).
- Axe, J. D. et al. Structural phase transformation and superconductivity in  $\text{La}_{2-x}\text{Ba}_x\text{CuO}_4$ . *Phys. Rev. Lett.* **62**, 2751–2754 (1989).
- Singer, P. M., Hunt, W. A. & Imai, T.  $^{63}\text{Cu}$  NQR evidence for spatial variation of hole concentration in  $\text{La}_{2-x}\text{Sr}_x\text{CuO}_4$ . *Phys. Rev. Lett.* **88**, 047602 (2002).
- Lang, K. M. et al. Imaging the granular structure of high- $T_c$  superconductivity in underdoped  $\text{Bi}_2\text{Sr}_2\text{CaCu}_3\text{O}_{10+x}$ . *Nature* **415**, 412–416 (2002).
- Howald, C., Fournier, P. & Kapitulnik, A. Inherent inhomogeneities in tunneling spectra of  $\text{Bi}_2\text{Sr}_2\text{CaCu}_3\text{O}_{10+x}$  crystals in the superconducting state. *Phys. Rev. B* **64**, 100504 (2001).
- Dordevic, S. V., Komoya, S., Ando, Y. & Basov, D. N. Josephson plasmon and inhomogeneous superconducting state in  $\text{La}_{2-x}\text{Sr}_x\text{CuO}_4$ . *Phys. Rev. Lett.* **91**, 167401 (2003).
- Katano, S., Sato, M., Yamada, K., Suzuki, T. & Fukase, T. Enhancement of static antiferromagnetic correlations by magnetic field in a superconductor  $\text{La}_{2-x}\text{Sr}_x\text{CuO}_4$  (with  $x = 0.12$ ). *Phys. Rev. B* **62**, R14677–R14680 (2000).
- Lake, B. et al. Antiferromagnetic order induced by an applied magnetic field in a high-temperature superconductor. *Nature* **415**, 299–302 (2002).
- Miller, R. L. et al. Evidence for static magnetism in the vortex cores of ortho-II  $\text{YBa}_2\text{Cu}_3\text{O}_{6-x}$ . *Phys. Rev. Lett.* **88**, 137002 (2002).
- Mitrovic, V. I. et al. Spatially resolved electronic structure inside and outside the vortex cores of a high-temperature superconductor. *Nature* **413**, 501–504 (2002).
- Kakuyanagi, K., Kumagai, K., Matsuda, Y. & Hasegawa, M. Antiferromagnetic vortex core in  $\text{Tl}_2\text{Ba}_2\text{CuO}_{8+x}$  studied by nuclear magnetic resonance. *Phys. Rev. Lett.* **90**, 197003 (2003).
- Machtoub, L. H., Keimer, B. & Yamada, K. Large magnetic field-induced spectral weight enhancement of high-energy spin excitations in  $\text{La}_{1.88}\text{Sr}_{0.12}\text{CuO}_4$ . *Phys. Rev. Lett.* **94**, 107009 (2005).
- Savici, A. T. et al. Muon spin relaxation studies of magnetic-field-induced effects in high  $T_c$  superconductors. *Phys. Rev. Lett.* **95**, 157001 (2005).
- Dagotto, E. Open questions in CMR manganites relevance of clustered states and analogies with other compounds including the cuprates. *New J. Phys.* **7**, 1–28 (2005).
- Kivelson, S. A., Aeppli, G. & Emery, V. J. Thermodynamics of the interplay between magnetism and high-temperature superconductivity. *Proc. Natl Acad. Sci.* **98**, 11903–11907 (2001).
- Chou, F. C., Belk, N. R., Kastner, M. A., Birgeneau, R. J. & Aharony, A. Spin-glass behavior in  $\text{La}_{1.96}\text{Sr}_{0.04}\text{CuO}_4$ . *Phys. Rev. Lett.* **75**, 2204–2207 (1995).

## Acknowledgements

We thank H. Ronnow, S. Kivelson, and E. Dagotto for the thoughtful discussions and K. Conder for carrying out TGA measurements on our samples. The research at the University of Connecticut was supported by the US-DOE through contract DE-FG02-00ER45801; research at Brookhaven was supported by US-DOE, Office of Basic Energy Sciences, Division of Materials Science, under contract DE-AC02-98CH10886; and research at MIT (E.-C.C.) was partially supported by the MRSEC Program of the NSF under award number DMR 02-13282. C.M.S.-NTU was partially supported by the National Science Council of Taiwan under contract NSC-95-2112-M-002-026. L.U. is supported by the Danish Research Council for Technology and Production Sciences under the Framework Programme on Superconductivity. The muon work was carried out at the Swiss Muon Source, PSI, Villigen, Switzerland. Correspondence and requests for materials should be addressed to B.O.W. Supplementary Information accompanies this paper on [www.nature.com/naturematerials](http://www.nature.com/naturematerials).

## Competing financial interests

The authors declare that they have no competing financial interests.

Reprints and permission information is available online at <http://npg.nature.com/reprintsandpermissions/>

PHYSICAL REVIEW B **73**, 224510 (2006)**Recursion method for the quasiparticle structure of a single vortex with induced magnetic order**Linda Udby,<sup>1</sup> Brian M. Andersen,<sup>2</sup> and Per Hedegård<sup>3</sup><sup>1</sup>*Materials Science Department, Risø National Laboratory, Frederiksborgvej 399, DK-4000 Roskilde, Denmark*<sup>2</sup>*Department of Physics, University of Florida, Gainesville, Florida 32611-8440, USA*<sup>3</sup>*Ørsted Laboratory, Niels Bohr Institute, Universitetsparken 5, DK-2100 Copenhagen Ø, Denmark*

(Received 13 March 2006; published 13 June 2006)

We use a real-space recursion method to calculate the local density of states (LDOS) within a model that contains both *d*-wave superconducting and antiferromagnetic order. We focus on the LDOS in the superconducting phase near single vortices with either normal or antiferromagnetic cores. Furthermore, we study the low-energy quasiparticle structure when magnetic vortices operate as pinning centers for surrounding unidirectional spin density waves (stripes). We calculate the Fourier transformed LDOS and show how the energy dependence of relevant Fourier components can be used to determine the nature of the magnetic field-induced order, and predict field-induced LDOS features that can be tested by future scanning tunneling microscopy experiments.

DOI: 10.1103/PhysRevB.73.224510

PACS number(s): 74.20.-z, 74.72.-h, 74.25.Jb, 74.25.Ha

**I. INTRODUCTION**

It is becoming evident that competing phases cause many of the anomalous properties of doped Mott insulators. An example is given by the vortex state of underdoped high- $T_c$  superconductors where antiferromagnetism (AF) “pops up” near the vortices.<sup>1,2</sup> Initial experimental evidence for this claim came from scanning tunneling microscopy (STM) experiments on  $\text{YBa}_2\text{Cu}_3\text{O}_y$  (YBCO) and  $\text{Bi}_2\text{Sr}_2\text{CaCu}_2\text{O}_{8+x}$  (BSCCO) observing weak low-energy quasiparticle peaks around 5–7 meV.<sup>3,4</sup> This strongly contradicts the expected local density of states (LDOS) in the vortex center of a pure BCS *d*-wave superconductor (dSC) which is dominated by the so-called zero-energy state (ZES), a single broad resonance centered at the Fermi level.<sup>5</sup> Further evidence for AF cores has come from both nuclear magnetic resonance measurements<sup>6</sup> and muon spin rotation experiments.<sup>7</sup> The field-induced magnetization is not necessarily restricted to the core regions as determined by the coherence length  $\xi$ . For instance, elastic neutron scattering on underdoped  $\text{La}_{2-x}\text{Sr}_x\text{CuO}_2$  (LSCO) showed that the intensity of the incommensurate peaks in the superconducting phase is considerably increased when a magnetic field is applied perpendicular to the  $\text{CuO}_2$  planes<sup>8</sup> or when Zn is doped into the samples.<sup>9</sup> Similar results have been found in the oxygen doped sample  $\text{La}_2\text{CuO}_{4+y}$ .<sup>10</sup> The momentum position and field-enhanced sharpening of this elastic signal corresponds to a spin density wave period of roughly eight lattice constants  $8a$  extending far outside the vortex cores, suggesting that the magnetic cores operate as pinning centers for surrounding spin density waves.<sup>11,12</sup> This unusual behavior agrees with in-field STM measurements on optimally doped BSCCO which found local field-induced checkerboard LDOS patterns with a period close to  $4a$ .<sup>13</sup> Similar structure has been reported in zero field STM experiments.<sup>14</sup> Pronounced checkerboard ordering has also been detected in  $\text{Na}_x\text{Ca}_{2-x}\text{CuO}_2\text{Cl}_2$ .<sup>15</sup> More recently, Levy *et al.*<sup>16</sup> confirmed the results of Ref. 13 and found that the checkerboard modulation does not disperse with energy, and mapped out the energy dependence of the amplitude of the Fourier compo-

nent corresponding to the ordering vector of the modulation.

Theoretically, several groups have proposed that the origin of the unexpected behavior inside the cores is related to locally nucleated AF,<sup>17,18</sup> but other scenarios have also been proposed.<sup>19,20</sup> From a computational point of view, in order to model the existence of nano-scale inhomogeneity, it is necessary to use methods that easily allows one to obtain the LDOS as a function of energy and large real-space regions. Traditionally this is done by numerical diagonalization of the Bogoliubov–de Gennes (BdG) equations, which, at present, is typically restricted to quite small lattices ( $\leq 40 \times 40$  sites). In this paper we use a recursion method generalized to the *d*-wave superconducting state to calculate the LDOS near an increasingly complex single vortex. This method is easily applied to large systems allowing for, e.g., high-resolution Fourier LDOS images. First we study the pure dSC vortex for realistic band structure parameters relevant for overdoped cuprates. Second, we discuss the case of an AF vortex core in the optimally doped regime and focus on the spatial dependence of the expected LDOS. Finally, we calculate the LDOS when the vortex pins surrounding incommensurate stripe order as may be relevant for LSCO and underdoped BSCCO, and discuss the energy dependence of the resulting Fourier transform. As opposed to most earlier theoretical work on the AF vortex problem,<sup>17</sup> we focus on the final LDOS structure and the Fourier transformed LDOS maps which can be used as an STM tool to determine the nature of the field-induced order and the origin of the ZES splitting. Lastly, we compute the LDOS resulting from the recently proposed pair-density wave ordered state.

**II. MODEL AND METHOD**

In the following we study the mean-field Hamiltonian defined on a two-dimensional (2D) lattice

$$\hat{H} = - \sum_{\langle ij \rangle \sigma} t_{ij} \hat{c}_{i\sigma}^\dagger \hat{c}_{j\sigma} - \mu \sum_{i\sigma} \hat{c}_{i\sigma}^\dagger \hat{c}_{i\sigma} + \sum_{\langle ij \rangle} (\Delta_{ij} \hat{c}_{i1}^\dagger \hat{c}_{j1}^\dagger + \text{H.c.}) + \sum_i m_i (\hat{c}_{i1}^\dagger \hat{c}_{i1} - \hat{c}_{i1}^\dagger \hat{c}_{i1}), \quad (1)$$

where  $\hat{c}_{i\sigma}^\dagger$  creates an electron with spin  $\sigma$  at site  $i$ ,  $t_{ij}$  is the

UDBY, ANDERSEN, AND HEDEGÅRD

PHYSICAL REVIEW B **73**, 224510 (2006)

hopping integral to nearest ( $t$ ) or next-nearest ( $t'$ ) neighbors and  $\mu$  is the chemical potential. The AF and dSC order parameters are given by  $m_i$  and  $\Delta_{ij}$ , respectively. The Hamiltonian (1) is the effective mean-field model obtained after performing two Hubbard-Stratonovich transformations of the extended Hubbard model with the on-site repulsion causing the AF, and the attractive nearest neighbor interaction resulting in the dSC. It has been used extensively in the past few years to gain insight into the electronic structure of phases of coexisting AF and dSC order.<sup>12,17,21–23</sup>

Below, we solve the Hamiltonian (1) using appropriate Ansätze for both  $\Delta_{ij}$  and  $m_i$ . The lack of self-consistency can sometimes be useful in clarifying, for instance, the nature/or origin of vortex core states.<sup>30</sup> We restrict the discussion to the case when the applied magnetic field is much smaller than  $H_{c2}$  and consequently ignore the vector potential  $\mathbf{A}$ .

In order to obtain the LDOS near single vortices we use a recursion method<sup>24,25</sup> generalized to the superconducting state. The starting point is to generate a new orthonormal basis of states from the recursion relation

$$\hat{H}|n\rangle = a_n|n\rangle + b_{n+1}|n+1\rangle + b_n|n-1\rangle. \quad (2)$$

For each recursion the Greens function of the  $n$ th level is generated recursively from the Lanczos coefficients  $a_n$  and  $b_n$

$$G_n(\omega) = \frac{1}{\omega - a_n - b_{n+1}^2 G_{n+1}(\omega)}. \quad (3)$$

Hence, the local Greens function can be found if  $G_N(\omega)=0$  for some number  $N$ , or if an appropriate analytical solution of  $G_N$  for an infinite chain can be attached.

The retarded Greens function is

$$G_{i\sigma}^R(\omega) = \sum_{\alpha} \left( \frac{|\langle \alpha | c_{i\sigma}^{\dagger} | 0 \rangle|^2}{\omega - E_{\alpha\sigma} + i\eta} + \frac{|\langle \alpha | c_{i\sigma} | 0 \rangle|^2}{\omega + E_{\alpha\sigma} + i\eta} \right), \quad (4)$$

where  $\eta$  is used as an artificial smearing factor with  $\eta = 0.02t$ . In general, it is not necessary to perform four recursions (I from  $c_{i\uparrow}^{\dagger}|0\rangle$ ; II from  $c_{i\downarrow}|0\rangle$ ; III from  $c_{i\uparrow}^{\dagger}|0\rangle$ ; IV from  $c_{i\downarrow}|0\rangle$ ) to calculate the spin-summed LDOS since  $G_{n=0}^{IV}(-\omega) = G_{n=0}^I(\omega)$  and  $G_{n=0}^{III}(\omega) = G_{n=0}^{II}(-\omega)$ . Thus, it is sufficient to perform only two recursions to obtain the total LDOS,  $\rho(i, \omega)$ , in the form of a continued fraction

$$\rho(i, \omega) = \text{Im} \frac{-\frac{1}{\pi}}{\omega - a_0^I + i\eta - \frac{(b_1^I)^2}{\omega - a_1^I + i\eta - \frac{(b_2^I)^2}{\omega - a_2^I + i\eta - \dots}} + [\omega \rightarrow -\omega, a^I \rightarrow a^{II}, (b^I)^2 \rightarrow (b^{II})^2]}, \quad (5)$$

which can be compared to the differential tunneling conductance as measured by, e.g., an STM tip. Of course, when there is spin degeneracy (here:  $m_i=0$ ) only one recursion is needed to produce the total LDOS.

In the cases studied, we find that the Lanczos coefficients converge nicely when increasing the number of recursions, i.e., the system size. Below we simply perform the truncation

$G_N=0$  where  $N$  is some number of order  $10^3$ , and have checked that this choice does not affect the reported results.

### III. RESULTS

In this section we use the recursion method to study  $\rho(i, \omega)$  around a single vortex in the dSC state both with and without antiferromagnetism in the core region. This is supposed to model the vortex LDOS in the overdoped and optimally doped regime, respectively. The core center is positioned at the origin (0, 0) and lengths are measured in units of the lattice constant  $a$ .

#### A. A single vortex without induced stripe order

As is well-known, in an  $s$ -wave BCS superconductor the vortex generates states localized transverse to the flux line. These have been studied in great detail both theoretically<sup>26–28</sup> and experimentally.<sup>29</sup> The core states result from the opposite sign of the supercurrent term in the particle and hole part of the BdG equations.<sup>26,30,31</sup> The reduction of the pair potential near the vortex core causes only minor quantitative changes to these states. We have verified that the recursion method described above applied to  $s$ -wave superconductors successfully reproduce these Caroli–de Gennes–Matricon bound states.

To model an isolated  $d$ -wave vortex the following pairing potential is used:

$$\Delta_{ij} = \Delta \tanh(|\mathbf{r}|/\xi) \exp(i\varphi_{ij}), \quad (6)$$

where  $\Delta$  is positive (negative) on  $x$  ( $y$ ) links,  $\mathbf{r} = (\mathbf{r}_i + \mathbf{r}_j)/2$  and  $\exp(i\varphi_{ij}) = (x+iy)/r$  with  $\mathbf{r} = (x, y)$ . In agreement with Refs. 30 and 31, we find that the suppression of the gap in the core region results in only minor quantitative changes: in general the suppression tends to push the states slightly further toward the Fermi level. In the pure dSC state, the vortex is dominated by the well-known ZES.<sup>5</sup> However, the ZES is centered exactly at zero energy only for  $\mu=t'=0$ . As opposed to the Caroli–de Gennes–Matricon states in the  $s$ -wave vortex, the ZES is made up of several states that merge to form the broad peak as the system size is increased in agreement with the extended nature of this peak.<sup>20</sup> In Fig. 1 we show  $\rho(i, \omega)$  of a dSC vortex along the antinodal (a)–(b) and nodal (c)–(d) directions for  $\Delta=0.1t$ ,  $\xi=5$  and  $\mu=t'=0$  (a),(c),(e), and  $\mu=-1.18t$ ,  $t'=-0.4t$  (b),(d),(f). The latter parameter set provides a reasonable fit to the Fermi surface of slightly overdoped BSCCO with a van Hove singularity at  $\omega_{vH} = -\sqrt{(4t'-\mu)^2 + (4\Delta)^2}$ . It is the  $d$ -wave symmetry that causes the angular dependence [compare, e.g., Figs. 1(a) and 1(c)] of the higher energy core states at  $\mathbf{r} \neq 0$ . The energy and amplitude of these core states are seen to be sensitive to the band parameters. This is also true for the ZES state as seen from Figs. 1(e) and 1(f): at  $t'=0$  the low-energy spatial form of the LDOS has a star-shape due to the nodal dSC phase.<sup>5,32,33</sup> However, for the more realistic BSCCO band parameters, the star is rotated with small maximum intensity along the antinodal directions, which is our prediction for the overdoped regime of BSCCO where competing AF order is expected to be absent. For  $t'=0$ , it is well-known that a

RECURSION METHOD FOR THE QUASIPARTICLE...

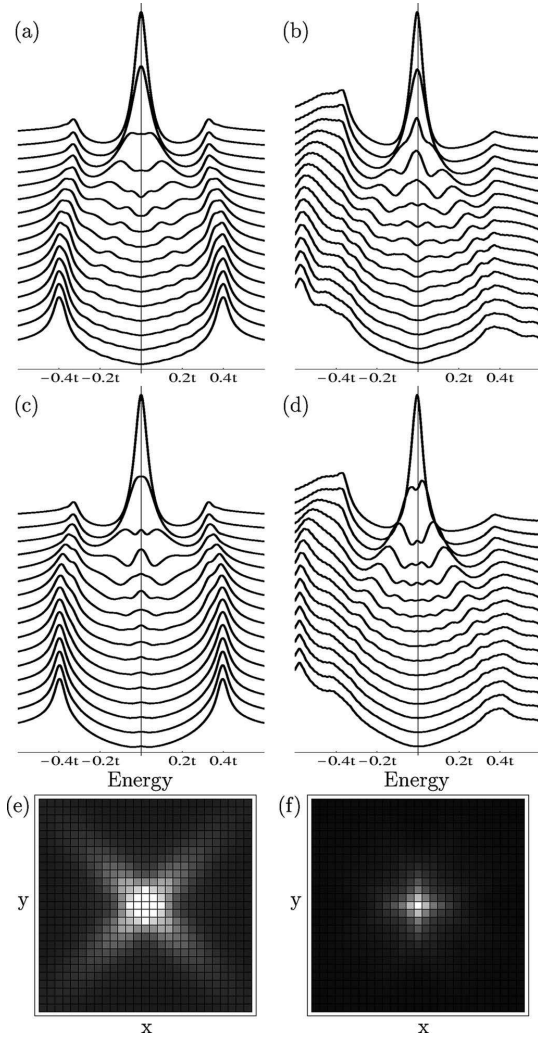
PHYSICAL REVIEW B **73**, 224510 (2006)

FIG. 1. LDOS along the antinodal (a),(b) and nodal (c)(d) direction for a single dSC vortex. (e)(f) Spatial 2D structure of the ZES. Left column:  $\mu=t'=0$ ,  $\Delta=0.1t$ . Right column:  $\mu=-1.18t$ ,  $t'=-0.4t$ , and  $\Delta=0.1t$ .

similar  $\pi/4$  rotation takes place at higher energies revealing the spatial form of the higher energy core states.<sup>33,34</sup>

We turn now to the simplest AF core situation where the suppression of the dSC gap inside the core causes a concomitant increase of the competing AF order.<sup>2</sup> For simplicity, we model the AF core by

$$m_i = m(-1)^{(x+y)} [1 - \tanh(|\mathbf{r}_i|/\xi)], \quad (7)$$

where  $\mathbf{r}_i=(x,y)$ . Due to an associated local increase of the electron density, such vortices will in general be charged,<sup>35</sup> and have been shown to remain stable when including the

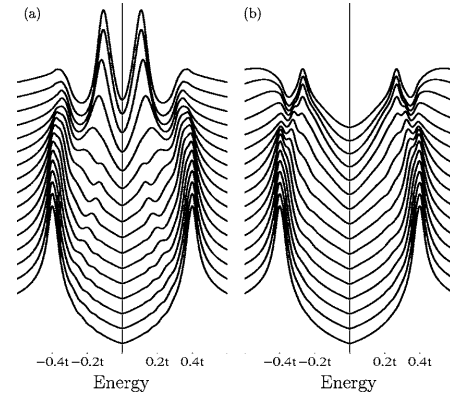


FIG. 2. LDOS along the antinodal direction for a dSC vortex with antiferromagnetic core. Parameters used:  $\mu=t'=0$ ,  $\Delta=0.1t$ ,  $m=0.2t$  (a) and  $m=0.5t$  (b).

long-range Coulomb repulsion.<sup>18</sup> Below, we therefore use  $\mu=t'=0.0$  in order to model the close to half-filled vortex core regions as found in the self-consistent studies.<sup>17,18</sup> In Fig. 2 we show the final LDOS as a function of energy and distance to the AF vortex core. The induced magnetization leads to a splitting of the ZES as found previously.<sup>17,18</sup> With increased magnetic order  $m$ , the resonant core states are pushed to higher energies and lose spectral weight. The vortex region is fully void of apparent core states for  $m \geq t$ . In this limit the low-energy LDOS has an apparent similarity with that of the pseudogap.

Spatial averaging may mask the observability of the dispersive core states in Fig. 2. For example, in Fig. 3 we show  $\rho(i, \omega)$  [same parameters as in Fig. 2(a)] at  $(0, 0)$  and  $(0, 7.5)$  averaged over a coherence length  $\xi$ . As seen, the resulting LDOS appears to be that of approximately nondispersing resonant states which rapidly lose weight when moving away from the core region. This is similar to the measured differential tunneling conductance near the vortex cores of YBCO and BSCCO.<sup>3,4</sup> However, an unambiguous experimental de-

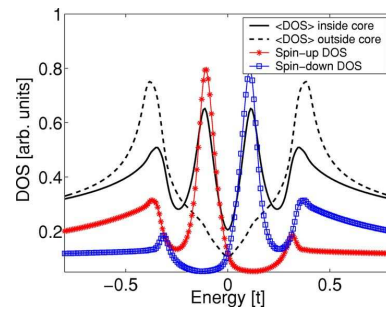


FIG. 3. (Color online) DOS averaged over a coherence length  $\xi$  within the core (solid black line), and just outside the core (dashed black line). The red line with asterisks symbols (blue with  $\square$  symbols) show the spin-up (spin-down) resolved LDOS at the core center similar to the top scan in Fig. 2(a).

UDBY, ANDERSEN, AND HEDEGÅRD

PHYSICAL REVIEW B **73**, 224510 (2006)

termination of the type of order that induces the splitting of the ZES is important, and is related to the general discussion of time-reversal symmetry breaking for zero-energy Andreev states in  $d$ -wave superconductors.<sup>36</sup> Of course, vortices that support AF cores would lead to a field-induced commensurate  $(\pi, \pi)$  signal in neutron scattering. However, purely from a tunneling point of view, it is possible to distinguish AF and, e.g.,  $d_{x^2-y^2} + id_{xy}$  induced order by using spin polarized STM.<sup>37</sup> This is also shown in Fig. 3 where the positive (negative) bias peak is seen to be related to the spin-down (spin-up) LDOS, respectively. Importantly, this bias asymmetry will alternate with site, allowing for an unambiguous experimental test of AF order by a magnetic STM tip scanned through the vortex core region.

### B. A single vortex with induced stripe order

In this section we calculate  $\rho(i, \omega)$  around a dSC vortex which operates as a pinning center for unidirectional spin- and charge-density modulations (stripes), expected to be relevant for STM experiments in the underdoped regime. Such inhomogeneous stripe solutions indeed exist in a regime of intermediate AF coupling within self-consistent mean-field models that include the competition between AF and dSC order.<sup>17</sup> We also briefly discuss the expected LDOS resulting from the recently proposed pair-density-wave (PDW) induced order consisting of a density wave of Cooper pairs without global phase coherence.<sup>38,39</sup>

Whereas the previous section dealt with the details of  $\rho(i, \omega)$  inside the core, the field-induced periodic order can most conveniently be studied in Fourier space

$$\rho_{\mathbf{q}}(\omega) = \frac{1}{N} \sum_i \rho(i, \omega) e^{-i\mathbf{q} \cdot \mathbf{r}_i}. \quad (8)$$

Below, we model site-centered stripes with period of 8 lattice constants by the configuration,  $\uparrow\downarrow\uparrow\downarrow\uparrow\downarrow\uparrow\downarrow$ , with AF ordering along the stripes, and the strength of the spin order set by the parameter  $m$ . Specifically, the stripe configuration can be written as  $m(-1)^{x+y} \prod_{\{x_s\}} \Theta(x - x_s)$  where  $\Theta(x) = -\Theta(-x) = 1$  is the antisymmetric step function with  $\Theta(0) = 0$ , and  $\{x_s\}$  denotes the set of the positions of the site-centered charge stripes, i.e.,  $\{x_s\} = \{\dots, 0, 4, 8, \dots\}$ .<sup>22</sup> Figure 4(a) shows the resulting LDOS  $\rho(i, \omega)$  summed over the energy range  $\omega \in [-0.04t, 0.04t]$  in the case with  $m/t = 1$ . The checkerboard pattern arises from including both vertical and horizontal stripes, which is a simple way to include the assumed slow fluctuation of the stripe domains. In addition, as shown recently, quenched disorder can severely smear any clear distinction between stripe and checkerboard symmetry breaking.<sup>40</sup> Figure 4(b) shows  $|\rho_{\mathbf{q}}|$  as a function of  $q_x$  for  $q_y = 0.0$  for various energies  $\omega$ . The nondispersive peak at the charge ordering vector  $\mathbf{Q} = (2\pi/4, 0)$  resulting from the stripes is seen to completely dominate other quasiparticle interference effects. It is evident from Fig. 4(b) that  $|\rho_{\mathbf{Q}}(\omega)|$  displays a nonmonotonic dependence on energy. In fact, as pointed out in Ref. 41 for the case of *weak* translational symmetry breaking, useful information about the induced order and the underlying quasiparticle structure is contained in

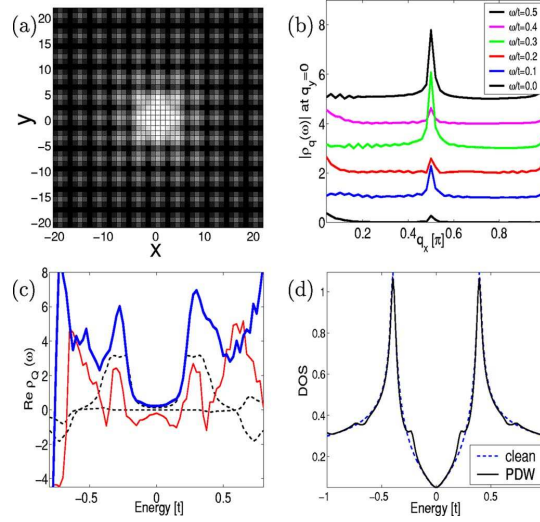


FIG. 4. (Color online) (a) LDOS summed in the window  $\omega \in [-0.04t, 0.04t]$  with  $m/t = 1.0$ . White (black) corresponds to high (low) LDOS. (b)  $|\rho_{\mathbf{q}}(\omega)|$  at  $q_y = 0.0$  vs  $q_x$  for the energies  $\omega/t = 0.0, 0.1, 0.2, 0.3, 0.4, 0.5$ . The curves are offset for clarity. (c)  $\rho'_{\mathbf{Q}}(\omega)$  vs  $\omega$  for a  $\mu$  wave ( $\Delta$ -wave, PDW) with  $t' = \mu = 0.0$ ,  $A = 0.05t$  as shown by the antisymmetric (symmetric) dashed, black line, and the full vortex induced stripe situation with  $t' = -0.4t$ ,  $\mu = -1.18$ ,  $m/t = 0.4$  (thin red line), and  $m/t = 1.0$  (thick blue line). Note that for all the curves  $\rho'_{\mathbf{Q}}(0) = 0$  (within a window set by the smearing  $\eta$ ) as expected for a  $d$ -wave superconductor at  $T = 0$ . (d) LDOS for the clean dSC (PDW) shown by the dashed (solid) line.

$\rho'_{\mathbf{Q}}(\omega)$ , the real part of  $\rho_{\mathbf{q}}(\omega)$  at the ordering vector  $\mathbf{Q}$ . In general, for weak induced order  $\rho'_{\mathbf{Q}}(\omega)$  will exhibit peaks near  $\omega = \omega_{vH}$  due to the logarithmic divergence coming from the van Hove points at  $(0, \pm\pi)$  and  $(\pm\pi, 0)$ , and near energies determined from degeneracy points  $E_{\mathbf{k}} = E_{\mathbf{k}+\mathbf{Q}}$ , where  $E_{\mathbf{k}}$  is the quasiparticle spectrum for the homogeneous dSC.<sup>41</sup> For the simple nested Fermi surface ( $t' = \mu = 0$ ) and in the case a weak unidirectional  $\mu$  wave [ $\mu = A \sin(2\pi/4x)$ ] or  $\Delta$  wave [ $\Delta = \Delta_0 + A \sin(2\pi/4x)$ ], this is illustrated in Fig. 4(c) by the black dashed lines. For the  $\Delta$  wave ( $\mu$  wave)  $\rho'_{\mathbf{Q}}(\omega)$  is symmetric (antisymmetric) with characteristic peaks inside (outside) the bulk gap as well as weight at  $\omega = 0.4t$  which is the van Hove energy for this band structure.<sup>38,41</sup> In Fig. 4(c) we also show the full numerical result for  $\rho'_{\mathbf{Q}}(\omega)$  in the vortex state for different strengths of the magnetic order  $m$ . As seen, the stripe induced features in  $\rho'_{\mathbf{Q}}(\omega)$  are roughly symmetric around  $\omega = 0.0$ .<sup>42</sup> We find that sign changes in  $\rho'_{\mathbf{Q}}(\omega)$  at low energy  $\omega \lesssim \Delta$  are only present for weak induced order  $m/t \lesssim 0.45$ . We have checked that  $\rho'_{\mathbf{Q}}(\omega)$  is determined almost entirely by the stripe order: omission of the vortex flow causes only minor quantitative changes at  $\omega \lesssim \Delta$ . We expect the qualitative results presented in Fig. 4(c) to apply primarily to LSCO and LBCO. In BSCCO, on the other hand, it is becoming clear that a strong component of the LDOS inhomogeneity is given by gap disorder.<sup>38,41,43</sup>

We now turn briefly to the discussion of the LDOS near vortices with induced PDW order which, for simplicity, is modeled with a  $\Delta$  wave. It is clear that PDW modulations cannot be the only induced order since that would not lead to a splitting of the ZES in the core center, and would not explain the enhanced spin response in the neutron experiments in the mixed state. Nevertheless, the question remains whether for certain regions of the phase diagram it coexists with or dominates the induced spin and/or charge order surrounding the cores, resulting in distinct features of the measured LDOS. As shown in Fig. 4(c), in the case of particle-hole symmetric bands  $\rho_Q(\omega)$  is a good probe of the induced order since  $\rho'_Q(\omega)$  is symmetric or antisymmetric with respect to the bias voltage for periodic modulations in the  $\tau_1$  or  $\tau_3$  channel of Nambu space, respectively. However, realistic band parameters and possible coexistence of other symmetry breakings will strongly modify  $\rho'_Q(\omega)$  making detailed fitting to various assumed order parameters necessary.<sup>41</sup> Here, we propose the alternative possibility to search for PDW order using STM by identifying the Andreev resonant states exist-

ing in any gap modulated landscape.<sup>43</sup> In Fig. 4(d) we show the LDOS far away from the core region in the case where  $\Delta$  is modulated by an additional sinusoidal wave of period four and an amplitude of 30% of the average gap. As seen, the Andreev states result in a distinct subgap shoulder in  $\rho(i, \omega)$  inside the bulk gap in regions well outside the vortex core. Such subgap structure will be approximately nondispersing and hence distinct from dispersing core states extending outside the core region.

#### IV. CONCLUSIONS

We have presented theoretical results for the quasiparticle structure near an increasingly complex vortex of a  $d$ -wave superconductor. We have discussed distinct LDOS features expected when magnetic or pair density wave order is induced by an applied magnetic field, and have suggested new tunneling experiments to test for field-induced antiferromagnetic order near the vortex cores of high- $T_c$  materials.

- <sup>1</sup>S. C. Zhang, *Science* **275**, 1089 (1997).
- <sup>2</sup>D. P. Arovas, A. J. Berlinsky, C. Kallin, and S. C. Zhang, *Phys. Rev. Lett.* **79**, 2871 (1997).
- <sup>3</sup>I. Maggio-Aprile, C. Renner, A. Erb, E. Walker, and Ø. Fischer, *Phys. Rev. Lett.* **75**, 2754 (1995).
- <sup>4</sup>S. H. Pan, E. W. Hudson, A. K. Gupta, K.-W. Ng, H. Eisaki, S. Uchida, and J. C. Davis, *Phys. Rev. Lett.* **85**, 1536 (2000).
- <sup>5</sup>Y. Wang and A. H. Macdonald, *Phys. Rev. B* **52**, R3876 (1995).
- <sup>6</sup>N. J. Curro, C. Milling, J. Haase, and C. P. Slichter, *Phys. Rev. B* **62**, 3473 (2000); V. F. Mitrovic, E. E. Sigmund, M. Eschrig, H. N. Bachman, W. P. Halperin, A. P. Reyes, P. Kuhns, and W. G. Muolton, *Nature (London)* **413**, 501 (2001); K. Kakuyanagi, K. Kumagai, Y. Matsuda, and M. Hasegawa, *Phys. Rev. Lett.* **90**, 197003 (2003).
- <sup>7</sup>R. I. Miller, R. F. Kiefl, J. H. Brewer, J. E. Sonier, J. Chakhalian, S. Dunsiger, G. D. Morris, A. N. Price, D. A. Bonn, W. H. Hardy, and R. Liang, *Phys. Rev. Lett.* **88**, 137002 (2002); J. E. Sonier, F. D. Callaghan, J. H. Brewer, W. N. Hardy, D. A. Bonn, and R. Liang, cond-mat/0508079 (unpublished).
- <sup>8</sup>B. Lake, H. M. Rønnow, N. B. Christensen, G. Aeppli, K. Lefmann, D. F. McMorrow, P. Vorderwisch, P. Smeibidl, N. Mangkorntong, T. Sasagawa, M. Nohara, H. Takagi, and T. E. Mason, *Nature (London)* **415**, 299 (2002).
- <sup>9</sup>H. Kimura, M. Kofu, Y. Matsumoto, and K. Hirota, *Phys. Rev. Lett.* **91**, 067002 (2003); H. Kimura, K. Hirota, H. Matsushita, K. Yamada, Y. Endoh, S. H. Lee, C. F. Majkrzak, R. Erwin, G. Shirane, M. Greven, Y. S. Lee, M. A. Kastner, and R. J. Birgeneau, *Phys. Rev. B* **59**, 6517 (1999).
- <sup>10</sup>B. Khaykovich, Y. S. Lee, R. Erwin, S.-H. Lee, S. Wakimoto, K. J. Thomas, M. A. Kastner, and R. J. Birgeneau, *Phys. Rev. B* **66**, 014528 (2002).
- <sup>11</sup>E. Demler, S. Sachdev, and Y. Zhang, *Phys. Rev. Lett.* **87**, 067202 (2001).
- <sup>12</sup>B. M. Andersen, P. Hedegård, and H. Bruus, *Phys. Rev. B* **67**, 134528 (2003).
- <sup>13</sup>J. E. Hoffman, E. W. Hudson, K. M. Lang, V. Madhavan, H. Eisaki, S. Uchida, and J. C. Davis, *Science* **295**, 466 (2002).
- <sup>14</sup>C. Howald, H. Eisaki, N. Kaneko, M. Greven, and A. Kapitulnik, *Phys. Rev. B* **67**, 014533 (2003).
- <sup>15</sup>T. Hanaguri, C. Lupien, Y. Kohsaka, D.-H. Lee, M. Azuma, M. Takano, H. Takagi, and J. C. Davis, *Nature (London)* **430**, 1001 (2004).
- <sup>16</sup>G. Levy, M. Kugler, A. A. Manuel, Ø. Fischer, and M. Li, *Phys. Rev. Lett.* **95**, 257005 (2005).
- <sup>17</sup>N. Ogata, *Int. J. Mod. Phys. B* **13**, 3560 (1999); B. M. Andersen, H. Bruus, and P. Hedegård, *Phys. Rev. B* **61**, 6298 (2000); M. Ichioka, M. Takigawa, and K. Machida, *J. Phys. Soc. Jpn.* **70**, 33 (2001); J.-X. Zhu and C. S. Ting, *Phys. Rev. Lett.* **87**, 147002 (2001); A. Ghosal, C. Kallin, and A. J. Berlinsky, *Phys. Rev. B* **66**, 214502 (2002); M. Takigawa, M. Ichioka, and K. Machida, *J. Phys. Soc. Jpn.* **73**, 450 (2004).
- <sup>18</sup>D. Knapp, C. Kallin, A. Ghosal, and S. Mansour, *Phys. Rev. B* **71**, 064504 (2005).
- <sup>19</sup>J. H. Han and D.-H. Lee, *Phys. Rev. Lett.* **85**, 1100 (2000); J.-I. Kishine, P. A. Lee, and X.-G. Wen, *ibid.* **86**, 5365 (2001); Q.-H. Wang, J. H. Han, and D.-H. Lee, *ibid.* **87**, 167004 (2001); C. Berthod and B. Giovannini, *ibid.* **87**, 277002 (2001).
- <sup>20</sup>M. Franz and Z. Tesanovic, *Phys. Rev. Lett.* **80**, 4763 (1998).
- <sup>21</sup>B. M. Andersen, P. Hedegård, and H. Bruus, *J. Low Temp. Phys.* **131**, 281 (2003).
- <sup>22</sup>M. Granath, V. Oganesyan, D. Orgad, and S. A. Kivelson, *Phys. Rev. B* **65**, 184501 (2002).
- <sup>23</sup>B. M. Andersen, I. V. Bobkova, P. J. Hirschfeld, and Yu. S. Barash, *Phys. Rev. B* **72**, 184510 (2005).
- <sup>24</sup>R. Haydock, *Solid State Physics*, edited by Ehrenreich, F. Seitz, and D. Turnbull (Academic Press, New York, 1980), Vol. 35.
- <sup>25</sup>G. Litak, P. Miller, and B. L. Györfy, *Physica C* **251**, 263 (1995); P. Miller and B. L. Györfy, *J. Phys.: Condens. Matter* **7**, 5579 (1995).
- <sup>26</sup>C. Caroli, P. G. de Gennes, and J. Matricon, *Phys. Lett.* **9**, 307

UDBY, ANDERSEN, AND HEDEGÅRD

PHYSICAL REVIEW B **73**, 224510 (2006)

- (1964).
- <sup>27</sup>F. Gygi and M. Schlüter, Phys. Rev. Lett. **65**, 1820 (1990); Phys. Rev. B **43**, 7609 (1991).
- <sup>28</sup>J. D. Shore, M. Huang, A. T. Dorsey, and J. P. Sethna, Phys. Rev. Lett. **62**, 3089 (1989).
- <sup>29</sup>H. F. Hess, R. B. Robinson, R. C. Dynes, J. M. Valles, Jr., and J. V. Waszczak, Phys. Rev. Lett. **62**, 214 (1989).
- <sup>30</sup>C. Berthod, Phys. Rev. B **71**, 134513 (2005).
- <sup>31</sup>T. Dahm, S. Graser, C. Iniotakis, and N. Schopohl, Phys. Rev. B **66**, 144515 (2002).
- <sup>32</sup>P. I. Soininen, C. Kallin, and A. J. Berlinsky, Phys. Rev. B **50**, 13883 (1994).
- <sup>33</sup>M. Ichioka, N. Hayashi, N. Enomoto, and K. Machida, Phys. Rev. B **53**, 15316 (1996).
- <sup>34</sup>J. X. Zhu, C. S. Ting, and A. V. Balatsky, cond-mat/0109503 (unpublished).
- <sup>35</sup>Y. Chen, Z. D. Wang, J.-X. Zhu, and C. S. Ting, Phys. Rev. Lett. **89**, 217001 (2001).
- <sup>36</sup>M. Sigrist, Prog. Theor. Phys. **99**, 899 (1998).
- <sup>37</sup>A. Wachowiak, J. Wiebe, M. Bode, O. Pietzsch, M. Morgenstern, and R. Wiesendanger, Science **298**, 577 (2002).
- <sup>38</sup>H. D. Chen, J.-P. Hu, S. Capponi, E. Arrigoni, and S.-C. Zhang, Phys. Rev. Lett. **89**, 137004 (2002); H. D. Chen, O. Vafek, A. Yazdani, and S.-C. Zhang, *ibid.* **93**, 187002 (2004).
- <sup>39</sup>Z. Tesanovic, Phys. Rev. Lett. **93**, 217004 (2004); A. Melikyan and Z. Tesanovic, Phys. Rev. B **71**, 214511 (2005).
- <sup>40</sup>J. A. Robertson, S. A. Kivelson, E. Fradkin, A. C. Fang, and A. Kapitulnik, cond-mat/0602675 (unpublished); A. Del Maestro, B. Rosenow, and S. Sachdev, cond-mat/0603029 (unpublished).
- <sup>41</sup>D. Podolsky, E. Demler, K. Damle, and B. I. Halperin, Phys. Rev. B **67**, 094514 (2003).
- <sup>42</sup>B. M. Andersen and P. Hedegård, Phys. Rev. Lett. **95**, 037002 (2005).
- <sup>43</sup>T. S. Nunner, B. M. Andersen, A. Melikyan, and P. J. Hirschfeld, Phys. Rev. Lett. **95**, 177003 (2005); A. C. Fang, L. Capriotti, D. J. Scalapino, S. A. Kivelson, N. Kaneko, M. Greven, and A. Kapitulnik, *ibid.* **96**, 017007 (2006).



# Bibliography

- [1] Charles Kittel. *Introduction to Solid State Physics, 7th ed.* John Wiley & Sons, 1996.
- [2] Raffaele Gilardi. *Inelastic and small angle neutron scattering study of the  $La_{2-x}Sr_xCuO_4$  high- $T_c$  superconductor in a magnetic field.* PhD thesis, ETHZ, 2004.
- [3] Johan Chang. *Magnetic and electronic properties of the high-temperature superconductor  $La_{2-x}Sr_xCuO_4$ .* PhD thesis, Laboratorium f. Neutronenstreuung, ETHZ, 2008.
- [4] Asger Bech Abrahamsen. *Superconductor based energyproduction.* Risø-DTU (2009).
- [5] H. Hilgenkamp and J. Mannhart. *Rev. Mod. Phys.*, 74:485, 2002.
- [6] M. Tinkham. *Introduction to Superconductivity.* McGraw-Hill, 1975.
- [7] J. Bardeen, L. N. Cooper, and J. R. Schrieffer. *Phys. Rev.*, 108:1175, 1957.
- [8] Linda Udby. Recursive solution of schrödingers equation for inhomogeneous superconductors including high- $t_c$  cuprates. Master's thesis, Niels Bohr Institute, University of Copenhagen, 2008.
- [9] J. G. Bednorz and K. A. Müller. *Z. Phys. B*, 64:189, 1986.
- [10] Yoichi Kamihara, Takumi Watanabe, Masahiro Hirano, and Hideo Hosono. *J. Am. Chem. Soc.*, 130:3296, 2008.
- [11] M. Buchanan. *Nature*, 409:8, 2001.
- [12] K. Lefmann, B. Lake, G. Aeppli, S.-W. Cheong, N. B. Christensen, K. N. Clausen, S. Hayden, T. E. Mason, D. F. McMorrow, H. A. Mook, H. M. Rönnow, and H. Takagi. *Journal of Low Temperature Physics*, 135:621, 2004.
- [13] M. K. Wu, J. R. Ashburn, C. J. Torng, P. H. Hor, R. L. Meng, L. Gao, Z. J. Huang, Y. Q. Wang, and C. W. Chu. *Phys. Rev. Lett.*, 58:908, 1987.
- [14] H. Maeda, Y. Tanaka, M. Fukutomi, and T. Asano. *Jnp. J. Appl. Phys*, 27, 1988.

- [15] L. Gao, Y. Y. Xue, F. Chen, Q. Xiong, R. L. Meng, D. Ramirez, and C. W. Chu. *Phys. Rev. B*, 50:4260, 1994.
- [16] H. E. Mohottala, B. O. Wells, W. A. Hines, Ch. Niedermayer, and F. C. Chou. *Phys. Rev. B*, 78:064504, 2008.
- [17] B. Zhao, W. H. Song, X. C. Wu, W. D. Huang, M. H. Pu, J.J. Du, Y. P. Sun, and H. C. Ku. *Superconductor Science and Technology*, 13:165, 2000.
- [18] I. A. Rudnev, B. P. Mikhailov, and P. V. Bobin. *Tech. Phys. Lett.*, 31:176, 2005.
- [19] M. H. Pu, W. H. Song, B. X. C. Wu, T. Hu, Y. P. Sun, and J. J. Du. *Superconductor Science and Technology*, 14:305, 2001.
- [20] J. E. Hoffman, E. W. Hudson K. M Lang, V. Madhavan, H. eisaki, S. Uchida, and J. C. Davis. *Science*, 295:466, 2002.
- [21] H. Kimura, H. Goka, M. Fujita, Y. Noda, K. Yamada, and N. Ikeda. *Phys. Rev. B*, 67:140503(R), 2003.
- [22] J. M. Tranquada, H. Woo, T. G. Perring, H. Goka, G. D. Gu, G. Xu, M. Fujita, and K. Yamada. *Nature*, 429:534, 2004.
- [23] B. M. Andersen, P. Hedegård, and H. Bruus. *Phys. Rev B*, 67:134528, 2003.
- [24] L. Udby, B. M. Andersen, and P. Hedegård. *Phys. Rev. B*, 73:224510, 2006.
- [25] K. Lefmann, P.K. Willendrup, L.Udby, B. Lebech, K. Mortensen, J.O. Birk, K. Klenø, P. Christiansen, J. Saroun, J. Kulda, U. Filges, M. Koennecke, P. Tregenna-Pigot, J. Peters, K. Leutenant, G. Zsigmond, P. Bentley, and E. Farhi. *Virtual experiments: The ultimate aim of neutron ray-tracing simulations*, accepted for printing Jour. Neutr. Res. (2009).
- [26] M. Fujita, K. Yamada, H. Hiraka, P.M Gehring, S. H. Lee, S. Wakamoto, and G. Shirane. *Phys. Rev. B*, 65:064505, 2002.
- [27] S. Nakamae, K. Behnia, N. Mangkorntong, M. Nohara, H. Takagi, S. J. C. Yates, and N. E. Hussey. *Phys. Rev. B*, 68:100502, 2003.
- [28] H. Ding, T. Yokoya, J. C. Campuzano, T. Takahashi, M. Randeria, M. R. Norman, T. Mochiku, K. Kadowari, and J. Giapintzakis. *Nature*, 382:51, 1996.
- [29] V. J. Emery and S. A. Kivelson. *Nature*, 374:434, 1995.
- [30] J. Corson, R. Mallozzi, J. Orenstein, J. N. Eckstein, and I. Bozovic. *Nature*, 398:221, 1999.
- [31] Z. A. Xu, N. P. Ong, Y. Wang, T. Kakeshita, and S. Uchida. *Nature*, 406:486, 2000.

- [32] Yayu Wang, N. P. Ong, Z. A. Xu, T. Kakeshita, S. Uchida, D. A. Bonn, R. Liang, and W. N. Hardy. *Phys. Rev. Lett.*, 88:257003, 2002.
- [33] Yayu Wang, S. Ono, Y. Onose, G. Gu, Yoichi Ando, Y. Tokura, S. Uchida, and N. P. Ong. *Science*, 299:86, 2003.
- [34] N. D. Marthur, F. M Grosche, S. R. Julian, I. R. Walker, D. M. Freye, R. K. W. Haselwimmer, and G. G. Lonzarich. *Nature*, 394:39, 1998.
- [35] G. Aeppli, T. E. Mason, S. M. Hayden, H. A. Mook, and J. Kulda. *Science*, 278:1432, 1997.
- [36] J. Chang, N. B. Christensen, Ch. Niedermayer, K. Lefmann, H.M. Rønnow, D. F. McMorrow, A. Schneidewind, P. Link, A. Hiess, M. Boehm, R. Mottl, S. Pailh es, N. Momono, M. Oda, M. Ido, and J. Mesot. *Phys. Rev. Lett.*, 102:177006, 2009.
- [37] J. Chang, Ch. Niedermayer, R. Gilardi, N. B. Christensen, H.M. Rønnow, D. F. McMorrow, M. Ay, J. Stahn, O. Sobolev, A. Hiess, S. Pailhes, C. Baines, N. Momono, M. Oda, M. Ido, and J. Mesot. *Phys. Rev. B*, 78:104525, 2008.
- [38] M. Kofu, S.-H. Lee, M. Fujita, H.-J. Kang, H. Eisaki, and K. Yamada. *Phys. Rev. Lett.*, 102:047001, 2009.
- [39] E. Demler, S. Sachdev, and Y. Zhang. *Phys. Rev. Lett.*, 87:067202, 2001.
- [40] Y. Zhang, E. Demler, and S. Sachdev. *Phys. Rev. B*, 66:094501, 2002.
- [41] B. Lake, H. M. Rønnow, N. B. Christensen, G. Aeppli, K. Lefmann, D. F. McMorrow, P. Vorderwisch, P. Smeibild, N. Mangkorntong, T. Sasagawa, N. Nohara, H. Takagi, and T. E. Mason. *Nature*, 415:299, 2002.
- [42] B. Lake, G. Aeppli, K. N. CLausen, D. F. McMorrow, K. Lefmann, N. E. Hussey, N. Mangkorntong, M. Nohara, H. Takagi, T. E. Mason, and A. Schroder. *Science*, 291:1759, 2000.
- [43] B. Khaykovich, S. Wakimoto, R. J. Birgeneau, M. A. Kastner, Y. S. Lee, P. Smeibidl, P. Vorderwisch, and K. Yamada. *Phys. Rev. B*, 71:220508(R), 2005.
- [44] H. Kimura, M. Kofu, Y. Matsumoto, and K. Hirota. *Phys. Rev. Lett.*, 91:067002, 2003.
- [45] K. Hirota, K. Yamada, I. Tanaka, and H. Kojima. *Physica B*, 441:817, 1998.
- [46] M. Matsuda, R. J. Birgeneau, H. Chou, Y. Endoh, M. A. Kastner, H. Kojima, K. Kuroda, G. Shirane, I. Tanaka, and K. Yamada. *J. Phys. Soc. Jpn.*, 62:443, 1993.
- [47] L. Udby, N. H. Andersen, F. C. Chou, N. B. Christensen, S. B. Emery, K. Lefmann, J. W. Lynn, H. E. Mohottala, Ch. Niedermayer, and B. O. Wells. *Magnetic ordering in electronically phase separated Sr/O co-doped  $La_{2-x}Sr_xCuO_{4+y}$* , <http://arxiv.org/abs/0904.0095>, 2009.

- [48] J. M. Tranquada, B. J. Sternlieb, J. D. Axe, Y. Nakamura, and S. Uchida. *Nature*, 375:561, 1995.
- [49] J. M. Tranquada. *Neutron Scattering Layered Copper-Oxide Superconductors*. Kluwer, Dordrecht, The Netherlands, 1998.
- [50] H. Kimura, H. Goka, M. Fujita, Y. Noda, K. Yamada, and N. Ikeda. *Phys. Rev. B*, 67:140503(R), 2003.
- [51] M. Braden, G. Heger, P. Schweiss, Z. Fisk, K. Gamayunov, I. Tanaka, and H. Kojima. *Phys. C*, 191:455, 1992.
- [52] C. Chailout, J. Chenevas, S.W. Cheong, Z. Fisk, M. Marezio, and B. Morosin. *Physica C*, 170:87, 1990.
- [53] B. O. Wells, R. J. Birgeneau, F. C. Chou, Y. Endoh, D. C. Johnston, M. A. Kastner, Y. S. Lee, G. Shirane, and J. M. Tranquada. *Z. Phys. B*, 100:535, 1996.
- [54] X. Chen and C. Gong. *Phys. Rev B*, 59:4513, 1999.
- [55] M.-H. Julien. *Physica. B*, 329-333:693, 2003.
- [56] R.J. Birgeneau, C. Stock, J. M. Tranquada, and K. Yamada. *Journal of the Physical Society of Japan*, 75:111003, 2006.
- [57] M. Matsuda, M. Fujita, K. Yamada, R. J. Birgeneau, Y. Endoh, and G. Shirane. *Phys. Rev. B*, 65:134515, 2002.
- [58] N. Ichikawa, S. Uchida, J. M. Tranquada, T. Niemöller, P. M. Gehring, S.-H. Lee, and J. R. Schneider. *Phys. Rev. Lett.*, 85:1738, 2000.
- [59] M. Fujita, H. Goka, K. Yamada, and M. Matsuda. *Phys. Rev. Lett.*, 88:167008, 2002.
- [60] J. M. Tranquada, J. D. Axe, N. Ichikawa, Y. Nakamura, S. Uchida, and B. Nachumi. *Phys. Rev. B*, 54:7489, 1996.
- [61] M. Matsuda, M. Fujita, K. Yamada, R. J. Birgeneau, M. A. Kastner, H. Hiraka, Y. Endoh, S. Wakimoto, and G. Shirane. *Phys. Rev. B*, 62:9148, 2000.
- [62] K. Yamada, C. H. Lee, K. Kurahashi, J. Wada, S. Wakimoto, S. Ueki, H. Kimura, and Y. Endoh. *Phys. Rev. B*, 57:6165, 1998.
- [63] H. Matsushita, H. Kimura, M. Fujita, K. Yamada, K. Hirota, and Y. Endoh. *Journal of Physics and Chemistry of Solids*, 60:1071, 1999.
- [64] N. Christensen, H. M. Rønnow, J. Mesot, R. A. Ewings, N. Momono, M. Oda, M. Ido, M. Enderle, D. F. McMorrow, and A. T. Boothroyd. *Phys. Rev. Lett.*, 98:197003, 2007.
- [65] C.-H. Lee, K. Yamada, Y. Endoh, G. Shirane, R. J. Birgeneau, M. A. Kastner, M. Greven, , and Y.-J. Kim. *J. Phys. Soc. Jpn.*, 69:1170, 2000.

- [66] Ph. Bourges, B. Keimer, S. Pailhès, L. P. Regnault, Y. Sidis, and C. Ulrich. *Physica C*, 424:45, 2005.
- [67] N. B. Christensen, D. F. McMorrow, H. M. Rønnow, B. Lake, S.M. Hayden, G. Aeppli, T.G. Perring, M. Mangkorntong and M. Nohara, and H. Takagi. *Phys. Rev. Lett.*, 93:147002, 2004.
- [68] B. Vignolle, S. M. Hayden, D. F. McMorrow, H. M. Rønnow, B. Lake, C. D. Frost, and T. G. Perring. *Nature Physics*, 3:163, 2009.
- [69] B. Lake, G. Aeppli, T. E. Mason, A. Schröder, D. F. McMorrow, K. Lefmann, M. Isshiki, M. Nohara, H. Takagi, and S. M. Hayden. *Nature*, 400:43, 1999.
- [70] K. Yamada, S. Wakimoto, G. Shirane, C. H. Lee, M. A. Kastner, S. Hosoya, M. Greven, Y. Endoh, and R. J. Birgeneau. *Phys. Rev. Lett.*, 75:1626, 1995.
- [71] S. Petit, A. H. Moudden and B. Hennion, A. Vietkin, and A. Revcolevschi. *Physica B*, 234-236:800, 1997.
- [72] T. E. Mason, G. Aeppli, S. M. Hayden, A. P. Ramirez, and H. A. Mook. *Physica B*, 199-200:284, 1988.
- [73] J. Chang, A. P. Schnyder, R. Gilardi, H. M. Rønnow, S. Pailhes, N. B. Christensen, Ch. Niedermayer, D. F. McMorrow, A. Hiess, A. Stunault, M. Enderle, B. Lake, O. Sobolev, N. Momono, M. Oda, M. Ido, C. Mudry, and J. Mesot. *Phys. Rev. Lett.*, 98:077004, 2007.
- [74] W. Bao, Y. Chen, K. Yamada, A. T. Savici, P. L. Russo, J. E. Lorenzo, and J.-H. Chung. *Phys. Rev. B*, 76:180406, 2007.
- [75] J. M. Tranquada, C. H. Lee, K. Yamada, Y. S. Lee, L. P. Regnault, and H. M. Rønnow. *Phys. Rev B*, 69:174507, 2004.
- [76] A. Rømer. *in preparation (2009)*.
- [77] M. F. Hansen, F. Børdker, S. Mørup, K. Lefmann, K. N. Clausen, , and P.-A. Lindgård. *Phys. Rev. Lett.*, 79:4910, 1997.
- [78] Jacob Garde. *Numerical simulations of magnetic dynamics in nanoparticles*. Master's thesis, University of Copenhagen, 2008.
- [79] P. G. de Gennes. *Superconductivity of metals and alloys*. W. A. Benjamin inc., 1966.
- [80] B. Nachumi, A. Keren, K. Kojima, M. Larkin, G. M. Luke, J. Merrin, O. Tchernyshöv, Y. J. Uemura, N. Ichikawa, M. Goto, and S. Uchida. *Phys. Rev. Lett.*, 77:85421, 1996.
- [81] T. Adachi, S. Yairi, K. Takahashi, Y. Koike, I. Watanabe, and K. Nagamine. *Phys. Rev B*, 69:184507, 2004.

- [82] J. M. Tranquada G. Shirane, S. M. Shapiro. *Neutron Scattering with a Triple-Axis Spectrometer*. Cambridge University Press, 2002.
- [83] Léon van Hove. *Physical Review*, 95:249, 1954.
- [84] G. L. Squires. *Introduction to the Theory of Thermal Neutron Scattering*. Dover Publications Inc., 1978.
- [85] M. J. Cooper and R. Nathans. *Acta Crystallographica*, 23:357, 1967.
- [86] J. Als-Nielsen and D. McMorrow. *Elements of Modern X-Ray Physics*. John Wiley & Sons Ltd., 2001.
- [87] M. F. Collins. *Magnetic critical scattering*. Oxford University Press, 1989.
- [88] C. A. Lucas, E. Gartstein, and R. A. Cowley. *Acta Cryst. A*, 45:416, 1989.
- [89] Davor Balsler: Voigt function model in diffraction line-broadening analysis. Microstructure analysis from diffraction, 1999.
- [90] T. Fliig, N.H. Andersen, J. Berlin, and P.A. Lindgård. *Phys. Rev. B*, 51:12246, 1995.
- [91] Jari í Hjøllum. *Antiferromagnetism in YBCO and CoO Nanoparticles*. PhD thesis, University of Copenhagen, August 2008.
- [92] Jonas Okkels Birk. *Kritiske faseovergange i CoO nanopartikler studeret med neutronspreddning*. Master's thesis, University of Copenhagen, 2009.
- [93] J.R.D. Copley. *J. Neut. Res.*, 1:21, 1993.
- [94] F. James. *Rep. Prog. Phys.*, 43:1145, 1980.
- [95] P. Willendrup, E. Knudsen, E. Farhi, and K. Lefmann. *User and Programmers Guide to the Neutron Ray-tracing Package McStas, version 1.12*. Risø-DTU, 2009.
- [96] More information about the NeXus data format available at <http://www.nexusformat.org>.
- [97] J. D. Jorgensen, B. Dabrowski, S. Pei, D. G. Hinks, L. Soderholm, B. Morosin, J. E. Schirber, E. L. Venturini, and D. S. Ginley. *Phys. Rev B*, 38:11337, 1988.
- [98] P.G. Radaelli, J.D. Jorgensen, A.J. Schultz, B. A. Hunter, J.L. Wagner, F. C. Chou, and D. C. Johnston. *Phys. Rev. B*, 48:499, 1993.
- [99] Y. S. Lee, R. J. Birgeneau, M. A. Kastner, Y. Endoh, S. Wakimoto, K. Yamada, R. W. Erwin, S. H. Lee, and G. Shirane. *Phys. Rev. B*, 60:3643, 1999.
- [100] B. W. Statt, P. C. Hammel, Z. Fisk, S-W. Cheong and F. C. Chou, D. C Johnston, and J. E. Schirber. *Phys. Rev. B*, 52:15575, 1995.

- 
- [101] R. K. Kremer, E. Sigmund, V. Hiznyakov, F. Hentsch, A. Simon, K. A. Müller, and M. Mehring. *Z. Phys. B*, 86:319, 1992.
- [102] R. K. Kremer, V. Hiznyakov, E. Sigmund, A. Simon, and K. A. Müller. *Z. Phys. B*, 91:169, 1993.
- [103] V. J. Emery, S. A. Kivelsen, and H. Q. Lin. *Phys. Rev. Lett.*, 64:475, 1990.
- [104] E. Sigmund, V. Hiznyakov, R.K. Kremer, and A. Simon. *Z. Phys. B*, 94:17, 1994.
- [105] P.G. Radaelli, J.D. Jorgensen, R. Kleb, B. A. Hunter, F. C. Chou, and D. C Johnston. *Phys. Rev. B*, 49:6239, 1994.
- [106] B. O. Wells, Y. S. Lee, M. A. Kastner, R. J. Christianson, R. J. Birgeneau, K. Yamada, Y. Endoh, and G. Shirane. *Science*, 277:1067, 1997.
- [107] J. M. Tranquada, Y. Kong, J. E Lorenzo, D. J. Buttrey, D. E. Rice, and V. Sachan. *Phys. Rev. B*, 50:6340, 1994.
- [108] Y. S. Lee, F. C. Chou, A. Tewary, M. A. Kastner, S. H. Lee, and R. J. Birgeneau. *Phys. Rev. B*, 69:020502, 2004.
- [109] B. Khaykovich, Y. S. Lee, R.W. Erwin, S.-H Lee, S. Wakimoto, K.J. Thomas, M.A. Kastner, and R.J. Birgeneau. *Phys. Rev. B*, 66:014528, 2002.
- [110] B. Khaykovich, R. J. Birgeneau, F. C. Chou, R. W. Erwin, M. A. Kastner, S.-H. Lee, Y. S. Lee, P. Vorderwisch P. Smeibidl, and S. Wakimoto. *Phys. Rev. B*, 67:054501, 2003.
- [111] X. Xiong, P. Wochner, S.C. Moss, Y. Cao, K. Koga, and M. Fujita. *Phys. Rev. Lett.*, 76:2997, 1996.
- [112] H. E. Mohottala, B. O. Wells, J. I. Budnick, W. A. Hines, Ch. Niedermayer, L. Udby, C. Bernhard, A. R. Moodenbaugh, and F. C. Chou. *Nature Materials*, 5:377, 2006.
- [113] C. Rial, U. Amador, E. Morán, M.A. Alario-Franco, and N.H. Andersen. *Physica C*, 234:237, 1994.
- [114] Hashini E. Mohottala. *LSCO+O*. PhD thesis, University of Connecticut, 2006.
- [115] C. Rial, , E. Morán, M.A. Alario-Franco, U. Amador, and N.H. Andersen. *Physica C*, 254:233, 1995.
- [116] C. Rial, , E. Morán, M.A. Alario-Franco, U. Amador, and N.H. Andersen. *Physica C*, 278:278, 1997.
- [117] Linda Udby. Experimental report from BW5, October 2008.
- [118] Linda Udby. Experimental report from BW5, December 2007.

- [119] Linda Udby. Experimental report from BW5, February 2006.
- [120] T. B. S. Jensen. Experimental report from BW5, February 2009.
- [121] D. Vaknin, S. K. Sinha, D. E. Moncton, D. C. Johnston, J. M. Newsam, C. R. Safinya, and H. E. King Jr. *Phys. Rev. Lett.*, 58:2802, 1987.
- [122] J. M. Tranquada, J. D. Axe, N. Ichikawa, A. R. Moodenbaugh, Y. Nakamura, and S. Uchida. *Phys. Rev. B*, 78:338, 1997.
- [123] J. M. Tranquada, D. J. Buttrey, and D. E. Rice. *Phys. Rev. Lett.*, 70:445, 1993.
- [124] J. M. Tranquada, D. J. Buttrey, V. Sachan, and J. E. Lorenzo. *Phys. Rev. Lett.*, 73:1003, 1994.
- [125] S. A. Kivelson, I. P. Bindloss, E. Fradkin, V. Oganesyan, J. M. Tranquada, A. Kapitulnik, and C. Howald. *Reviews of Modern Physics*, 75:1201, 2003.
- [126] S. Shamoto, M. Sato, J. M. Tranquada, B. J. Sternlieb, and G. S. Shirane. *Phys. Rev. B*, 48:13817, 1993.
- [127] Susumu Katano, Masugu Sato, Kazuyoshi Yamada, Takao Suzuki, and Tetsuo Fukase. *Phys. Rev. B*, 62(22):R14677–R14680, 2000.
- [128] Linda Udby. Experimental report from RITA-II, November 2005.
- [129] M.v. Zimmermann, J.R. Schneider, T. Frello, N.H. Andersen, J.H. Madsen, M. Käll, H.F. Poulsen, R. Liang, P. Dosanjh, and W.N. Hardy. *Phys. Rev. B*, 68:104515, 2003.
- [130] G. Uemin. *Phys. Rev. B*, 50:9531, 1994.
- [131] L. Udby et al., *Neutron- and hard-xray study of the staging structure in co-doped  $La_{2-x}Sr_xCuO_{4+y}$* , in preparation, 2009.
- [132] More information about the SINQ target available at. <http://asq.web.psi.ch/ASQ/facilities/SINQSYSTEMS.html#ch2>.
- [133] S.N. Klausen, K. Lefmann, D.F. McMorrow, F. Altorfer, S. Janssen, and M. Lüthy. *Appl. Phys. A*, 74:S1508, 2002.
- [134] McStas website. <http://www.mcstas.org>.
- [135] S. M. Shapiro and N. J. Chesser. *Nuc. Instr. Meth.*, 101:183, 1972.
- [136] C. R. H. Bahl, K. Lefmann, A. B. Abrahamsen, H. M. Rønnow, F. Saxild, T. B. S. Jensen, L. Udby, N. H. Andersen, N. B. Christensen, H. S. Jacobsen, T. Larsen, P. S. Häfliger, S. Streule, and Ch. Niedermayer. *Nucl. Instr. and Meth. in Phys. Res. B*, 246:452, 2006.
- [137] C.R.H. Bahl, P. Andersen, S.N. Klausen, and K. Lefmann. *Nucl. Instr. Meth. Phys. Res. B*, 226:667, 2004.

- 
- [138] J. Baruchel, J. L. Hodeau, M. S. Lekmann, J. R. Regnard, and C. Schlenker. *Neutron and synchrotron radiation for condensed matter studies*. Les Editions de Physique / Springer-Verlag, 1993.
- [139] K. Lefmann. *Neutron Scattering: Theory, Instrumentation and Simulation*. University of Copenhagen, 2009.
- [140] K. Lefmann, D.F. McMorrow, H.M. Rønnow, K. Nielsen, K.N. Clausen, B. Lake, and G. Aeppli. *Physica B*, 283:343, 2000.
- [141] More information about the calibration of  $\Omega_A$  of the seven blade analyser at RITA-II is found at. <http://spectroscopy.web.psi.ch/rita2/files/OMAcalib.pdf>.
- [142] J. G. Barker, C. J. Glinka, J. J. Moyer, M. H. Kim, A. R. Drewsb, and M. Agamalianc. *J. Appl. Cryst.*, 38:1004, 12005.
- [143] H. A. Graf, J. R. Schneider, K. Freund, and M. S. Lehmann. *Acta Cryst.*, 37:863, 1981.
- [144] Y.-J. Kim, G. D. Gu, T. Gog, and D. Casa. *Phys. Rev. B*, 77:064520, 2008.
- [145] Linda Udby. Experimental report from RITA-II, August 2005.
- [146] Linda Udby. Experimental report from RITA-II, June 2008.